University of Kentucky
UKnowledge

Theses and Dissertations--Earth and Environmental Sciences

Earth and Environmental Sciences

2020

TESTING INTERPRETATIONS OF THE DISPLACEMENT MAGNITUDE OF THE TETON FAULT AND UPLIFT OF THE TETON RANGE, WYOMING WITH INTEGRATED FLEXURAL-KINEMATIC AND THERMAL MODELING

Autumn Helfrich
University of Kentucky, autumnhelfrich21@gmail.com
Author ORCID Identifier:
https://orcid.org/0000-0002-8288-7236
Digital Object Identifier: https://doi.org/10.13023/etd.2020.487

Right click to open a feedback form in a new tab to let us know how this document benefits you.

Recommended Citation

Helfrich, Autumn, "TESTING INTERPRETATIONS OF THE DISPLACEMENT MAGNITUDE OF THE TETON FAULT AND UPLIFT OF THE TETON RANGE, WYOMING WITH INTEGRATED FLEXURAL-KINEMATIC AND THERMAL MODELING" (2020). *Theses and Dissertations--Earth and Environmental Sciences*. 84.
https://uknowledge.uky.edu/ees_etds/84

This Master's Thesis is brought to you for free and open access by the Earth and Environmental Sciences at UKnowledge. It has been accepted for inclusion in Theses and Dissertations--Earth and Environmental Sciences by an authorized administrator of UKnowledge. For more information, please contact UKnowledge@lsv.uky.edu.

STUDENT AGREEMENT:

I represent that my thesis or dissertation and abstract are my original work. Proper attribution has been given to all outside sources. I understand that I am solely responsible for obtaining any needed copyright permissions. I have obtained needed written permission statement(s) from the owner(s) of each third-party copyrighted matter to be included in my work, allowing electronic distribution (if such use is not permitted by the fair use doctrine) which will be submitted to UKnowledge as Additional File.

I hereby grant to The University of Kentucky and its agents the irrevocable, non-exclusive, and royalty-free license to archive and make accessible my work in whole or in part in all forms of media, now or hereafter known. I agree that the document mentioned above may be made available immediately for worldwide access unless an embargo applies.

I retain all other ownership rights to the copyright of my work. I also retain the right to use in future works (such as articles or books) all or part of my work. I understand that I am free to register the copyright to my work.

REVIEW, APPROVAL AND ACCEPTANCE

The document mentioned above has been reviewed and accepted by the student's advisor, on behalf of the advisory committee, and by the Director of Graduate Studies (DGS), on behalf of the program; we verify that this is the final, approved version of the student's thesis including all changes required by the advisory committee. The undersigned agree to abide by the statements above.

Autumn Helfrich, Student

Dr. J. Ryan Thigpen, Major Professor

Dr. Michael McGlue, Director of Graduate Studies

TESTING INTERPRETATIONS OF THE DISPLACEMENT MAGNITUDE OF THE TETON FAULT AND UPLIFT OF THE TETON RANGE, WYOMING WITH INTEGRATED FLEXURAL-KINEMATIC AND THERMAL MODELING

THESIS

A thesis submitted in partial fulfillment of the
requirements for the degree of Master of Science in the
College of Arts and Sciences
at the University of Kentucky

By

Autumn Lynne Helfrich

Lexington, Kentucky

Director: Dr. J. Ryan Thigpen, Professor of Earth and Environmental Sciences

Lexington, Kentucky

2020

Copyright © Autumn Lynne Helfrich 2020
https://orcid.org/0000-0002-8288-7236

ABSTRACT OF THESIS

TESTING INTERPRETATIONS OF THE DISPLACEMENT MAGNITUDE OF THE TETON FAULT AND UPLIFT OF THE TETON RANGE, WYOMING WITH INTEGRATED FLEXURAL-KINEMATIC AND THERMAL MODELING

The Teton fault is a range-front normal fault in northwestern Wyoming. Previous estimates of the maximum displacement (D_{max}) on the Teton fault cover a wide range (2 - 11 km). Discrepancies also exist regarding the slip onset timing, which spans 2 - 13 Ma. To address these discrepancies, the exhumation history of the Teton Range is here investigated using forward flexural-kinematic (*Move*) and thermal-kinematic (*Pecube)* models that can be compared with previously reported apatite fission track (AFT) and apatite (U-Th)/He (AHe) ages from Mount Moran, which has been previously hypothesized to represent the paleo-center of the Teton fault.

In this study, kinematic models that include flexural isostasy and erosion were constructed to test possible structural solutions for Teton fault evolution. Free parameters include fault dip angle, elastic thickness (T_e), depth of detachment (Z_d) and magnitude (D_{max}) and duration of slip. Flexural parameters and the fault subsurface geometry were constrained by comparing model results with the present-day wavelength of footwall uplift and structural configuration of the Jackson Hole basin. This led to the identification of a reference model that includes a surface fault dip of 70°, T_e of 5 km, and Z_d of 15 km. This reference model structural evolution is then used to create velocity fields for the thermal-kinematic models, which produces a 2D thermal history that includes predicted AFT and AHe ages, to be compared with the observed ages.

The flexural-kinematic models yield predictions of the footwall uplift contribution to total fault slip, which can then be compared to the range of D_{max} estimates. Using these model results, previous estimates for D_{max} (2 - 9 km) correspond to footwall uplifts of 0.7-2.4 km. For comparison, the modern footwall relief at Mount Moran (~1.8 km) and Grand Teton (~2.2 km) would yield modeled D_{max} estimates of 6 - 8 km, which is a minimum estimate, as these values do not account for an estimated ~2 km of overburden erosion. Thus, these model results indicate that the D_{max} for the Teton fault is likely >9 km. To produce the footwall uplift necessary to exhume reset AFT ages observed at the base of the Moran transect (~4.2 km), flexural-kinematic models require D_{max} estimates of 13 - 17 km. Results from the thermal-kinematic history that best match observed AHe and AFT data include D_{max} estimates of 15 - 17 km. These preferred models also suggest that the onset Teton fault motion and footwall exhumation began ~12 Ma.

KEYWORDS: Teton Range, Tectonics, Flexural-kinematic modeling, Thermal-kinematic modeling

Autumn Lynne Helfrich

(Name of Student)

11/19/2020

Date

TESTING INTERPRETATIONS OF THE DISPLACEMENT MAGNITUDE OF THE TETON FAULT AND UPLIFT OF THE TETON RANGE, WYOMING WITH INTEGRATED FLEXURAL-KINEMATIC AND THERMAL MODELING

By
Autumn Lynne Helfrich

Dr. J. Ryan Thigpen
Director of Thesis

Dr. Michael McGlue
Director of Graduate Studies

11/19/2020
Date

ACKNOWLEDGEMENTS

I would first like to thank those organizations and funds that generously contributed financially to the completion of my thesis research, professional conference travel and fees, and field travel – Geological Society of America Graduate Student Research Grant, University of Kentucky Earth and Environmental Sciences (EES) Ferm fund, EES Brown-McFarlan fund, and EES Pirtle Fellowship. Additionally, thank you to the National Science Foundation, award 1932808, for funding the larger interdisciplinary Teton project at UK.

This thesis would not have been possible without the guidance from my advisor Dr. Ryan Thigpen and his wife, Summer Brown. Ryan, you have an outstanding way of telling a geologic story and painting the bigger picture. Your guidance and knowledge were invaluable for my work. Throughout my two years at UK we ran into some wild hurdles, namely: legal battles for free software and a global pandemic. During each, you were an anchor and immeasurably supportive towards me and my work. I watched you work tirelessly towards your academic goals, pursuing grant after grant, planning one field season after another, and unceasingly adapting to advising more students and providing for their unique needs. You stuck true to your motto: "I would never ask you to do anything I would not do myself" and I learned along the way how to push myself harder each semester towards my own goals. Our research group was always a shared success environment and I feel incredibly fortunate to have learned from you both in the lab and in the field. Summer, thank you for initiating the "Teton project" that many of us in the *Thigpen School of Geosciences* have been fortunate enough to build upon. I am grateful to you for support professionally and personally over the past few years. With

you as an exemplar, I am encouraged to continue in my pursuits as a professional, determined, woman in the geosciences. A special thank you to Thurso Brown-Thigpen and Bodie Thigpen-Brown for comfort in trying times.

I would also like to extend thanks to my committee members, Dr. Mike McGlue and Dr. Jason Dortch for direction and resources along the way. Thank you to Sarah Johnson, Brandon Spencer, Ryan Goldsby, and Dr. Sean Gallen for your encouragement and insight in our weekly SPFI meetings.

Victoria and Dr. McQuarrie, thank you for your willingness to provide lab space, software, and generous modeling support throughout the completion of my thesis. None of this work would have been possible without you and the resources you provided at the University of Pittsburgh. Thank you to Midland Valley for the generous academic license donation of Move used for kinematic modeling. Thank you also to the communities behind the multiple open-source software packages on which this project depended.

Thank you to an extensive list of individuals that provided both field assistance and lab support including, but not limited to: Cooper Cearley, Hillary Johnson, Giliane Rasbold, Spencer Dixon, Amber Dunn, Elisha Miller, Gillian Clark, and Madison Preece. My success in this program is largely in thanks to abundant comradery in the office from Meredith Swallom, Bailee Hodelka, Felicia Harris, Antonia Bottoms, Aspen Davis, Nick Powell, and Bill Swanger.

This graduate work would not have been accomplished without the people surrounding me who had faith in both my ability and the process. Most notably, my mother and father, for their love and support, and their feedback during my time in Kentucky. The lessons taught to me while growing up encouraged perseverance and

confidence, both of which have suited me well in pursuing the opportunities that have led me to success throughout my formal education. Secondly, the support from my siblings, Sierra and Brandon for a lifetime of emotional support and unofficial counseling. My interest in geology was gained primarily on the early trips in my life visiting uncles Brian, Joe, and Mark in Oregon and Alaska, where I developed a love for big skies and even bigger mountains – I would not be in this position if not for their inspiration to explore outdoors.

TABLE OF CONTENTS

ACKNOWLEDGEMENTS.....iii
LIST OF TABLES.....viii
LIST OF FIGURES.....ix
LIST OF ABBREVIATIONS AND SYMBOLS.....xii
CHAPTER 1. Introduction.....1
1.1 Scientific Motivation.....1
1.2. Study Approach.....3
CHAPTER 2. Background.....8
2.1 Basin and Range normal faulting.....8
2.2 Regional overview.....9
2.3 Displacement and age interpretations for the Teton Fault.....10
CHAPTER 3. Methodology.....15
3.1 Flexural – kinematic modeling.....16
3.1.1 Defining modeled fault geometries.....18
3.1.2 Generating observed swath topographic profiles.....18
3.2 Thermal – kinematic modeling.....19
CHAPTER 4. Results.....27
4.1 Flexural – kinematic modeling.....27
4.2 Identifying a reference flexural-kinematic model.....29
4.3 Thermal – kinematic modeling.....30
CHAPTER 5. Discussion.....71
5.1 Using flexural – kinematic modeling to determine a minimum threshold D_{max}.....71
5.2 Thermal structure of the crust during Teton fault evolution.....71
5.3 Comparing observed and model predicted AHe cooling ages.....73
5.4 Age-elevation relationships in the predicted AHe data vs. observed AHe data.....74
5.5 Comparing observed and model predicted AFT cooling ages.....78
5.6 Previous estimates for D_{max} in the context of new data.....80
CHAPTER 6. Conclusions.....94
APPENDIX: Thermal-kinematic (*Pecube*) models 1 - 12.....95
REFERENCES CITED.....140

VITA.....157

LIST OF TABLES

Table 1.1 Previous estimates of displacement on the Teton Fault……..…...5
Table 3.1 Flexural-kinematic model parameters tested in *2D-Move*……...…….…….....21
Table 3.2 Mechanical properties for *2D-Move* flexural-kinematic models……...….....22
Table 3.3 Material properties and numerical parameters tested in *Pecube* thermal kinematic models…….....……...……...…….....23
Table 3.4 Constant velocity models tested in *Pecube* thermal-kinematic models…..…….24
Table 4.1 Flexural-kinematic (*Move*) forward models tested and the measured results.....33
Table 4.2 Predicted and observed AHe and AFT data…….....34

LIST OF FIGURES

Figure 1.1 Regional DEM of the Teton -Yellowstone area in northwestern Wyoming…....6
Figure 3.1 Simplified schematic of step-wise process in flexural-kinematic modeling software……25
Figure 3.2 Modern day DEM from which the observed elevations are extracted as minimum, mean, and maximum elevation profiles.....26
Figure 4.1 Flexural-kinematic (*Move*) model with a fault dip angle of 70°, T_e = 5 km, and Z_d = 15 km.....37
Figure 4.2 Flexural-kinematic model 1 evaluates a 70° fault, with T_e = 5, Z_d = 20, and D_{max} = 13 km.....38
Figure 4.3 Flexural-kinematic model 2 evaluates a 70° fault, with T_e = 5, Z_d = 15, and D_{max} = 13 km.....39
Figure 4.4 Flexural-kinematic model 3 evaluates a 60° fault, with T_e = 15, Z_d = 20, and D_{max} = 13 km.....40
Figure 4.5 Flexural-kinematic model 4 evaluates a 45° fault, with T_e = 15, Z_d = 20, and D_{max} = 13 km.....41
Figure 4.6 Flexural-kinematic model 5 evaluates a 45° fault, with T_e = 10, Z_d = 20, and D_{max} = 13 km.....42
Figure 4.7 Flexural-kinematic model 6 evaluates a 70° fault, with T_e = 10, Z_d = 15, and D_{max} = 13 km.....43
Figure 4.8 Flexural-kinematic model 7 evaluates a 70° fault, with T_e = 15, Z_d = 20, and D_{max} = 13 km.....44
Figure 4.9 Flexural-kinematic model 8 evaluates a 60° fault, with T_e = 5, Z_d = 15, and D_{max} = 13 km.....45
Figure 4.10 Flexural-kinematic model 9 evaluates a 45° fault, with T_e = 5, Z_d = 15, and D_{max} = 13 km.....46
Figure 4.11 Flexural-kinematic model 10 evaluates a 60° fault, with T_e = 5, Z_d = 20, and D_{max} = 13 km.....47
Figure 4.12 Flexural-kinematic model 11 evaluates a 45° fault, with T_e = 5, Z_d = 15, and D_{max} = 17 km.....48
Figure 4.13 Flexural-kinematic model 12 evaluates a 60° fault, with T_e = 5, Z_d = 15, and D_{max} = 17 km.....50
Figure 4.14 Flexural-kinematic model 13 evaluates a 70° fault, with T_e = 5, Z_d = 15, and D_{max} = 17 km.....52
Figure 4.15 Modeled flexural-kinematic topographic profiles for fault dip angles of 45°, 60°, and 70° and D_{max} = 13 km and D_{max} = 17.....54
Figure 4.16 Simplified schematic of the Teton fault.....55
Figure 4.17 Thermal-kinematic model 13 evaluated for a constant slip rate with fault slip onset at 5 Ma for D_{max} = 11 km.....56
Figure 4.18 Thermal-kinematic model 13 evaluated in *Pecube* for a constant slip rate with fault slip onset at 5 Ma for D_{max} = 13 km.....57
Figure 4.19 Thermal-kinematic model 13 evaluated in *Pecube* for a constant slip rate with fault slip onset at 5 Ma for D_{max} = 15 km.....58

Figure 4.20 Thermal-kinematic model 13 evaluated in *Pecube* for a constant slip rate with fault slip onset at 5 Ma for D_{max} = 17 km.....59
Figure 4.21 Thermal-kinematic model 13 evaluated in *Pecube* for a constant slip rate with fault slip onset at 12 Ma for D_{max} = 11 km.....60
Figure 4.22 Thermal-kinematic model 13 evaluated in *Pecube* for a constant slip rate with fault slip onset at 12 Ma for D_{max} = 13 km.....61
Figure 4.23 Thermal-kinematic model 13 evaluated in *Pecube* for a constant slip rate with fault slip onset at 12 Ma for D_{max} = 15 km.....62
Figure 4.24 Thermal-kinematic model 13 evaluated in *Pecube* for a constant slip rate with fault slip onset at 12 Ma for D_{max} = 17 km.....63
Figure 4.25 Thermal-kinematic model 13 evaluated in *Pecube* for a constant slip rate with fault slip onset at 19 Ma for D_{max} = 9 km.....64
Figure 4.26 Thermal-kinematic model 13 evaluated in *Pecube* for a constant slip rate with fault slip onset at 19 Ma for D_{max} = 11 km.....65
Figure 4.27 Thermal-kinematic model 13 evaluated in *Pecube* for a constant slip rate with fault slip onset at 19 Ma for D_{max} = 13 km.....66
Figure 4.28 Thermal-kinematic model 13 evaluated in *Pecube* for a constant slip rate with fault slip onset at 19 Ma for D_{max} = 14 km.....67
Figure 4.29 Thermal-kinematic model 13 evaluated in *Pecube* for a constant slip rate with fault slip onset at 19 Ma for D_{max} = 15 km.....68
Figure 4.30 Thermal-kinematic model 13 evaluated in *Pecube* for a constant slip rate with fault slip onset at 19 Ma for D_{max} = 16 km.....69
Figure 4.31 Thermal-kinematic model 13 evaluated in *Pecube* for a constant slip rate with fault slip onset at 19 Ma for D_{max} = 17 km.....70
Figure 5.1 Measured surface heat flow (Q_o) in the Snake River Plain and the Teton-Yellowstone Region.....83
Figure 5.2 Modeled geothermal gradients produced for a range of parameters for basal mantle heat flow (Q_m; W m^{-2}) and internal heat generation values to produce a range of surface heat flows (Q_o, W m^{-2}) which can be compared to the measured Q_o from Figure 5.1.....84
Figure 5.3 Conceptual figure illustrating potentiation age-elevation trends of AHe or AFT ages during tectonic exhumation.....85
Figure 5.4 Google Earth image of the relative sample locations from Brown et al., (2017) subvertical transects at Mount Moran.....86
Figure 5.5 Age-elevation plots for predicted AHe, where fault slip onset begins at 5 Ma.....87
Figure 5.6 Age-elevation plots for predicted AHe, where fault slip onset begins at 12 Ma.....88
Figure 5.7 Age-elevation plots for predicted AHe, where fault slip onset begins at 19 Ma.....89
Figure 5.8 Age-elevation plots for predicted AFT data, where fault slip onset begins at 5 Ma.....90
Figure 5.9 Age-elevation plots for predicted AFT data, where fault slip onset begins at 12 Ma.....91
Figure 5.10 Age-elevation plots for predicted AFT data, where fault slip onset begins at 19 Ma.....92

Figure 5.11 Interpreted cross section through Mount Moran, Moran Bay, and the Jackson Lake basin.....93

LIST OF ABBREVIATIONS AND SYMBOLS

°C	temperature in degrees Celsius
A_0	volumetric heat production
AFT	apatite fission track
AHe	apatite (U-Th)/He
c	specific heat capacity
D	flexural rigidity
DEM	digital elevation model
D_{max}	maximum displacement
E	Young's modulus
ef	e-folding depth
g	acceleration due to gravity
GPa	gigapascal
K	curvature
k	thermal conductivity
ka	thousand years
km	kilometer(s)
m	meter(s)
Ma	million years
M_e	elastic bending moment
q	applied vertical load
T	temperature

t	time
T_c	closure temperature
T_e	effective elastic thickness
v	Poisson's ratio
w	vertical deflection
yr	year
Z_d	depth to detachment
$\mu W\ m^{-3}$	microwatt per meter cubed
ρ_c	load density
ρ_m	mantle density

CHAPTER 1. INTRODUCTION

1.1 Scientific Motivation

The Basin and Range province is characterized by large-scale extensional faulting across part of the western United States. One such active crustal-scale structure, the Teton fault, accommodates intraplate extension in the northeastern Basin and Range province in Wyoming (Figure 1.1a). Both the age of fault initiation and total displacement along the Teton fault has remained controversial and enigmatic (e.g., Byrd et al., 1994 and references therein). Because the total displacement of the Teton fault is critical for constraining slip history, total lateral extent, and the consequent seismic hazard in the Teton-Yellowstone region, it is of increasing importance that this controversy is resolved. Previous studies have proposed a range of Teton fault displacement estimates between 2.1 – 11.0 km (Table 1.1). Stratigraphic interpretations yield displacement estimates, which largely rely on the presence and location of the Precambrian-Paleozoic unconformity in Jackson Hole (6 – 9 km of throw; Behrendt et al., 1968, Love and Reed, 1971) or post-depositional rotation of the Huckleberry Ridge Tuff (~3 km of throw; Gilbert et al., 1983; Smith et al., 1993a). Other studies have proposed total footwall uplift estimates of 2.5 – 3.5 km, with a maximum throw of 8 km, using inverse ray tracing and gravity modeling to deduce throw magnitudes (Byrd et al., 1994). However, geophysical techniques such as gravity modeling and seismic refraction have not yet been able to clearly image the deep subsurface geometry of the Teton fault.

Alternately, low temperature thermochronology can be used to directly date the cooling of the range and thus provide estimates for the total magnitude of footwall

exhumation, which can be used as a potential indicator of total displacement. The development of new apatite fission track (AFT) calibration techniques (Fitzgerald et al., 1995) and the introduction of apatite (U-Th)/He (AHe) thermochronology (Farley, 2000) have led to more comprehensive methods for constraining near-surface T-t paths in the upper ~5 km of crust. Low temperature thermochronometers such as AFT and AHe can record the time that rock particles passed through those closure temperatures (T_c ~110°C and 65°C, respectively) and therefore provide critical information about the evolving thermal structure of the crust in active tectonic settings (Stüwe et al., 1994; Rahn and Grasemann, 1999; Ehlers and Farley, 2003). AFT and AHe techniques have been used to reconstruct exhumation histories (Crowley et al., 2002) and to deduce timing, rate, total displacement, and footwall uplift in normal fault systems (Ehlers et al., 2003; Stockli et al., 2000; Armstrong et al., 2003), specifically in young extensional settings (Ehlers et al., 2001; Densmore et al. 2005) and in the Basin and Range province (e.g. Fitzgerald et al., 1991; Foster et al., 1993; Miller et al., 1999; Armstrong et al., 2003; Stockli, 2005).

In the Teton Range, thermochronologic data was limited to a single pre-zeta calibration AFT dataset (e.g., Roberts and Burbank, 1993) until more recent studies introduced an increasingly comprehensive AHe and AFT dataset for the Teton Range (Brown, 2010; Brown et al., 2017; Hoar, 2018; Swallom, 2019). In the Brown et al. (2017) study, AHe cooling ages from a transect at Mount Moran were used to estimate the minimum amount of footwall uplift (~2.4 km) that has occurred by assuming a geothermal gradient of 25°C km^{-1}. Provided that footwall uplift accounts for 30 – 40% of total exhumation as indicated by generic models of normal faults (Thompson and Parsons, 2009), this data suggests a minimum estimate for total throw of 6 – 8 km. This

estimate does not include AFT ages of 13.6 ± 4.0 Ma and 9.5 ± 2.8 Ma, also analyzed in this study, which record exhumation younger than the age of slip onset and suggest an increase in minimum footwall uplift of 3.1 – 3.6 km. Using the same assumptions as above increases the minimum total displacement estimate to 9 – 11 km. If correct, these studies indicate that total displacement on the Teton fault may be substantially greater than that proposed by previous geophysical and stratigraphic studies.

1.2 Study Approach

In an attempt to resolve the evolving debate of maximum displacement (D_{max}) on the Teton fault, this study tests the full range of proposed displacement estimates using flexural-kinematic (*Move;* Petroleum Experts) and thermal-kinematic (*Pecube*; Braun, 2003) modeling to derive fault evolution(s) that most closely reproduce: (a) the flexural wavelength of the footwall uplift and the resulting erosional history, (b) the flexural wavelength of the adjacent hanging wall basin, and (c) the cooling history derived from the most comprehensive and extensive footwall AFT and AHe transect near Mount Moran (Brown, 2010; Brown et al., 2017; Hoar, 2018; Swallom, 2019), which is interpreted to preserve the D_{max} along the Teton fault (Roberts and Burbank, 1993; Brown et al., 2017). To do this, flexural-kinematic models are used to constrain the subsurface fault geometry and the effective elastic thickness of the crust based on comparisons between the modeled and observed isostatic response, which controls the width of the flexural uplift and that of the adjacent hanging wall basin. With the subsurface geometry constrained, fault displacement magnitude and fault slip timing can be further evaluated using comparisons between AFT and AHe cooling data and the results of thermal-

kinematic models. The results of this study provide new insight for the controversial kinematic evolution of the Teton fault and the resulting footwall topographic history. Additionally, these models may help define the range of critical parameters (e.g. fault geometry, effective elastic thickness, thermal-kinematic conditions, and the relative contribution of hanging wall drop and footwall uplift to total normal fault slip magnitude), that directly influence the magnitude of footwall exhumation and the resultant cooling histories in intracontinental extensional settings such as the Basin and Range.

Table 1.1 – Previous estimates of displacement on the Teton Fault. Table modified from Byrd et al. (1994).

Study	**Throw (km)**	**Criteria**
Blackwelder, 1915	>3	physiographic, stratigraphic
Edmund, 1951	2.1 – 4.3	stratigraphic, structural
Fryxell et al., 1941	2.4	stratigraphic, geomorphic
Lavin and Bonini, 1957	5 – 6	gravity model
Behrendt et al., 1968	7	gravity, seismic refraction
Tibbetts et al., 1969	7	seismic refraction
Love and Reed, 1971	7.6 – 9.1	stratigraphic
Love, 1977; 1987	9 – 11	stratigraphic
Gilbert et al., 1983	2.1 – 2.9	Huckleberry Ridge Tuff
Roberts and Burbank, 1993	3.5	fission track data (AFT)
Byrd et al., 1994	2.5 – 3.5	gravity, seismic refraction, geodetic data, fault models
Brown et al., 2017	>6	apatite helium data (AHe) and AFT
Thigpen et al., (in prep)	9 – 11	AFT/AHe

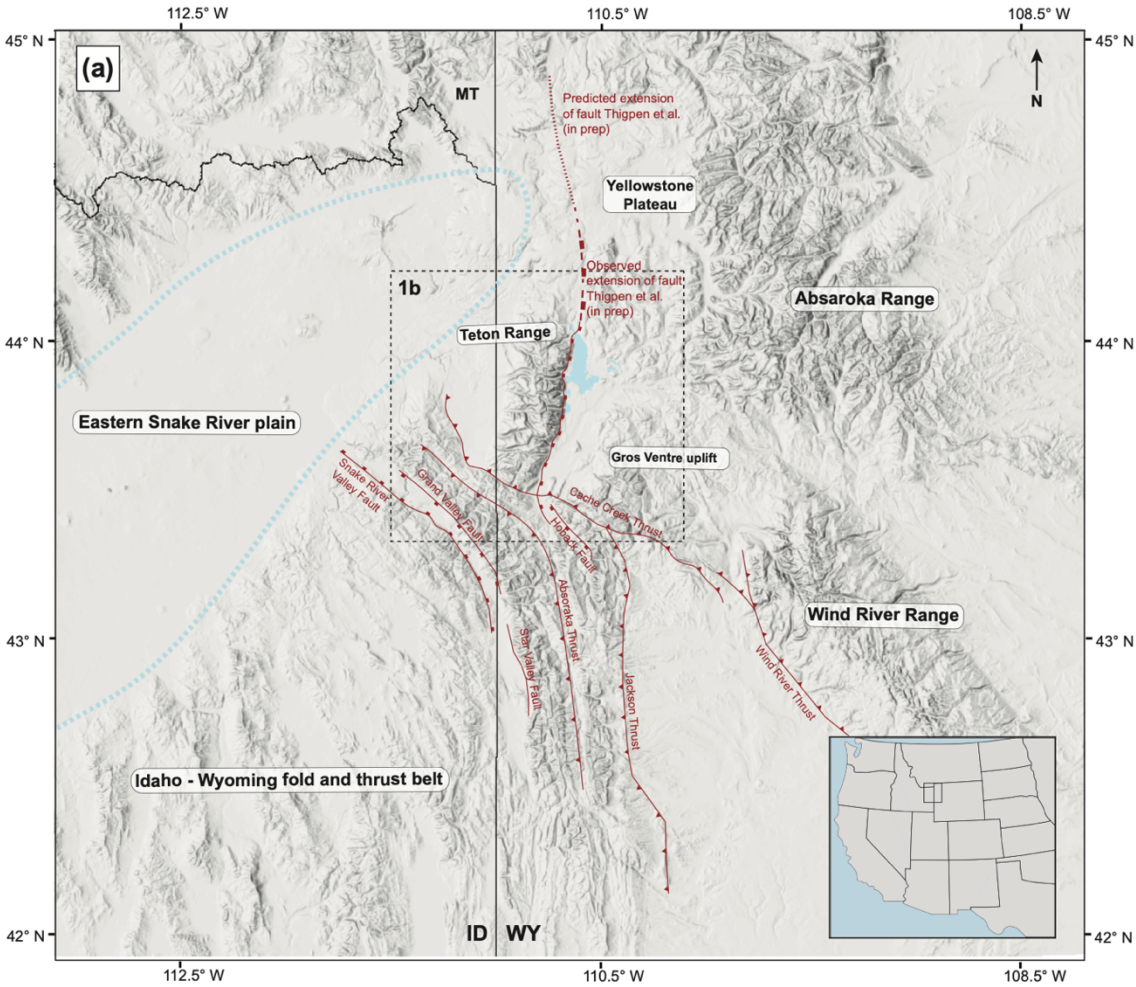

Figure 1.1 – (a) Regional DEM of the Teton-Yellowstone area in northwestern Wyoming showing the extent of the Basin and Range, eastern Snake River plain, Yellowstone plateau, Absaroka Range, Wind River Range, and the Idaho-Wyoming thrust belt. Map topography derived from 10 m digital terrain elevation data acquired from USGS EarthExplorer.

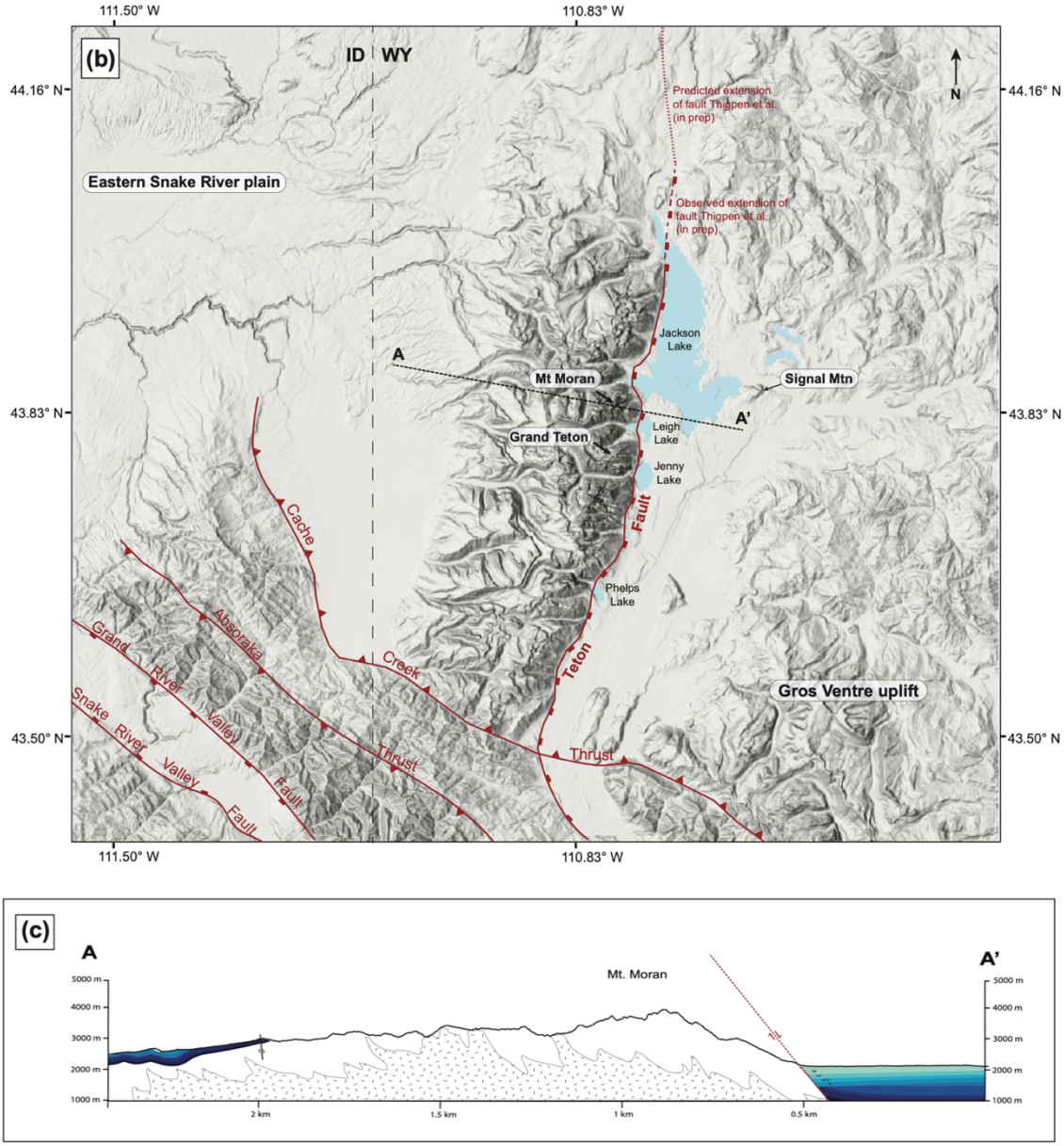

F*igure 1.2 – (continued) (b) local DEM of the Teton Range which is formed by displacement on the Teton fault and prominent lakes in the hanging wall (c) profile A-A' through Mount Moran is represented by a simplified schematic cross-section through the range. Modified from Brown et al., 2010.*

CHAPTER 2. BACKGROUND

2.1 Basin and Range normal faulting

Research on Basin and Range normal faults surrounding the Snake River plain (e.g. Lost River fault, Lemhi fault, Beaverhead fault) has led to a better understanding of the overall geometry and behavior of normal faults and the relationship between fault length, total displacement, and footwall uplift in extensional terranes (McQuarrie and Rodgers, 1998; Byrd, 1994; Pierce and Morgan, 1992; Anders and Sleep, 1992; Anders et al., 1989). In extensional terranes such as the Basin and Range, thinning of the upper crust along crustal-scale normal faults produces an isostatic imbalance and results in flexural uplift of the normal fault footwall coeval with the hanging wall drop due to extension (Walcott, 1970; Turcotte, 1979; Beaumont, 1978; Watts et al., 1982). The total magnitude of footwall uplift and the corresponding crustal length scale over which this occurs are directly impacted by lithospheric flexural rigidity, total fault displacement, near surface and deeper fault dip, and the depth to detachment (Densmore et al., 2005; Reiners et al., 2000). Because of this, it is possible to assess the isostatic behavior of the upper crust by testing a range of flexural rigidities, fault geometries and total slip magnitudes. Flexural rigidity is often expressed in terms of effective elastic thickness (T_e). In the Basin and Range, characteristic values of T_e range from 5 – 15 km (Lowry and Smith, 1994; Watts and Burov, 2003, Tesauro et al., 2015). Although Basin and Range normal faults have rarely been imaged in the subsurface (e.g. Velasco et al., 2010; Chavez-Perez et al., 1998; Von Tish et al., 1985; Wernicke and Burchfiel, 1982) they are often interpreted to be steeply dipping (45 –70°) near the surface and flatten into shallow listric detachments (10 – 20°) at depths of 15 km – 20 km, near the brittle-ductile

transition zone (Smith and Bruhn, 1984; Mohapatra and Johnson, 1998). Previous estimates for the dip of the Teton fault span a wide range (35 – 90°). Early approximations proposed a fault dip of 60 – 90° from gravity forward models (Lavin and Bonini, 1957) and later Behrendt et al. (1968) used seismic forward modeling and delay time analysis to propose either a single, low dipping fault (35 – 45°) or a series of closely spaced, steeply dipping faults. Trenching studies by Byrd (1995) and seismic refraction, gravity and inverse ray-tracing modeling support a steeply dipping (75 – 85°) normal fault (Smith et al. 1993b; Byrd et al., 1994) and most recent studies involve an interpretation with steeply dipping (>45°) stepped normal faults (Love et al. 2003; Hampel et al., 2007; White et al., 2009).

2.2 Regional overview

The Teton fault, which lies at the junction of four distinct tectonic provinces (Basin and Range, Snake River volcanic plain, Laramide uplift, Sevier fold-thrust belt), is interpreted as the northeasternmost fault in the Basin and Range (e.g., Brown et al., 2017). Given this dynamic setting, the area has been subjected to varying levels of Mesozoic to early Tertiary crustal shortening involving thrust faulting and folding, Late Tertiary to Quaternary E-W extension and normal faulting, and Late Tertiary to Quaternary volcanism, crustal uplift and subsidence associated with the Yellowstone volcanic province (Smith et al. 1990). The Teton Range also lies within the Intermountain Seismic belt (Smith and Sbar, 1974), a region characterized by diffuse shallow seismicity extending from southern Nevada, Arizona and Utah through western Wyoming to northwestern Montana. Here, Quaternary normal faults generate earthquakes in response to intraplate extension (Arabasz et al, 1980; Doser and Smith, 1983).

Historical earthquakes, including the 1983 Lost River Fault earthquake (Ms = 7.3) in Borah Peak, Idaho (Doser and Smith, 1985; Richins et al., 1987; Crone et al., 1987) and the 1959 Hebgen Lake fault earthquake (Ms = 7.5) in Montana (Myers and Hamilton 1964; Doser and Smith, 1985) serve as relevant analogs to the Teton fault given that these earthquakes occurred along similarly dipping (45° – 75°) normal faults in the eastern Basin and Range. Evidence for Quaternary motion on the Teton fault is observed in postglacial moraine ruptures, with total offset from 3 – 52 m (Smith et al., 1989, 1993a; Gilbert et al., 1983; Susong et al., 1987). The youngest fault motion recorded was found in trenching studies conducted at the mouth of Granite Canyon, which exposed two prehistoric fault ruptures occurring at 7.98 and 4.80 ka, for a total of 4.1 m of displacement (Byrd and Smith, 1990; Byrd, 1991; Smith et al., 1993a). However, the record of historic seismic activity (or lack thereof) along the Teton fault suggests seismic quiescence for ~5 ka (Smith et al., 1985) and this seismic gap may indicate that the Teton fault is capable of producing a moderate to large earthquake (Ms ~7.1; Smith 1988; White et al., 2009).

2.3 Displacement and age interpretations for the Teton Fault

In the Teton Range, displacement magnitudes and fault timing have been estimated based on (a) geophysical methods, (b) stratigraphic relationships, and (c) low-T thermochronology. A series of early forward gravity models by Lavin and Bonini (1957), reported a maximum total throw of 5.5 km. In these models, there was limited control on the extent of deformation on the Paleozoic-Precambrian contact and thus assumptions were made regarding the nature of pre-extensional deformation on that surface. This, in addition to the inherit ambiguity of gravity models, has led numerous workers to continue

efforts to estimate displacement with further techniques. Geophysical studies conducted by Behrendt et al. (1968) and Tibbetts et al. (1969) indicated a throw of ~7 km derived from seismic refraction modeling, standard gravity forward modeling and delay time analysis. However, these studies reported that poor data quality on the west end of the refraction profile and the absence of ray path coverage west of the Teton fault limited clear imaging of the subsurface fault geometry.

Estimates of displacement across the Teton fault based on observed stratigraphic and structural relationships (Table 1), range from 2.1 – 11 km. The Precambrian-Cambrian unconformity is one such stratigraphic marker that is exposed on the summit of Mount Moran (Love et al., 1992) and can be found throughout the Teton Range, specifically on the northwest, west, and southern portions of the range. By projecting the reconstructed unconformity surface from the summit of Mount Moran to the presumed depth of the unconformity located in the hanging wall, Behrendt et al. (1968) argue ~7 km of vertical displacement from the top of the range to the floor of Jackson Hole. It is worth noting that the unconformity surface is highly variable and has been affected by several episodes of deformation in the region (i.e. Mesozoic to early Tertiary, east-west compression, late Tertiary crustal extension, and late Cenozoic crustal deformation resulting from the Yellowstone volcanic system; Smith et al., 1990). Love and Reed (1971) proposed a stratigraphic displacement of 7.6 – 9.1 km based on angular unconformities and stratigraphic offset between the Miocene Colter and Teewinot formations and the Conant Creek Tuff (5.8 Ma). Other studies used stratigraphic interpretations of total throw (2.1 – 2.9 km) involving the Huckleberry Ridge Tuff (~2 Ma), by projecting the westward dipping surface of the tuff from exposures on Signal

Mountain toward the Teton fault to depths of 2.1 – 3.0 km Indicating at least ~2 km of throw along the fault since the eruption of the Huckleberry Ridge Tuff (Gilbert et al., 1983; Smith et al., 1989, 1993; Pierce and Morgan, 1992). This analysis of course assumes that there are no major faults between Signal Mountain and the projected location on the Teton fault (Fig. 1b). Byrd et al. (1994) used paleomagnetic data from an exposure of the Huckleberry Ridge Tuff (~2 Ma) to suggest a 10° post-emplacement tilt of the deposit. Although paleomagnetic measurements used for this estimate have limitations such as relying on assumptions relating to preexisting topography, demagnetization behavior, and including several sites with inconsistent negative inclination, incorporating this data with gravity, seismic models and detailed mapping led to length-averaged displacements of 2.5 – 3.5 km.

Timing of fault initiation of the Teton fault also remains uncertain. Many of the proposed fault timing estimates (13 Ma – 2 Ma) rely on similar stratigraphic relationships and the arguments involving the unconformity surface between the Miocene Colter and Teewinot Formations and the Conant Creek Tuff (5.8 Ma) lead to a wide range of onset timing interpretations (Barnosky, 1984; Smith et al., 1993b; Love, 1977). Barnosky (1984) derived an estimate for slip onset (13 – 9 Ma) directly from the angular unconformity (15°) between the Colter Formation and the overlying Teewinot Formation to the east of Jackson Hole. In another stratigraphic argument, Love (1977) suggests that faulting began about 5 to 6 Ma based on the lack of field evidence for clastic detritus in the Miocene Teewinot Formation, which is interpreted to indicate that the formation predated significant structural relief and thus, the range had not yet been uplifted. However, this explanation is contested by Shuey et al. (1977) and challenged again by

Byrd et al. (1994), as both studies note that the present-day material in Jackson Lake is largely silt and clay and lacks coarse material, despite the presence of modern-day relief. The areal distribution of the Kilgore Tuff (4.45 Ma) reaches as far east as Jackson Hole and the Gros Ventre Range. Morgan and McIntosh (2005) indicate that the Teton Range would have restricted eastward migration of the pyroclastic flow later to become the welded Kilgore Tuff, and therefore the observed presence at Signal Mountain and Pilgrim Peak implies the range had not begun to uplift until after ~4.5 Ma. This timing is again supported by work comparing distances of faults from Yellowstone to the age of those faults (Pierce and Morgan, 2009). Another study by Leopold et al. (2007) incorporated age data from pollen in the fine-grained sediments of the Shooting Iron Formation (~2 Ma). Underlying the late Pliocene Shooting Iron Formation and separated by an angular unconformity is the Miocene Teewinot Formation with a largely different pollen flora. Using this relationship and the absence of Precambrian clasts in the Tertiary valley deposits, authors indicate that the majority of fault movement must have occurred after ~2 Ma. Byrd et al. (1994) also suggested that the vast majority of displacement (2.5 – 3.5 km) on the Teton fault must have occurred within the Quaternary, specifically the past ~2 Ma, using the rotation angle of the Huckleberry Ridge Tuff from its assumed horizontal depositional orientation. However, this also assumed that the Teton fault had only accumulated <10 km of finite slip over its history.

Furthermore, low T thermochronologic studies have also provided displacement interpretations that are largely independent of the stratigraphic relationships and geophysical data previously discussed. Roberts and Burbank (1993) used AFT analyses to determine the timing of exhumation of the Teton Range, leading to total displacement

interpretations of ~3.5 km and slip onset at ~28 Ma or >2 Ma. However, this thermochronologic dataset pre-dated the modern zeta-calibration approach for AFT analysis, and thus these ages cannot be placed into a modern framework. A new AHe and AFT dataset was collected by Brown et al. (2017), from which a minimum total displacement of ~6 km was estimated based on AHe ages (Brown, 2010; Brown et al., 2017). Perhaps more importantly, zeta-calibrated AFT ages from that study (13.6 ± 0.6 Ma and 9.5 ± 2.8 Ma) were used to derive minimum footwall uplift estimate of 3.1 – 3.6 km, which in turn yielded a total displacement of 9 – 11 km.

CHAPTER 3. METHODOLOGY

To evaluate a range of displacement and fault onset timing scenarios, flexural-kinematic and thermal kinematic (*Pecube*) modeling was used to forward model the isostatic, erosional, and thermal evolution of the Teton Fault. The flexural-kinematic modeling component considered sequential deformation for each of the previously proposed estimates of total displacement D_{max} (2 km – 17 km) and age of slip onset initiation (5, 12, and 19 Ma) and, based on the results of these models, thermal-kinematic models were produced for the same slip onset timings but with displacements of 9 – 17 km in 2 km increments. The decision to only consider higher displacement scenarios in the thermal-kinematic models is discussed in the below and in the Results section.

First, a range of parameters, including fault dip (45° – 70°), depth to detachment (Z_d; 15 and 20 km), and effective elastic thickness (T_e; 5, 10, and 15 km) were implemented into the flexural-kinematic models to test which values may be appropriate for the evolution of the Teton fault. The results of each kinematic scenario were evaluated against a swath topographic profile extracted from a digital elevation model (DEM) of the modern Teton Range and compared to the flexural wavelengths of the footwall uplift and the hanging wall basin. From this set of models, the scenarios with geometries and kinematics that produced an acceptable flexural profile wavelength (within 1 km), basin width (~15 km), and footwall uplift (> 2 km) were selected for thermal-kinematic modeling. The thermal-kinematic models are then used to derive predicted cooling ages of exhumed rocks for each scenario. The resulting cooling history is then compared to AFT and AHe ages from the footwall transect near Mount Moran, which is interpreted by Brown et al. (2017) to record the D_{max} along the Teton fault.

3.1 Flexural – kinematic modeling

Flexural-kinematic models were produced using Petroleum Experts *Move (2019)* software to calculate the flexural response to isostasy for a range of fault geometries, D_{max}, Z_d, and T_e values (Table 3.1). Fault slip was forward modeled using the fault parallel flow algorithm (Egan et al. 1997; Kane et al. 1997), which works by translating particles in the hanging wall along flow lines parallel to the fault plane while maintaining line lengths in the hanging wall. Fault slip is implemented in 1 – 2 km incremental steps until the desired D_{max} is reached. A simplified schematic of the iterative process described below. Following each increment of fault slip (Figure 3.1), the flexural isostatic response is calculated with the flexural isostasy algorithm. The difference in the volume of material between the deformed topographic surface and the topography of the previous step represents the flexural-isostatic load to be accommodated, which is calculated by applying the defined values for load density (ρ_c) to the volume of material and T_e to the crust. When the load is removed, or "unloaded" the footwall rises isostatically by a quantity dependent on the flexural properties of the lithosphere (Figure 3.1c, Table 3.2). The flexural isostatic response to unloading using a continuous 2D beam is described by Watts (2001):

$$q = D \frac{d^4 w}{dx^4} + (\rho_m - \rho_c)\ g\ w \qquad (Eq.\ 1)$$

where q is the applied vertical load (N m^{-2}), D is the flexural rigidity, ρ_m is the density of the mantle (3300 kg m^{-3}), ρ_c is the density of the eroded load material (2750 kg m^{-3}), w is the vertical deflection of the beam, and g is the acceleration due to gravity (9.81 m s^{-2}). Lithospheric flexural rigidity D is described by:

$$D = \frac{E\,T_e{}^3}{12\,(1 - v^2)} \qquad (Eq.\ 2)$$

Where E is Youngs modulus (70 MPa for all models), T_e is the effective elastic thickness (5 – 15 km; Lowry and Smith, 1994; Watts and Burov, 2003, Tesauro et al., 2015), and v is Poisson's ratio. The effective elastic thickness is the most important variable controlling D, the flexural rigidity of a thin plate overlying a fluid without viscosity, and is characterized by Turcotte and Schubert (1982):

$$T_e = M_e\ 12\ (1 - v^2)\ EK^{1/3} \qquad (Eq.\ 3)$$

where elastic thickness (T_e) is described by the elastic bending moment (M_e), Poisson's ratio (v), and curvature (K).

After the slip and subsequent flexural response are calculated at each timestep, the resultant footwall topographic profile is incrementally eroded following a profile roughly parallel to the dip of the modern-day flexural uplift (Figure 3.1d). In this scenario, the difference in cross-sectional material is less significant (thickness <0.3 km) between the deformed and unloaded topographic surface and the eroded topographic profile. Again, the difference in material between the deformed and unloaded topographic surface (Figure 3.1c) and the eroded topographic surface (Figure 3.1d) represents the flexural-isostatic load to be accommodated, resulting in the final profile for the footwall (Figure 3.1e). For the final phase, the basin resulting from hanging wall drop is filled with accumulated syntectonic sediment (Figure 3.1f). During this process, an x-y point cloud with a grid spacing of 0.25 km is also deformed along with the section to produce the vectors that will be used as input for the *Pecube* thermal-kinematic models.

3.1.1 Defining modeled fault geometries

Detailed studies of Basin and Range normal faults have shown that some of these structures dip steeply at the surface (45° – 70°) and sole abruptly into subhorizontal detachments at depths of 15 – 20 km, which is interpreted by multiple studies to correspond to the brittle-ductile transition (Wernicke and Burchfiel 1982, Gans and Miller 1984, Jackson & McKenzie 1983). The near-surface dip of the Teton fault has been estimated to range from 35 – 85° (Byrd, 1994; Smith et al. 1991; Gilbert et al., 1983; Love, 1977; Behrendt et al., 1968, Lavin, 1957). To address this range of fault dips and detachment depths, initial flexural-kinematic models that were tested include near-surface fault dips of 45°, 60°, and 70° and listric detachment depths of 15 and 20 km. Model results incorporating this entire range of model parameters (T_e, Z_d, near surface fault dip) are then compared to the observed flexural profiles for footwall uplift and basin width derived from swath topographic profiles through the present-day Mount Moran transect (Figure 3.2).

3.1.2 Generating observed swath topographic profiles

The swath topographic profile that is compared with the resultant surface topography of the flexural-kinematic models was constructed using a 10 m DEM combined with the Swath Profiler ArcGIS add-in (Figure 3; Perez et al., 2017). For a user-defined vector feature (polyline) orthogonal to the Teton fault through Mount Moran, the SwathProfiler calculates maximum, minimum, and mean elevation profiles for each of the 50 equally spaced topographic profiles within the 6000 m swath width. The resultant mean swath profile of the observed topography (Figure 3.2b) is then compared with the range of results from the flexural-kinematic models to define a

reference case model that displays the best-fit between the modeled and observed topography.

3.2 Thermal – kinematic modeling

In the final step of the modeling workflow, the reference case flexural-kinematic model defined above is coupled with a thermal-kinematic *Pecube* model (Braun, 2002; Braun, 2003; Braun et al. 2012). Linking the kinematic model with the advection-diffusion thermal model is useful for calculating the evolving subsurface thermal field and for predicting cooling ages (e.g. McQuarrie and Ehlers, 2015). The software solves the heat transport equation to incorporate the influence of heat conduction and advection into the forward model of the crustal thermal field. The primary controls on the thermal state of the crust include: (1) radiogenic heat produced in the crust, (2) basal mantle heat flow, and (3) the bulk thermal conductivity of the crustal section. Heat transfer is described by the partial differential equation (Jaeger and Carslaw, 1959):

$$-div\,(-k\,\nabla T) + A = \rho c\,\frac{\partial T}{\partial t} \qquad (Eq.\ 4)$$

where T is temperature, t is time, k is thermal conductivity, A_0 is volumetric heat production and ρ and c are density and specific heat capacity of the crust, respectively. The value for bulk thermal conductivity (k, 3 $Wm^{-1}K^{-1}$) was assigned based on measured data from the Precambrian section in the Teton Range, consisting of gneiss, schist, and granite (Heasler, 1987). Specific heat capacity (c, 880 J $kg^{-1}K^{-1}$) for this model corresponds to the mean value for granite observed in measurements by Touloukian et al. (1989). In the *Pecube* code, variations to the geothermal gradient are controlled primarily by adjusting the surface heat production (A_0) value and e-folding depth (*ef*) which describes an exponential decrease in heat production with depth in the model space.

Crustal volumetric heat production (A_0, 2.45 μWm^{-3}) within the range of global average values for granite is applied and decreases with depth according to an exponential curve with an *ef* of 8.5 km (Haenel et al. 1988; Ehlers, 2005). The same mantle and crustal density values used in *Move* were again applied (ρ_m of 3300 kg m^{-3} and ρ_c of 2750 kg m^{-3}) in the thermal-kinematic models. Here, models are produced using constant temperature boundaries at the surface and base of each model of 4° C and 1300° C at 110 km depth, respectively (McQuarrie and Ehlers 2015). These values lead to an acceptable proxy for the observed geothermal gradient in this region of 18 – 27° C km^{-1} (Decker et al. 1980; Heasler et al. 1987; Brott et al., 1981; Blackwell et al., 1992, 2004). From the surface, temperature is set to decrease with elevation at an atmospheric lapse rate of 6° C km^{-1}, comparable to the reported value for the Wasatch Range (Dirks, 1982; Masbruch et al., 2012). A comprehensive list of material properties and numerical parameters used in thermal-kinematic models are shown in Table 3.3 and constant velocity models tested in Table 3.4.

Table 3.1 – Flexural-kinematic model parameters tested in 2D-Move and Pecube velocity input models.

Model Number	Dip Angle (°)	E_t (km)	Depth to Detachment (km)	Total Displacement (km)	Velocity model
1	70	5	20	9, 11, 13	A, B, C
2	70	5	15	9, 11, 13	A, B, C
3	60	15	20	9, 11, 13	A, B, C
4	45	15	20	9, 11, 13	A, B, C
5	45	10	20	9, 11, 13	A, B, C
6	70	10	15	9, 11, 13	A, B, C
7	70	15	20	9, 11, 13	A, B, C
8	60	5	15	9, 11, 13	A, B, C
9	45	5	15	9, 11, 13	A, B, C
10	60	5	20	9, 11, 13	A, B, C
11	45	5	15	9, 11, 13, 14, 15, 16, 17	A, B, C, D, E, F, G
12	60	5	15	9, 11, 13, 14, 15, 16, 17	A, B, C, D, E, F, G
13a	70	5	15	9, 11, 13, 14, 15, 16, 17	A, B, C, D, E, F, G
13b	70	5	15	11, 13, 15, 17	H, I, J, K
13c	70	5	15	11, 13, 15, 17	L, M, N, O

Table 3.2 – Mechanical properties and symbols for 2D-Move flexural-kinematic models. Dashes indicate parameters calculated within the model.

Parameter	
Maximum fault displacement (D_{max})	9, 11, 13, 14, 15, 16, 17 km
Effective elastic thickness (T_e)	5, 15, 20 km
Detachment depth (Z_d)	15, 20 km
Imposed slip / step	1 km, 2 km
Density of the crust (ρ_c)	2750 kg m^{-3}
Density of the mantle (ρ_m)	3300 kg m^{-3}
Acceleration due to gravity (g)	9.81 m s^{-2}
Young's modulus (E)	70 GPa
Poisson's ratio (v)	0.25
Applied vertical load (q)	-
Lithospheric flexural rigidity (D)	-
Flexural uplift or subsidence (w)	-

Table 3.3 – Material properties and numerical parameters tested for Pecube thermal-kinematic models.

Material Properties	
Property	**Model Input**
Heat production (A_0)	2.45, 3 μW m^{-3}
Thermal conductivity (k)	3 W m^{-1} K^{-1}
Specific heat capacity (c)	880 J kg^{-1} K^{-1}
e-folding depth (ef)	8.5, 11.5 km
Density of the crust (ρ_c)	2700 kg m^{-3}
Density of the mantle (ρ_m)	3300 kg m^{-3}

Numerical Parameters	
Parameter	**Model Input**
Model domain	110 km x 310 km x 5 km
Onset of fault motion	19 Ma, 12 Ma, 5 Ma
Grid spacing	0.5 x 0.5 km, 0.25 x 0.25 km
Surface temperature at sea level	4°C
Atmospheric lapse rate	6°C km^{-1}
Basal temperature	1300°C

Table 3.4 – Constant velocity models tested in Pecube thermal-kinematic models.

Velocity Model	D_{max} (km)	Slip onset (Ma)	Slip rate (km Myr^{-1})
A	9	19	0.47
B	11	19	0.58
C	13	19	0.68
D	14	19	0.74
E	15	19	0.79
F	16	19	0.84
G	17	19	0.89
H	11	5	2.20
I	13	5	2.60
J	15	5	3.00
K	17	5	3.40
L	11	12	0.92
M	13	12	1.08
N	15	12	1.25
O	17	12	1.42

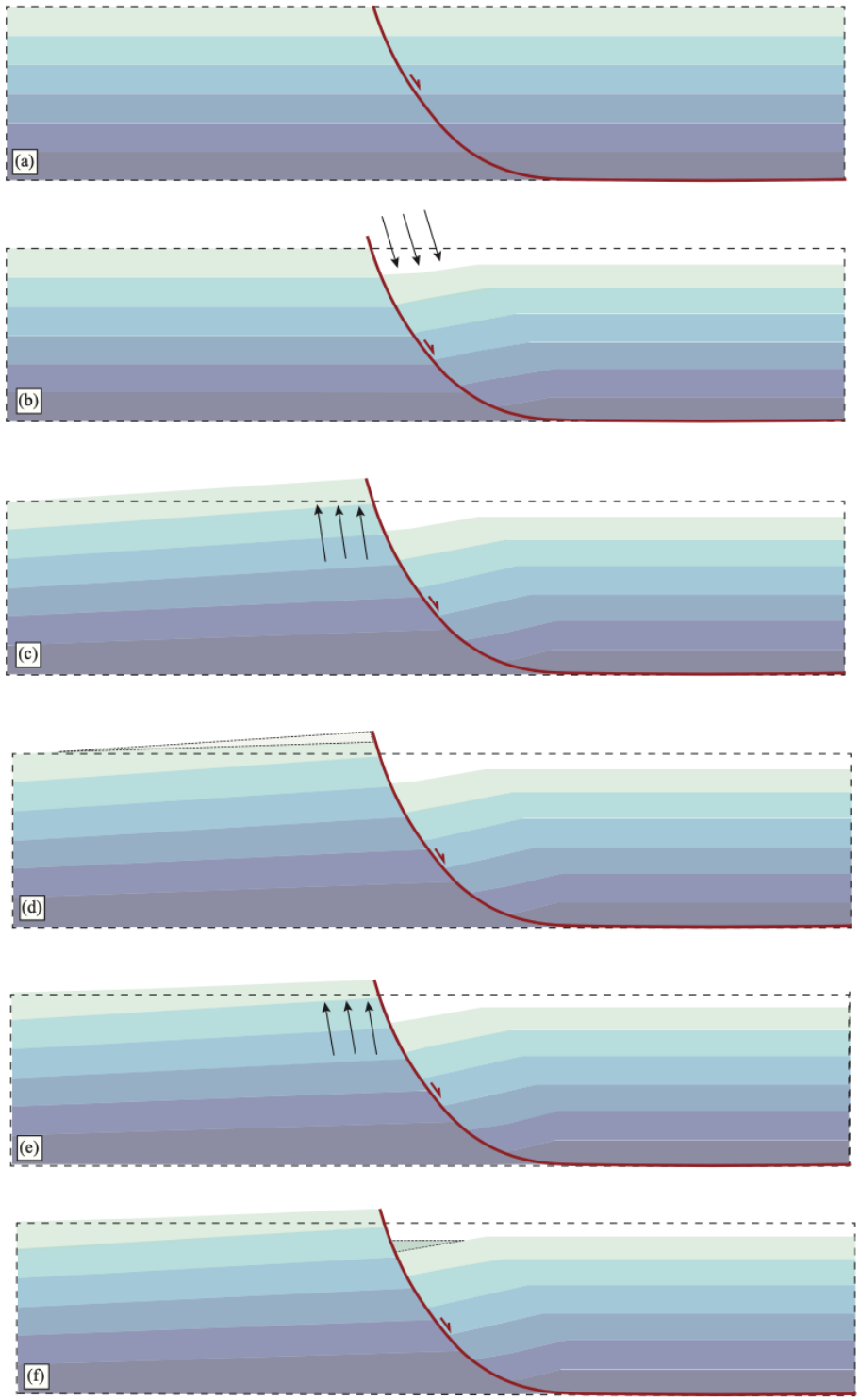

Figure 3.1 – Simplified schematic of step-wise process in flexural-kinematic modeling software, (a) undeformed, (b) deformation along normal fault, (c) isostatic unloading (black arrows) of material moved by fault, (d) erosion of material (black dashed wedge), (e) erosional unloading (black arrows) from removal of eroded material mass, (f) sediment loading from deposition of sediment. Steps are exaggerated.

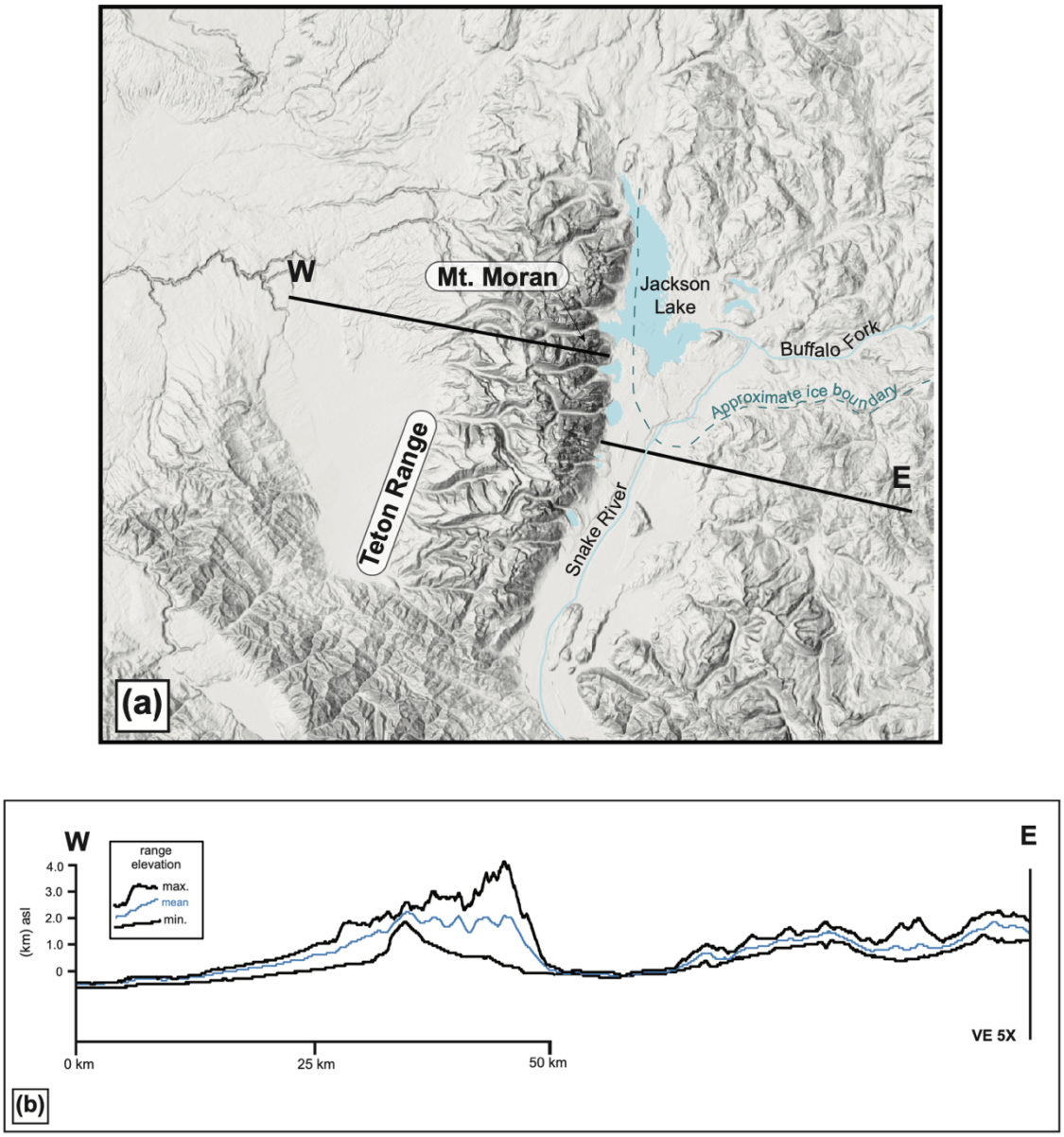

Figure 3.2 – (a) Modern day DEM from which the (b) observed elevations are extracted as minimum, mean, and maximum elevation profiles. The polyline (solid black line W – E) is split to capture flexural response in an area with minimal vertical glacial incision because erosion is not modeled in the hanging wall. The Buffalo Fork trough flowed westward towards Jackson Lake and the approximate ice boundary (dashed blue line) represents the glacial terminus during the Burned Ridge phase of the Pinedale glaciation (Smith et al., 1993b).

CHAPTER 4. RESULTS

4.1 Flexural-kinematic modeling

Flexural-kinematic models were first used to constrain the threshold displacement necessary to produce a footwall topographic profile that matches the present-day topography. In these systems, footwall uplift is primarily an isostatic response controlled by the magnitude of D_{max} and footwall erosion. These flexural-kinematic models yield predictions of the footwall uplift contribution to total fault slip, which can then be compared to the range of D_{max} estimates. To assess the effect of increasing D_{max}, a reference geometry was considered (fault dip angle of 70°, T_e = 5 km, and Z_d = 15 km) and the magnitude of footwall uplift was evaluated for D_{max} = 2 km, 7 km, 11 km, 17 km, and 20 km (Figure 4.1) without incorporating footwall erosion and hanging wall sediment loading in order to test the maximum effect of isostatic compensation. The amount of possible eroded material may be as high as ~2 km if the entire thickness of the Paleozoic section was removed. A consistent increase in the resulting footwall uplift corresponds to values of greater D_{max}. In models that test D_{max} of 2 km and 7 km the resulting footwall uplift (0.7 km and ~2 km; Figure 4.1) is less than or equal to the present-day footwall relief observed at Mount Moran (~1.8 km). For greater D_{max} (11 km), footwall uplift increases to 3.2 km above the model datum. The model predicted uplift continues to increase (4.2 and 2.5 km) for D_{max} of 17 km and 20 km, respectively (Figure 4.1). The modern footwall relief at Mount Moran (~1.8 km) would yield modeled D_{max} estimates of 6 – 8 km (Figure 4.2), which is a minimum estimate because erosion was not

incorporated into these models. Thus, D_{max} values of 2 and 7 km create insufficient footwall uplift and D_{max} for the Teton fault is likely > 9 km (Figure 4.2).

A set of 13 models incorporating footwall erosion and sediment loading of the hanging wall (Figure 4.2 – 4.14, Table 3.1) were run to evaluate the model response to variations in T_e and subsurface fault geometry, including near surface fault dip and Z_d. Each of these kinematic scenarios yield a different flexural response which can then be compared to the swath topographic profiles to define the reference case. Tables 4.1 and Figure 4.15 summarize the range of forward models, the input parameters, and the results of the swath topographic profiles from the Teton Range-Jackson basin.

Flexural rigidity is tested by varying T_e for models with the same fault dip angle and Z_d. For all fault dips, models with greater values of T_e (10 and 15 km) show <1 km of footwall uplift, while lower values (5 km) generally showed more than double that magnitude (1.8 - 2.8 km). Next, Z_d was varied to investigate responses in the wavelength of the resulting hanging wall basin and hanging wall flexure. Instances with deeper values for Z_d (20 km) yield longer basin wavelengths (20 – 24 km) compared to those with shallow Z_d (15 km) range 15 – 18 km. Models with the same T_e were then evaluated for different fault dip angles. As fault dip increases the height of the uplift of the footwall regularly increases. For instance, when fault dip = 45° and T_e = 5 km, the resultant footwall uplift is 1.8 km. With the same T_e, but increasing the fault dip angle to 60°, footwall uplift was ~2.0 km. Models with fault dip = 70° have footwall uplift between 2.1 – 2.6 km. In order to evaluate the effect of varying T_e on the flexural wavelength of the footwall a consistent Z_d was maintained for all fault dip angles. Where Z_d = 20 km and flexural rigidity is lowest (T_e = 15) models show a concave down flexural profile, with a

relatively low amount of uplift (0.6 – 0.9 km) that is regionally dispersed (56 – 72 km). Greater flexural rigidity (T_e = 5) generates models with an increased uplift (1.8 – 2.6 km) over shorter lateral wavelengths (35 - 44 km). For all models with Z_d = 20 km, basin wavelength remains ~22 km as fault dip varies from 45 – 70°.

4.2 Identifying a reference flexural-kinematic model

Final surface topographies from each flexural-kinematic model were compared to a detailed swath topographic profile extracted from a DEM of the observed topography to evaluate which parameter configurations best represent the observed profile. As discussed in the methods section, a reference case kinematic model was selected on the basis of three primary comparisons, including: (1) the wavelength of the footwall uplift (~29 km), (2) the wavelength of the hanging wall basin (~15 – 20 km), and (3) the magnitude of footwall uplift at Mount Moran (Figure 4.16). Flexural-kinematic models 2, 8, and 9 which have varying fault dip angles (70°, 60°, and 45°), T_e = 5 km and Z_d = 15 km yield the closest match to the observed flexural topography and yield footwall uplift values of 2.1 m, 2.1 m, and 1.8 m, respectively. In order to achieve greater footwall uplift, the same structural constraints from models 2, 8, and 9 were utilized in models 11, 12, and 13 testing greater D_{max} (17 km) in finer increments (1 km). The particle vectors from the modeled solution with the least variance from the observed topography (Model 13; wavelength of footwall uplift: 28 m, wavelength of hanging wall basin: 20 km, and total footwall uplift: 3.1 km) was identified as the reference case to be used in the next phase of thermal-kinematic modeling (Figure 4.17). In those models, velocity fields for a range of D_{max} values up to 17 km are exported to be used as input velocity fields for the thermal-kinematic models.

In addition to the footwall uplift and wavelengths of flexural response, another notable feature in the modeled topography develops in the hanging wall. This prominent isostatic uplift forms to the east of the basin within all flexural-kinematic models (Figure 15 and 4.16). For a swath topographic profile through Mount Moran trending directly to the east in the hanging wall, the observed terrain has unusually low relief compared to swaths along strike (Figure 3.2). Here, the gradually diminishing topography can be attributed to glacial scouring from a major ice sheet (Buffalo Fork lobe) that flowed through the Buffalo Fork Valley into Jackson Hole from the east during the Pinedale glaciation (Smith et al., 1993b, Pierce and Good, 1992). This area is now part of the modern floodplain for the Snake River and Buffalo Fork River. The swath topographic profile through the observed topography is split in order to account for this feature (Figure 3.2).

4.3 Thermal-kinematic modeling

In the final phase of modeling, *Pecube* models were run for a range of interpreted fault slip onsets (5, 12, and 19 Ma) and D_{max} values (9 – 17 km) to produce predicted cooling ages that can be compared with the observed data from Mount Moran. Fault slip onsets were chosen to represent the entire range of interpreted onsets in previous studies (Byrd et al., 1994; Love et al., 2003; Roberts and Burbank, 1993; Brown et al. 2017; Thigpen et al., in prep). *Pecube* solves the heat conduction equation (including advection) for the vector field defined by the reference case flexural-kinematic model. All thermal models use a constant rate of displacement (see Table 3.4) from the time of slip onset to present-day. Because the oldest current age in the Moran dataset is ~38 Myr (AFT, central age; Brown et al. 2017), models with slip onsets of 19, 12, and 5 Ma are run from

57, 50, and 43 Ma to present, respectively, which produces thermochronologic ages above the AFT T_c of ~38 Myr at the onset of fault slip, which assumes a relatively simple single uplift exhumation history. Because of the grid resolution used in the flexural-kinematic model (250 m x 250 m), 2 – 4 cooling ages are extracted along the fault plane from the thermal model for each time step. Predicted AHe and AFT cooling ages for all thermal models are shown in Table 4.2 and described in more detail in the following section. Pecube models results and corresponding kinematic solution are shown in Figures 4.17 – 4.31.

As can be expected, the absolute ages and age trends produced by the thermal-kinematic models, which all have linear fault slip rates, are controlled by the timing of fault slip onset. Models begin to thermally equilibrate ~38 m.y. prior to the onset of slip for constant velocity models with slip onset timings of 19 Ma-present, 12 Ma-present, and 5 Ma-present. The decision to begin each thermal model ~38 m.y. before fault slip onset is based upon the observed AFT age at the summit of Mount Moran (38.0 ± 2.6 Ma; Brown et al., 2017). The earliest possible cooling age is a function of when motion along the normal fault initiates and exhumation begins. For example, where slip onset begins at 19 Ma, the model runs from 57 Ma to 19 Ma and allows for the thermal model to equilibrate crustal temperatures. At the time that deformation begins (19 Ma), all thermochronometers are 38 Ma in age. Samples that are above the T_c and have already cooled prior to fault slip onset, will continue to age with increasing model time. Samples that are below the T_c may be exhumed through the closure temperature and reflect reset AHe ages if the value for D_{max} is sufficient in that given model. Because the majority of the thermal-model predicted AHe ages used in this analysis are reset and therefore,

younger than fault slip onset, more emphasis is placed on the age-elevation trends between reset samples than the absolute ages determined by the model start time.

In summary, when faulting begins at 5 Ma, the predicted AHe cooling ages range from 46.5 to 3.6 Ma for models with values of D_{max} 11 – 17 km. For a 12 Ma fault slip onset, AHe ages span 47.4 to 7.5 Ma again for a range of models with D_{max} 11 - 17 km. The range of AHe ages is slightly older for fault slip onset at 19 Ma for D_{max} 9 – 17 km. AFT data is also predicted by the thermal-kinematic model. For 5 Ma fault slip onset, predicted AFT ages for D_{max} = 11 – 17 km range from 43.5 – 33.3 Ma. Where faulting begins at 12 Ma, predicted AFT ages span 50.9 – 39.9 Ma. Models with D_{max} 9 – 17 km that begin at 19 Ma return AFT ages 51 – 41.4 Ma.

Table 4.1 – Flexural-kinematic (Move) forward models tested and the measured results.

	Input Parameters				**Measured Results**		
Model Number	Dip Angle (°)	E_t (km)	Z_d (km)	D_{max} (km)	Footwall wavelength (km)	Basin wavelength (km)	Footwall uplift (km)
1	70	5	20	13	43.5	22.7	2.65
2	70	5	15	13	35.0	16.0	2.14
3	60	15	20	13	72.0	24.0	0.8
4	45	15	20	13	32.3	21.8	0.60
5	45	10	20	13	61.2	19.6	1.00
6	70	10	15	13	60.8	17.1	0.90
7	70	15	20	13	56.8	22.6	0.90
8	60	5	15	13	44.3	15.3	2.10
9	45	5	15	13	42.9	18.3	1.80
10	60	5	20	13	39.8	21.4	2.00
11	45	5	15	13	22.0	18.4	2.60
12	60	5	15	13	25.4	28.5	2.80
13	70	5	15	17	28.0	20.0	3.20

Table 4.2 – Predicted and observed AHe and AFT data.

Elevation (Z) (km)	AHe age (Ma)	AFT age (Ma)
5 Ma – 11 km		
2.35	40.5	43.5
2.07	39.9	43.2
0.67	26.6	40.6
0.15	31.7	41.2
5 Ma – 13 km		
2.77	41.5	43.5
2.68	41.4	43.5
1.38	25.0	40.4
0.168	1.50	36.7
5 Ma – 15 km		
3.07	40.5	43.1
1.93	25.1	40.4
0.69	1.80	36.7
0.22	2.10	37.1
5 Ma – 17 km		
3.37	37.8	42.5
2.61	27.2	40.7
1.33	6.70	37.6
0.20	3.60	33.3
12 Ma – 11 km		
2.35	47.4	50.9
2.07	46.7	50.5
0.69	32.3	47.7
12 Ma – 13 km		
2.77	46.8	50.6
2.68	46.8	50.6
1.38	33.1	47.9
0.17	11.2	44.4
12 Ma – 15 km		
3.07	45.9	50.3
1.93	33.0	47.9
0.69	11.5	44.5
0.22	10.7	44.5

Table 4.2 (continued) – Predicted and observed AHe and AFT data.

Elevation (Z) (km)	AHe age (Ma)	AFT age (Ma)
12 Ma – 17 km		
3.37	44.5	49.9
2.61	33.4	48.0
1.33	12.0	44.6
0.20	7.50	39.9
19 Ma – 9 km		
1.47	46.5	50.6
0.12	35.0	48.1
19 Ma – 11 km		
2.07	47.1	50.9
0.69	35.6	48.3
19 Ma – 13 km		
2.68	47.1	51.0
1.38	36.3	48.5
0.17	16.5	45.4
19 Ma – 14 km		
2.92	47.1	52.0
1.63	36.3	48.5
0.40	16.5	45.4
19 Ma – 15 km		
3.07	47.1	50.7
1.93	36.3	48.6
0.69	16.6	45.5
19 Ma – 16 km		
3.21	46.4	50.7
2.26	36.4	48.6
0.97	16.8	45.5
19 Ma – 17 km		
3.37	45.5	50.4
2.61	36.5	48.7
1.33	17.0	45.5
0.20	12.7	43.4

Table 4.2 (continued) – Predicted and observed AHe and AFT data.

Elevation (Z) (km)	AHe age (Ma)	AFT age (Ma)
Brown et al., 2017 (observed)		Age ± 1σ
1.719	20.91	38.0 ± 3.1 TR-08-15
1.719	18.94	
1.719	26.32	
1.719	23.3	
0.859	7.12	13.6 ± 2.0 TR-08-03
0.859	12.95	
0.859	11.54	
0.334	7.27	TR-08-06
0.334	10.22	
0.334	8.21	
0.334	4.07	
0	8.36	11.7 ± 1.7 TR-08-32
0	11.34	
0	8.37	

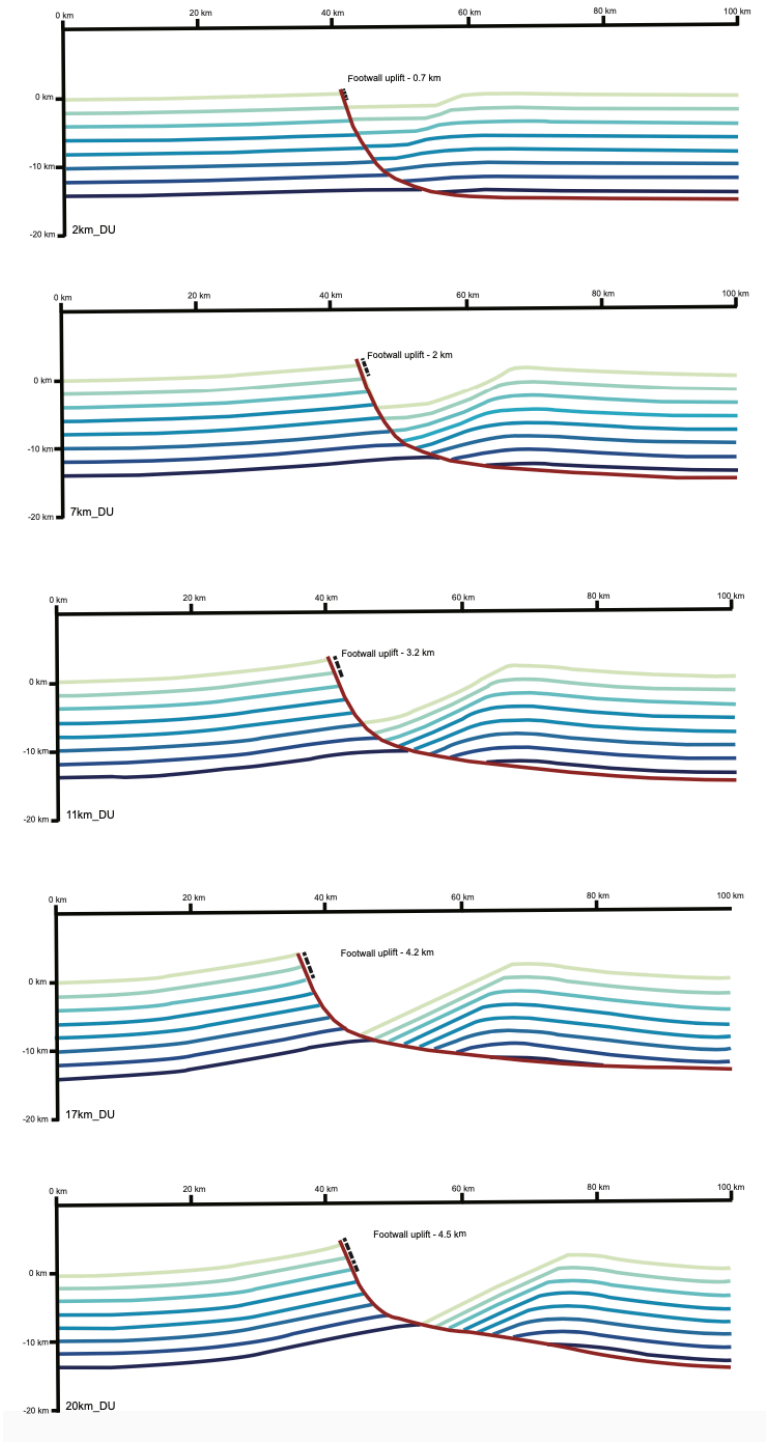

Figure 4.1 – Flexural-kinematic (Move) model with a fault dip angle of 70°, T_e *= 5 km, and* Z_d *= 15 km, modeled without footwall erosion or hanging wall sediment loading. Tested* D_{max} *values (2 km, 7 km, 11 km, 17 km, 20 km) yield footwall uplift 0.7 km, 2 km, 3.2 km, 4.2 km, and 4.5 km, respectively.*

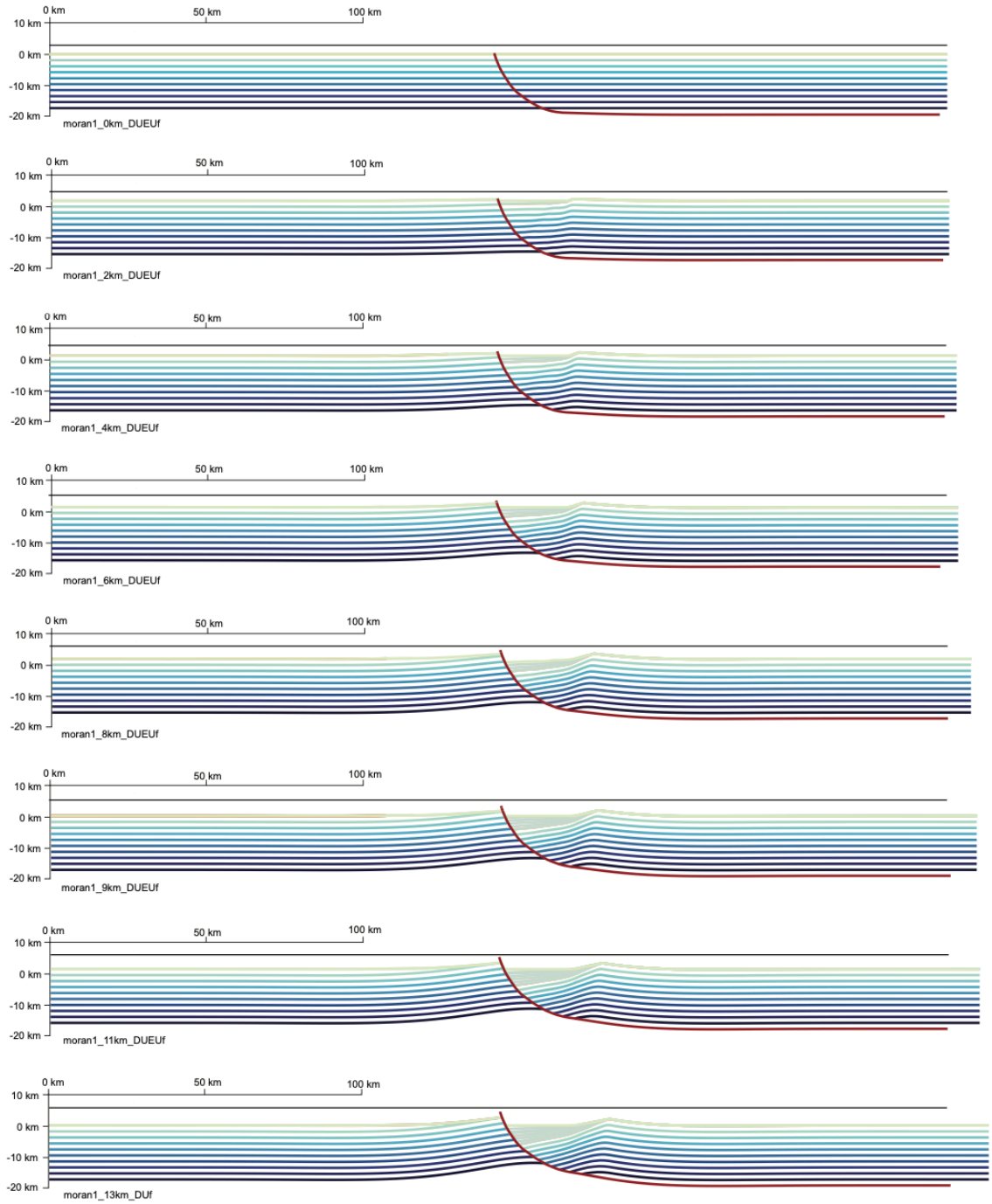

Figure 4.2 – Flexural-kinematic model 1 evaluates a 70° fault, with Te = 5, Zd = 20, and Dmax = 13 km.

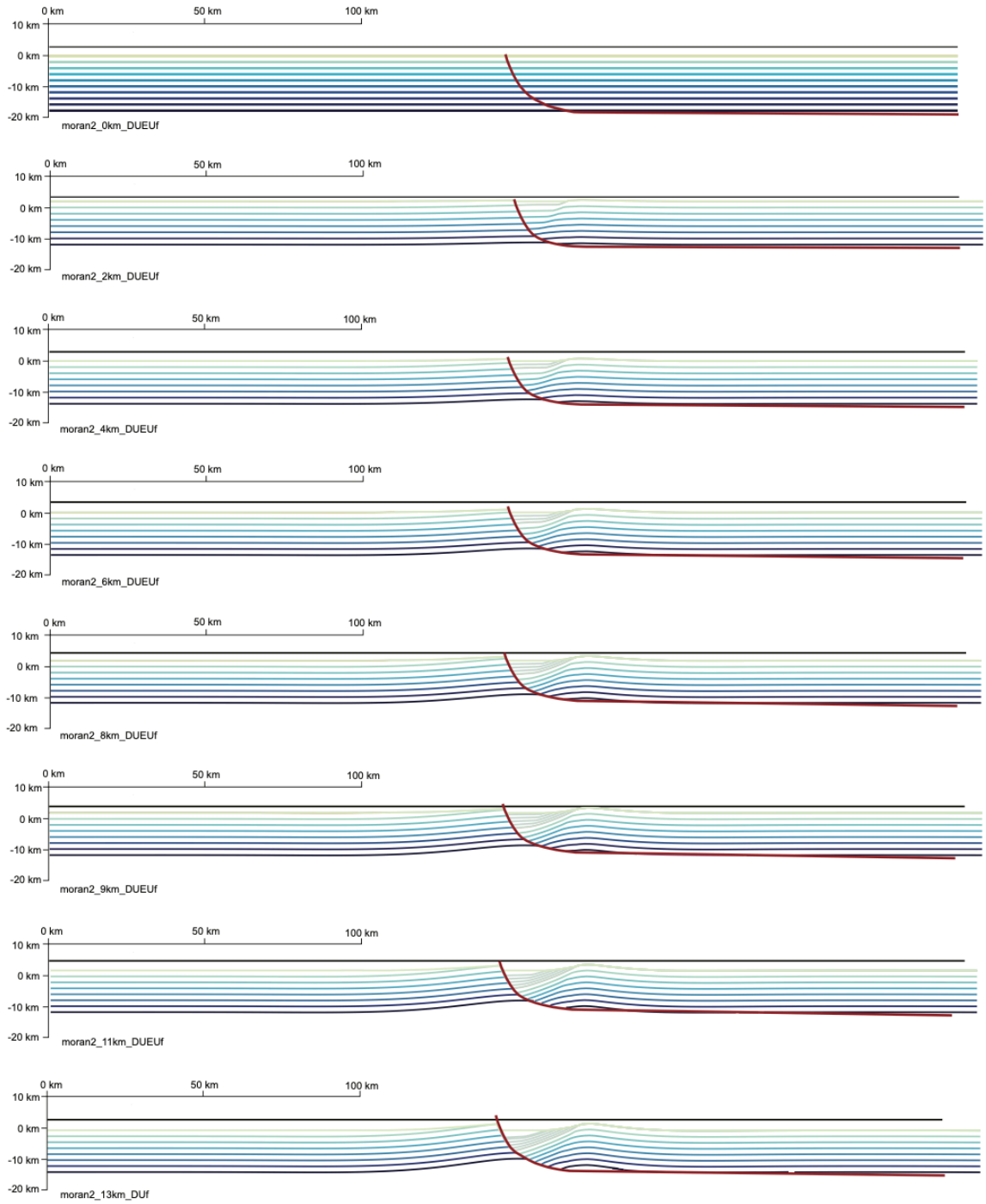

Figure 4.3 – Flexural-kinematic model 2 evaluates a 70° fault, with T_e = 5, Z_d = 15 , and D_{max} = 13 km.

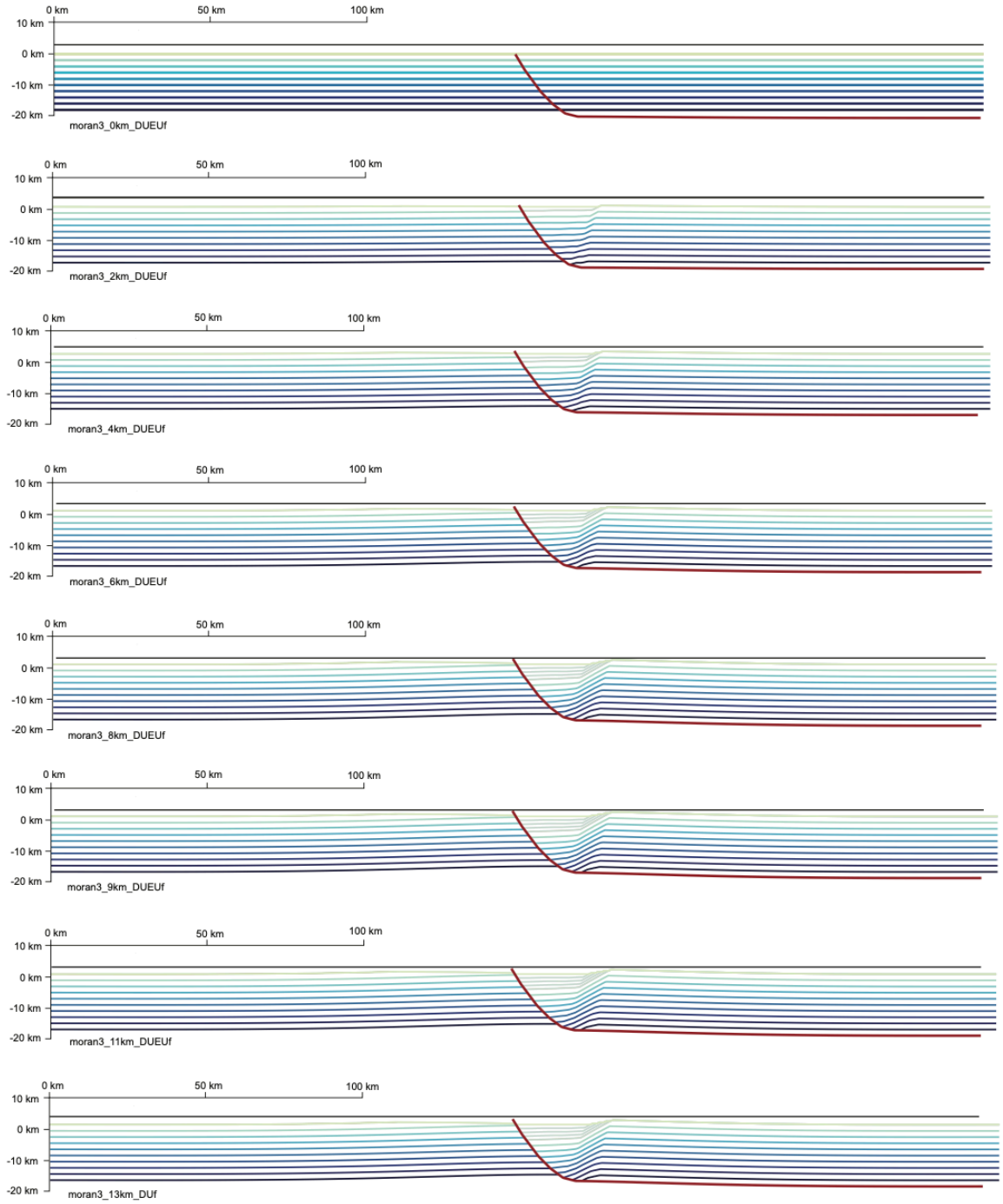

Figure 4.4 – Flexural-kinematic model 3 evaluates a 60° fault, with T_e = 15, Z_d = 20, and D_{max} = 13 km.

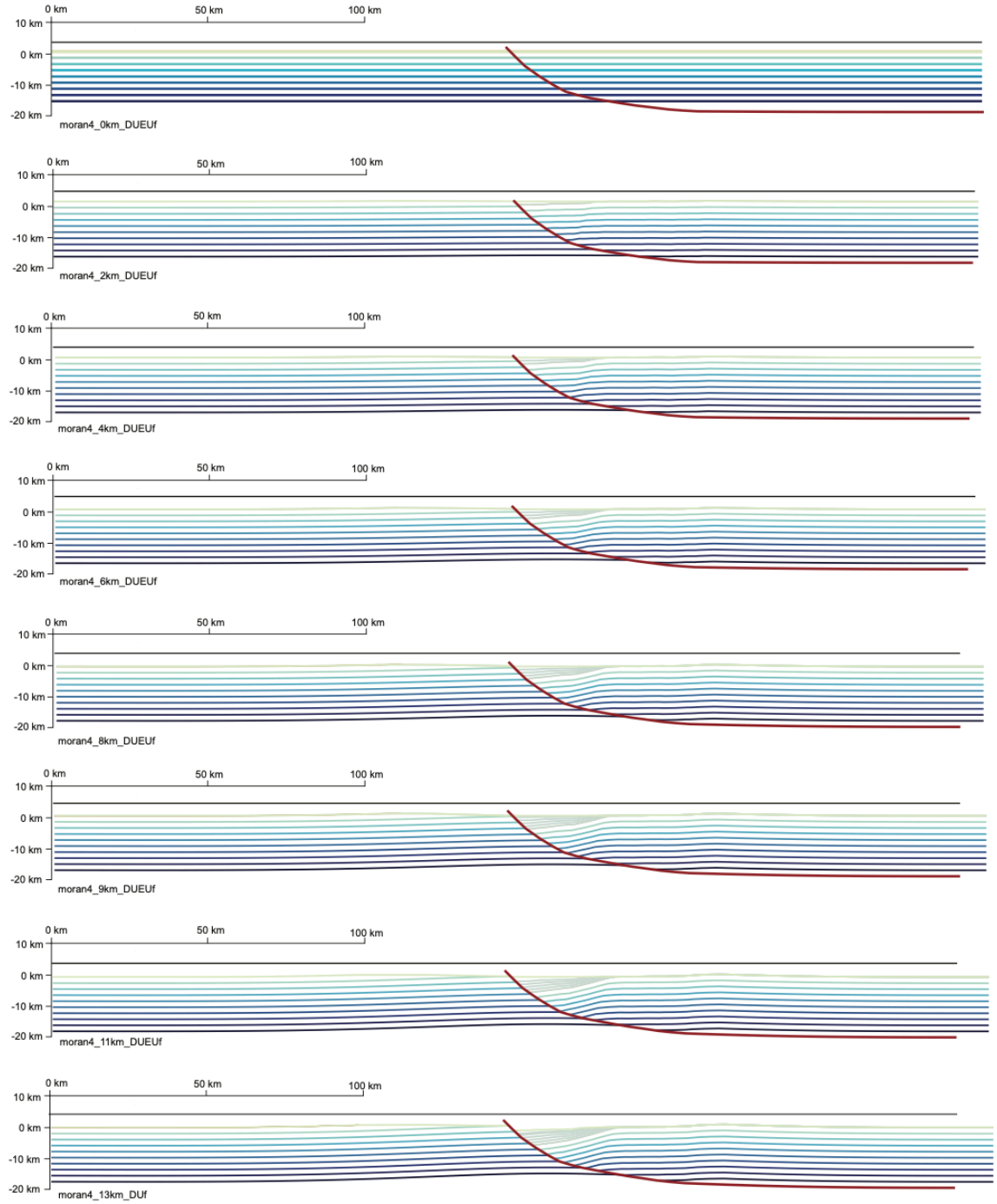

Figure 4.5 – Flexural-kinematic model 4 evaluates a 45° fault, with T_e = 15, Z_d = 20, and D_{max} = 13 km.

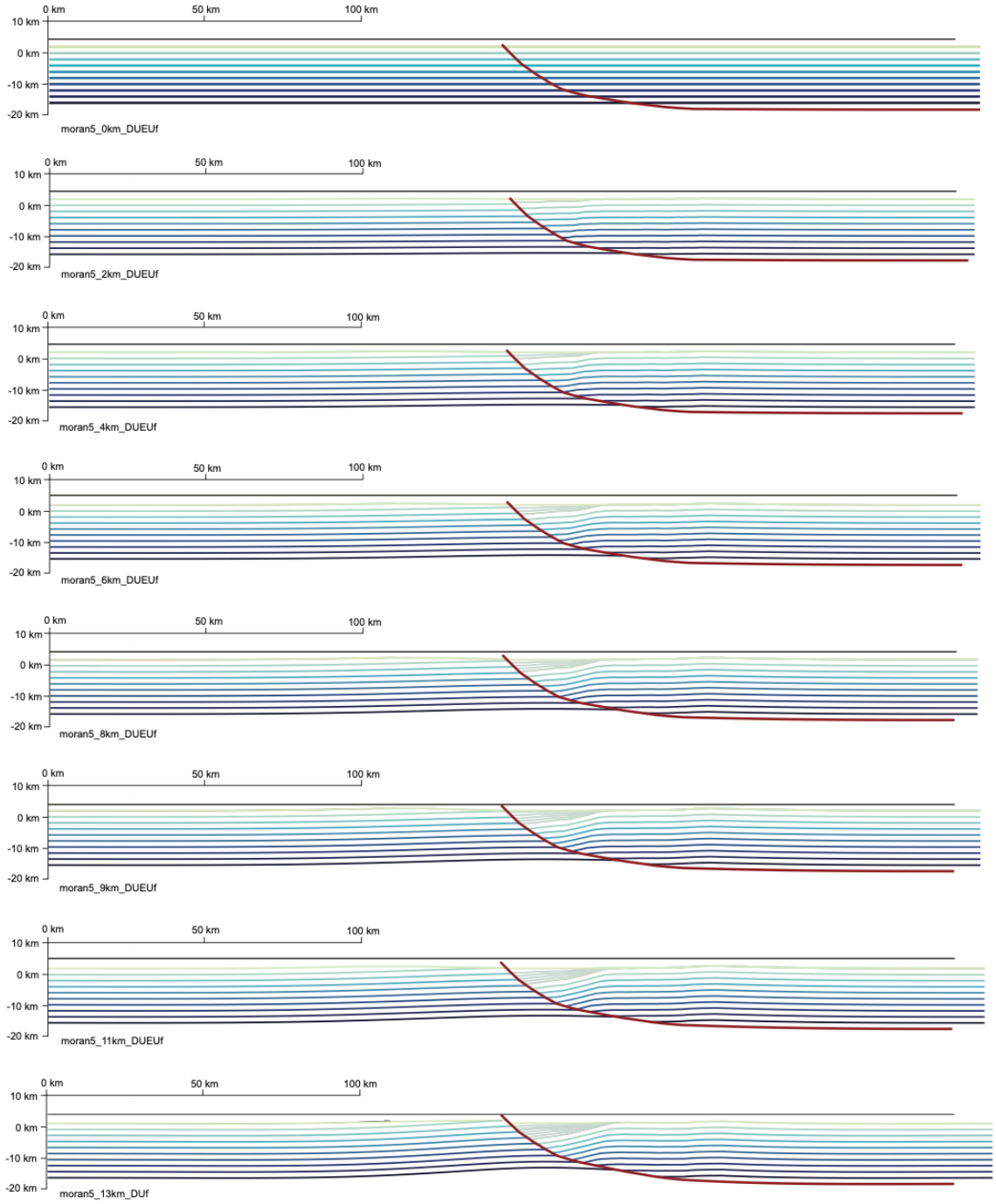

Figure 4.6 – Flexural-kinematic model 5 evaluates a 45° fault, with T_e = 10, Z_d = 20, and D_{max} = 13 km.

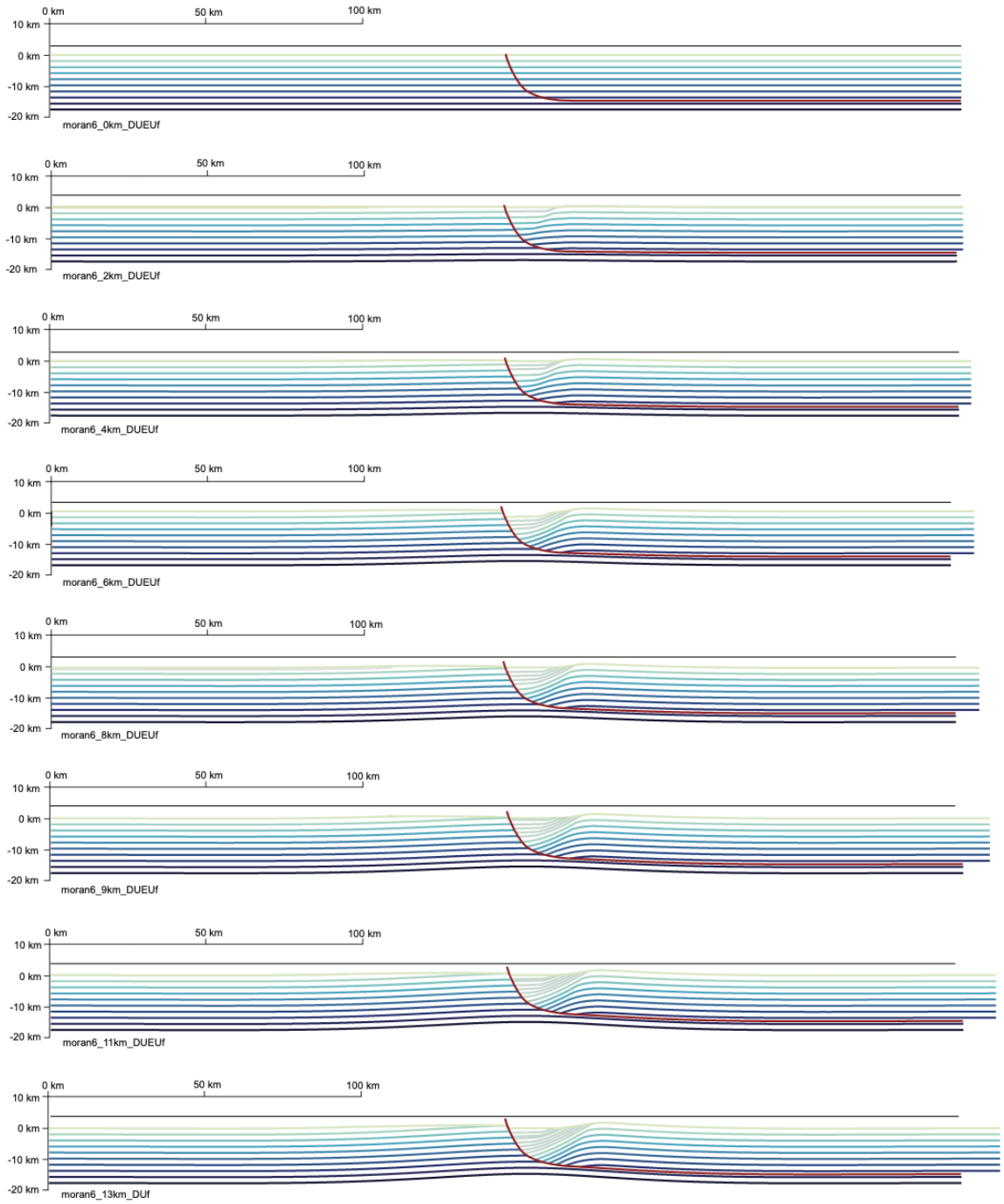

Figure 4.7 – Flexural-kinematic model 6 evaluates a 70° fault, with T_e = 10, Z_d = 15, and D_{max} = 13 km.

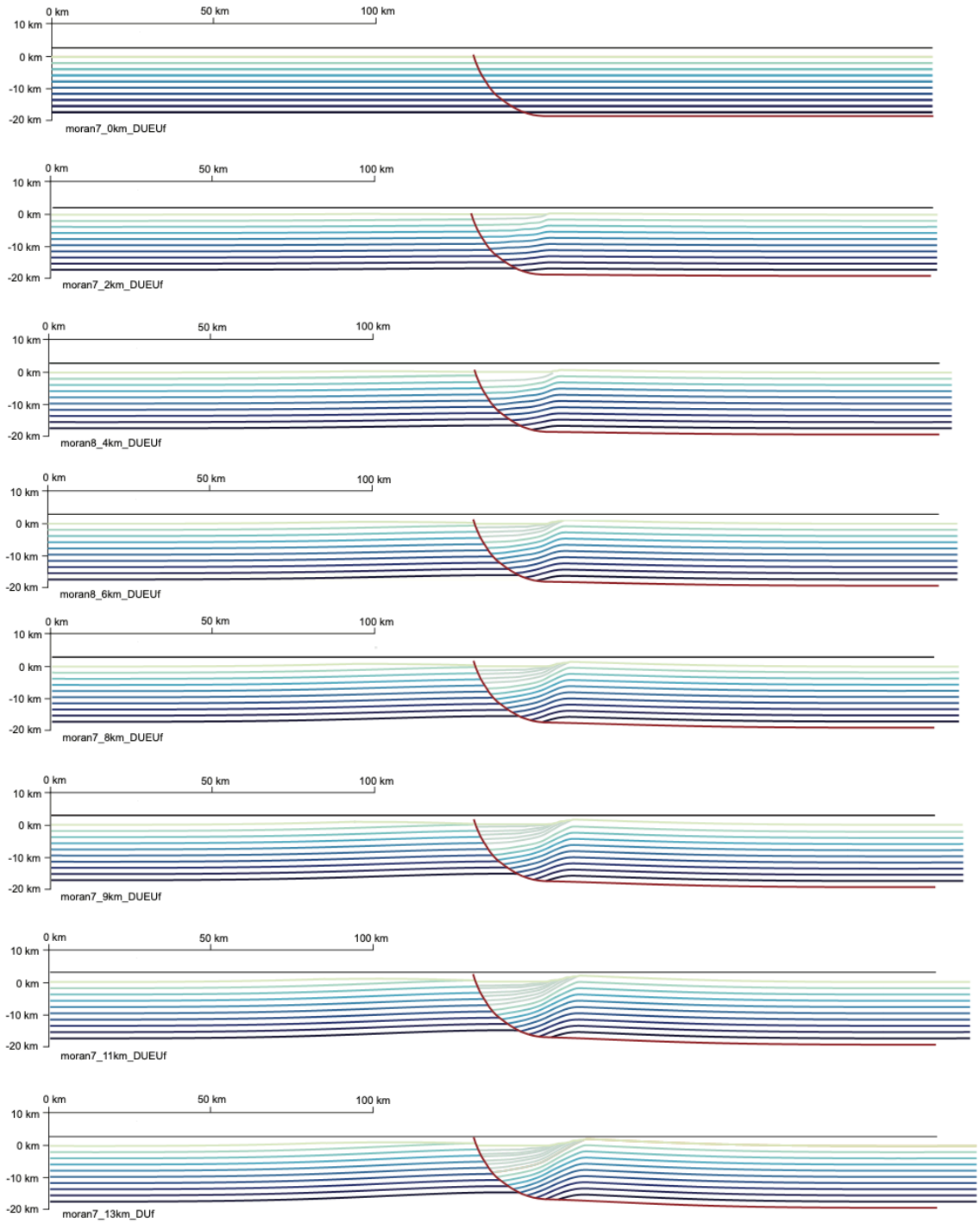

Figure 4.8 – Flexural-kinematic model 7 evaluates a 70° fault, with T_e = 15, Z_d = 20, and D_{max} = 13 km.

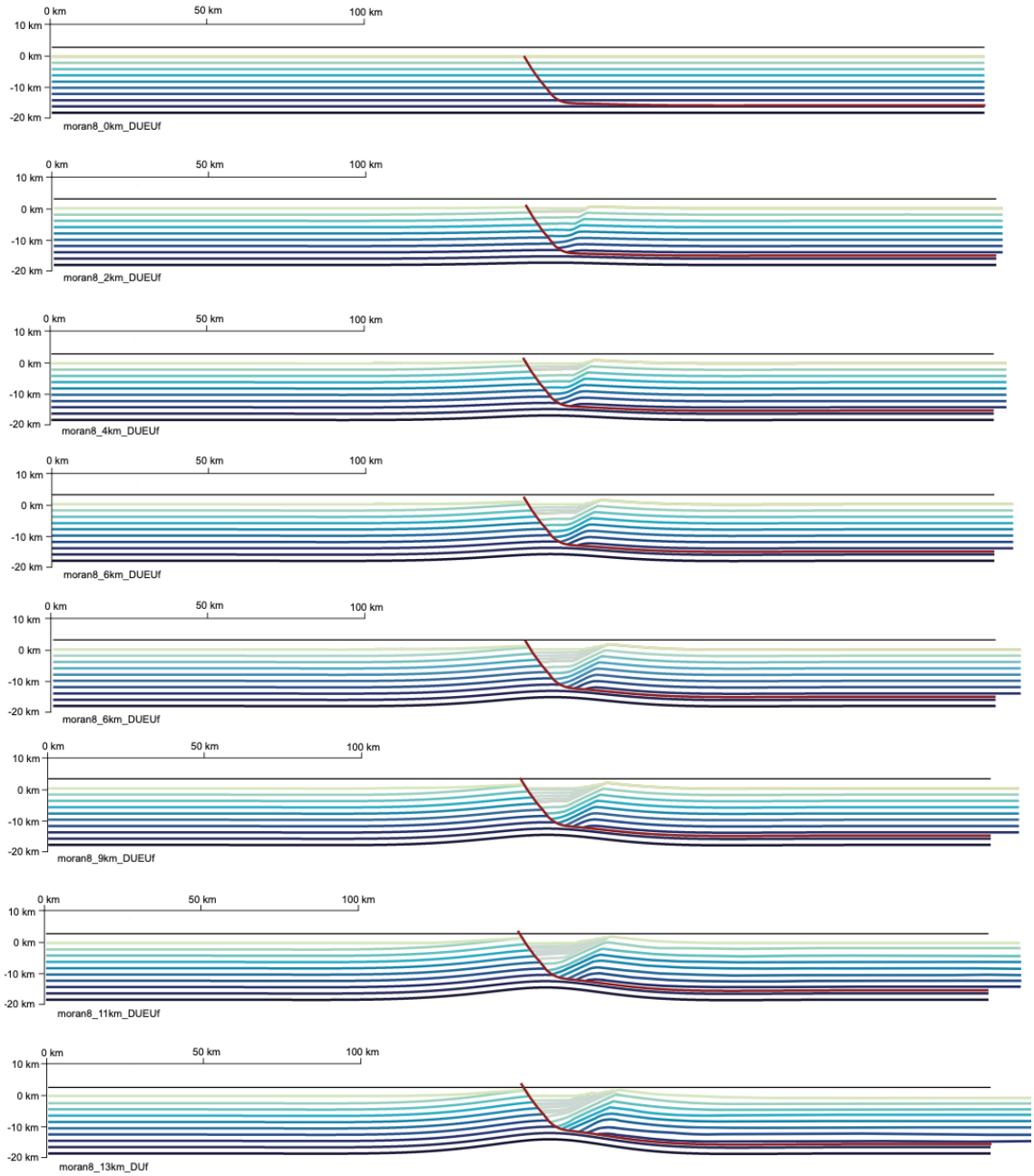

Figure 4.9 – Flexural-kinematic model 8 evaluates a 60° fault, with T_e = 5, Z_d = 15, and D_{max} = 13 km.

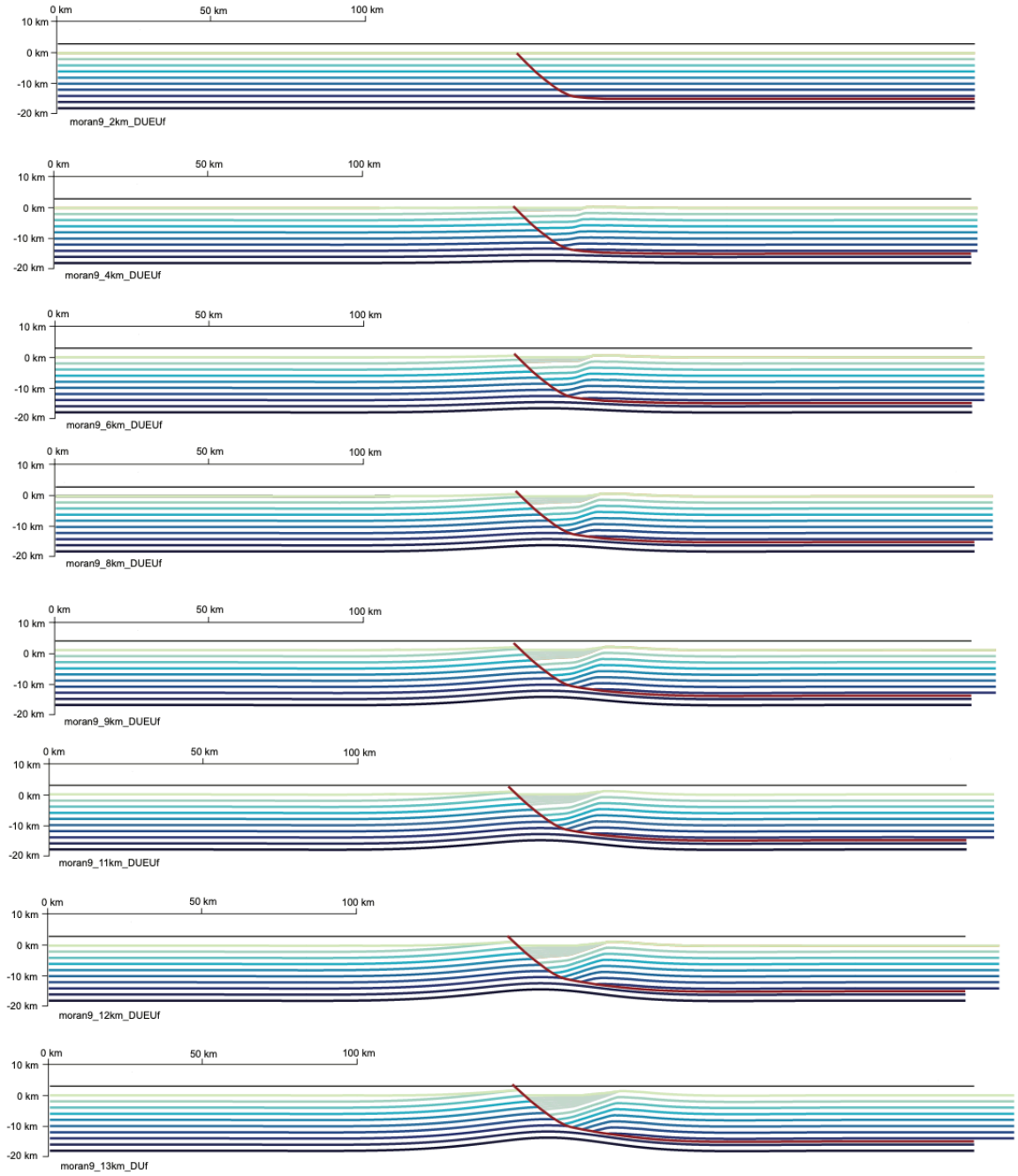

Figure 4.10 – Flexural-kinematic model 9 evaluates a 45° fault, with T_e = 5, Z_d = 15, and D_{max} = 13 km.

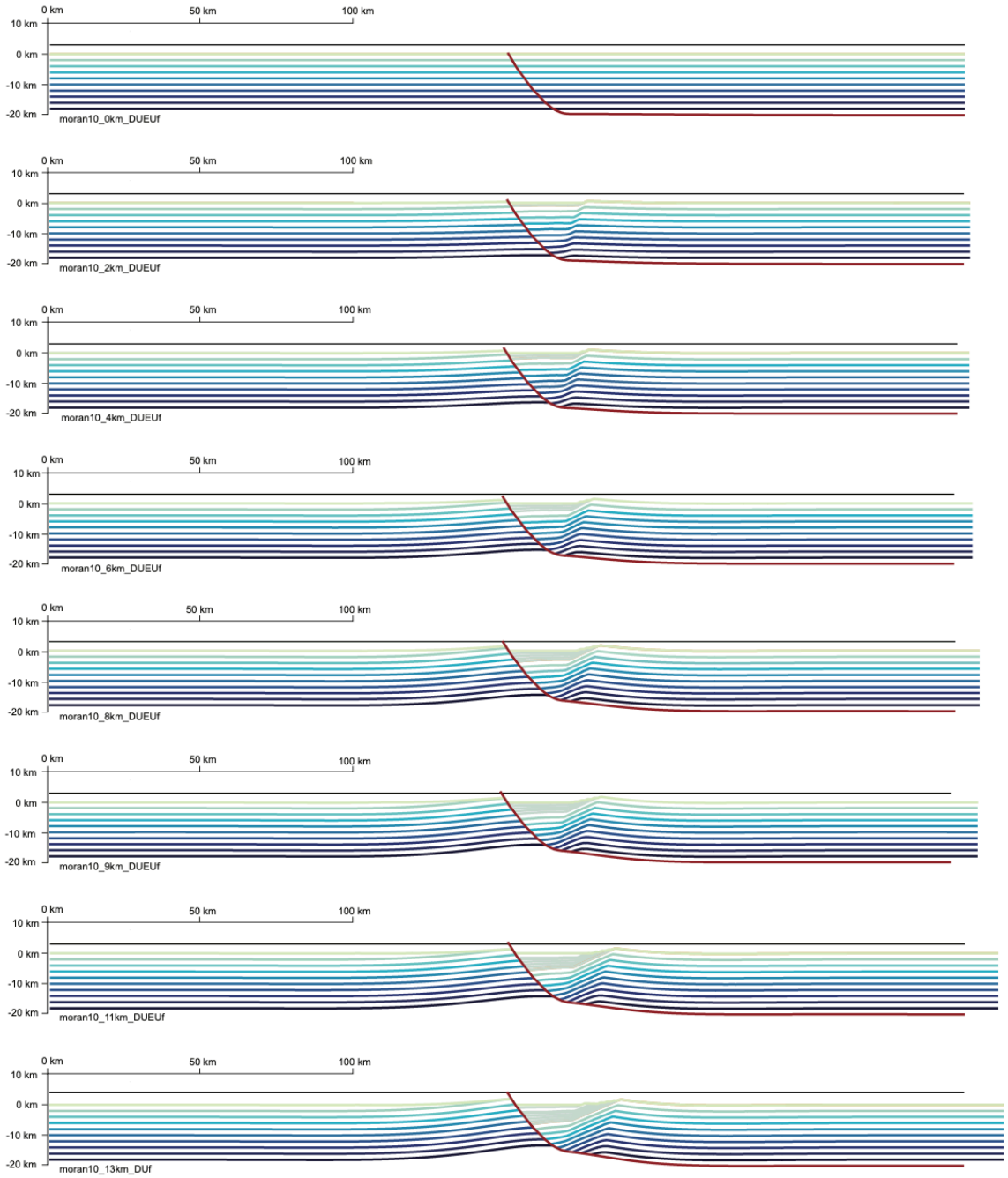

Figure 4.11 – Flexural-kinematic model 10 evaluates a 60° fault, with Te = 5, Zd = 20, and Dmax = 13 km.

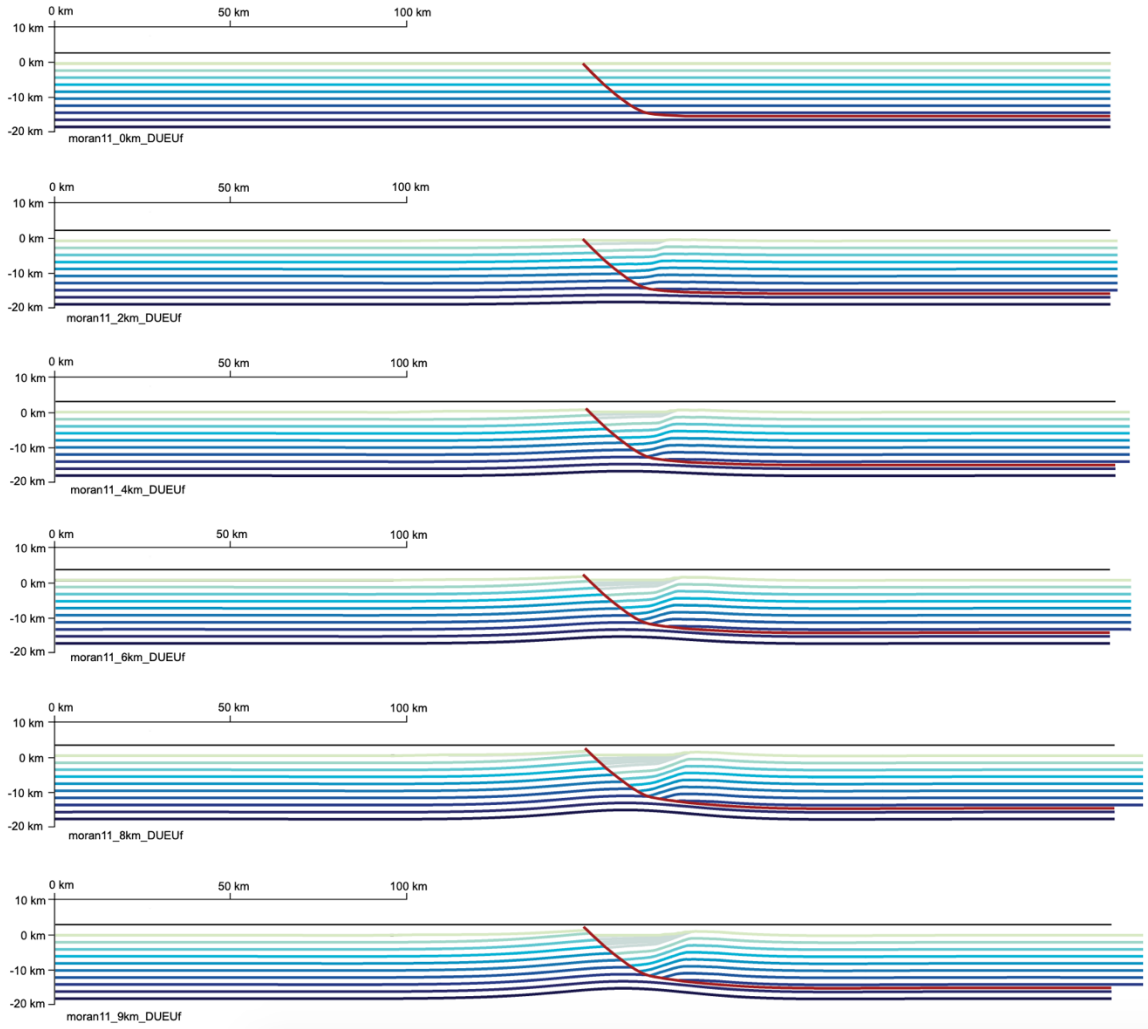

Figure 4.12 – Flexural-kinematic model 11 evaluates a 45° fault, with T_e = 5, Z_d = 15, and D_{max} = 17 km.

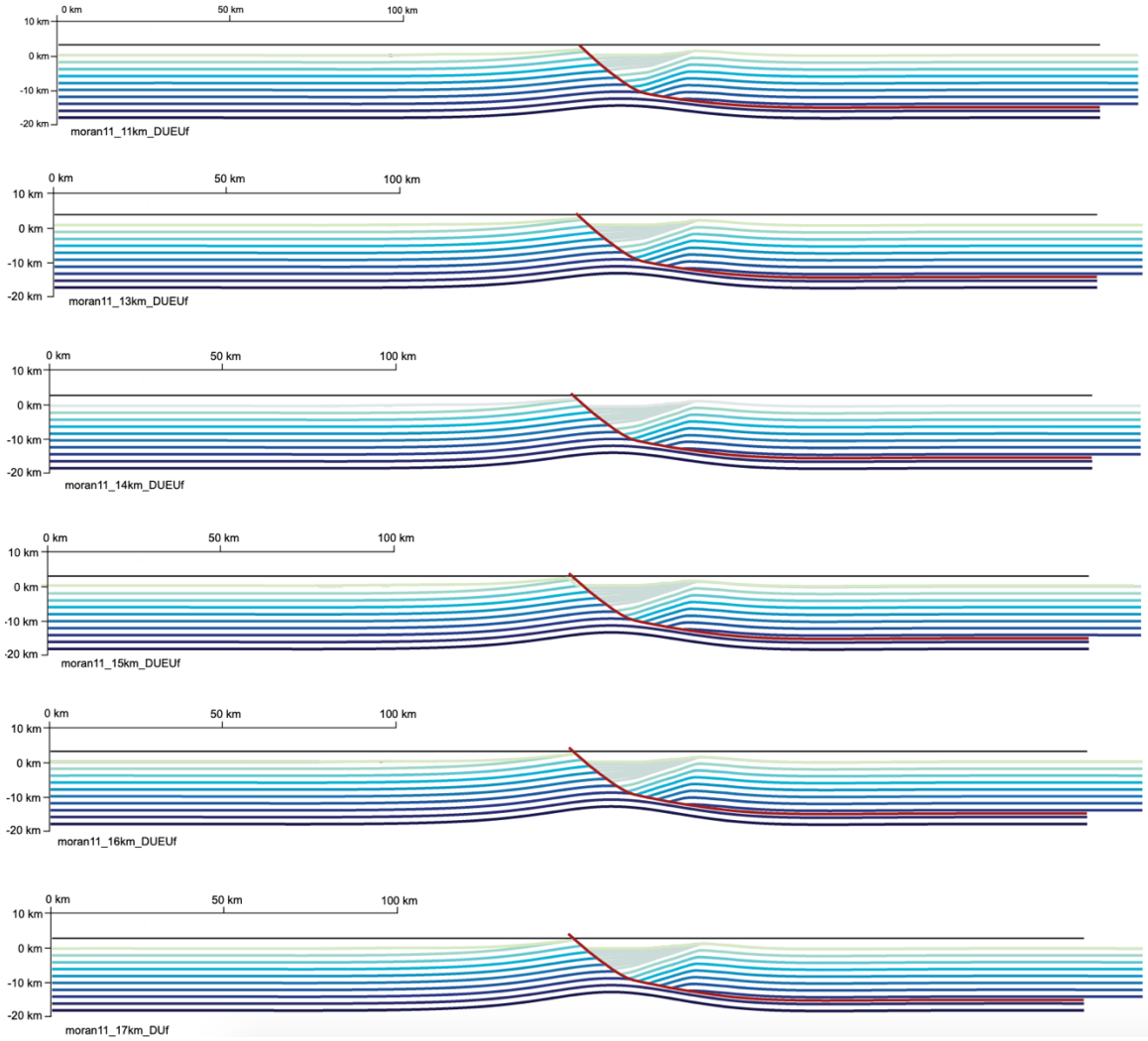

Figure 4.12 (continued) – Flexural-kinematic model 11 evaluates a 45° fault, with T_e = 5, Z_d = 15, and D_{max} = 17 km.

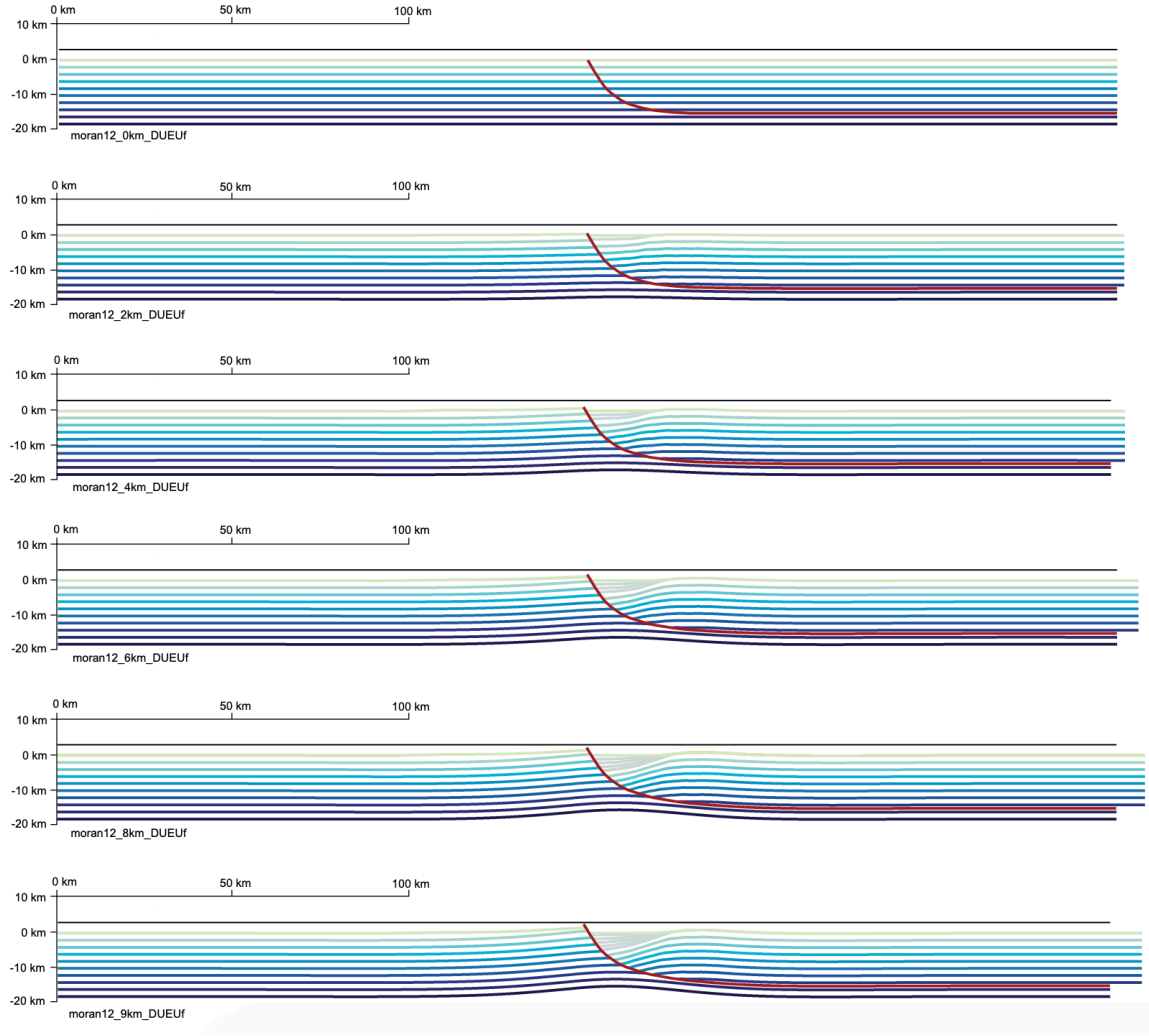

Figure 4.13 – Flexural-kinematic model 12 evaluates a 60° fault, with T_e = 5, Z_d = 15, and D_{max} = 17 km.

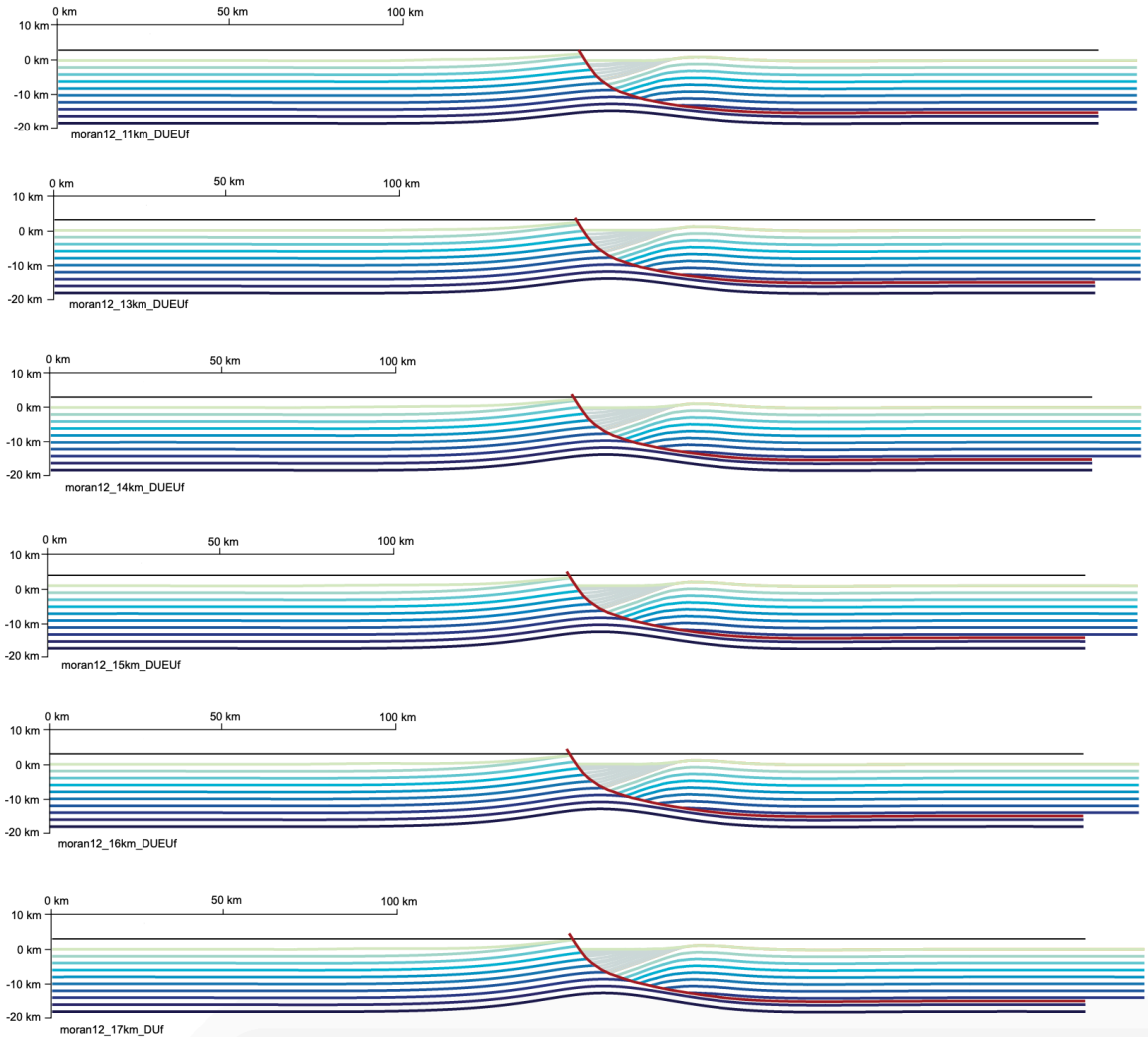

Figure 4.13 (continued) – Flexural-kinematic model 12 evaluates a 60° fault, with T_e = 5, Z_d = 15, and D_{max} = 17 km.

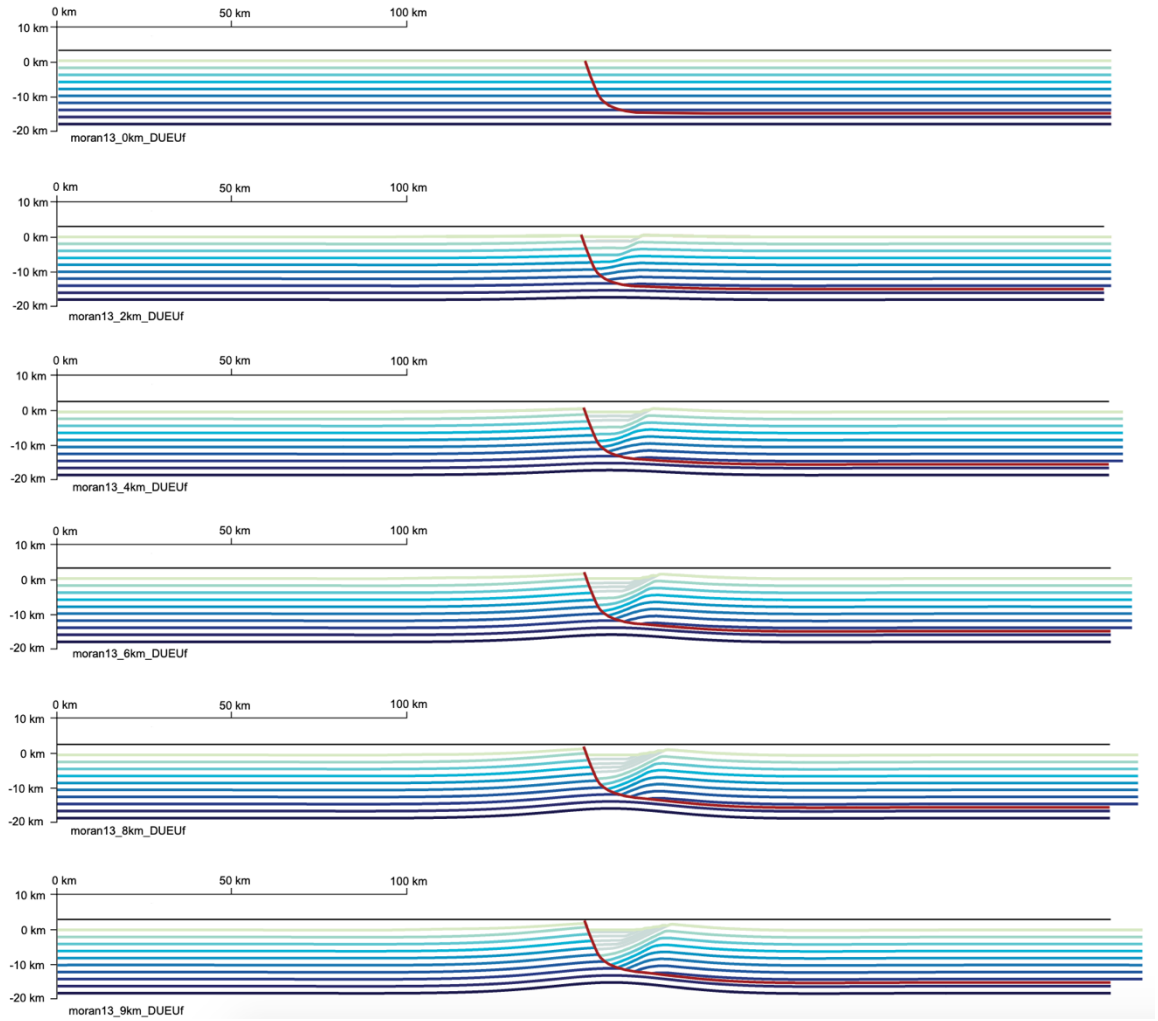

Figure 4.14 – Flexural-kinematic model 13 evaluates a 70° fault, with T_e = 5, Z_d = 15, and D_{max} = 17 km.

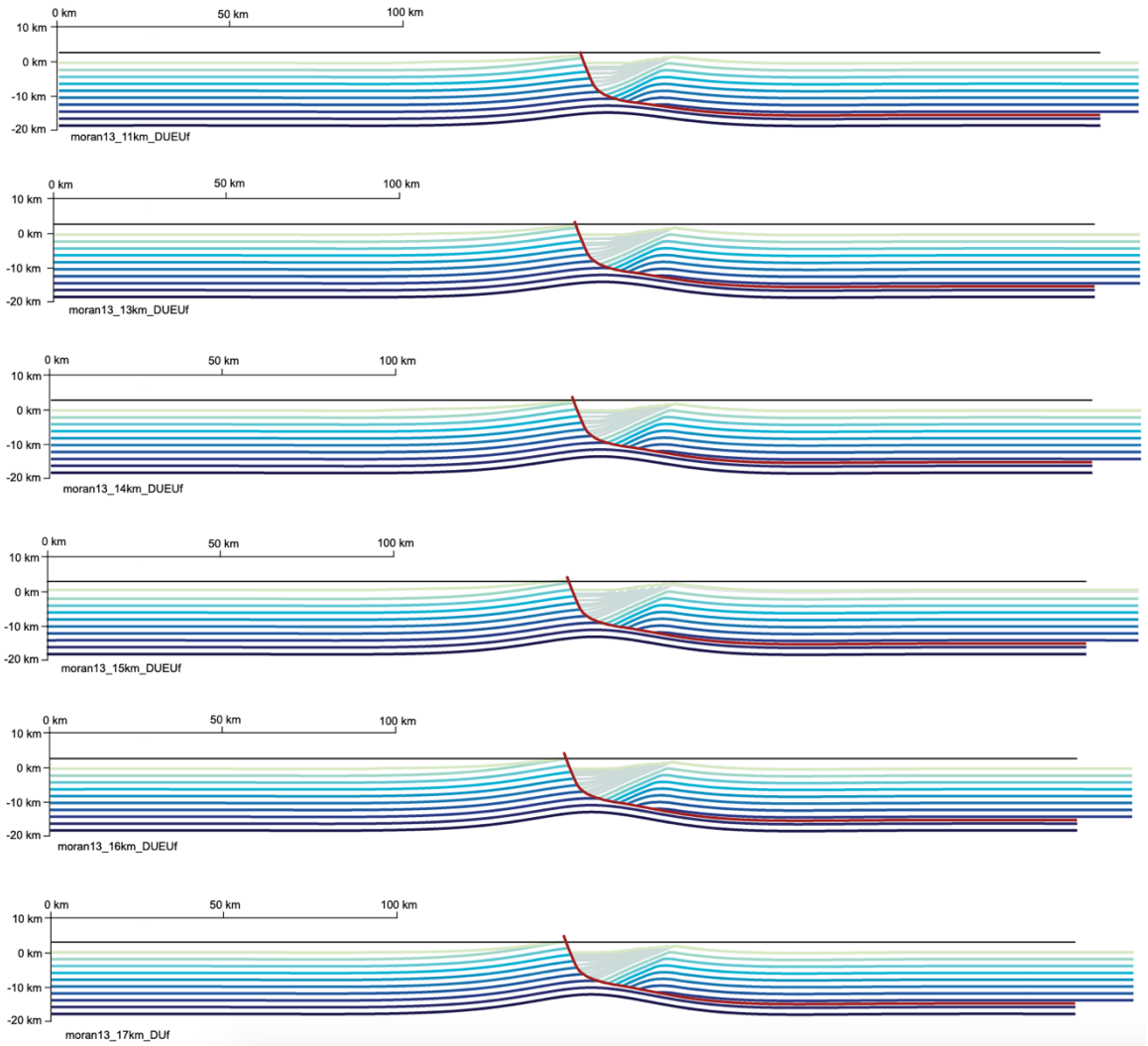

Figure 4.14 (continued) – Flexural-kinematic model 13 evaluates a 70° fault, with T_e = 5, Z_d = 15, and D_{max} = 17 km.

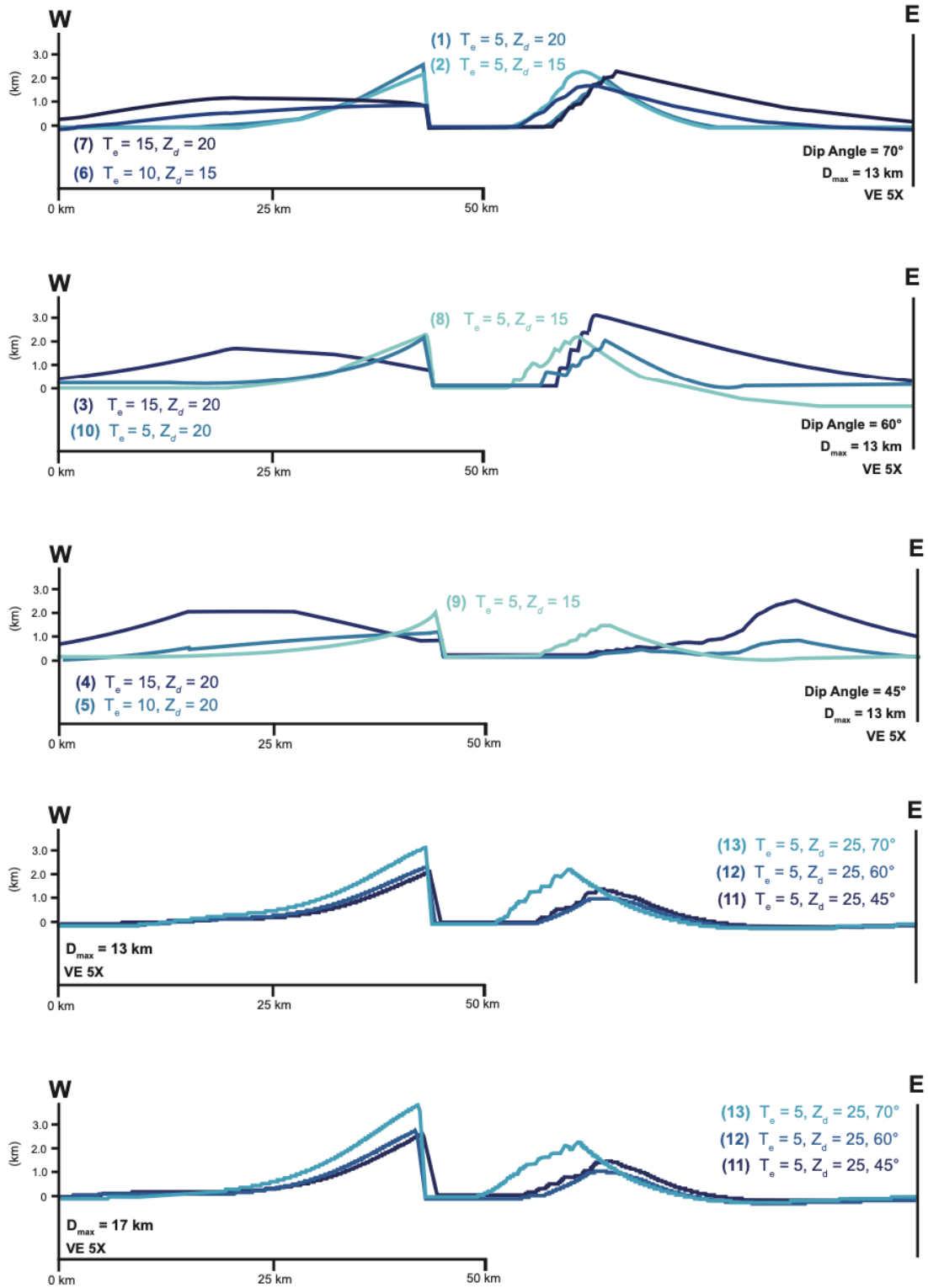

Figure 4.15 – Modeled flexural-kinematic topographic profiles for fault dip angles of 45°, 60°, and 70° and D_{max} = 13 km and D_{max} = 17. Profiles compare varying T_e and Z_d. Number in parenthesis indicates corresponding model number.

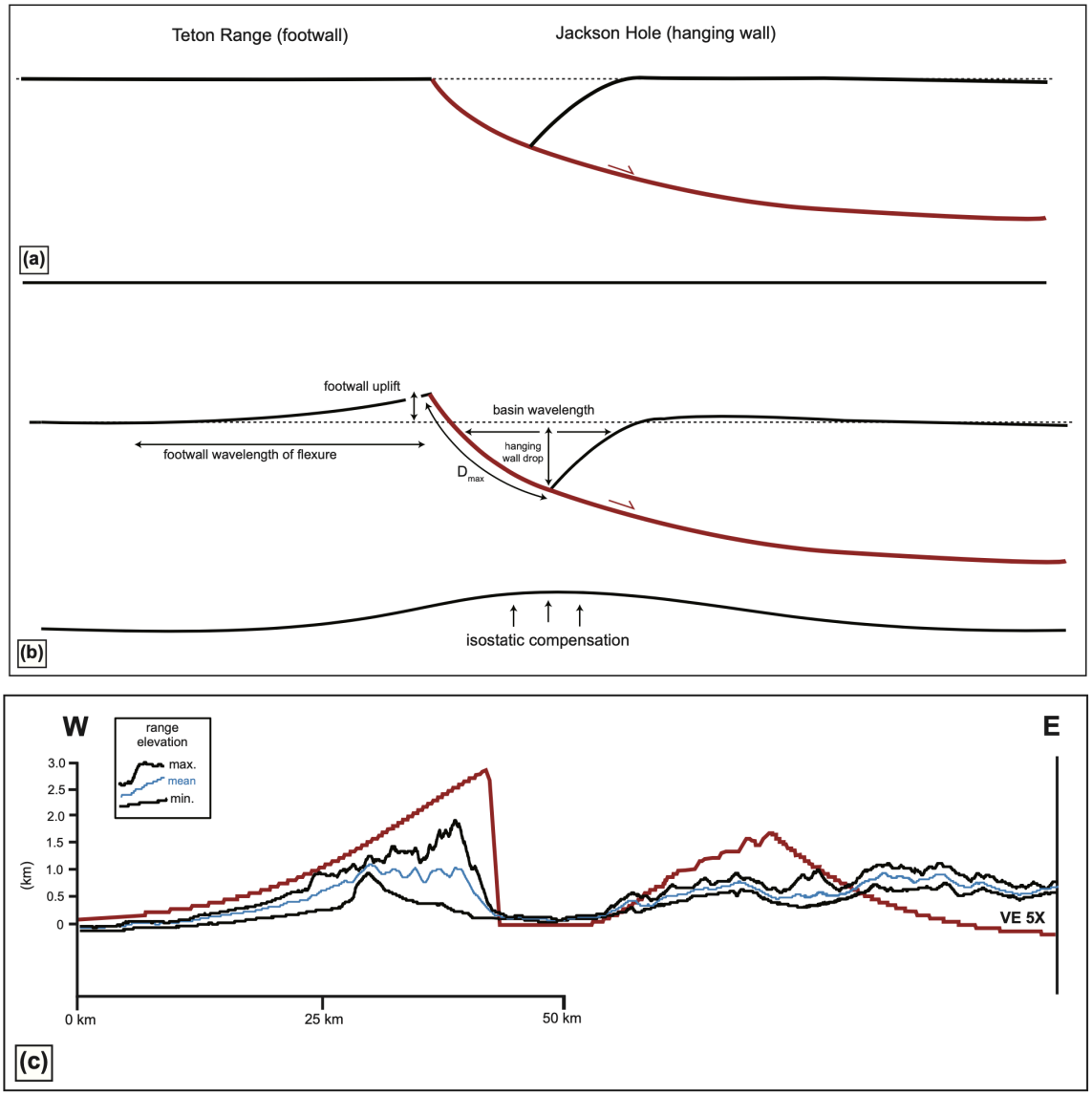

Figure 4.16 – (a) Simplified schematic of the Teton fault. (b) Constraints used to select a base case flexural-kinematic model including footwall flexural wavelength, footwall uplift, and basin flexural wavelength, where both footwall uplift and hanging wall drop contribute to D_{max}. (c) Base case flexural-kinematic model (red profile) with fault dip 70°, T_e = 5 km, Z_d = 15 km, and D_{max}= 17 km with 5X vertical exaggeration compared to the max, mean, and min swath topographic profile through Mount Moran and Jackson Hole basin.

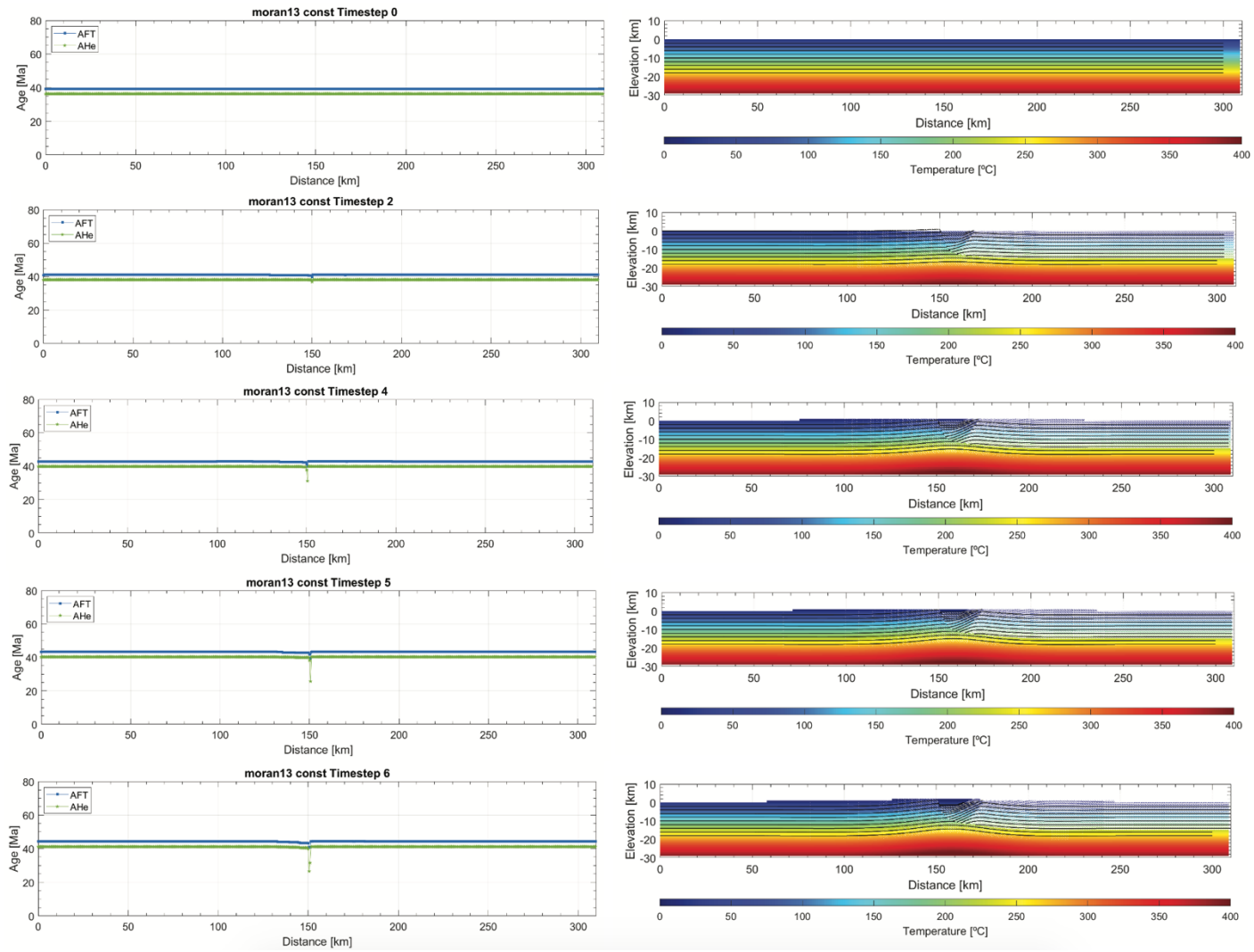

Figure 4.17 – Thermal-kinematic model 13 evaluated in Pecube for a constant slip rate with fault slip onset at 5 Ma for D_{max} = 11 km

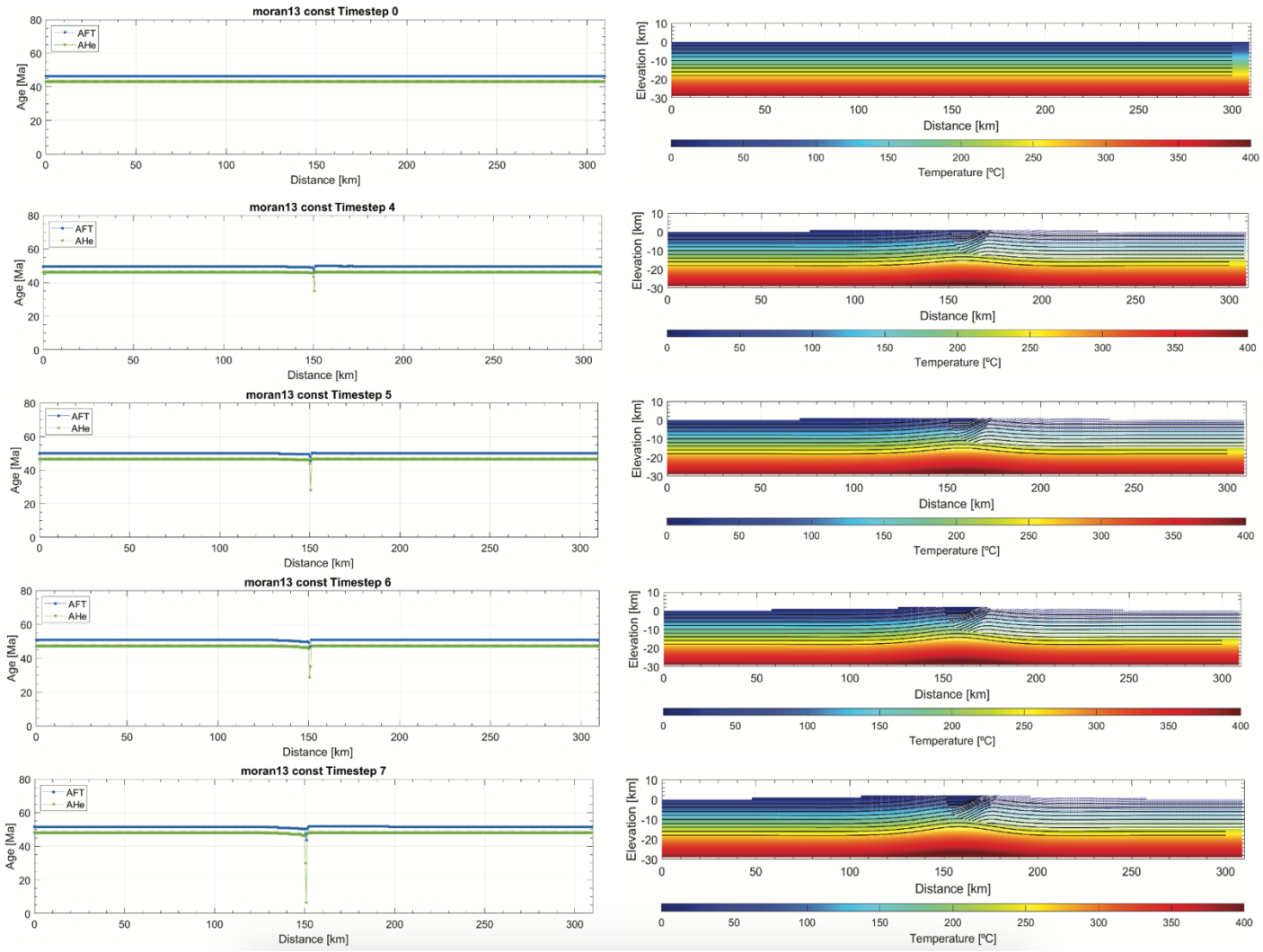

Figure 4.18 – Thermal-kinematic model 13 evaluated in Pecube for a constant slip rate with fault slip onset at 5 Ma for D_{max} = 13 km.

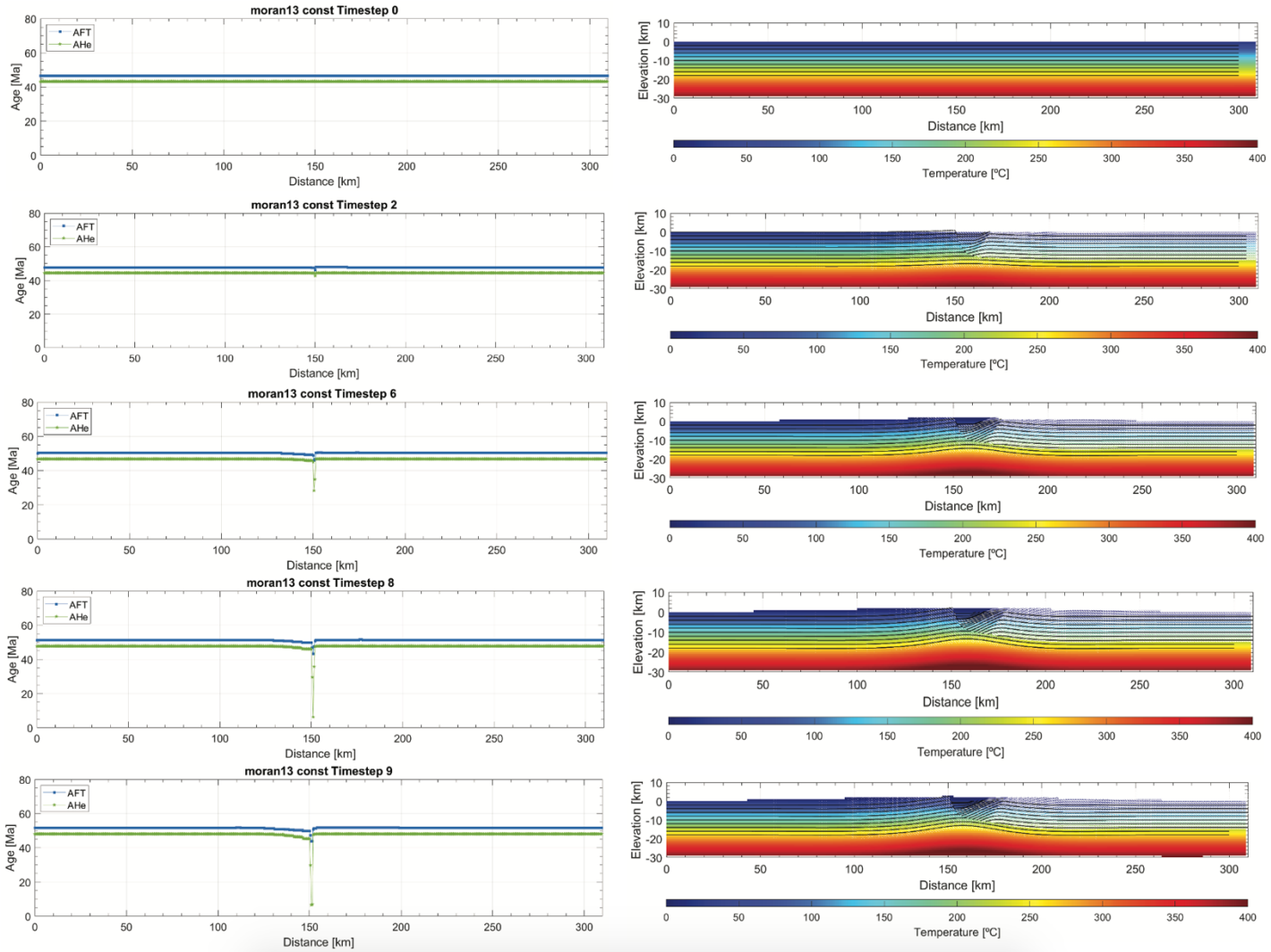

Figure 4.19 – Thermal-kinematic model 13 evaluated in Pecube for a constant slip rate with fault slip onset at 5 Ma for D_{max} = 15 km.

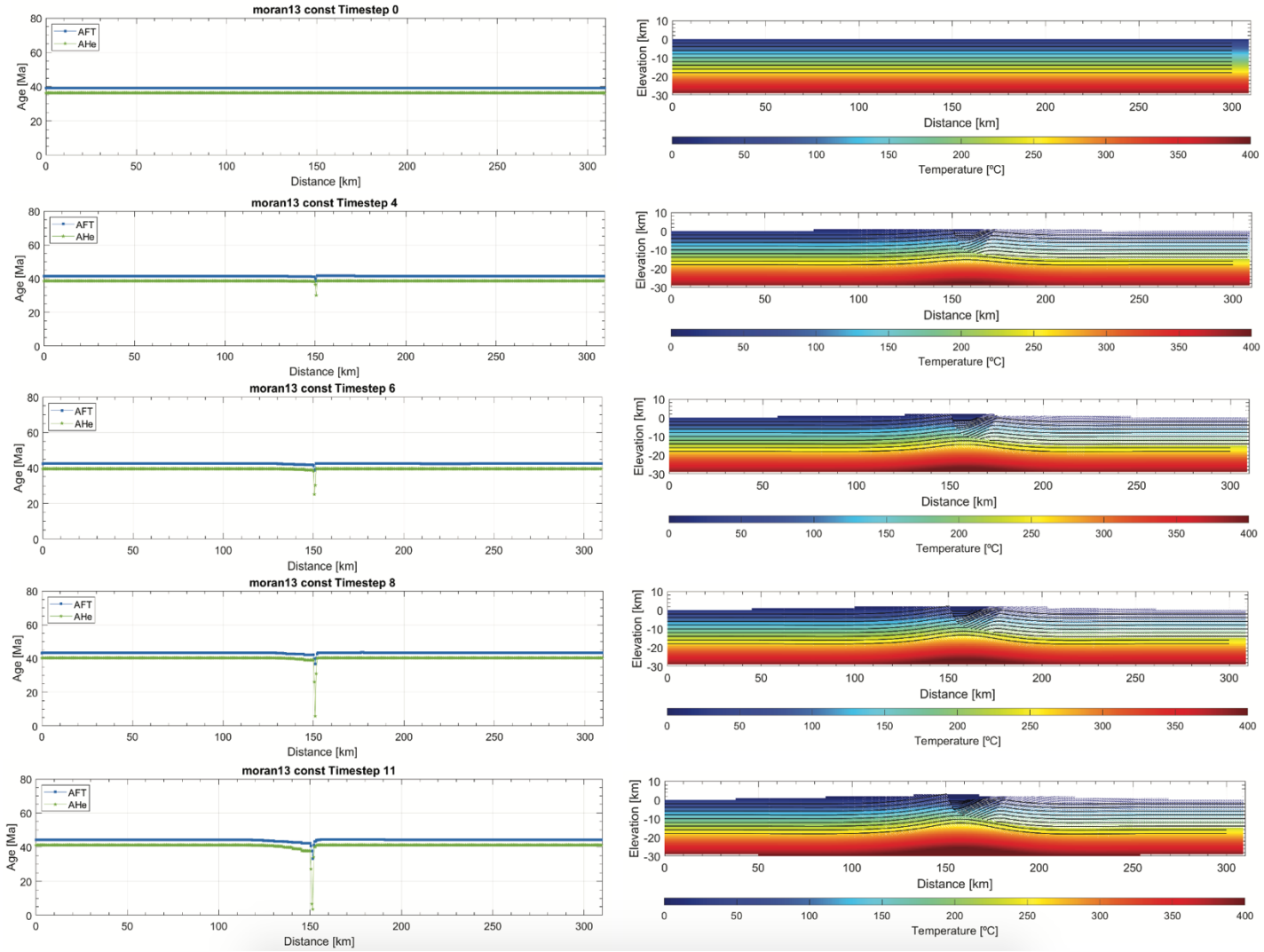

Figure 4.20 – Thermal-kinematic model 13 evaluated in Pecube for a constant slip rate with fault slip onset at 5 Ma for D_{max} = 17 km.

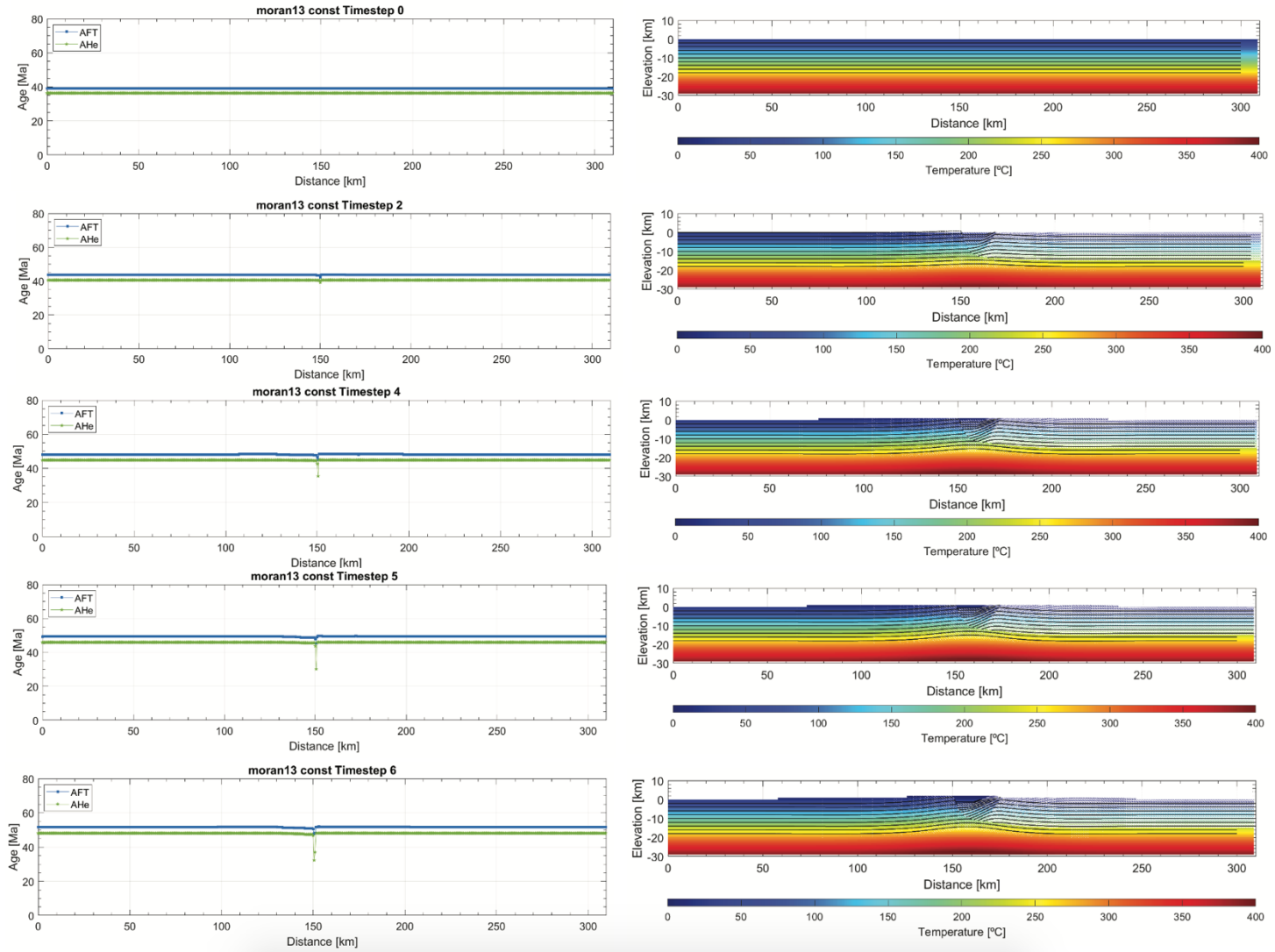

Figure 4.21 – Thermal-kinematic model 13 evaluated in Pecube for a constant slip rate with fault slip onset at 12 Ma for D_{max} = 11 km.

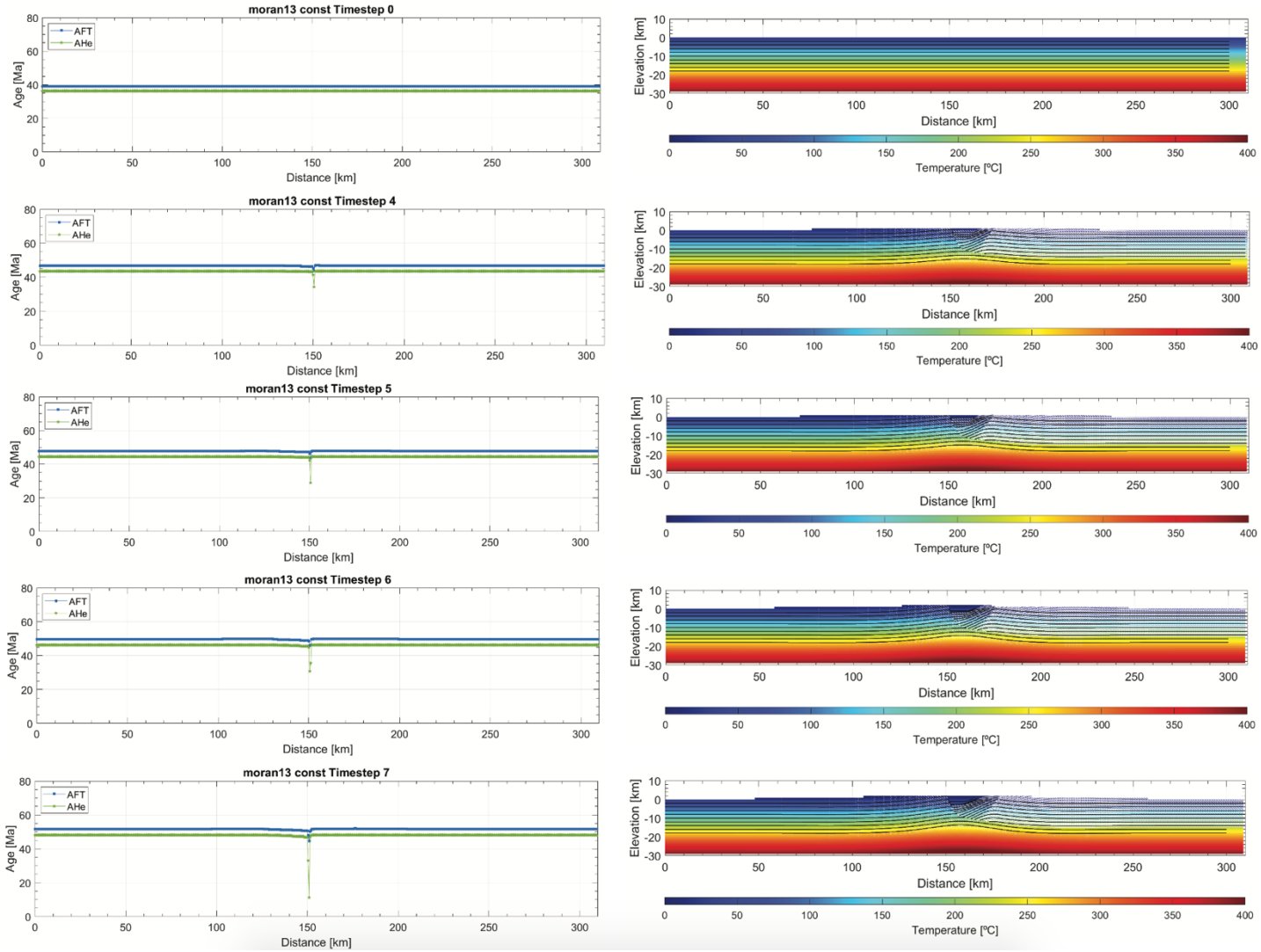

Figure 4.22 – Thermal-kinematic model 13 evaluated in Pecube for a constant slip rate with fault slip onset at 12 Ma for D_{max} = 13 km.

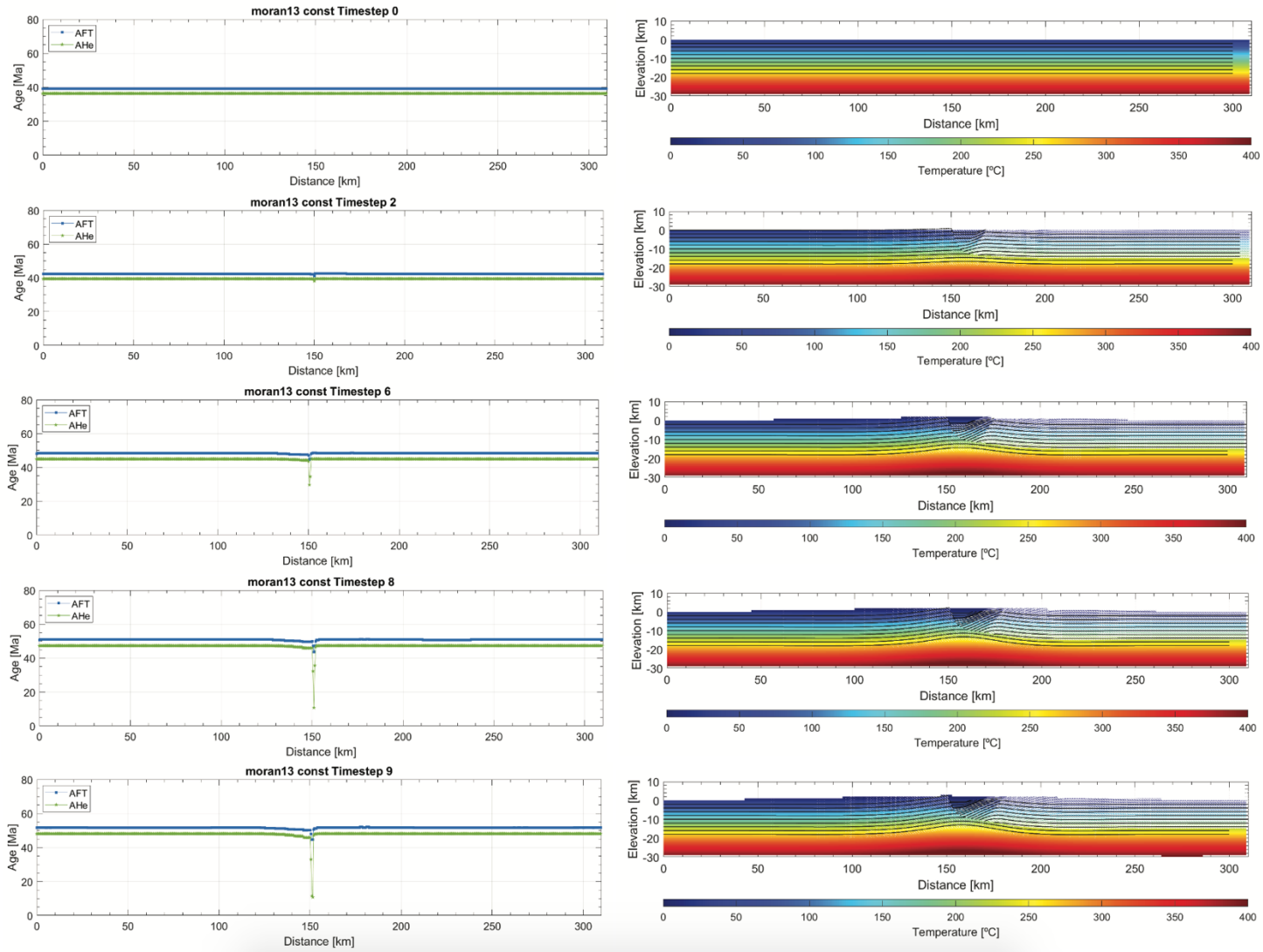

Figure 4.23 – Thermal-kinematic model 13 evaluated in Pecube for a constant slip rate with fault slip onset at 12 Ma for D_{max} = 15 km.

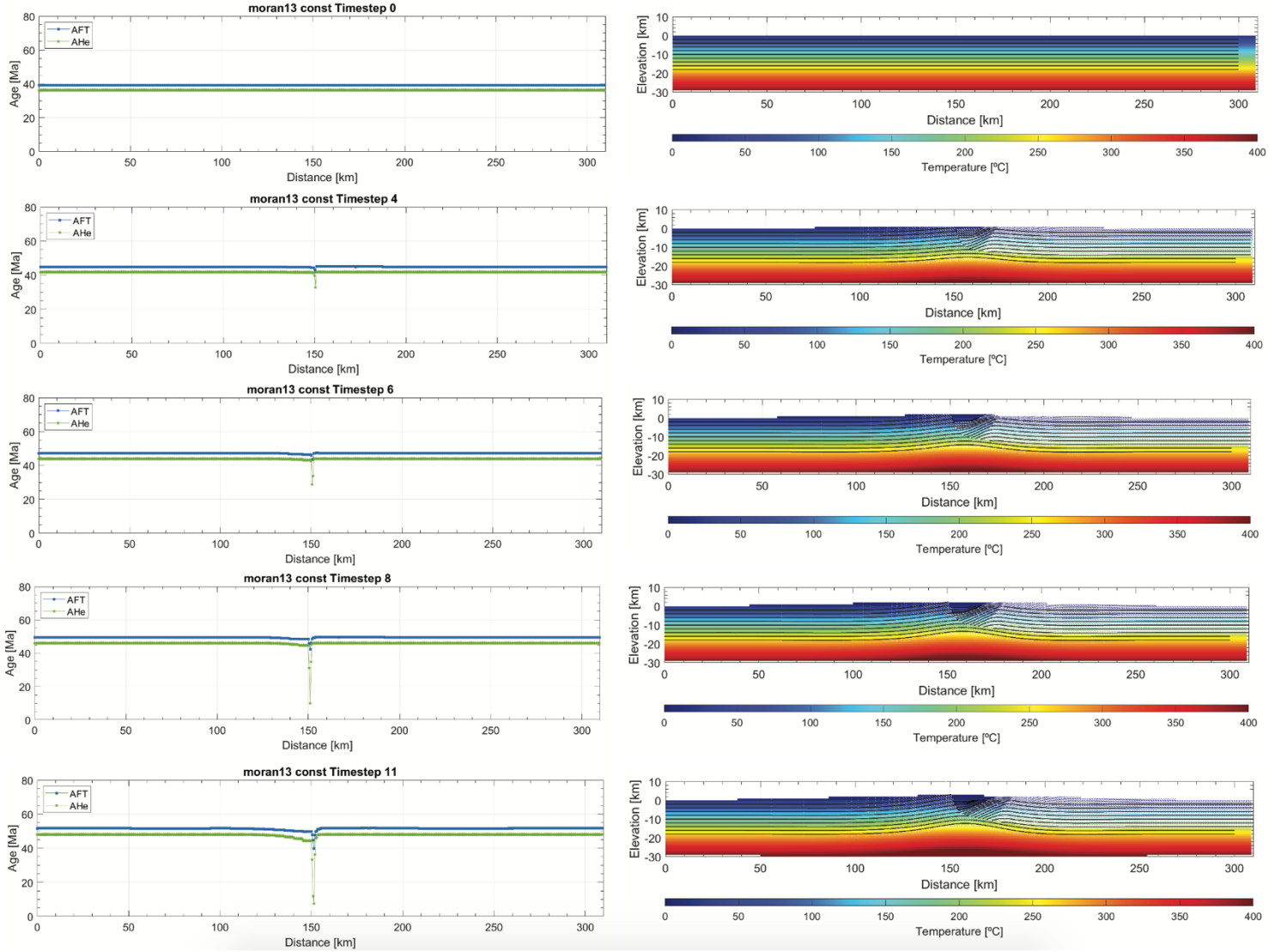

Figure 4.24 – Thermal-kinematic model 13 evaluated in Pecube for a constant slip rate with fault slip onset at 12 Ma for D_{max} = 17 km.

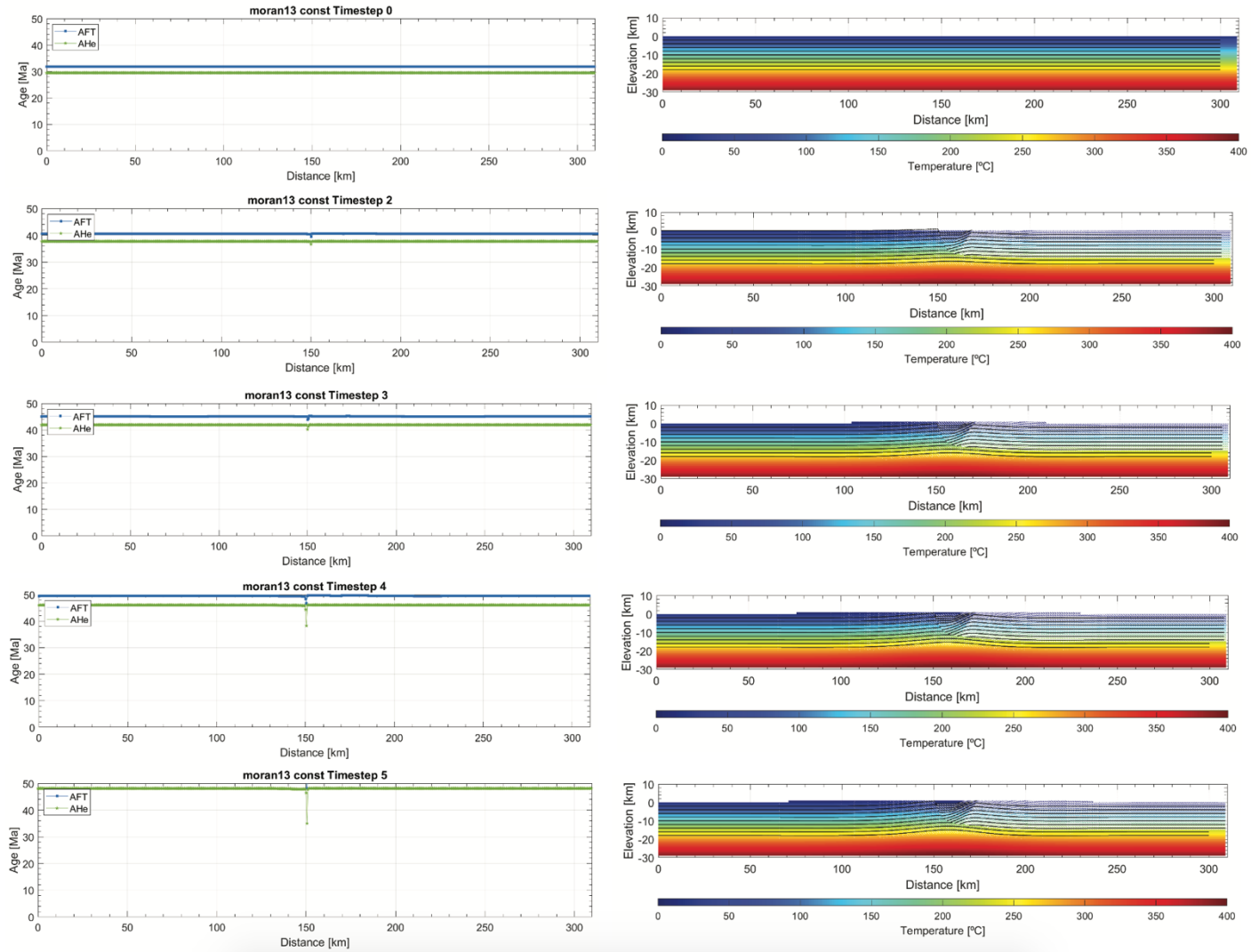

Figure 4.25 – Thermal-kinematic model 13 evaluated in Pecube for a constant slip rate with fault slip onset at 19 Ma for D_{max} = 9 km.

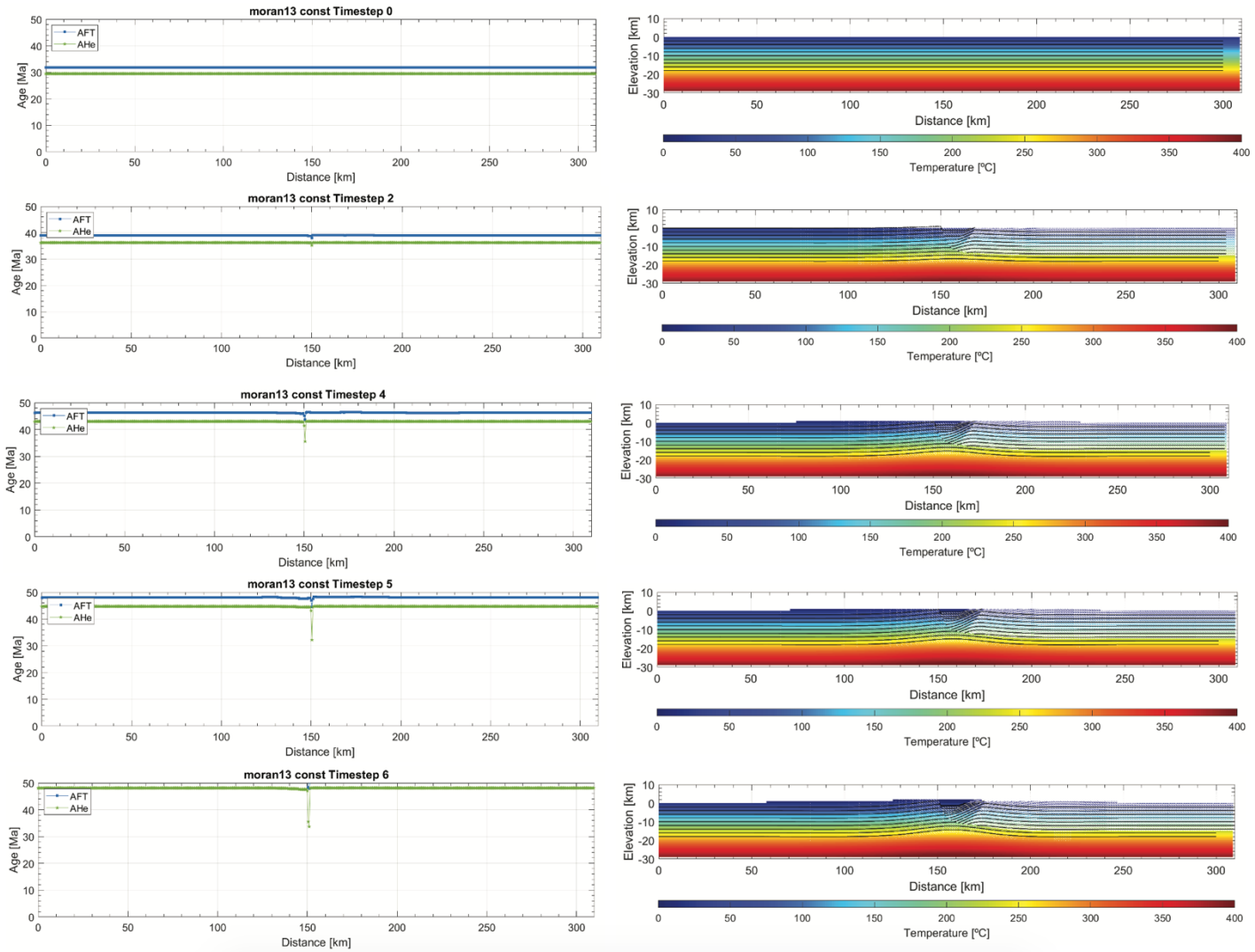

Figure 4.26 – Thermal-kinematic model 13 evaluated in Pecube for a constant slip rate with fault slip onset at 19 Ma for D_{max} = 11 km.

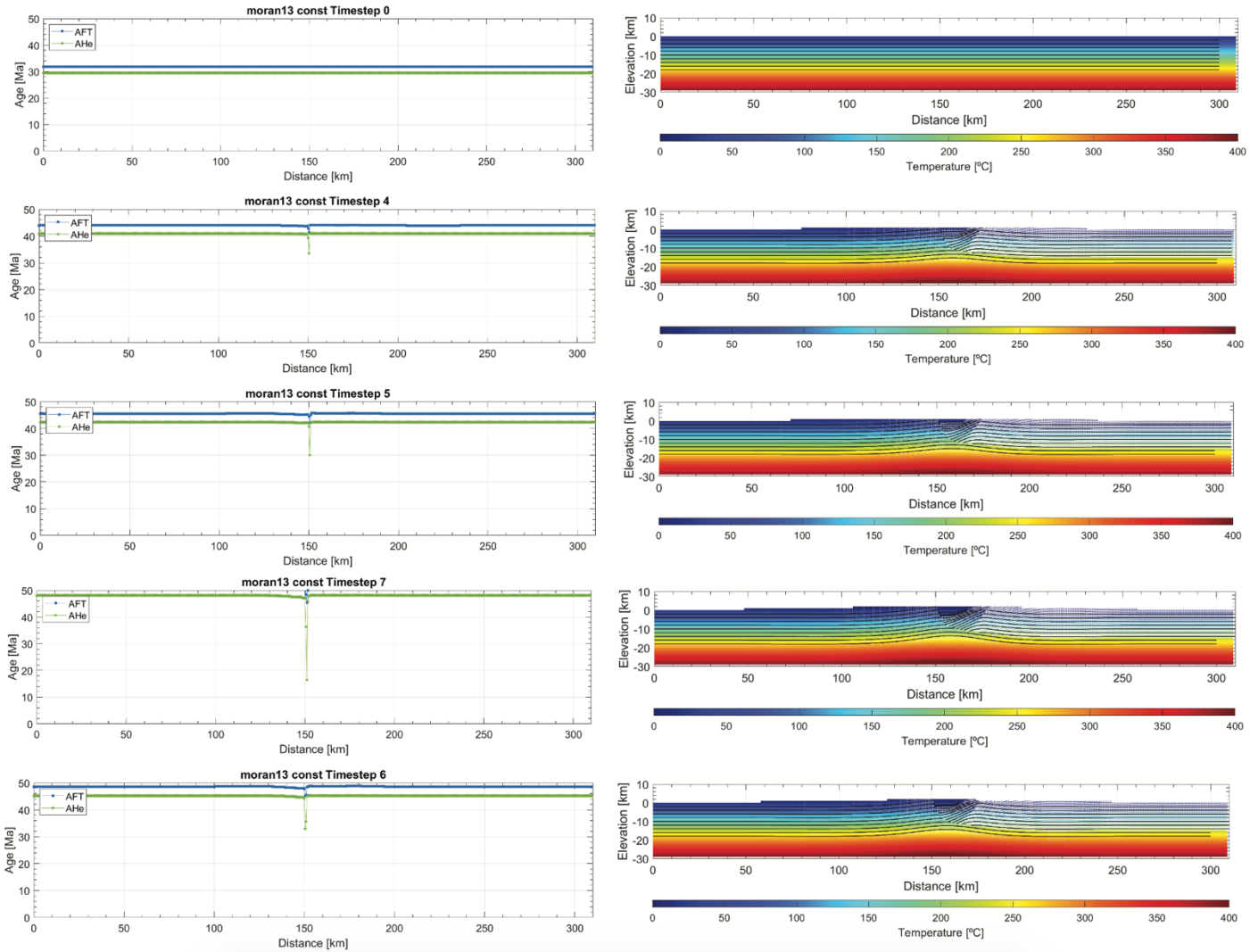

Figure 4.27 – Thermal-kinematic model 13 evaluated in Pecube for a constant slip rate with fault slip onset at 19 Ma for D_{max} = 13 km.

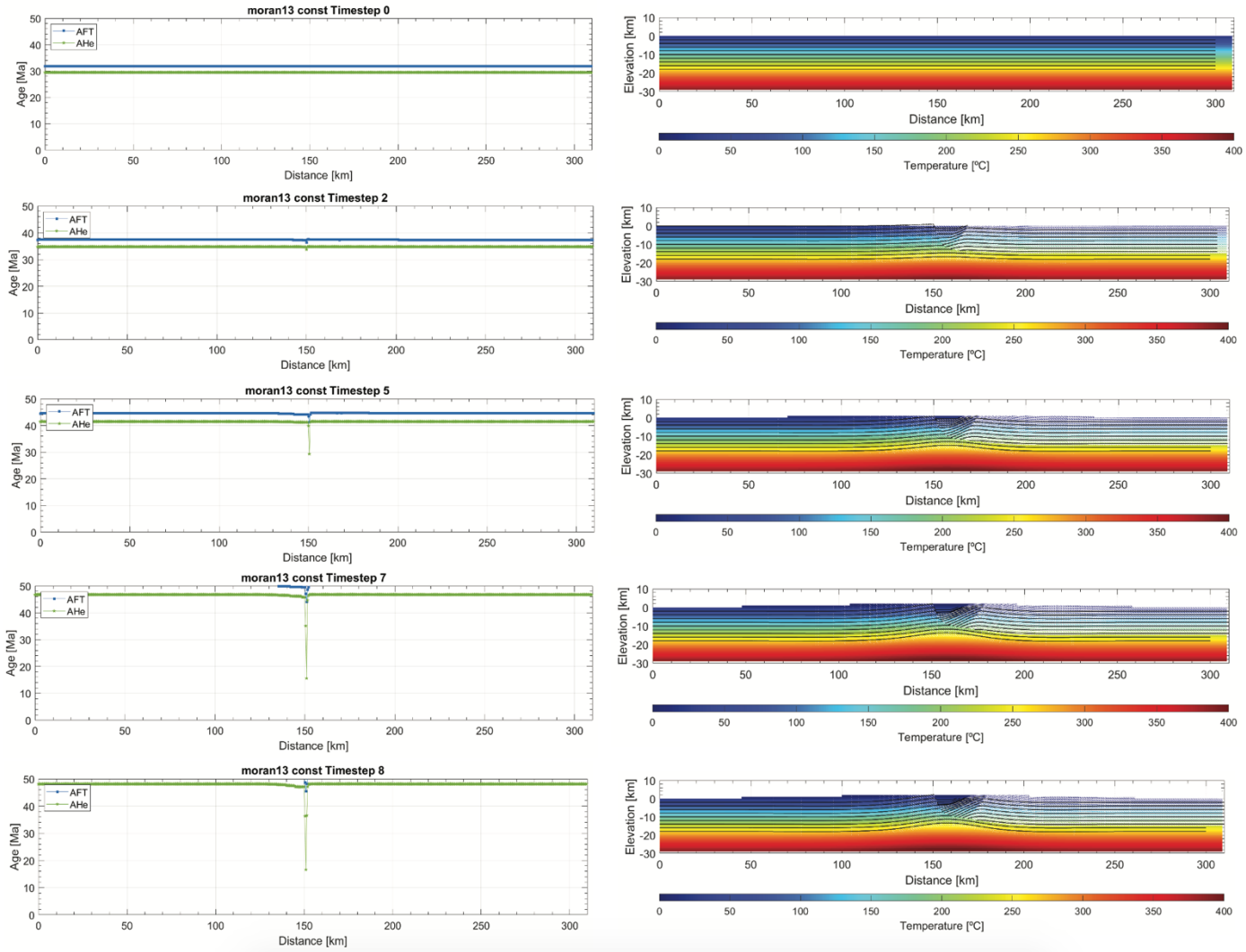

Figure 4.28 – Thermal-kinematic model 13 evaluated in Pecube for a constant slip rate with fault slip onset at 19 Ma for D_{max} = 14 km.

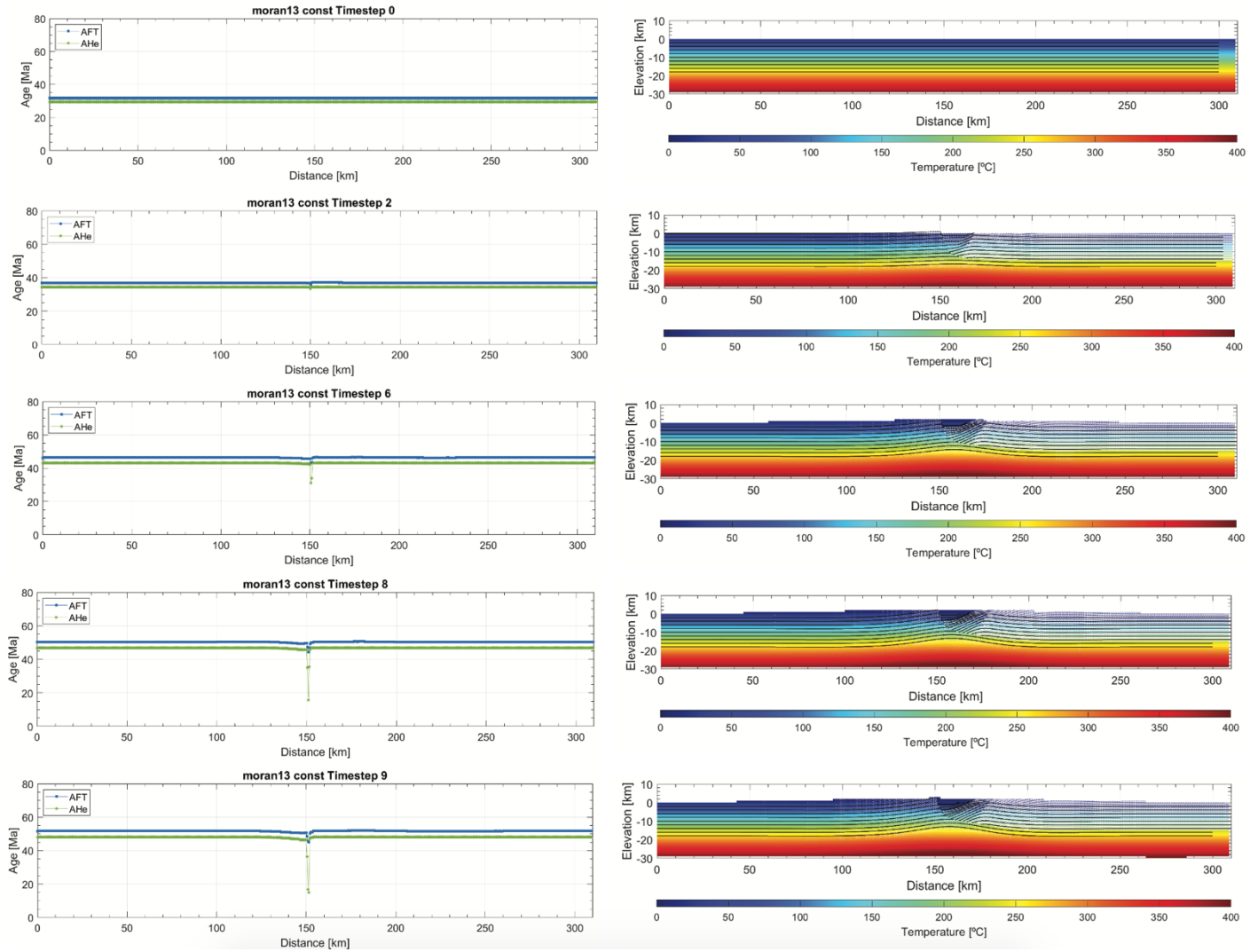

Figure 4.29 – Thermal-kinematic model 13 evaluated in Pecube for a constant slip rate with fault slip onset at 19 Ma for D_{max} = 15 km.

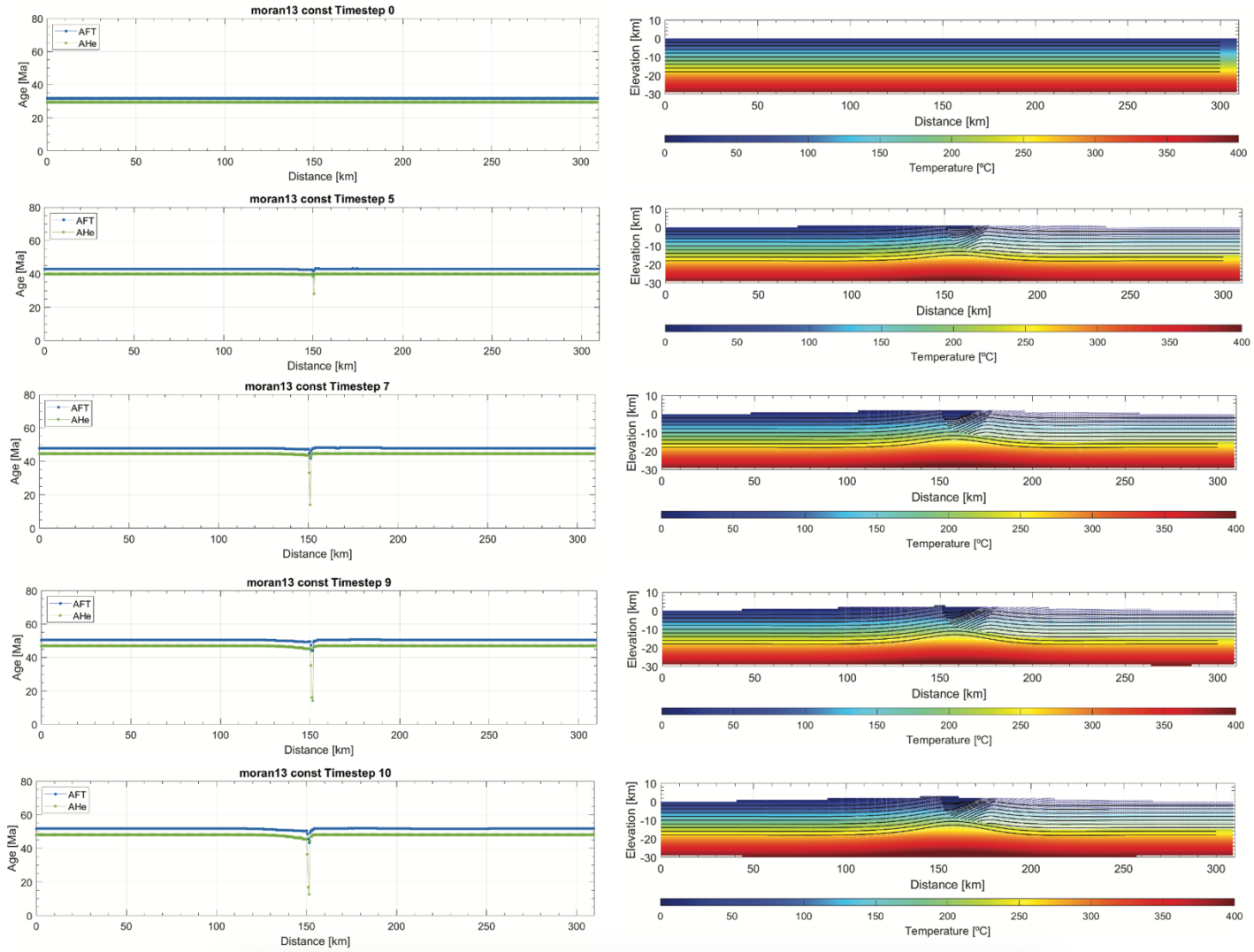

Figure 4.30 – Thermal-kinematic model 13 evaluated in Pecube for a constant slip rate with fault slip onset at 19 Ma for D_{max} = 16 km.

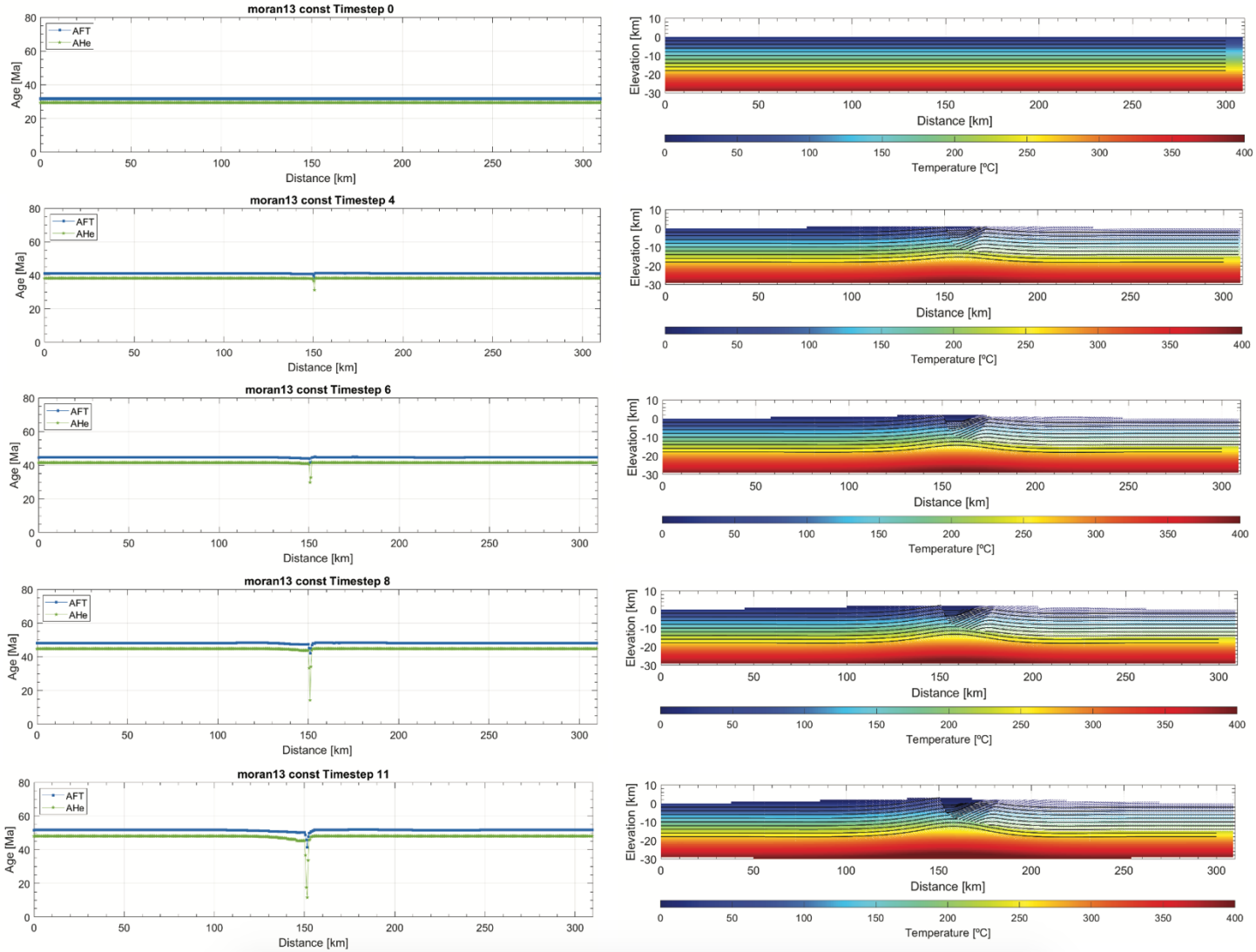

Figure 4.31 – Thermal-kinematic model 13 evaluated in Pecube for a constant slip rate with fault slip onset at 19 Ma for D_{max} = 17 km.

CHAPTER 5. DISCUSSION

5.1 Using flexural-kinematic modeling to determine a minimum threshold D_{max}

Comparisons of the topographic-isostatic response of the flexural-kinematic models to the observed topography were used to eliminate scenarios in which the modeled footwall uplift is inconsistent with the observed uplift at Mount Moran. In these systems, footwall uplift is primarily an isostatic response controlled by the magnitude of D_{max} and footwall erosion. In models that yield D_{max} values of 2 km and 7 km the resulting footwall uplift (0.7 km and ~2 km; Figure 4.1) is less than or equal to the present-day footwall relief observed at Mount Moran (~1.8 km). Importantly, values for predicted footwall uplift in this first phase of modeling do not include any influence of erosion, which may be as high as ~2 km, raising D_{max} to ~9 km if the entire thickness of the Paleozoic section in this region was removed. Thus, it is interpreted that for D_{max} values < 9 km, the model cannot reproduce the magnitude of observed footwall uplift at Mount Moran, therefore the second phase of thermal-kinematic modeling only includes evaluations of models with D_{max} > 9 km. However, displacement estimates (2.1 – 7 km) based on stratigraphic interpretations involving younger units (~2 Ma, Huckleberry Ridge Tuff; Gilbert et al., 1983; Smith et al., 1989, 1993; Pierce and Morgan, 1992, Love and Reed, 1971) can still be considered in the framework of models with D_{max} > 9 km.

5.2 Thermal structure of the crust during Teton fault evolution

The preferred structural solutions (D_{max} > 9 km) from the flexural-kinematic modeling were then integrated with thermal (*Pecube*) modeling to develop predicted AHe and AFT ages determined by the computed crustal thermal structure and temperature

history of the exhumed samples. In the thermal-kinematic models, temperature distribution and the resultant predicted cooling ages are controlled by the thermal evolution of the crust, which is a function of the input thermal parameters. The main thermal parameters governing the geothermal gradient can essentially be reduced to the basal mantle heat flow (Q_m) into the crust, surface heat flow (Q_0), bulk thermal conductivity (k), and crustal volumetric heat production (A_0). Because of the proximity of the Yellowstone plateau to the Teton Range, it is possible that Q_m may be both elevated and variable through time.

To evaluate the influence this may have on the geothermal gradient in the thermal-kinematic models, modeled values of Q_o can be compared to present-day Q_0 measurements. In the center of the Yellowstone Plateau, the observed Q_0 averages ~150 mWm^{-2}, but decreases considerably moving away from the modern-day hotspot (Figure 5.1). Where the Teton and Yellowstone regions begin to overlap, the range of Q_0 values is ~95 - 100 mWm^{-2} (Figure 5.1). Geothermal gradient models of Thigpen et al. (in prep) evaluate a range of possible Q_m values (4 – 100 mWm^{-2}) for the measured Q_o values in the northernmost Basin and Range, which yields a maximum geothermal gradient of ~34°C km^{-1} (Figure 5.2). Further from the hotspot in the southern portion of the Teton Range, measured surface heat flow values average ~70 mWm^{-2} (Figure 5.1). Here, the modeled geothermal gradient for a range of Q_m (12 – 72 mWm^{-2}) is calculated to be ~24°C km^{-1} (Thigpen et al., in prep). Because this study focuses on Mount Moran, located at the paleocenter of the Teton fault and between the areas of greatest (~95 mWm^{-2}) and least (~70 mWm^{-2}) measured Q_0, the value used in the thermal model for geothermal gradient (25° C km^{-1}) is interpreted to fall within the range of modeled values

(24 – 34° C km^{-1}; Figure 5.2, Thigpen et al., in prep). This also falls within the measured range of values for geothermal gradient in the southern Tetons (18 – 27° C km^{-1}; Heasler et al., 1987).

5.3 Comparing observed and model predicted AHe cooling ages

The age-elevation relationship (Figure 5.3), which is determined by analyzing cooling ages for samples collected along subvertical transects, can be used to characterize not only the exhumation rate through time, but also any changes in the exhumation rate that may have occurred in the time interval preserved along the elevation trend (Figure 5.3). The slope of the best fit trend line through the data is an inferred exhumation rate, where steeper gradients indicate more rapid exhumation and less steep slopes indicate slower exhumation (Figure 5.3). Inflection points in the age-elevation relationship can be used to estimate the onset of rapid exhumation and in some cases can be used as a proxy for fault initiation (Figure 5.3). In theory, this approach relies on the idea that samples travel from depth to their present elevation through unperturbed isotherms.

Age-elevation relationships from the observed AHe data (Brown et al., 2017) and the predicted AHe ages derived from the thermal-kinematic models for a range of D_{max} values (9 – 17 km) and fault slip onset timings (5, 12, and 19 Ma; Figures 5.5- 5.10) are compared to evaluate interpreted faulting and uplift scenarios at Mount Moran determine which thermal-kinematic models do not reproduce the observed data. Ages in the observed AHe dataset reported in Brown et al. (2017) range from 26.3 Ma at the top of the transect to 4.07 Ma at the base of the transect (Table 4.2, Figure 5.4). When plotted on an age-elevation profile, an inflection between the high elevation data and base of

transect data occurs. The age-elevation relationship between the higher elevation samples (3835 m) and the middle elevation samples (2975 m) yields an exhumation rate of ~0.09 km Myr^{-1} and between the lower elevations and the base of transect (2116 m) a slope of 0.30 km Myr^{-1}. Ages in the observed AFT dataset range from 9.5 Ma at the base of the transect to 38.0 Ma at the summit (Brown et al., 2017). When plotted on an age-elevation profile, an inflection between the higher and lower elevation data occurs between the elevations 0.86 – 1.7 km. The age-elevation relationship between the higher elevations yields a slope of ~0.05 km Myr^{-1} and for the lower elevations a slope of 0.14 km Myr^{-1}. AFT from this dataset are consistent with the AHe for the lower elevation samples but diverge for the higher elevation samples.

5.4 Age-elevation relationships in the predicted AHe data vs. observed AHe data

In models with a fault slip onset of 5 Ma and the lowest D_{max} value of 11 km, the predicted He data yields an exhumation rate of ~0.10 km Myr^{-1} from 40 - 26 Ma. Although these exhumation rates match some rates derived from the observed data, extrapolation of this trend predicts an AHe age that is >20 Ma at the base of the transect, which is far older than the 8 - 12 Ma observed ages. Also, because these ages are older than the onset of faulting, this indicates that these points were above and cooler than the AHe T_c prior to fault onset, demonstrating that the footwall section had not experienced a threshold level of uplift to exhume reset ages. With increasing D_{max} (13 km) and the same fault onset timing of 5 Ma, the lower elevation AHe ages of ~6 Ma are similar to the range of observed ages at the lower elevations (4 - 10 Ma), though the higher elevation samples in this model are much older than those from Mount Moran. However, these

older ages produce an age-elevation slope that is parallel to the higher elevation observed samples, suggesting this modeled exhumation rate of 0.08 km Myr^{-1} is similar to the exhumation rate preserved in the higher elevation Moran samples. In the 5 Ma onset model with 15 km, that relatively slow exhumation trend overlaps with the high elevation observed data, but linear extrapolation predicts an age of 0 Ma at low elevations, suggesting that an increase in the more recent rates is needed to match the data. Finally, the 17 km D_{max} model with a 5 Ma onset yields low elevation ages (3 - 7 Ma) that are similar to those in the observed data, but the high elevation samples are much younger than the observed high elevation samples, likely as a result of the higher exhumation rates throughout the model evolution. Additionally, the transition from a linear age-elevation relationship to a logarithmic relationship with late stage accelerated cooling recorded in the lower elevation samples may reflect the surface-directed heat advection producing compressed isotherms in the uplifting footwall, as this model includes the highest late stage exhumation rates (0.36 km Myr^{-1}) of any modeled scenario examined here. Although the ages do not match, this model highlights the likelihood that the observed data record an acceleration in cooling (and presumably uplift) at some point before 5 Ma.

Next, a fault slip onset of 12 Ma is evaluated for D_{max} values of 11 km – 17 km. At the lowest D_{max} value of 11 km, the predicted AHe data show an exhumation rate of ~0.10 km Myr^{-1} from 47 - 32 Ma, similar to the gradient of the observed high elevation data at Mount Moran. However, extrapolating the trend of the model ages yields a base of transect value of ~25 Ma, far older than the observed age of the low elevation samples. Also, the model ages are all older than ~32 Ma which indicates that a D_{max} of 11 km is not sufficient to exhume reset samples that were hotter than the AHe T_c at the onset of

faulting. For a modeled D_{max} of 13 km, the exhumation rate is ~0.07 km $Myr^{-1}$and the predicted gradient is roughly similar to rates observed in the high elevation samples, but the trend does not overlap the lower observed AHe ages. This indicates for a D_{max} of 13 km either an earlier fault slip onset time or a faster slip rate is necessary to match the observed ages. A low elevation age (~11 Ma) and linearly extrapolated base of transect age (~10 Ma) are close to the range of low elevation samples (4 – 10 Ma) but there are insufficient data points and greater D_{max} is needed to further define the trend. In the 12 Ma onset model with 15 km for D_{max}, the higher elevation data reflects a gradient with exhumation rate of ~0.07 km Myr^{-1}, almost parallel to the previous model (D_{max} 13 km) for the higher elevation samples. In this scenario, the trend does not overlap the high elevation ages. The range of low elevation ages (10 – 11 Ma) are near the observed data, however extrapolating a linear trend yields a base transect age of ~ 5 Ma, younger than observed. Finally, the 17 km D_{max} model yields a linear exhumation rate of ~0.06 km Myr^{-1} in the higher elevations accelerating to high modeled rates for the low elevation ages (~0.25 km Myr^{-1}). The predicted exhumations rates are comparable the rates derived from the observed data. In the 17 km D_{max} model with a 12 Ma onset model, the exhumation rates and low elevation data provide a better fit to the data, yet the high elevation samples are still too young. The high elevation samples do not match the observed data for D_{max} of 15 km and 17 km, which indicates that the exhumation rates may be too high. These models show that in order to match the observed low elevation exhumation rate either/or an acceleration in cooling rate occurs ~12 Ma or that time is when the Teton fault actually starts moving. In both scenarios, D_{max} must be equal to or greater than 15 km.

In models with a fault slip onset of 19 Ma and the lowest D_{max} values of 9 km and 11 km, the predicted He data yields an exhumation rate of ~0.10 km Myr^{-1} from 47 – 35 Ma that is similar to the observed rate from 22.5 – 11 Ma. When the modeled trend between ages for both D_{max} are linearly extrapolated, AHe ages at the transect base are >30 Ma and thus, older than the onset of faulting. Therefore, these models do not generate nearly enough uplift to produce reset ages necessary to match the observed low elevation AHe data. Similarly, increasing D_{max} values (13 km and 14 km) yields exhumation rates of ~0.08 km Myr^{-1} from 47 – 16.5 Ma, but it also produces modeled AHe ages (~16.5 Ma) that are too old for the observed low elevation data (4 – 10 Ma). For D_{max} values of 15 km, the predicted ages show a parallel slope to the lower D_{max} values (13 – 14 km) and yield higher elevation samples that are older than those from Mount Moran, however, 15 km of displacement in this model is adequate to yield an extrapolated base of transect age of ~8.5 Ma, which is within the range of low elevation sample ages (4 – 10 Ma). Moving to a higher D_{max} values of 16 km, the predicted He data yields an exhumation rate of ~0.08 km Myr^{-1} from 45 – 17 Ma, which is similar to the exhumation rate preserved in the higher elevation samples. By projecting the linear trend of this exhumation rate, an age of ~8.3 Ma would represent the base of the transect, matching the observed data. However, the higher elevation ages for this model do not correspond to the observed data. For D_{max} values of 17 km, a higher elevation trend of ~0.07 km Myr^{-1}, turns to a logarithmic trend for low elevation samples (~0.2 km Myr^{-1}) and extrapolating this trend yields age of ~11.5 Ma for the transect base. This model yields similar exhumation rates as compared to the observed for both the mid and low elevations.

In summary, comparisons of the age-elevation relationships for the thermal-model predicted AHe data the observed AHe data at Mount Moran (Brown et al., 2017) indicate two preferred solutions, 12 Ma onset with D_{max} of 15 km and 12 Ma onset with D_{max} of 17 km. The modeled solutions do not fully replicate the observed AHe data, but do provide constraints for D_{max}, fault slip onset timing, and ages of rapid cooling. Interpretations of the modeled data for 5 Ma indicate that in order to match the observed data, an acceleration of cooling must occur prior to ~5 Ma. Predicted exhumation rates and correlation of modeled ages with the observed lower elevation AHe data are better matched in models with fault slip onset at 12 Ma for D_{max} of 15 or 17 km, suggesting ~12 Ma represents the onset of rapid fault slip movement along the Teton fault. For D_{max} or 17 km with fault slip onset of 12 Ma, the predicted AHe data produces a shift from a slower linear slope in the higher elevation data to a logarithm trend for the lower elevation ages. The trend of the observed AHe data also shows a potential inflection between average ages 11 – 22 Ma. However, pinpointing the exact age of rapid cooling in either dataset (predicted or observed) requires additional data resolution. Comparisons of the predicted and observed data are interpreted to suggest onset of rapid cooling ~ 12 Ma.

5.5 Comparing observed and model-predicted AFT cooling ages

For fault slip onset of 5 Ma, the modeled AFT data for D_{max} (11 km and 13 km) show greater sensitivity for the younger onset time as compare to 12 and 19 Ma, but do not predict the young (9.5 – 13.6 Ma) lower elevation ages necessary to better constrain D_{max}. The predicted slope for D_{max} values of 15 km and 17 km are ~0.4 km Myr^{-1}, but

do not have enough exhumation to yield reset AFT ages. The high elevation sample for the 5 Ma onset model with 17 km for D_{max}, is ~38 Ma and is close to the observed age.

The predicted AFT ages for fault slip onset at 12 Ma yield age-elevation gradients show only a minor amount of age variation in response to increasing displacement. 12 Ma models for D_{max} of 9 – 17 km yield a range slopes of 0.50 – 0.31 km Myr^{-1}. For the greatest D_{max} value 17 km, the exhumation rate (0.31 km Myr^{-1}) is similar to the observed lower elevation data. However, because the threshold displacement necessary to achieve younger ages is still not met, the predicted ages are much older than observed.

For models with D_{max} values 9 – 17 km with fault slip onset at 19 Ma, modeled ages yield exhumation rates ranging from 0.55 – 0.35 km Myr^{-1}. With increasing displacement, the trends become more similar to the observed gradient between the mid- and low elevation AFT data. A linear extrapolation of the gradient for 19 Ma with D_{max} of 17 km, yields a base sample age of ~39 Ma. Decreasing displacement magnitudes (D_{max} = 16 – 13km, 11 km, and 9 km) for the same fault slip onset produce low elevation ages >39 Ma, and these ages are much older than the low elevation AFT samples from Mount Moran (11.7 Ma). This is interpreted to be the result of insufficient footwall uplift and thus, a need for greater D_{max} values and/or more erosion to exhume younger AFT sample ages. Because all predicted AFT ages are older than the onset of faulting, this indicates that these points were above and cooler than the AFT T_c prior to fault onset, suggesting that the footwall section had not experienced a threshold level of uplift to exhume reset ages. Future work will address the details of the erosion profiles (Figure 5.4) which influences the ability of the thermal model to reproduce the observed AFT ages even with increasing D_{max} and greater exhumation rates.

5.6 Previous estimates for D_{max} in the context of new data

Disagreements regarding the timing of initiation (13 – 2 Ma) and total displacement (2.1 – 11 km) on the Teton fault persist despite a myriad of studies implementing low-T thermochronology, geophysical and stratigraphic techniques to resolve these discrepancies. A single low-temperature thermochronology study by Roberts and Burbank (1993) was conducted prior to the observed dataset by Brown et al. (2017) but does not utilize the "zeta" method of calibrating fission-track data and consequently is not suitable for comparison. However, two key findings from this study are supported by the AHe and AFT dataset in Brown et al. (2017) which indicate that Mount Moran records the greatest displacement along the range and is the location of earliest onset of fault motion with southward migration of cooling onset age. Brown et al. (2017) interpret the onset of rapid cooling in the northern Tetons at ~13 Ma at the Mount Moran transect. This is consistent with studies based on the structural relationships between the Miocene Colter and Teewinot formations and the Conant Creek Tuff to the east of Jackson Hole suggest that displacement on the Teton fault initiated after 13 Ma and possibly as recently as 2 Ma (Barnosky, 1984; Love et al., 1992; and Smith et al., 1993), with rapid uplift occurring between 13 – 9.4 Ma (Love and Reed, 1971).

Many stratigraphic arguments for displacement and exhumation rates on the Teton have been made the basis of offset between prominent stratigraphic horizons or projections of tilting tuffs such as the basement rock (Precambrian), Colter and Teewinot Formations (Miocene), and the Huckleberry Ridge Tuff (~2 Ma). Estimates involving the vertical displacement (1.5 km) of the Huckleberry Ridge Tuff (~2 Ma) yield an average offset rate of 0.8 km Myr^{-1} in the past ~2 m.y. (Love, 1977). Byrd et al. (1994) indicates

that that the tuff has been offset by 2.5 – 3.5 km, while Gilbert et al. (1983), Smith et al. (1993), and Pierce and Morgan (1992) suggested displacement of 2.1 – 3.0 km since ~2 Ma using projections of the post emplacement tilt of the Huckleberry Ridge Tuff from exposure at Signal Mountain to the west beneath Jackson Hole. The range of exhumation rates derived from post-Huckleberry Ridge Tuff offsets and projections of tilt are reported that span 1.05 – 1.75 km Myr^{-1}. In any case, an acceleration of slip (~1 – 1.75 km Myr^{-1}) from ~ 2 Ma into the present is well defined and contributes 2 - 3 km to the predicted total displacement of 15 – 17 km from this study (Figure 5.11). Furthermore, in a geophysical study by Behrendt et al., (1968), a prominent reflector in the seismic refraction data is located ~5 km beneath Jackson Hole which is then correlated to the basement rock in the peaks of the Teton Range (~2 km) above valley bottom. From this, a total of 7 km of basement offset is interpreted during the past ~9 my (Love et al., 1973) for an exhumation rate of ~0.8 km Myr^{-1} (Figure 5.11).

Evidence for Quaternary slip activity is reported in offset Holocene moraine deposits showing surface offsets of 3 – 50 m that delineate sections along the Teton fault (Gilbert et al., 1983; Susong et al., 1987, Smith et al., 1989, 1993). Additionally, trenching studies by Byrd (1995) and Byrd et al. (1994) indicate two rupture events (1.3 and 2.8 m $event^{-1}$) for a total of 4.1 meters of slip have occurred since 7.9 thousand calibrated radiocarbon years (cal ka) for an average offset rate of ~2 km myr^{-1} from deglaciation (17 – 13 ka) to 7.9 ka. Furthermore, recent work by Pierce et al., (2018) reports ~12 m scarps cutting glacial moraines (~14 ka), for an average slip of ~0.82 m ka^{-1} (Thackray and Staley, 2017) and DuRoss et al., (2020) suggests a postglacial to mid

Holocene (14.4 – 4.6 ka) rate of slip averaging ~1.1 km Myr^{-1}. This evidence combined with estimates for slip rates from ~2 Ma to the present support continuing displacement.

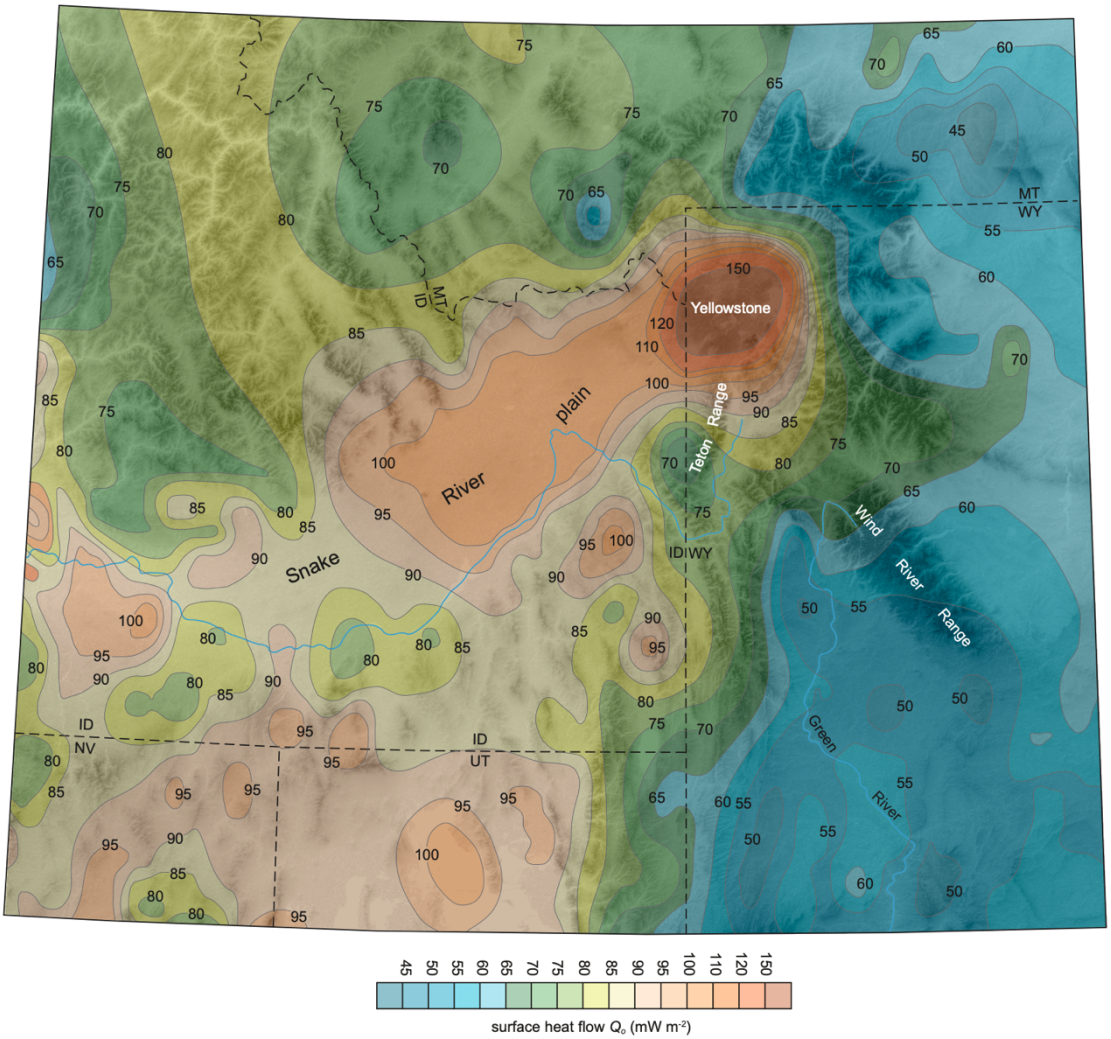

Figure 5.1 – Measured surface heat flow (Q_o) in the Snake River Plain and the Teton-Yellowstone Region. Figure from Thigpen et al., (in prep).

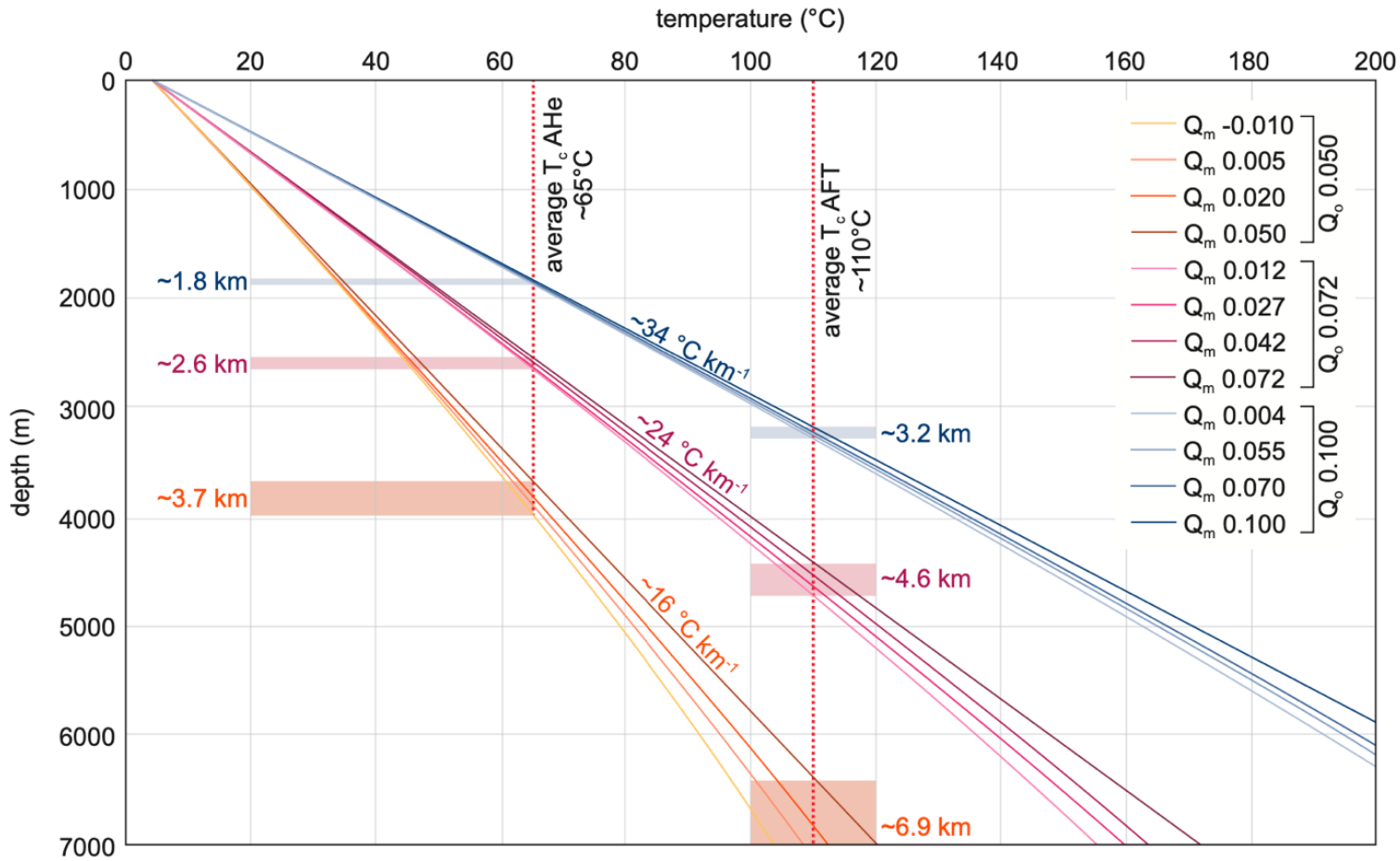

Figure 5.2 – Modeled geothermal gradients produced for a range of parameters for basal mantle heat flow (Qm; W m^{-2}) and internal heat generation values to produce a range of surface heat flows (Qo, W m^{-2}) which can be compared to the measured Qo from Figure 5.1. Figure from Thigpen et al., (in prep).

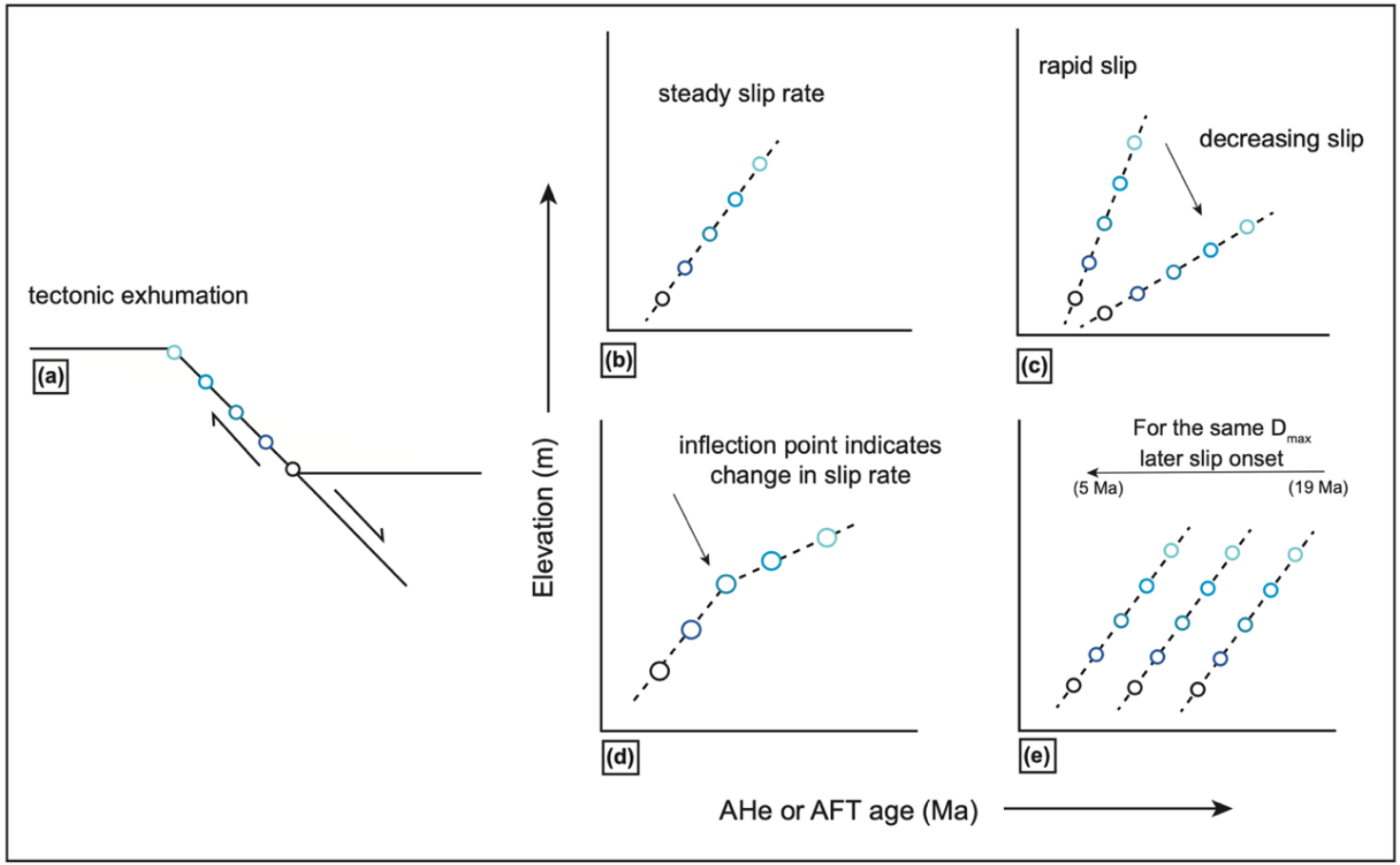

Figure 5.3 – (a) Conceptual figure illustrating potentiation age-elevation trends of AHe or AFT ages during tectonic exhumation, (b) in the case of steady exhumation, (c) for greater slip rate the resulting profile will be steeper, (d) changing slip rates result in inflection points, and (e) profiles translate along the x-axis depending on fault slip onset time for the same D_{max}.

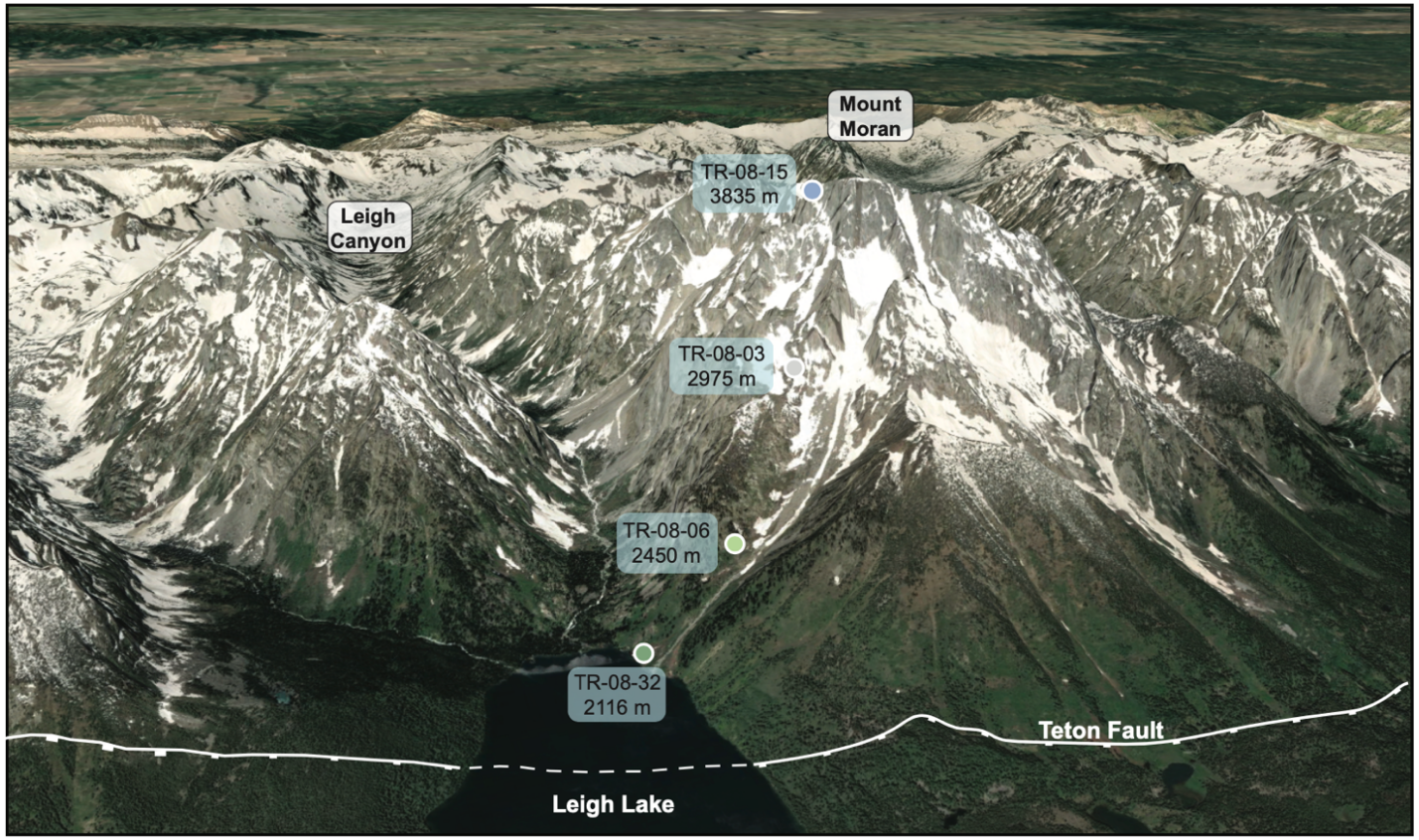

Figure 5.4 – Google Earth image of the relative sample locations from Brown et al. (2017) subvertical transect at Mount Moran.

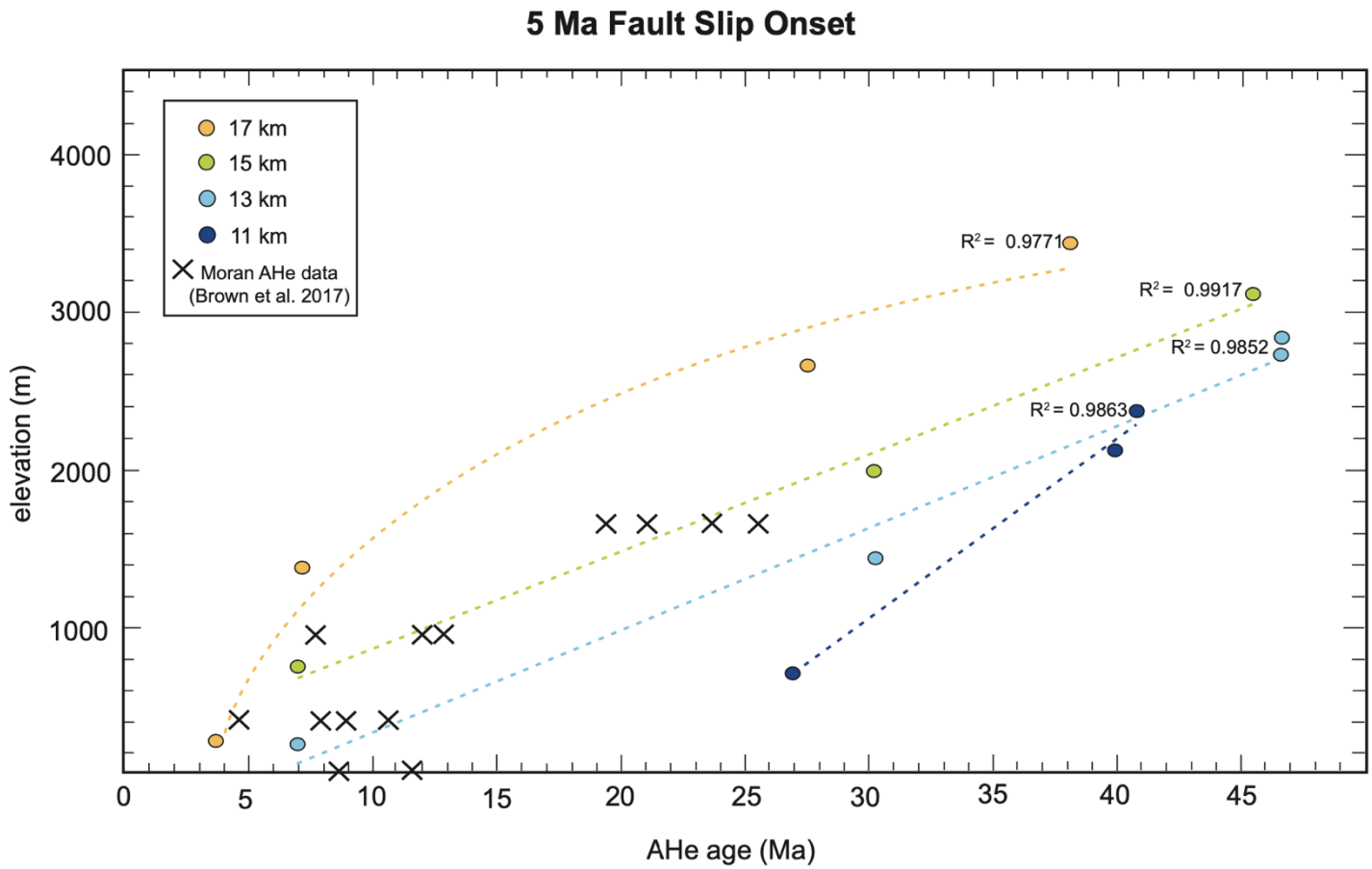

Figure 5.5 – Age-elevation plots for predicted apatite (U-Th)/He (AHe), where fault slip onset begins at 5 Ma. Modeled cooling ages are calculated using the Pecube code (Braun, 2003). Observed cooling ages result from samples collected up the range front along a sub-vertical transect of Mount Moran (Brown et al., 2017). This dataset is adjusted to a base level elevation of 0 meters in order to be directly compared with modeled cooling ages.

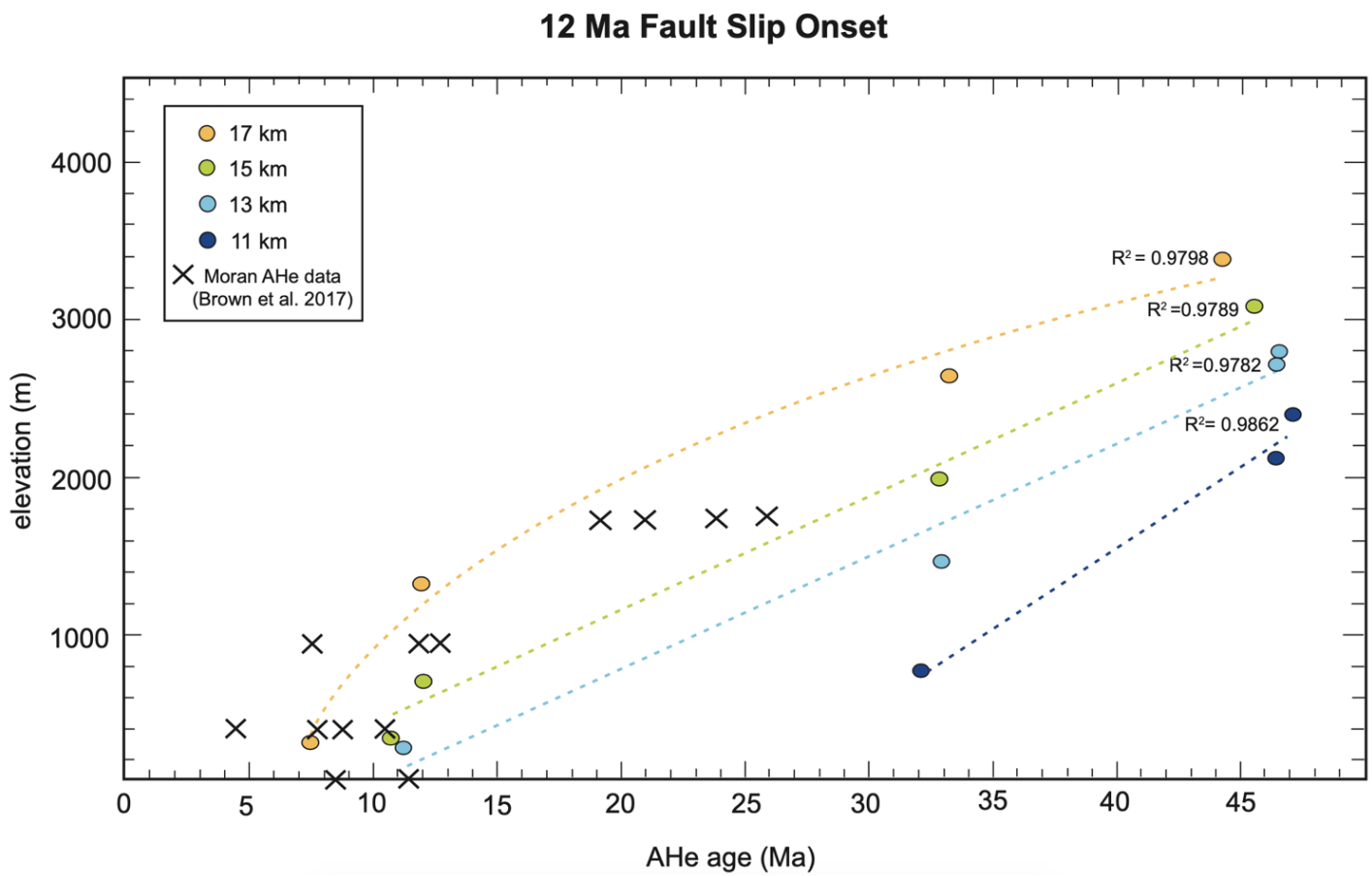

Figure 5.6 – Age-elevation plots for predicted apatite (U-Th)/He (AHe), where fault slip onset begins at 12 Ma. Modeled cooling ages are calculated using the Pecube code (Braun, 2003). Observed cooling ages result from samples collected up the range front along a sub-vertical transect of Mount Moran (Brown et al., 2017). This dataset is adjusted to a base level elevation of 0 meters in order to be directly compared with modeled cooling ages.

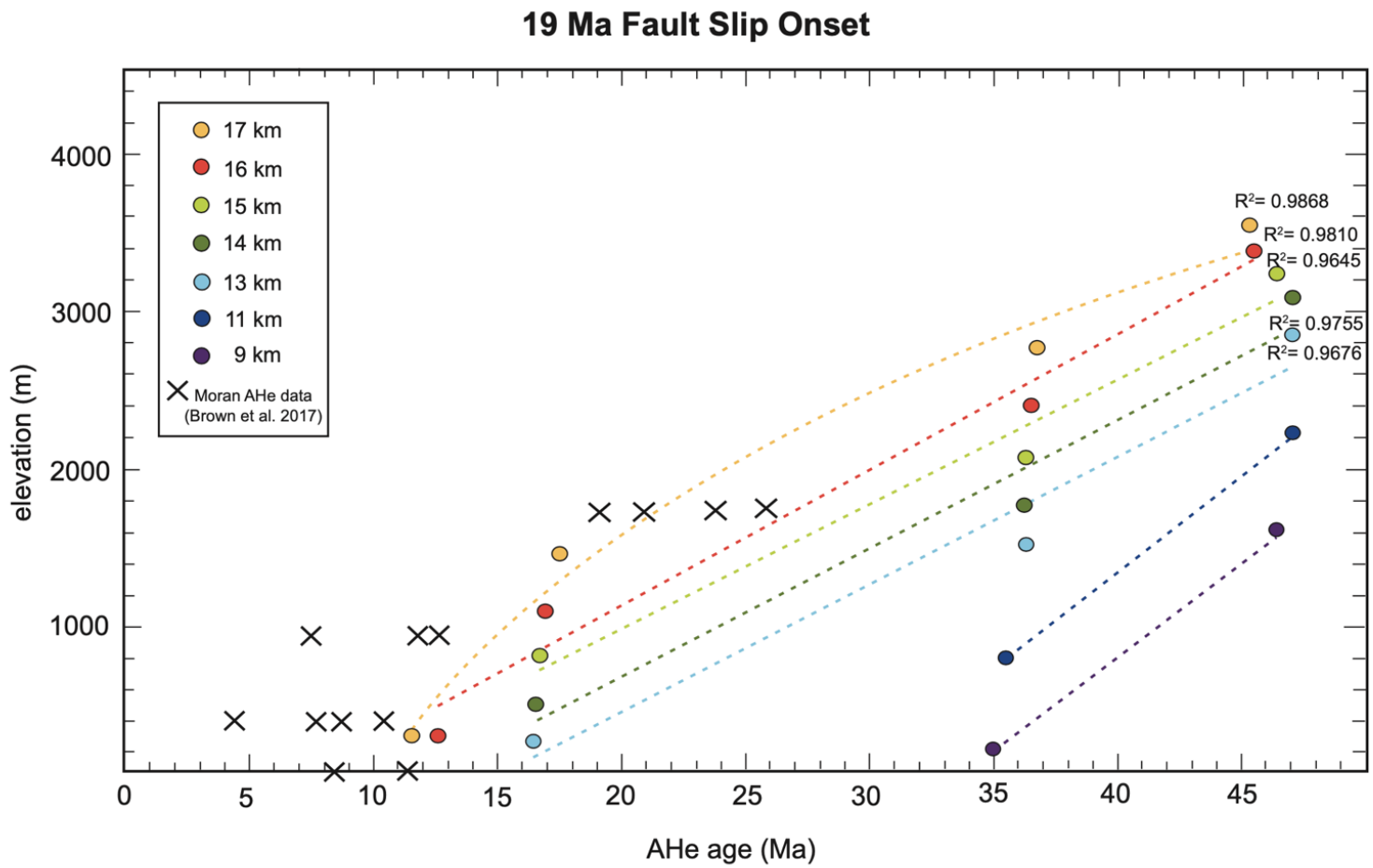

Figure 5.7 – Age-elevation plots for predicted apatite (U-Th)/He (AHe), where fault slip onset begins at 19 Ma. Modeled cooling ages are calculated using the Pecube code (Braun, 2003). Observed cooling ages result from samples collected up the range front along a sub-vertical transect of Mount Moran (Brown et al., 2017). This dataset is adjusted to a base level elevation of 0 meters in order to be directly compared with modeled cooling ages.

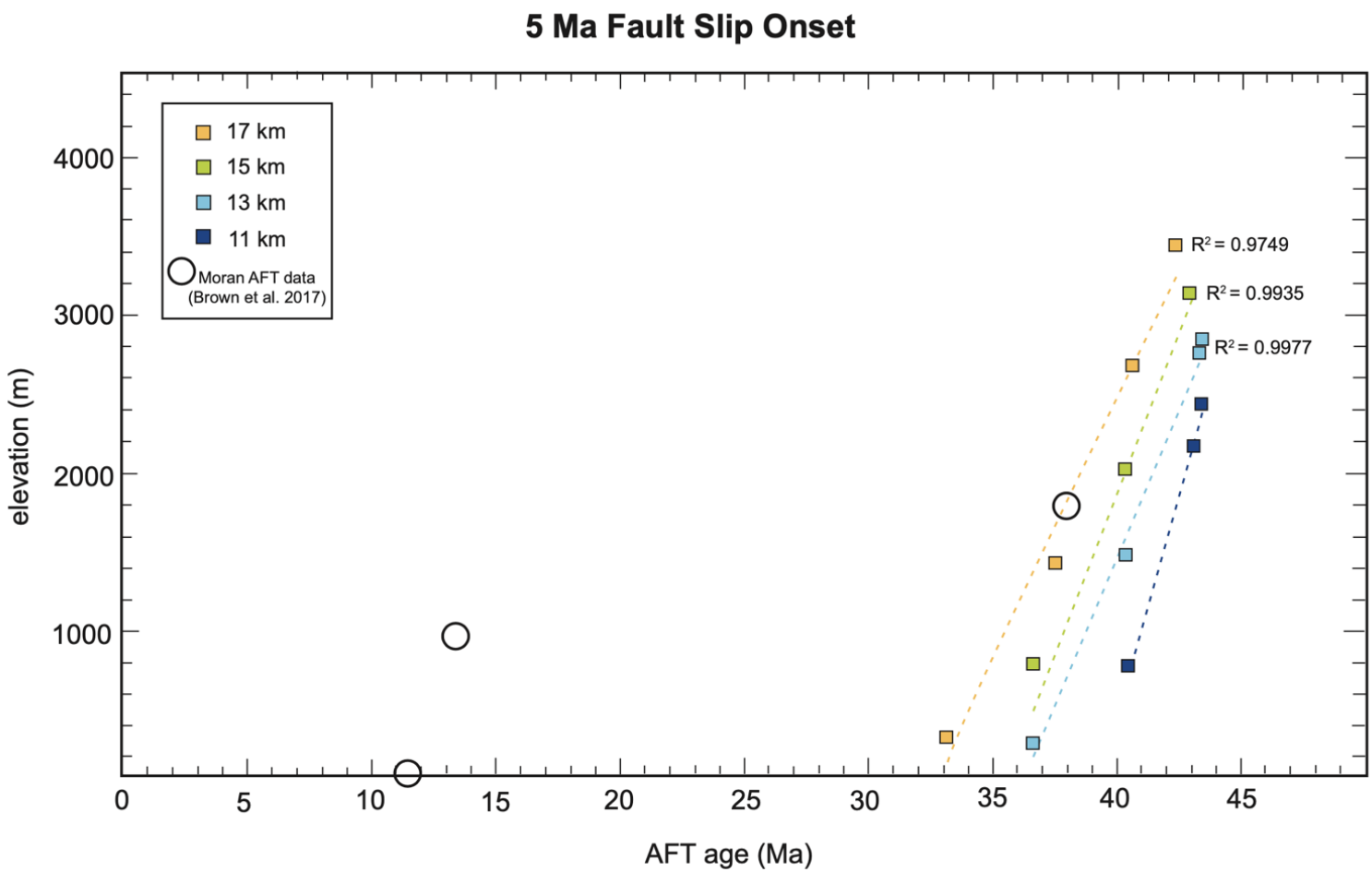

Figure 5.8 – Age-elevation plots for predicted AFT data, where fault slip onset begins at 5 Ma. Modeled cooling ages are calculated using the Pecube code (Braun, 2003). Observed cooling ages result from samples collected up the range front along a sub-vertical transect of Mount Moran (Brown et al., 2017). This dataset is adjusted to a base level elevation of 0 meters in order to be directly compared with modeled cooling ages.

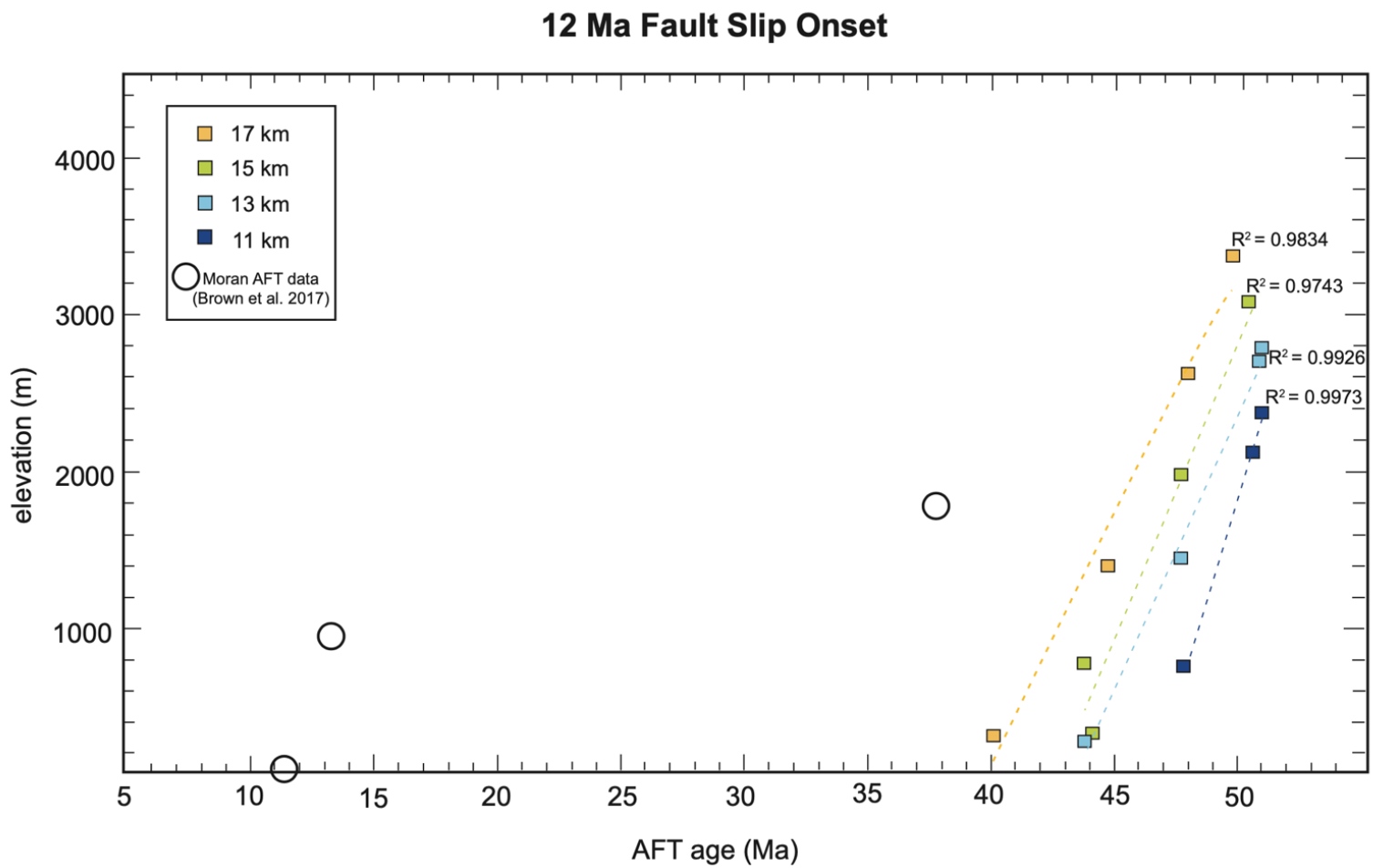

Figure 5.9 – Age-elevation plots for predicted AFT data, where fault slip onset begins at 12 Ma. Modeled cooling ages are calculated using the Pecube code (Braun, 2003). Observed cooling ages result from samples collected up the range front along a sub-vertical transect of Mount Moran (Brown et al., 2017). This dataset is adjusted to a base level elevation of 0 meters in order to be directly compared with modeled cooling ages.

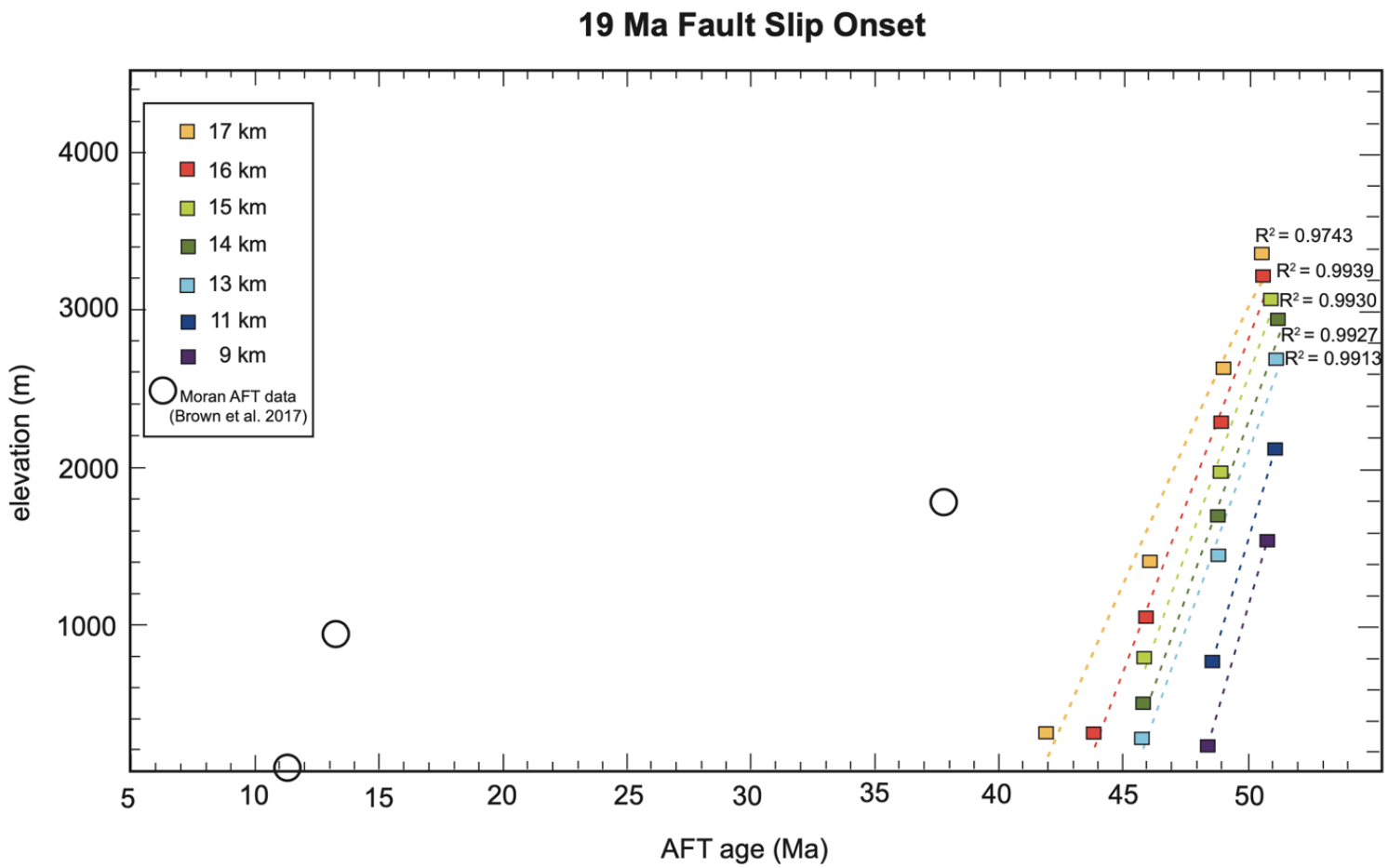

Figure 5.10 – Age-elevation plots for predicted AFT data, where fault slip onset begins at 19 Ma. Modeled cooling ages are calculated using the Pecube code (Braun, 2003). Observed cooling ages result from samples collected up the range front along a sub-vertical transect of Mount Moran (Brown et al., 2017). This dataset is adjusted to a base level elevation of 0 meters in order to be directly compared with modeled cooling ages.

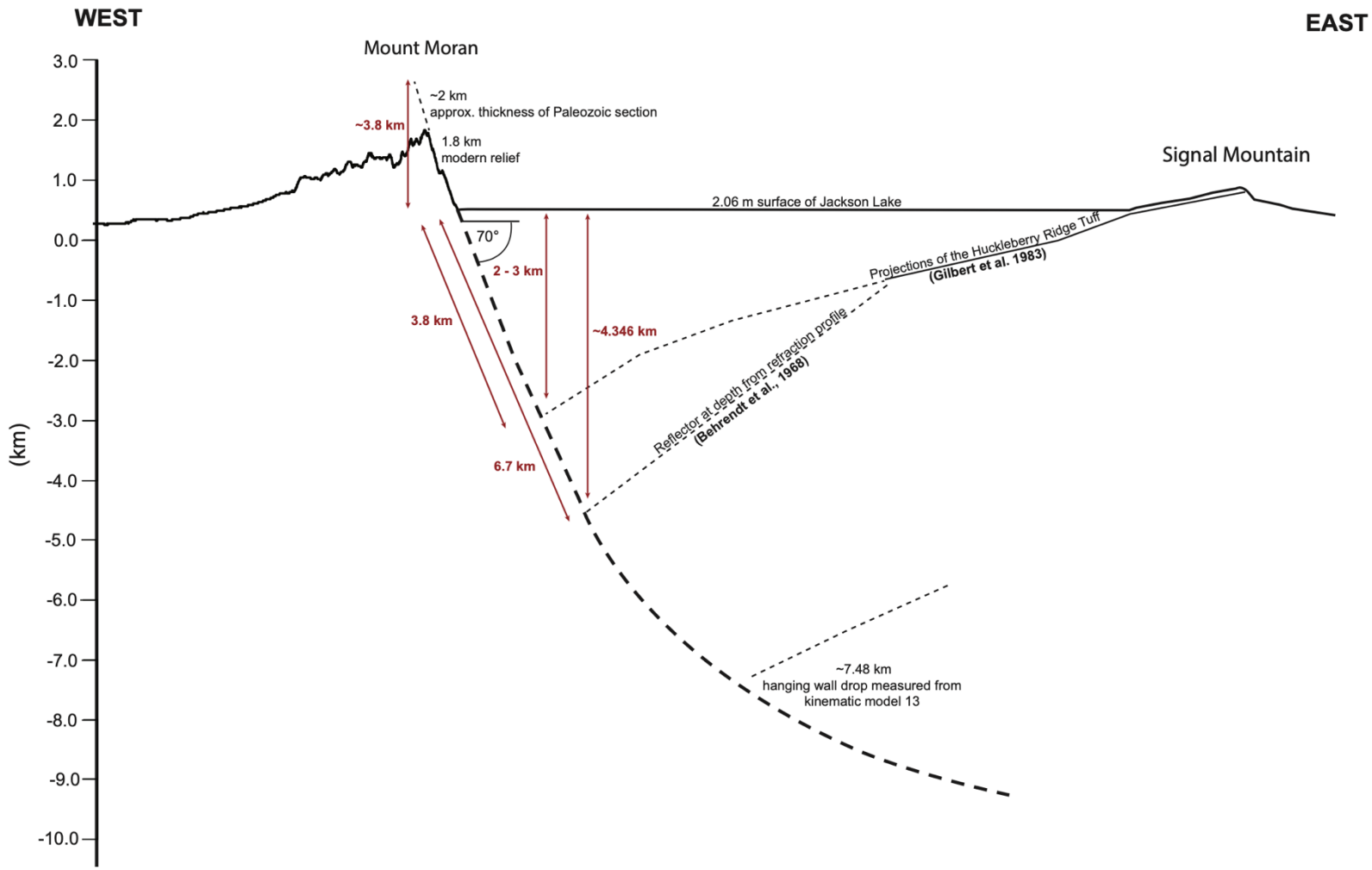

Figure 5.11 – Interpreted cross section through Mount Moran and the Jackson Lake basin. The cross section illustrates the upper crustal projection of the Huckleberry Ridge Tuff (from Gilbert et al., 1983) and surface exposures at Signal Mountain (solid lines) and north of Jackson Lake (dashed). Figure modified from Smith et al., 1993b.

CHAPTER 6. CONCLUSIONS

This study presents coupled flexural-kinematic (*Move*) and thermal-kinematic (*Pecube*) models that test the viability of a range of previous D_{max} estimates for the Teton fault by examining cross section geometry and predicted thermochronologic data. Results from detailed flexural-kinematic modeling indicate that D_{max} on the Teton Fault must be > 9 km in order to match the observed topographic profile and flexural wavelength constraints. Comparisons between the predicted AHe ages of the thermal-kinematic model with the observed data at Mount Moran indicate a preferred fault slip onset at ~12 Ma onset with D_{max} ranging from 15 km to 17 km. The model derived AHe predictions do not fully replicate the observed AHe data but do provide constraints for D_{max} and the onset of rapid cooling. Previous estimates for D_{max} of 2 – 3 km based solely on displacement of the Huckleberry Ridge tuff from ~2 Ma – present are likely gross underestimates of actual D_{max}, but these slip magnitudes from ~2 Ma to present are consistent with models from this study, however models from this study indicate that much more slip had accumulated prior to the Quaternary than previously estimated.

APPENDIX

THERMAL-KINEMATIC (*PECUBE*) MODELS 1 - 12

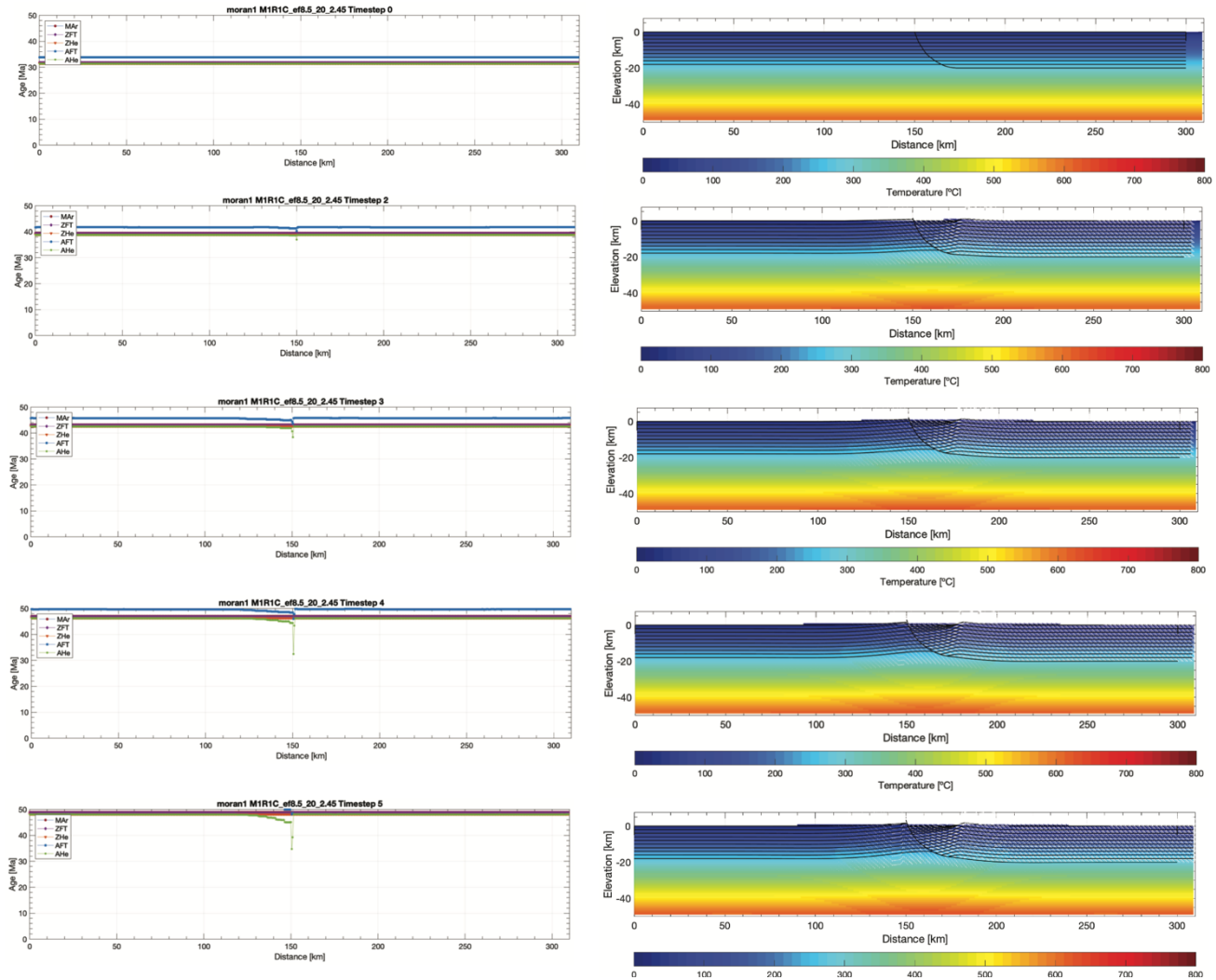

Thermal-kinematic model 1 evaluated in Pecube for a constant slip rate with fault slip onset at 19 Ma for D_{max} = 9 km.

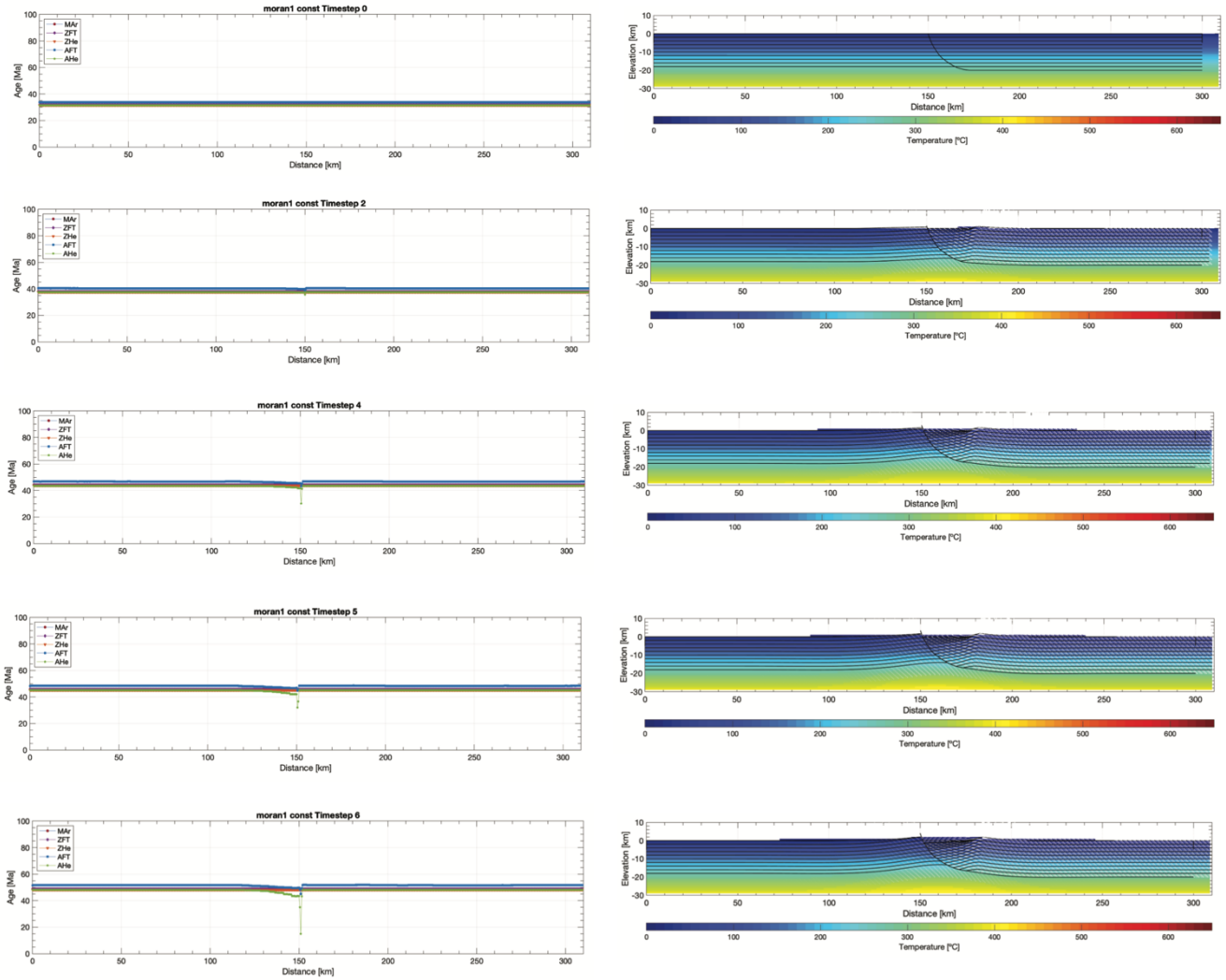

Thermal-kinematic model 1 evaluated in Pecube for a constant slip rate with fault slip onset at 19 Ma for D_{max} = 11 km.

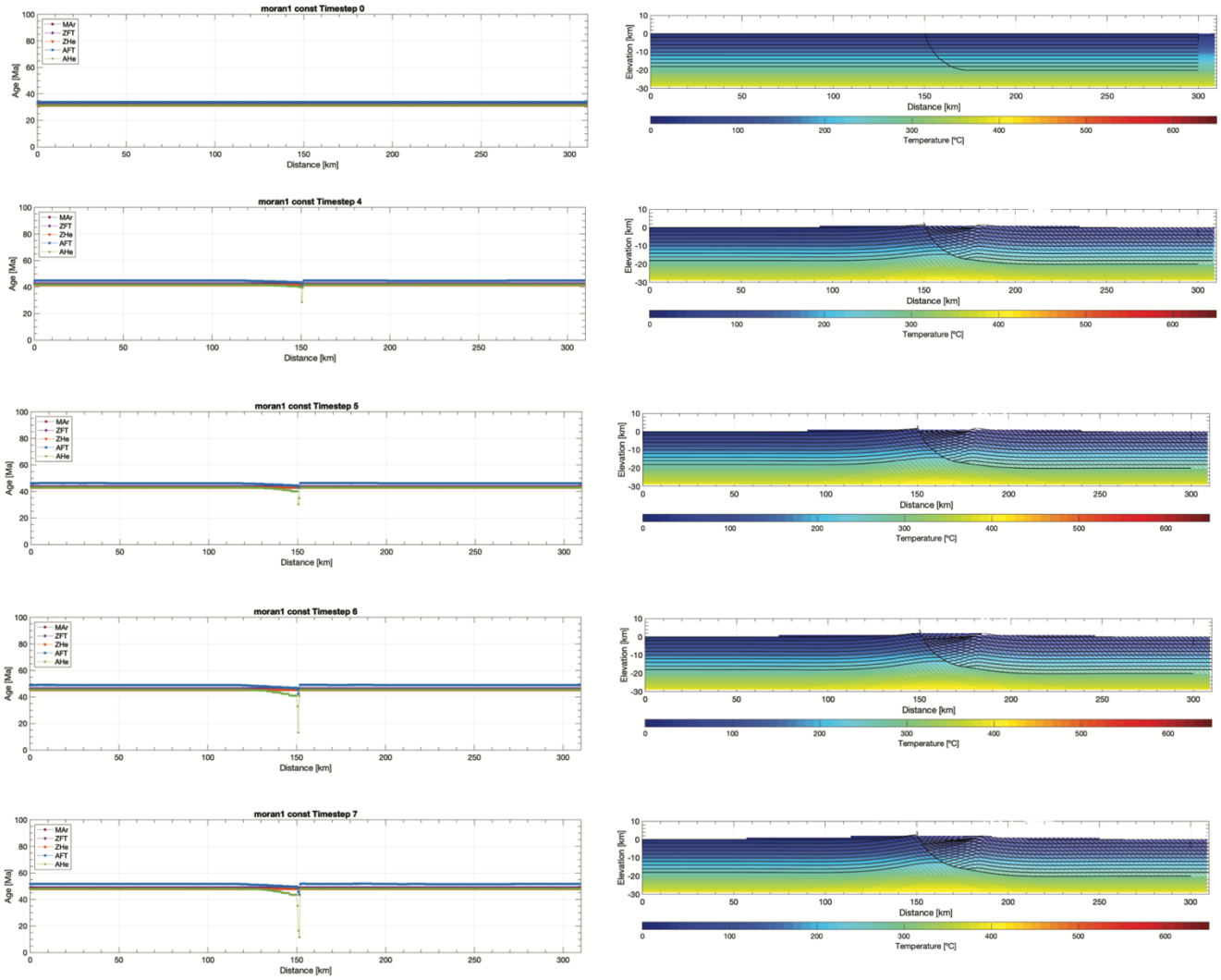

Thermal-kinematic model 1 evaluated in Pecube for a constant slip rate with fault slip onset at 19 Ma for D_{max} = 13 km.

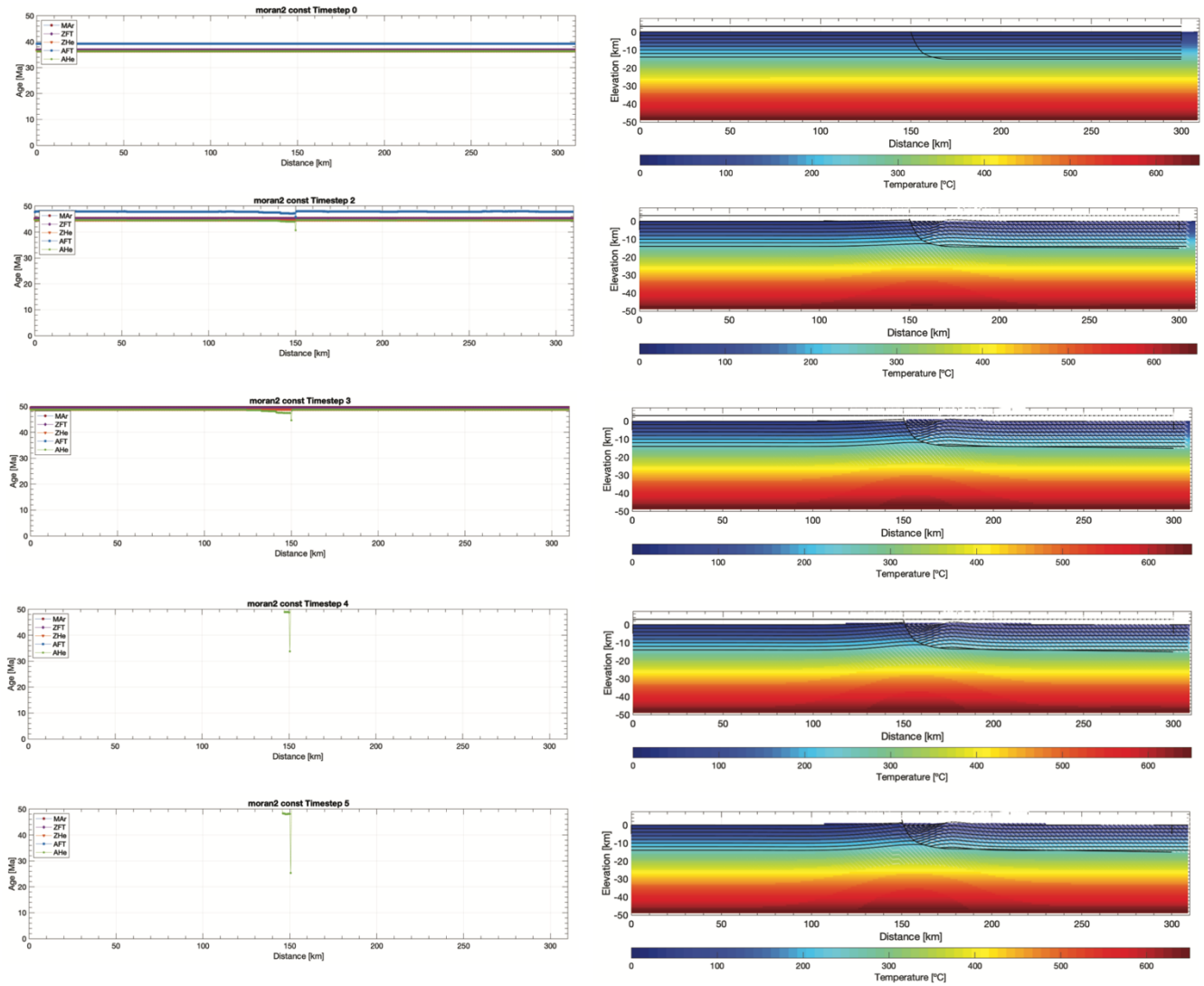

Thermal-kinematic model 2 evaluated in Pecube for a constant slip rate with fault slip onset at 19 Ma for D_{max} = 9 km.

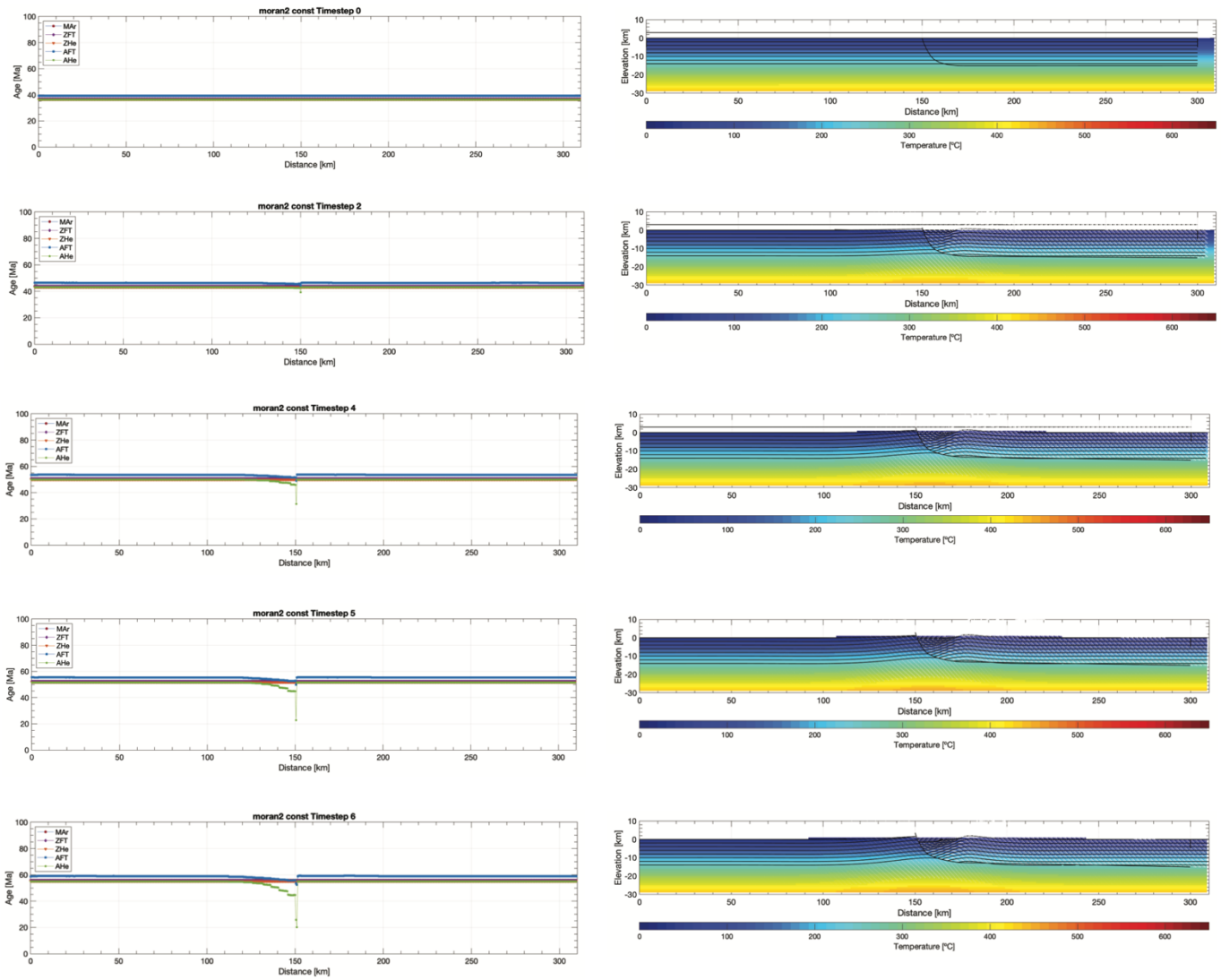

Thermal-kinematic model 2 evaluated in Pecube for a constant slip rate with fault slip onset at 19 Ma for D_{max} = 11 km.

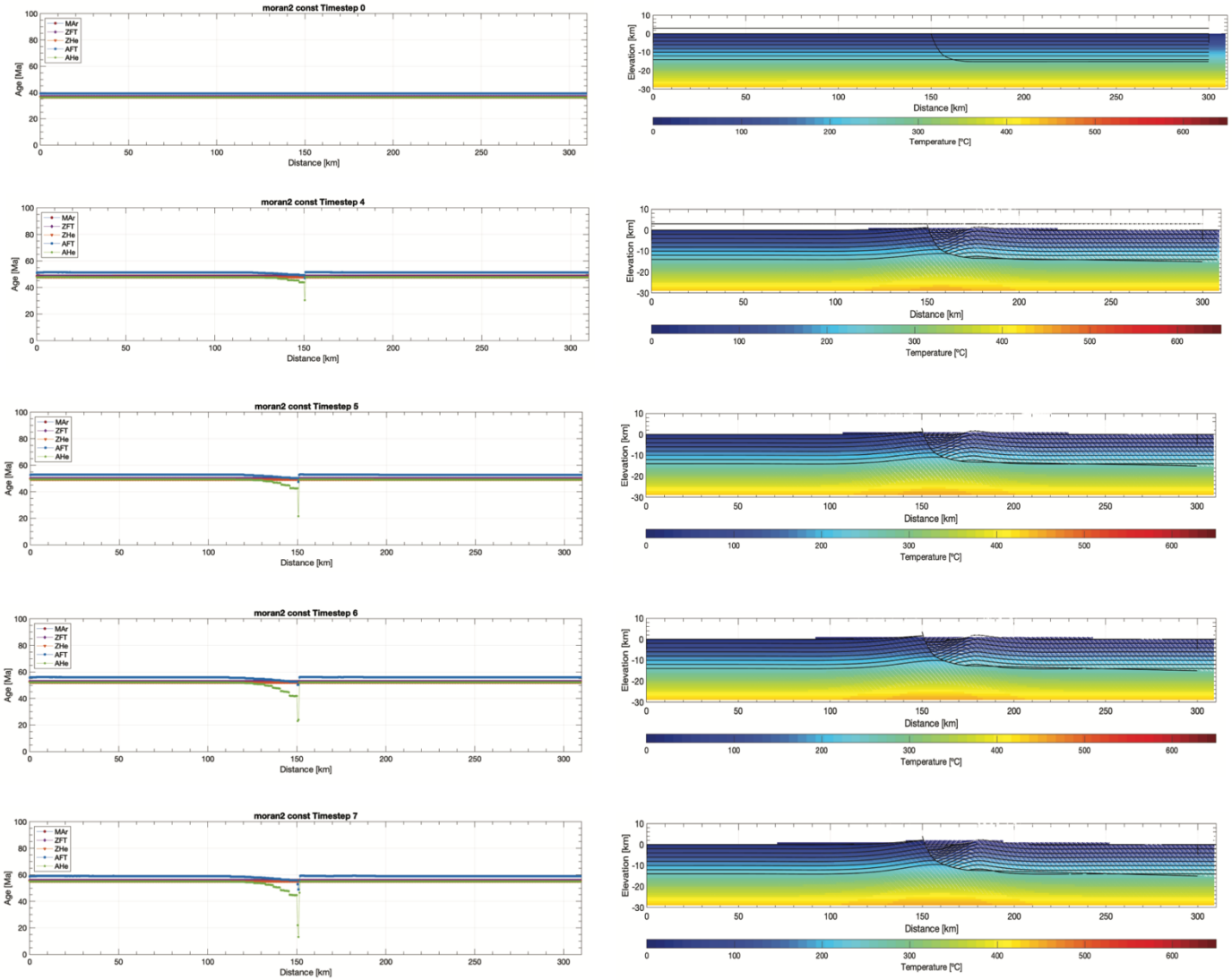

Thermal-kinematic model 2 evaluated in Pecube for a constant slip rate with fault slip onset at 19 Ma for D_{max} = 13 km.

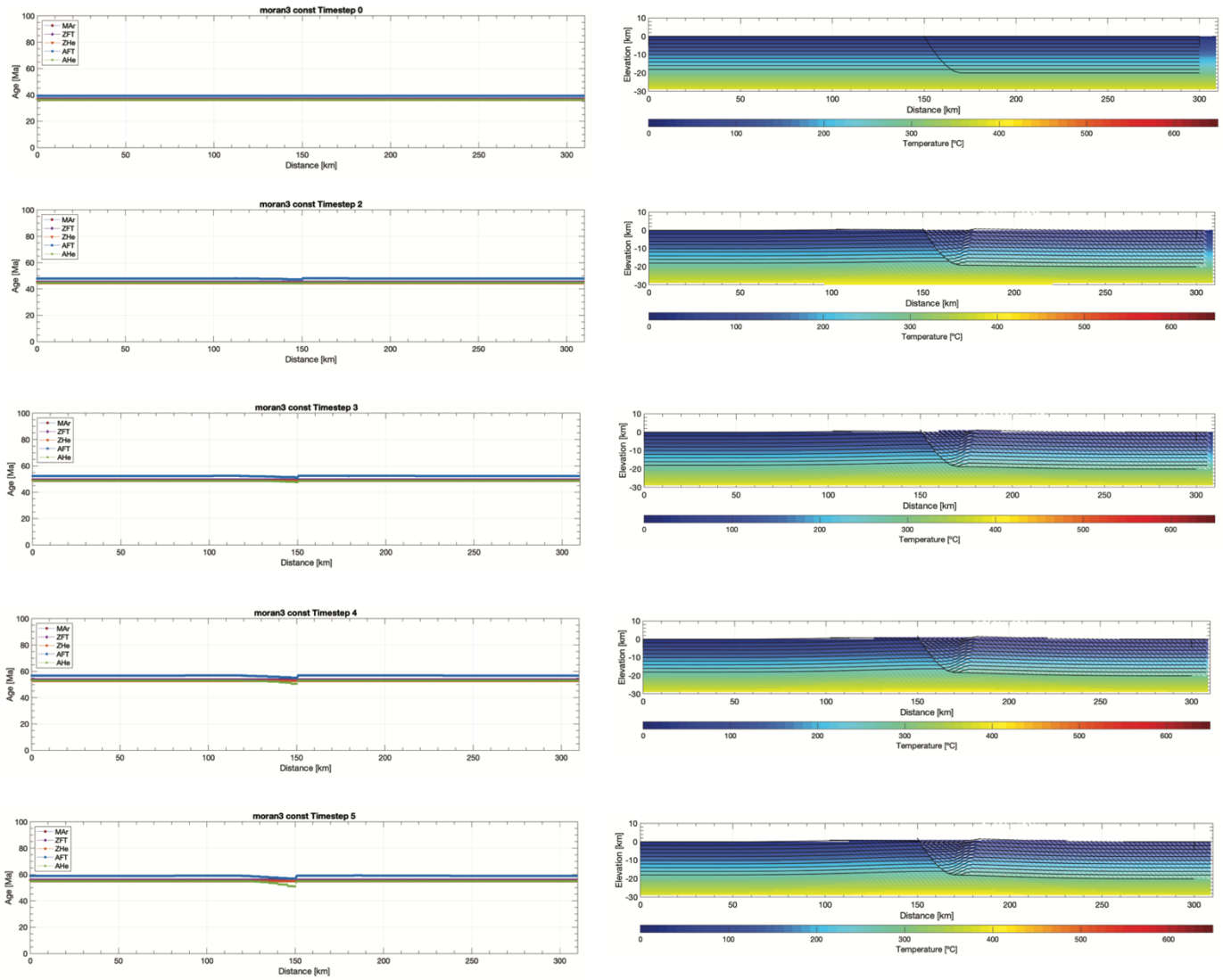

Thermal-kinematic model 3 evaluated in Pecube for a constant slip rate with fault slip onset at 19 Ma for D_{max} = 9 km.

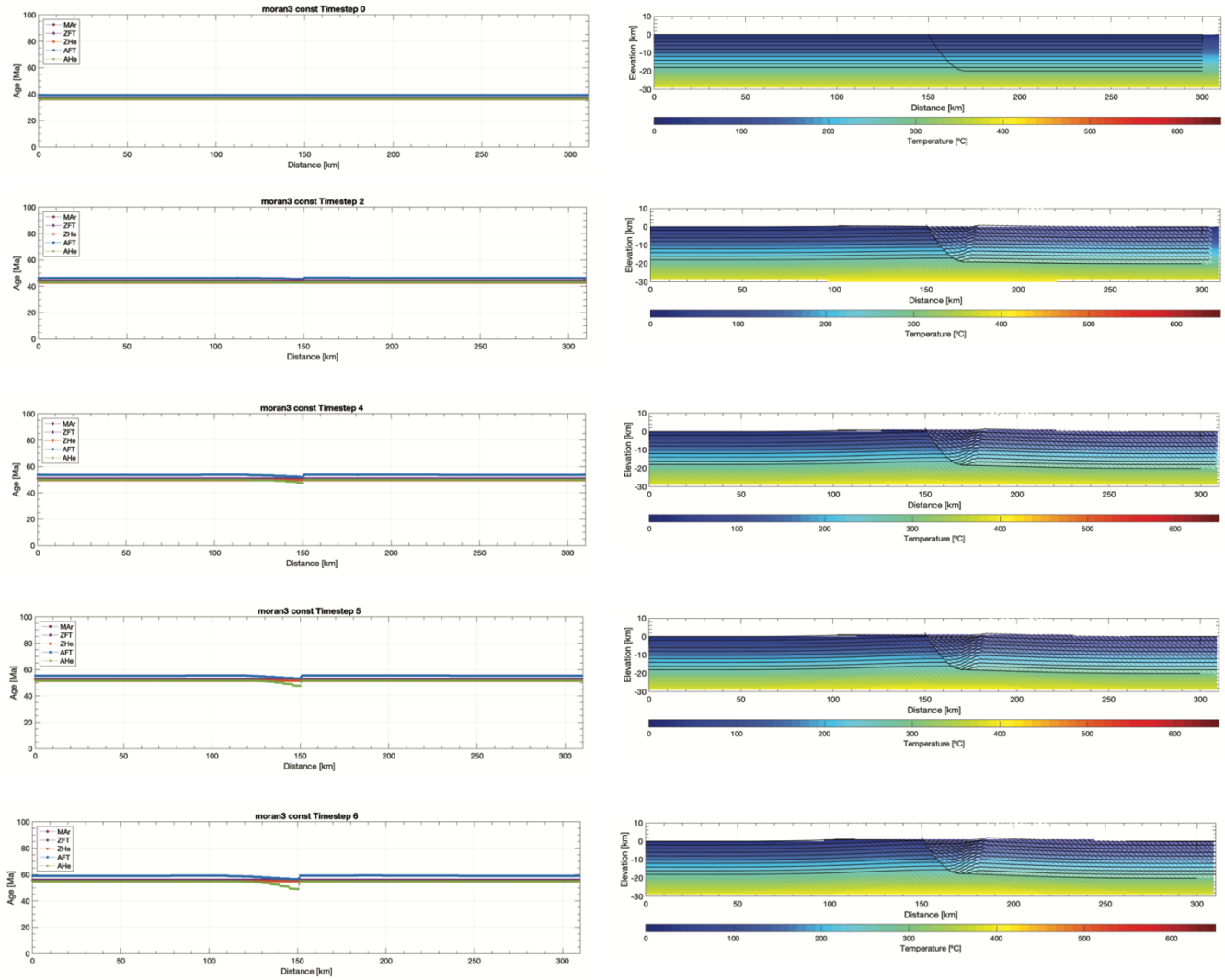

Thermal-kinematic model 3 evaluated in Pecube for a constant slip rate with fault slip onset at 19 Ma for D_{max} = 11 km.

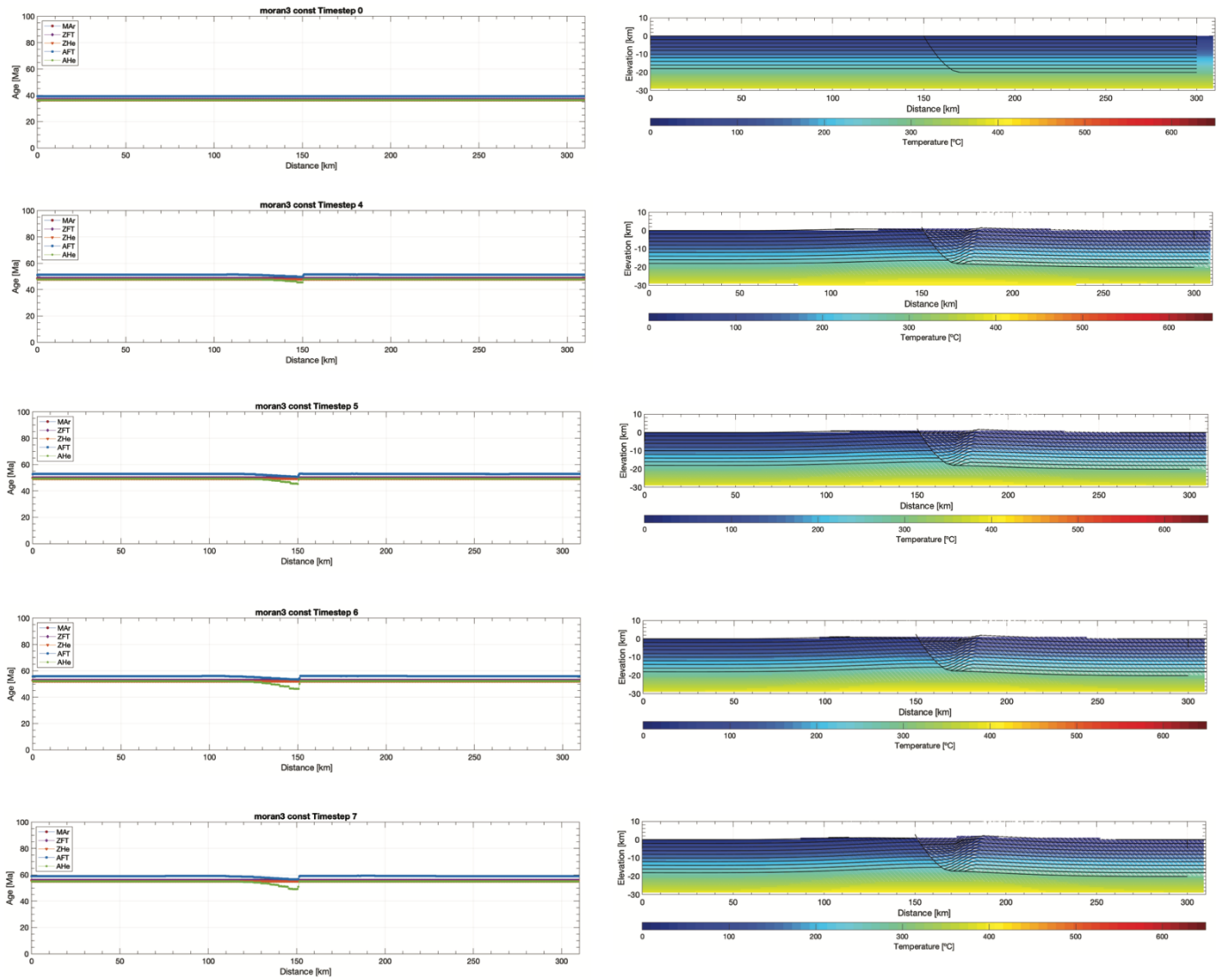

Thermal-kinematic model 3 evaluated in Pecube for a constant slip rate with fault slip onset at 19 Ma for D_{max} = 13 km.

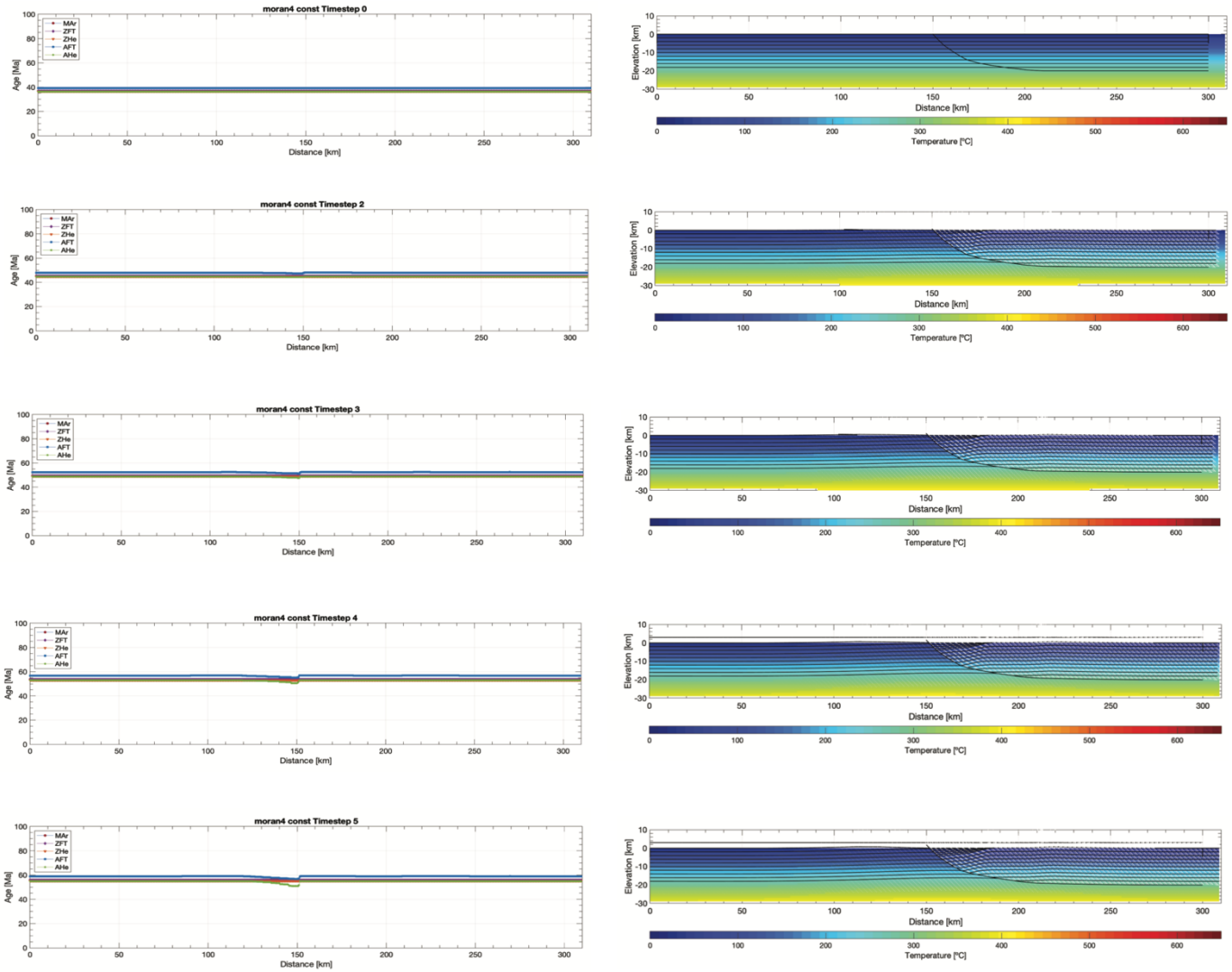

Thermal-kinematic model 4 evaluated in Pecube for a constant slip rate with fault slip onset at 19 Ma for D_{max} = 9 km.

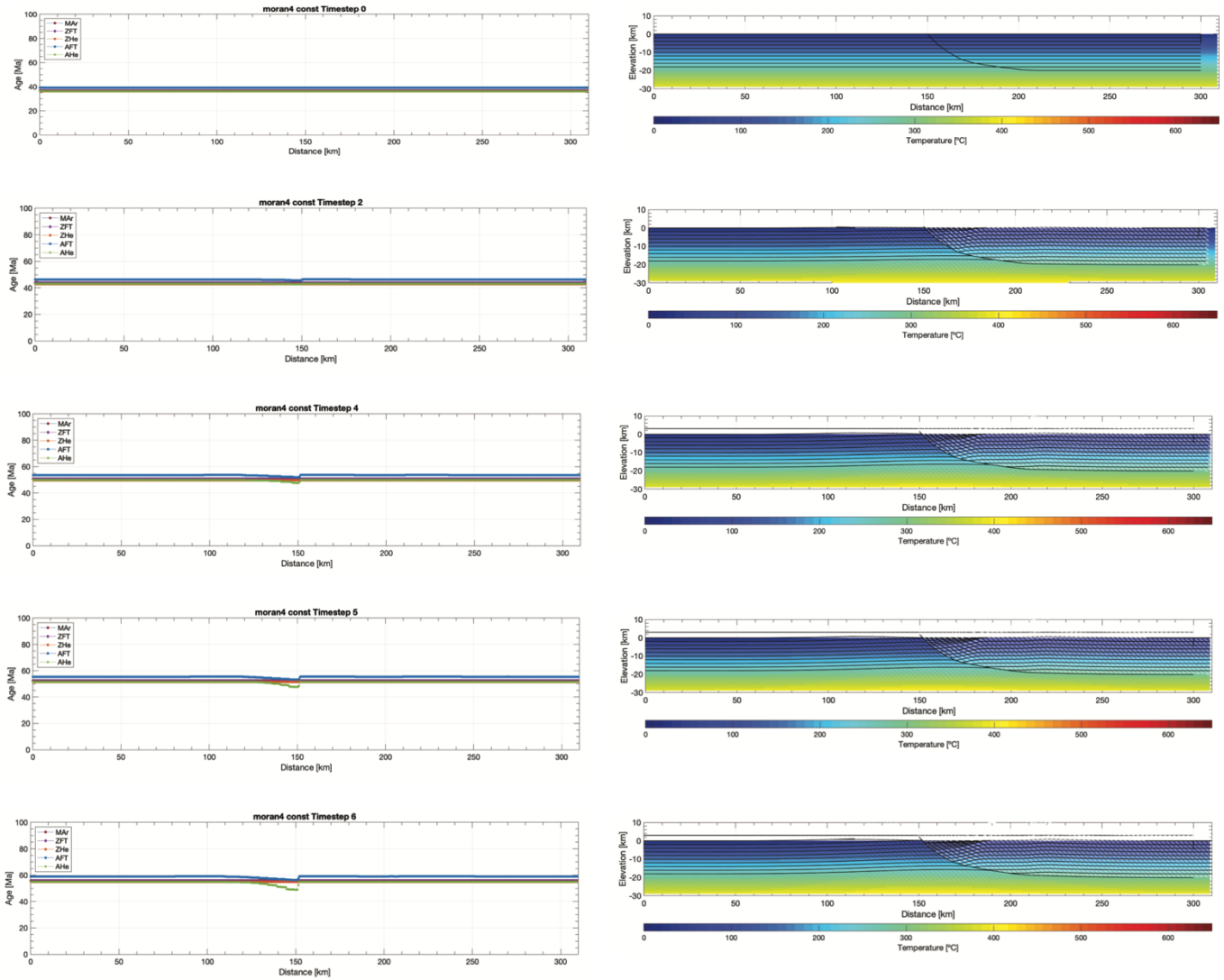

Thermal-kinematic model 4 evaluated in Pecube for a constant slip rate with fault slip onset at 19 Ma for D_{max} = 11 km.

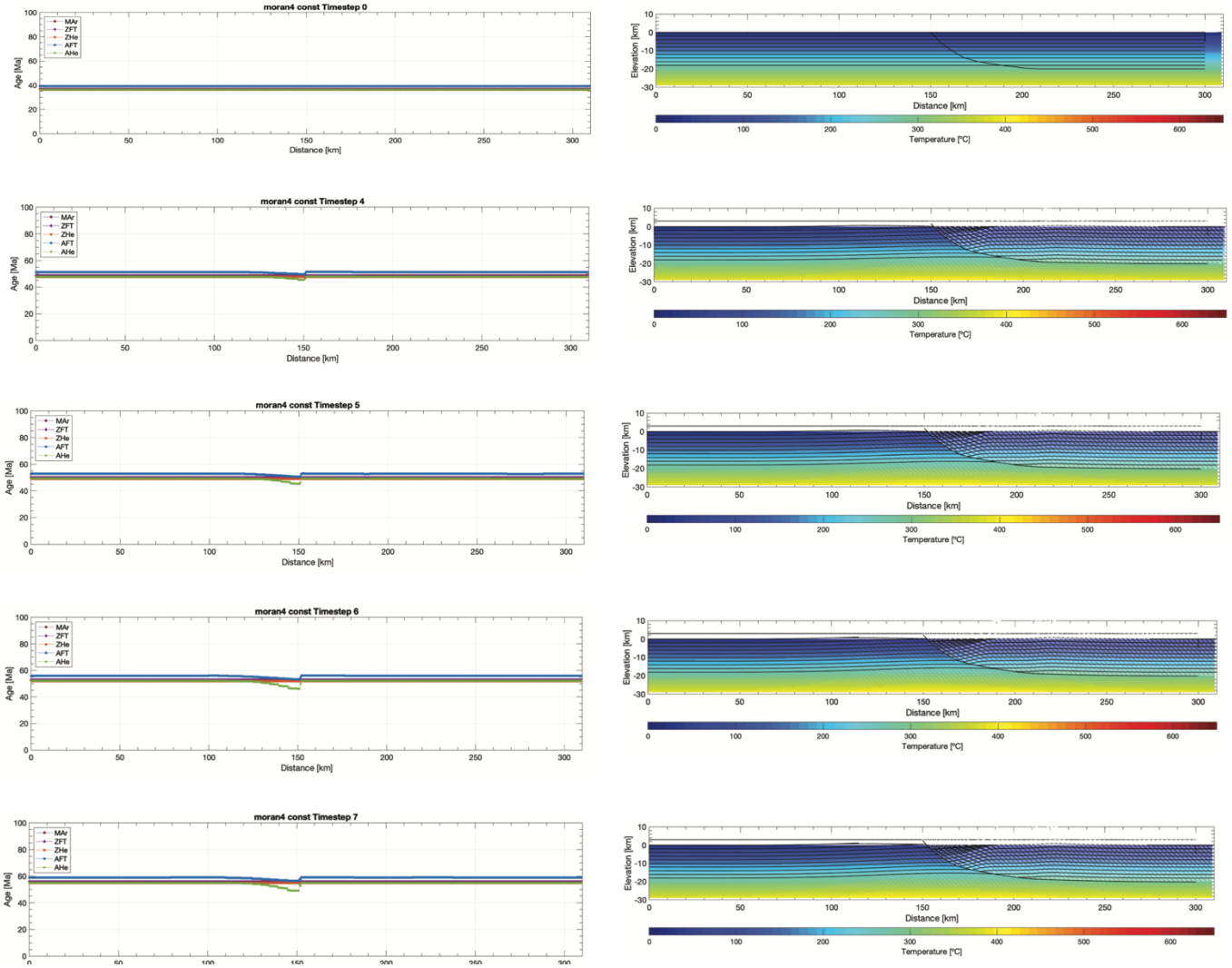

Thermal-kinematic model 4 evaluated in Pecube for a constant slip rate with fault slip onset at 19 Ma for D_{max} = 13 km.

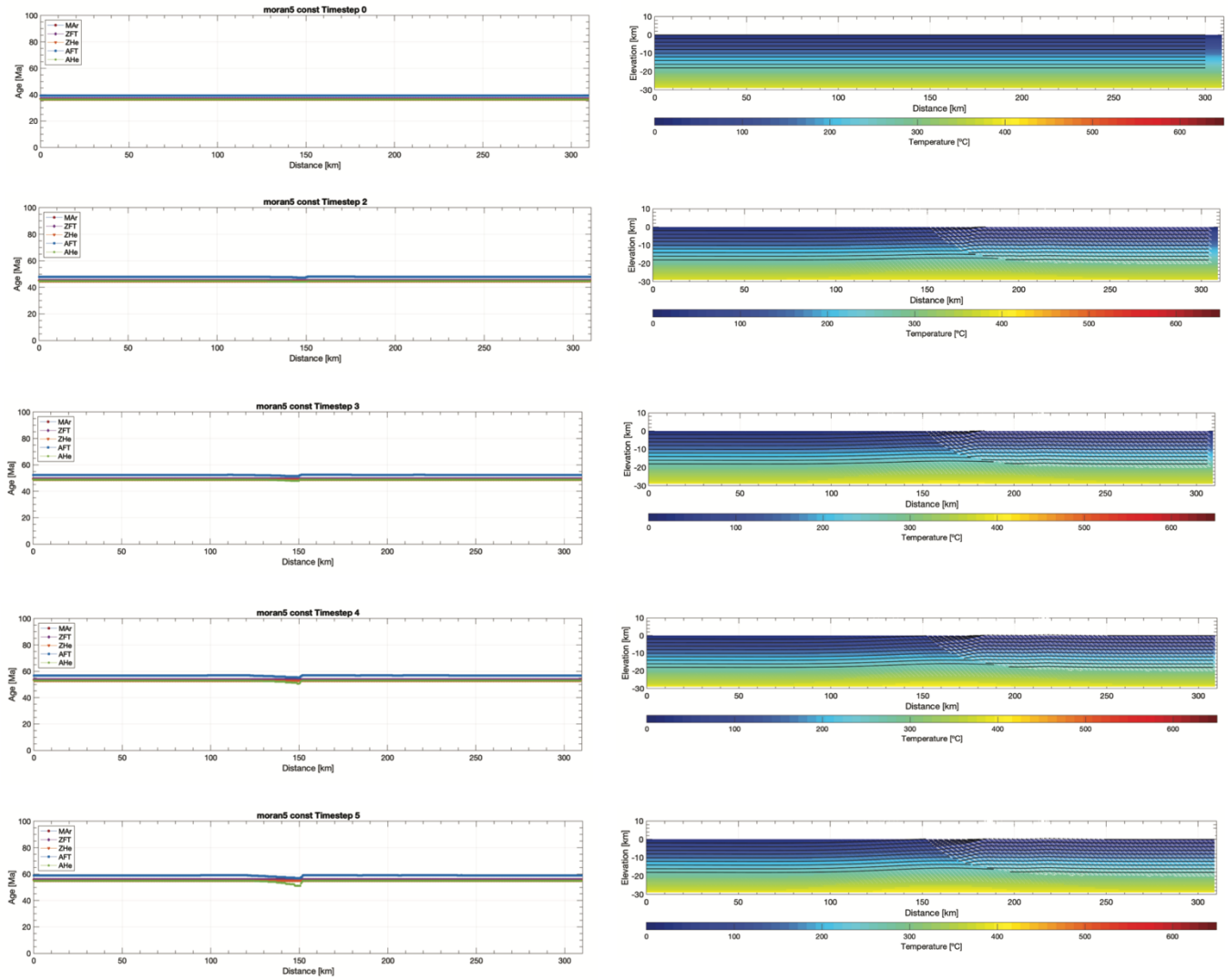

Thermal-kinematic model 5 evaluated in Pecube for a constant slip rate with fault slip onset at 19 Ma for D_{max} = 9 km.

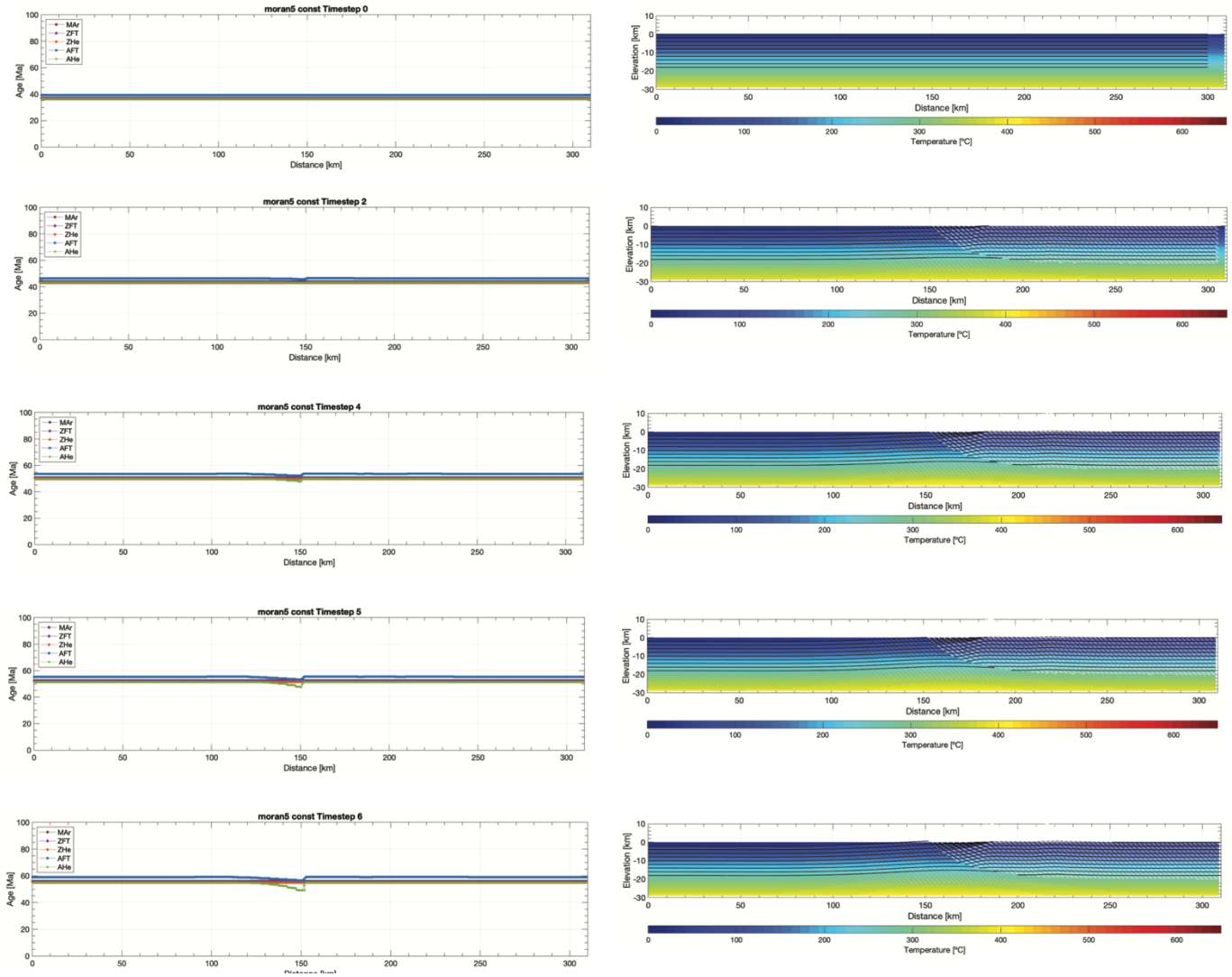

Thermal-kinematic model 5 evaluated in Pecube for a constant slip rate with fault slip onset at 19 Ma for D_{max} = 11 km.

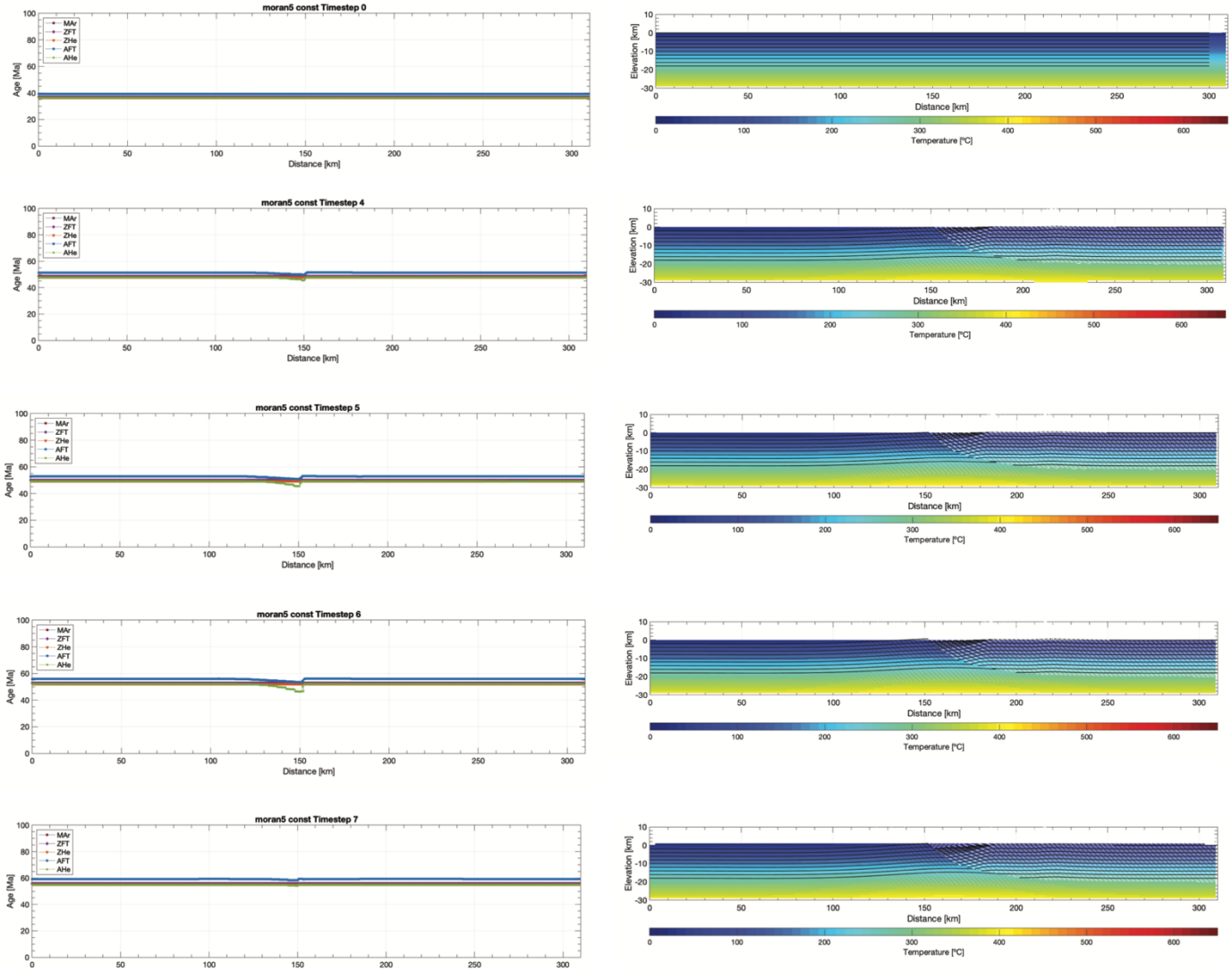

Thermal-kinematic model 5 evaluated in Pecube for a constant slip rate with fault slip onset at 19 Ma for D_{max} = 13 km.

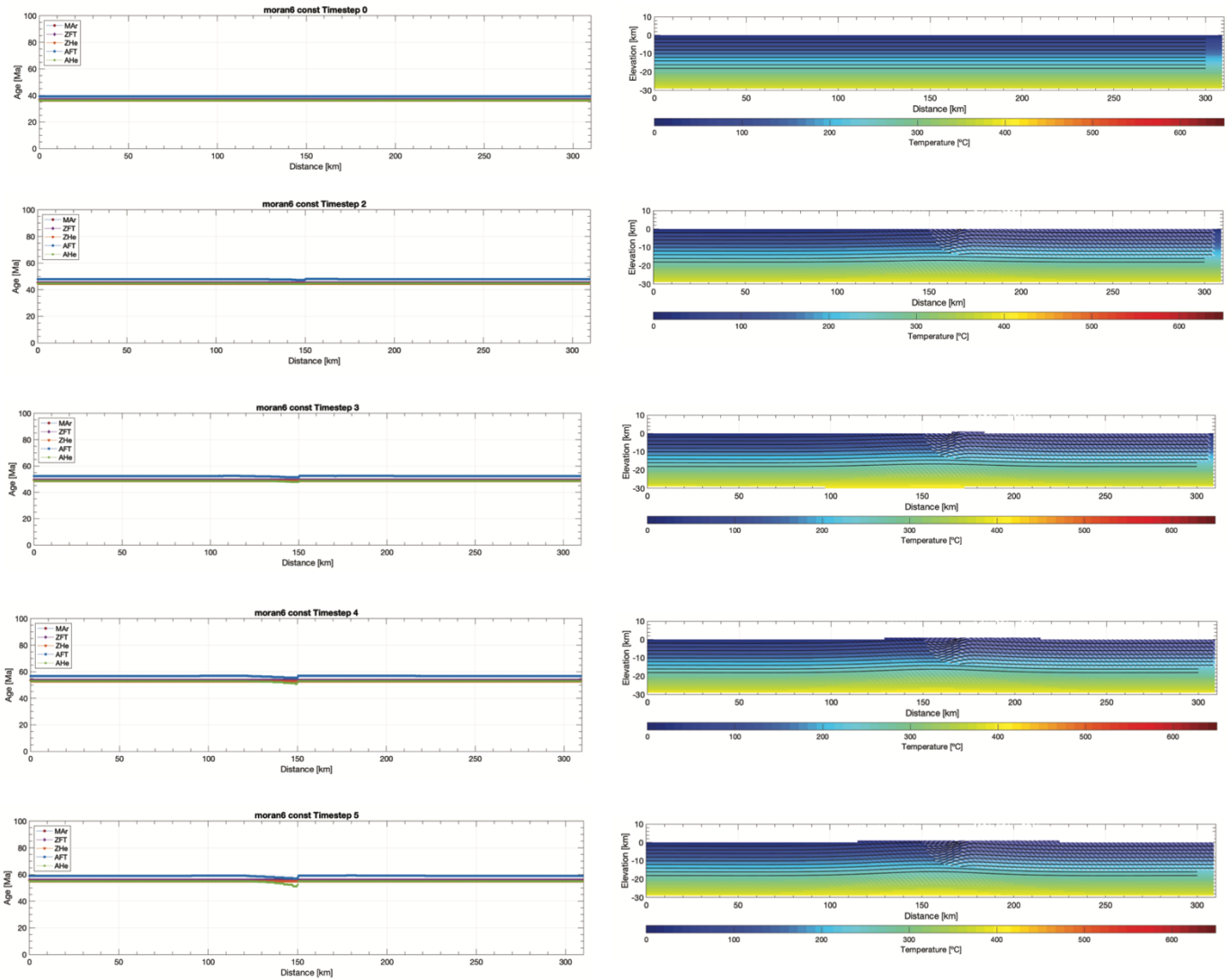

Thermal-kinematic model 6 evaluated in Pecube for a constant slip rate with fault slip onset at 19 Ma for D_{max} = 9 km.

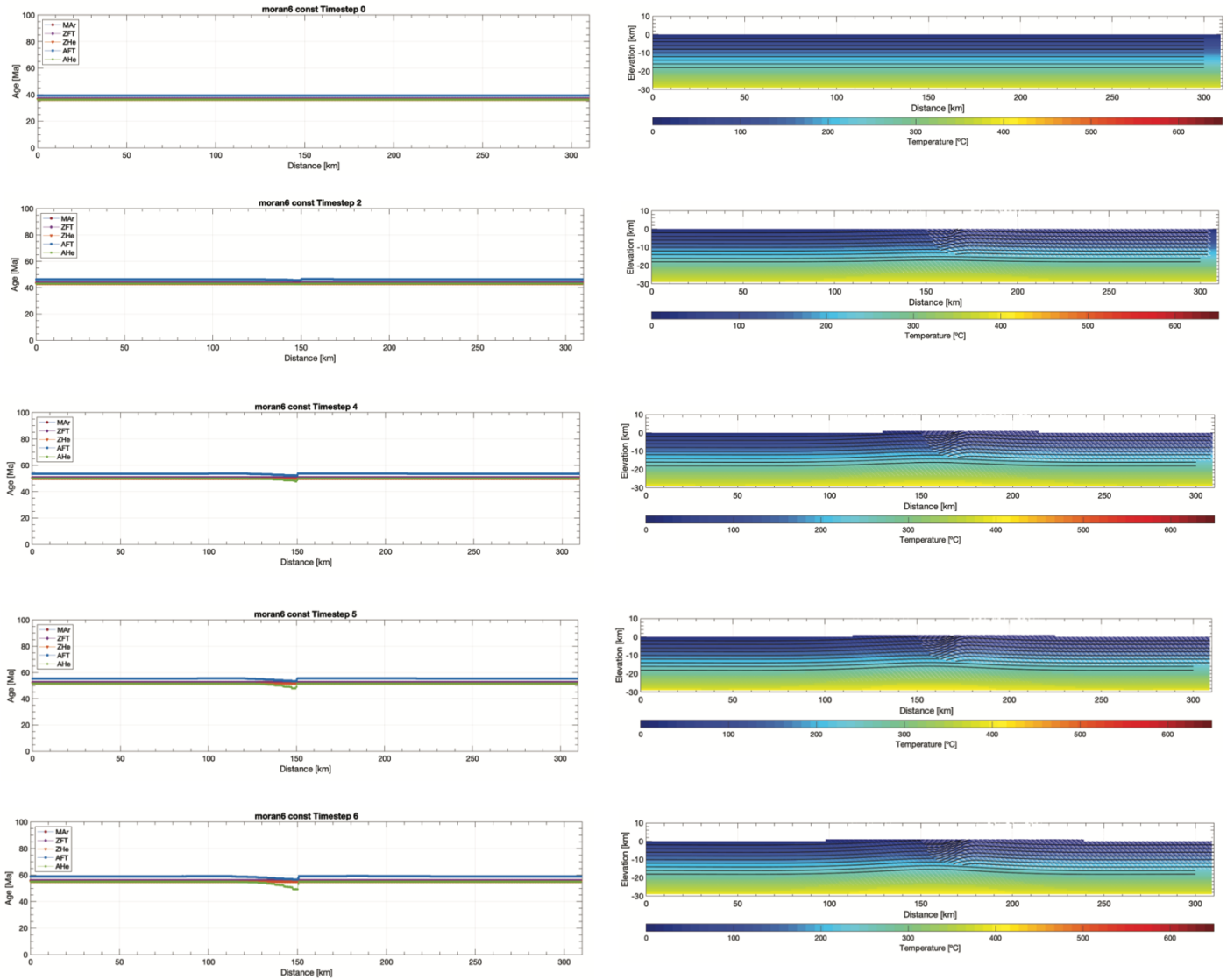

Thermal-kinematic model 6 evaluated in Pecube for a constant slip rate with fault slip onset at 19 Ma for D_{max} = 11 km.

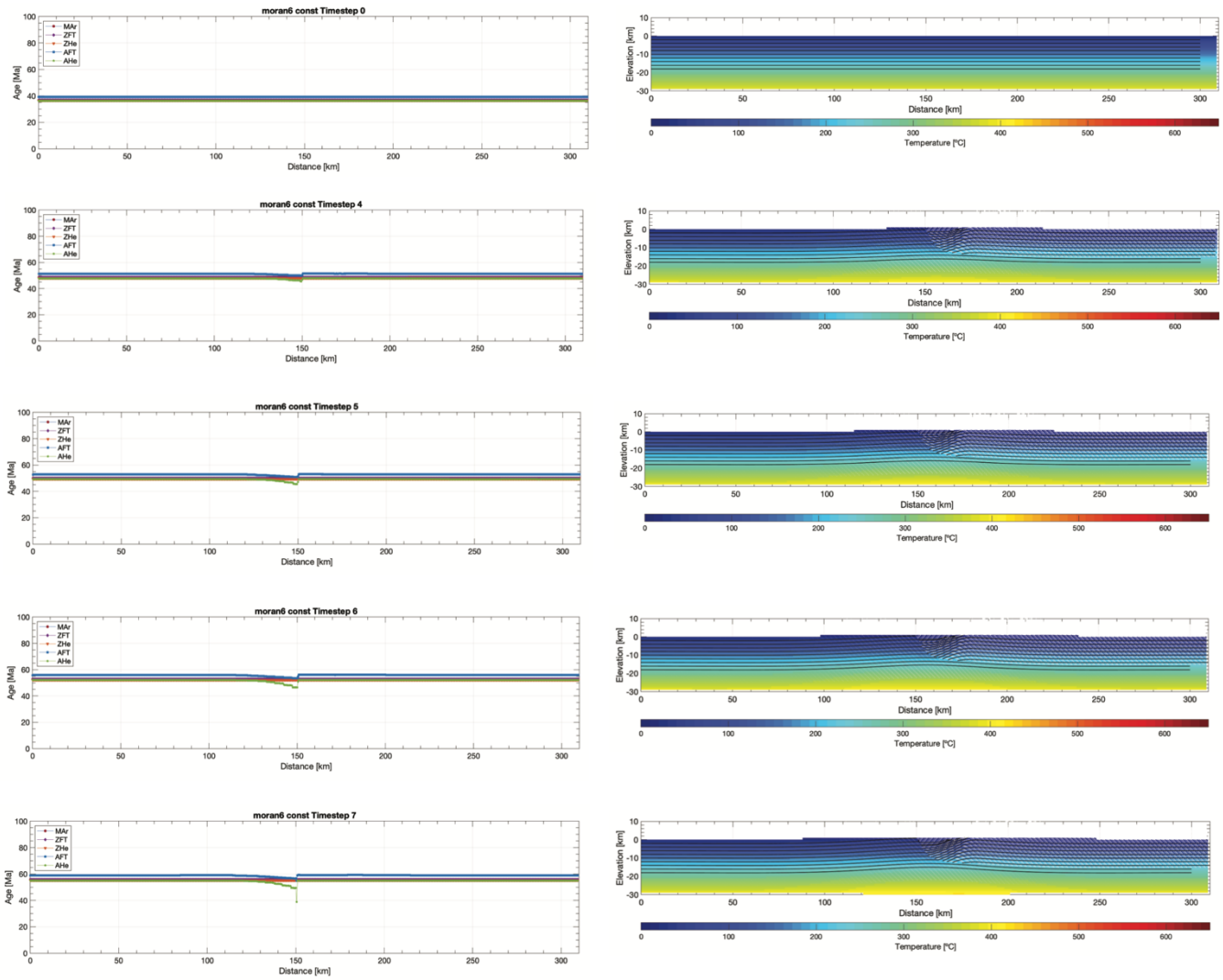

Thermal-kinematic model 6 evaluated in Pecube for a constant slip rate with fault slip onset at 19 Ma for D_{max} = 13 km.

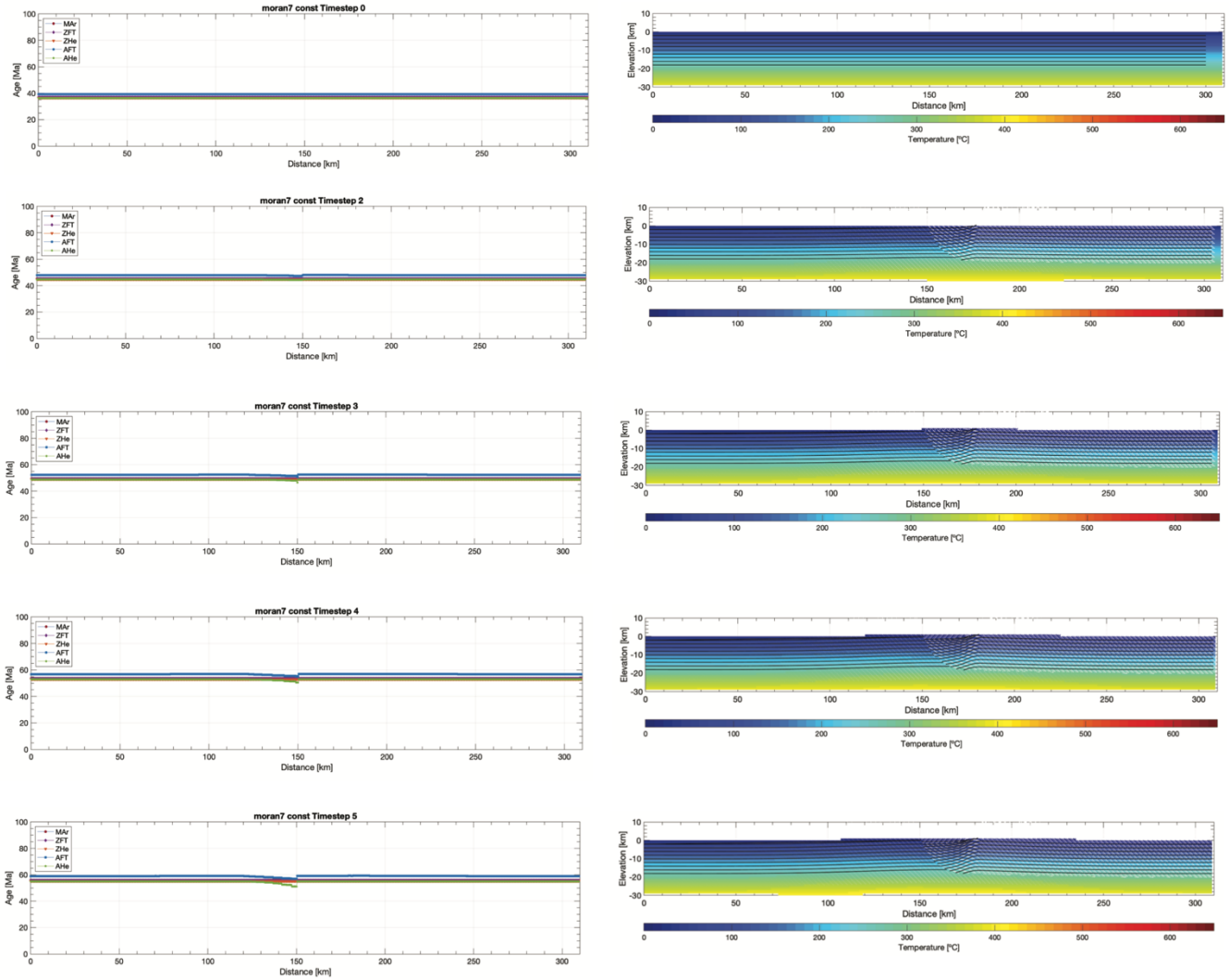

Thermal-kinematic model 7 evaluated in Pecube for a constant slip rate with fault slip onset at 19 Ma for D_{max} = 9 km.

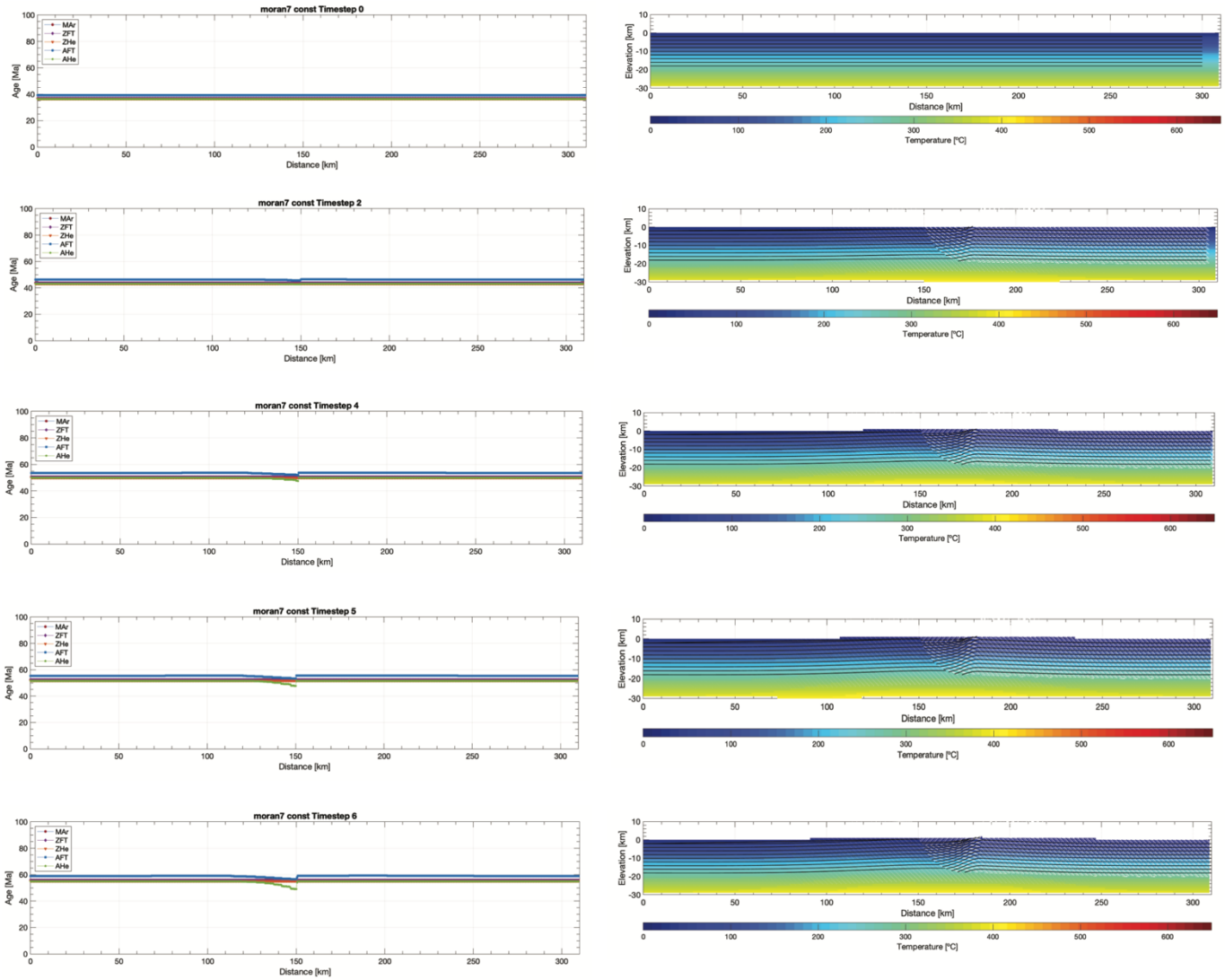

Thermal-kinematic model 7 evaluated in Pecube for a constant slip rate with fault slip onset at 19 Ma for D_{max} = 11 km.

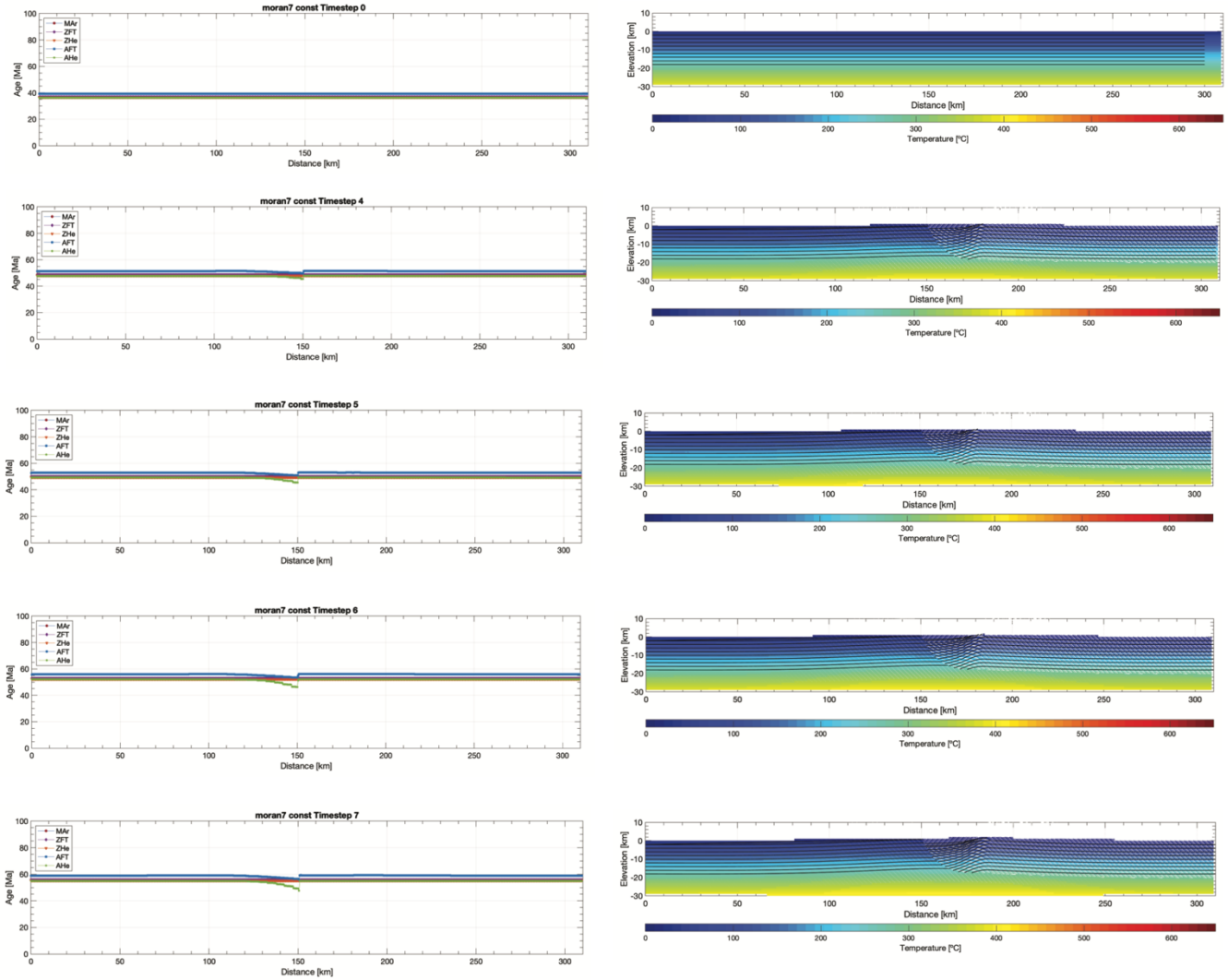

Thermal-kinematic model 7 evaluated in Pecube for a constant slip rate with fault slip onset at 19 Ma for D_{max} = 13 km.

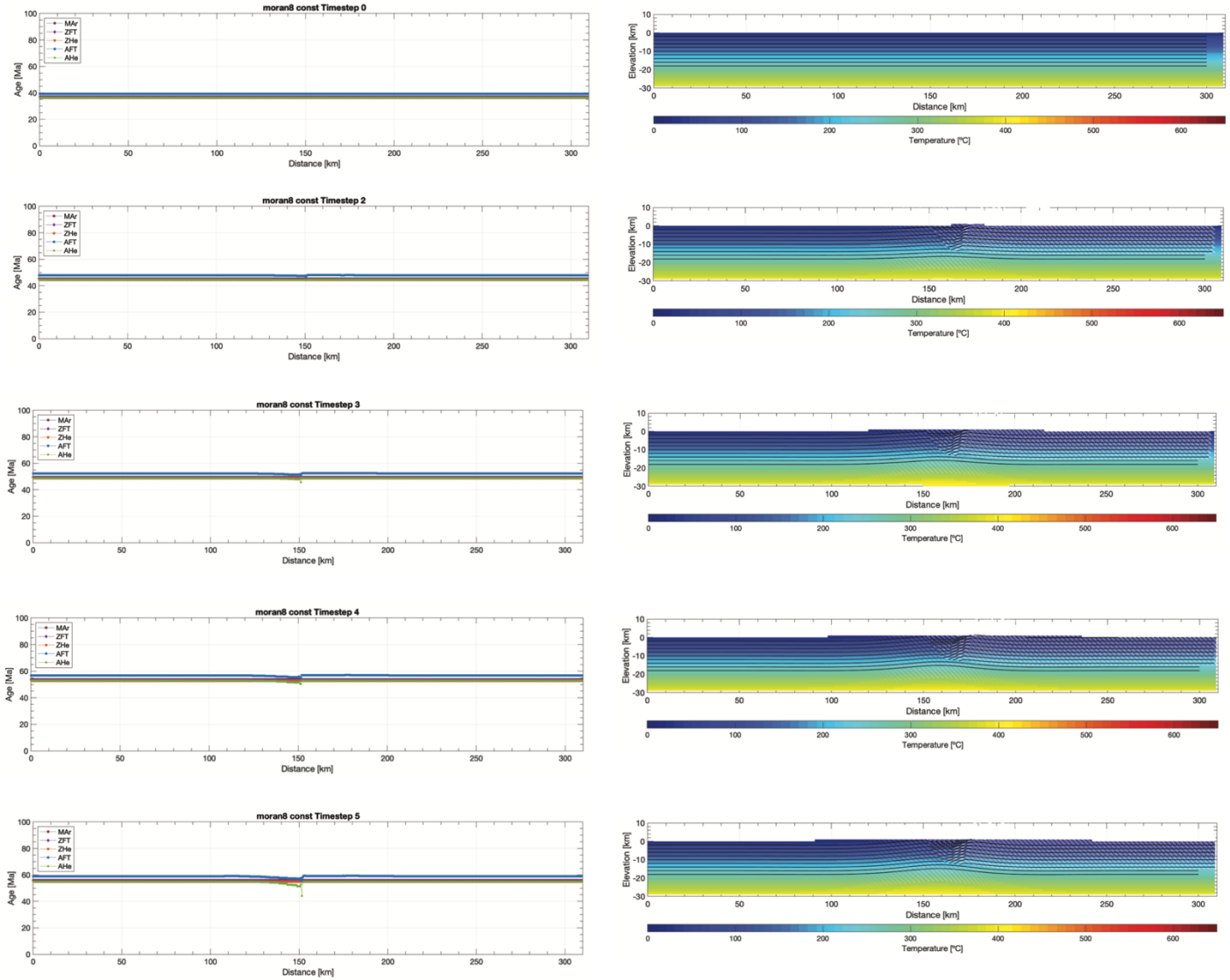

Thermal-kinematic model 8 evaluated in Pecube for a constant slip rate with fault slip onset at 19 Ma for D_{max} = 9 km.

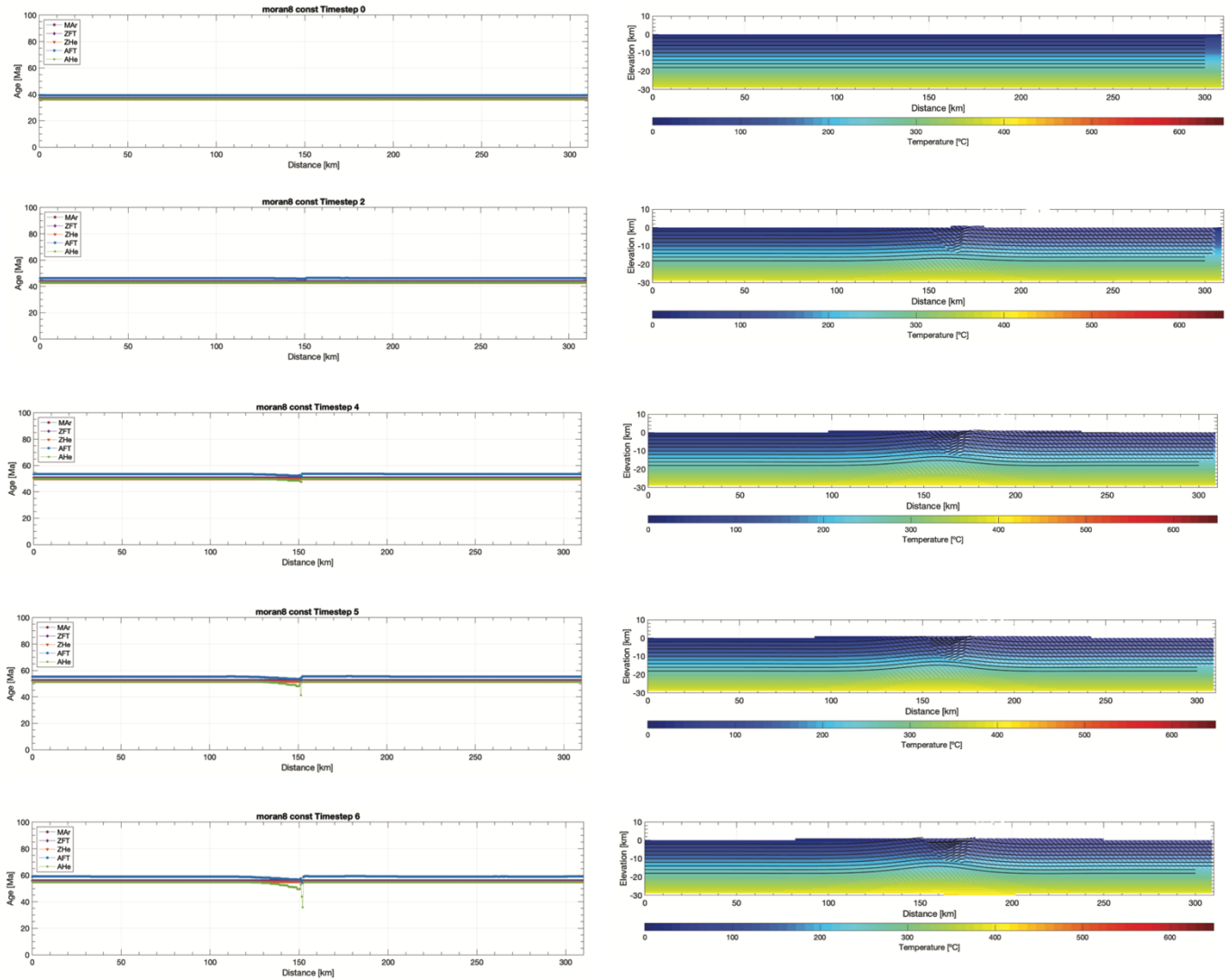

Thermal-kinematic model 8 evaluated in Pecube for a constant slip rate with fault slip onset at 19 Ma for D_{max} = 11 km.

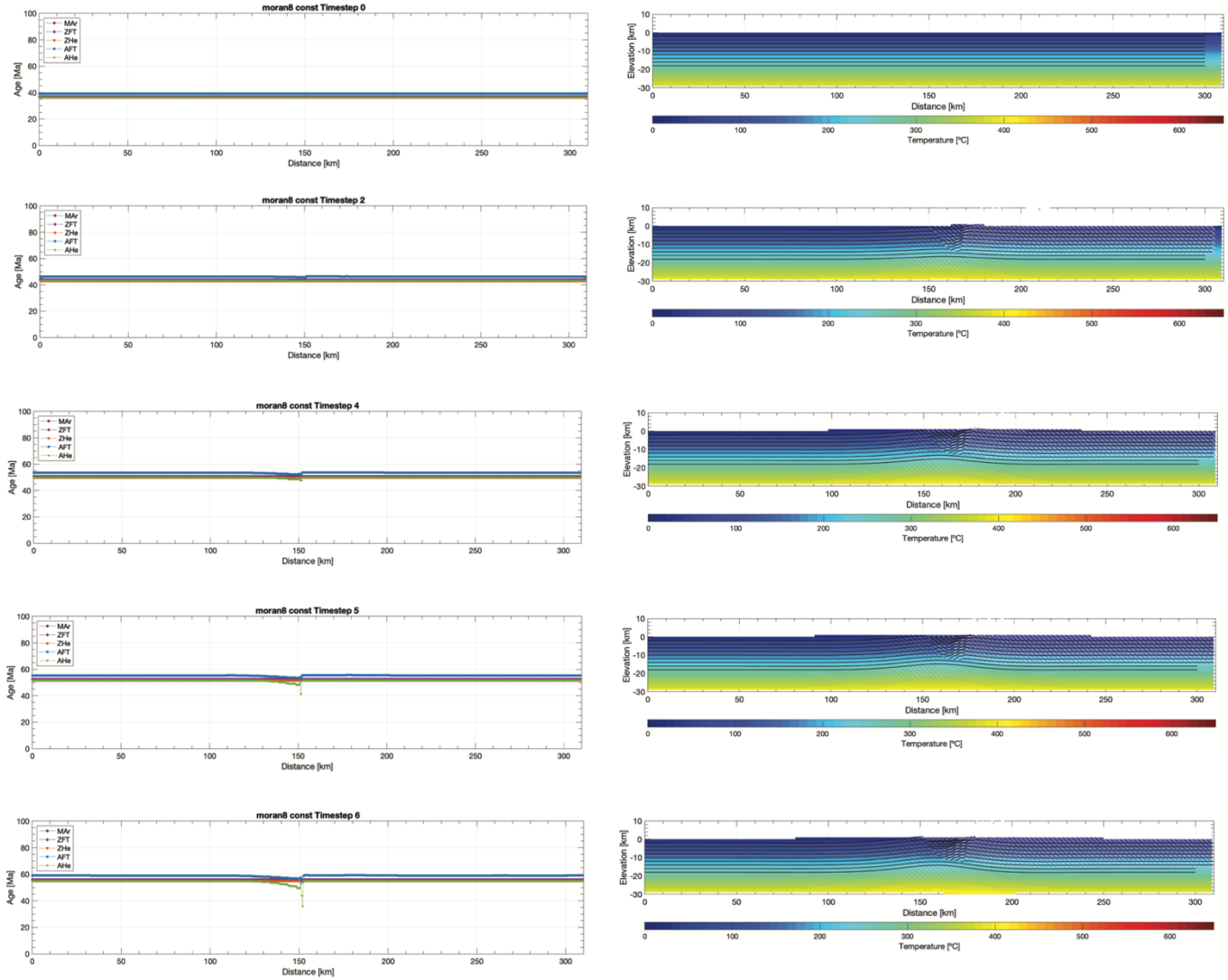

Thermal-kinematic model 8 evaluated in Pecube for a constant slip rate with fault slip onset at 19 Ma for D_{max} = 13 km.

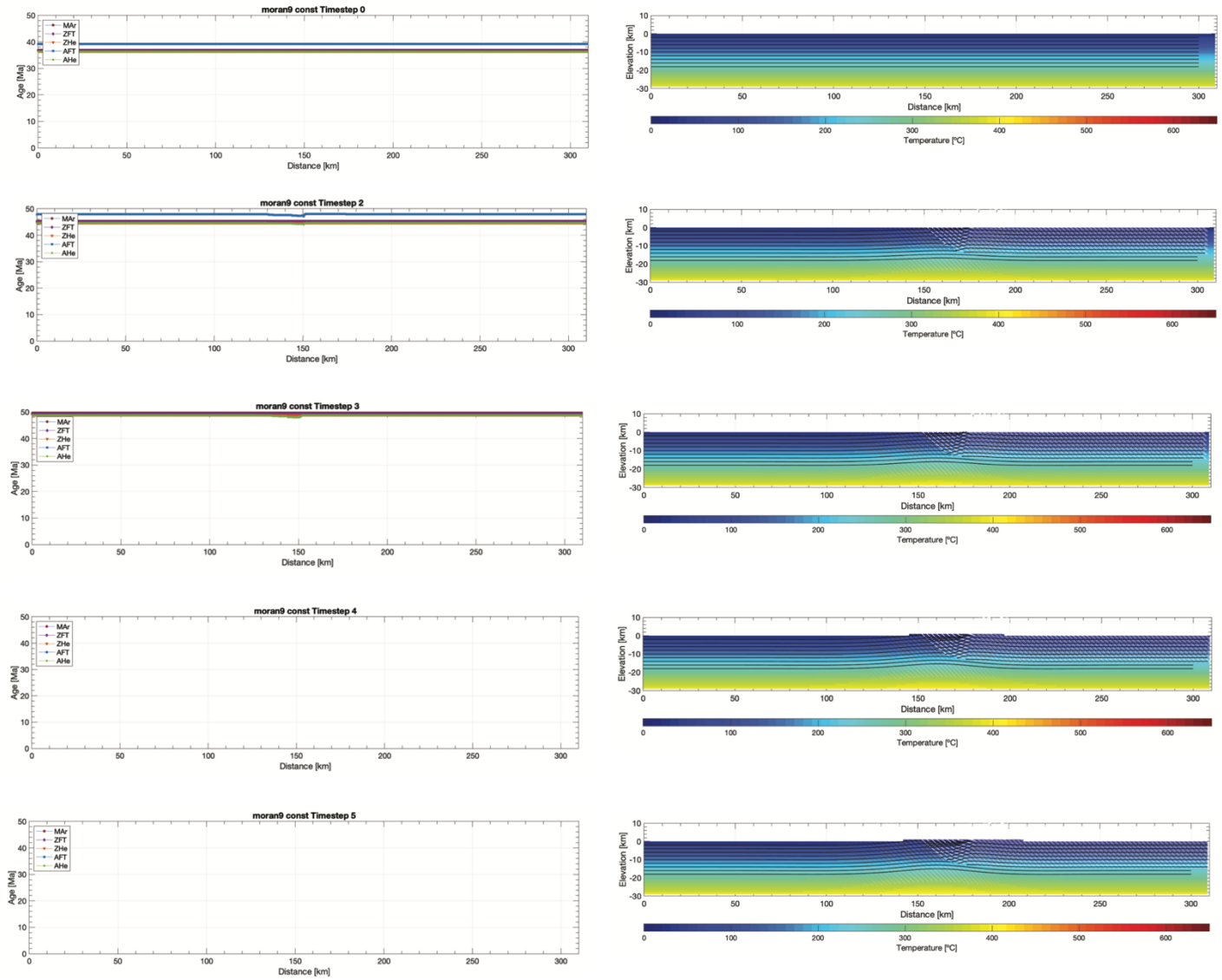

Thermal-kinematic model 9 evaluated in Pecube for a constant slip rate with fault slip onset at 19 Ma for D_{max} =9 km.

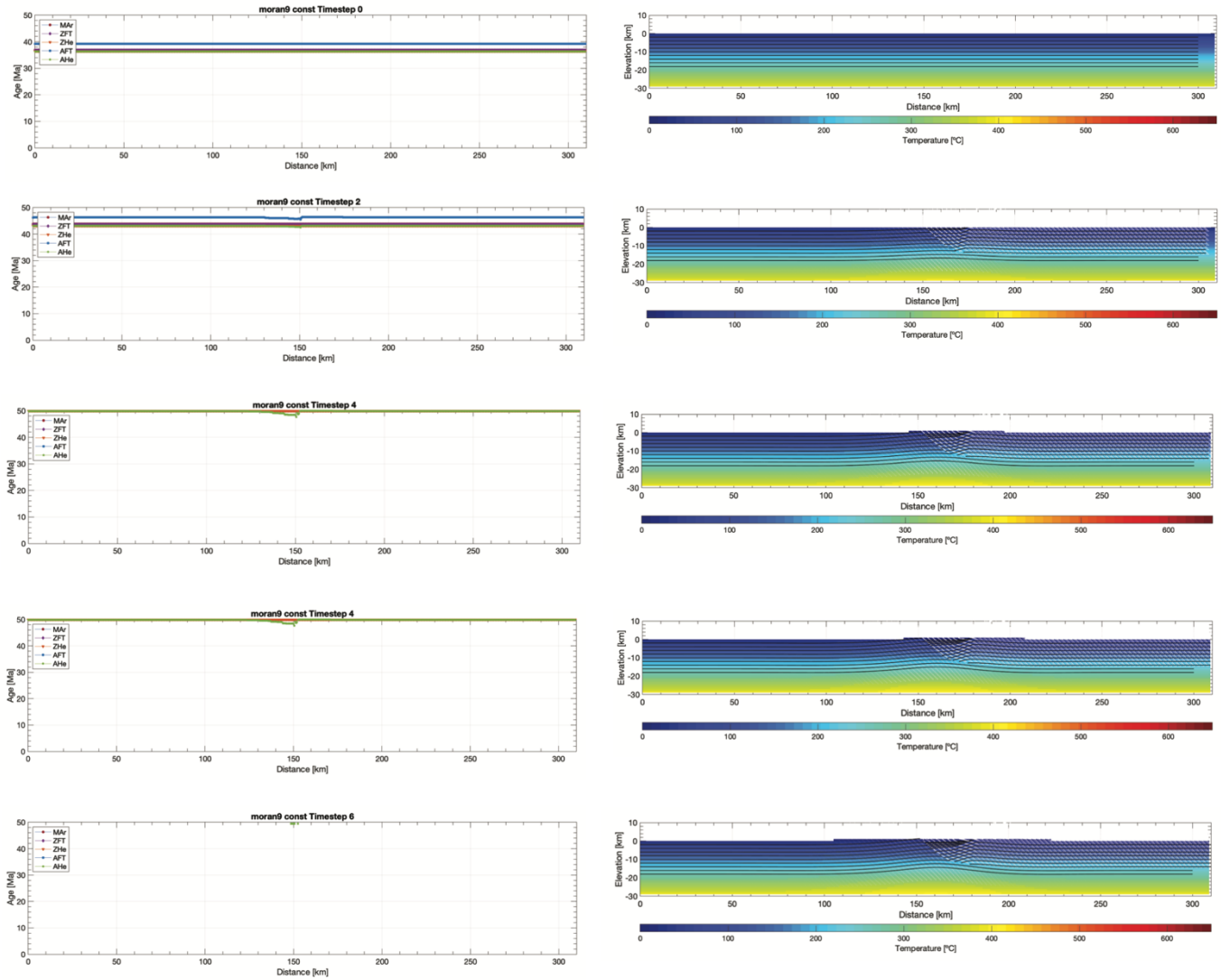

Thermal-kinematic model 9 evaluated in Pecube for a constant slip rate with fault slip onset at 19 Ma for D_{max} =11 km.

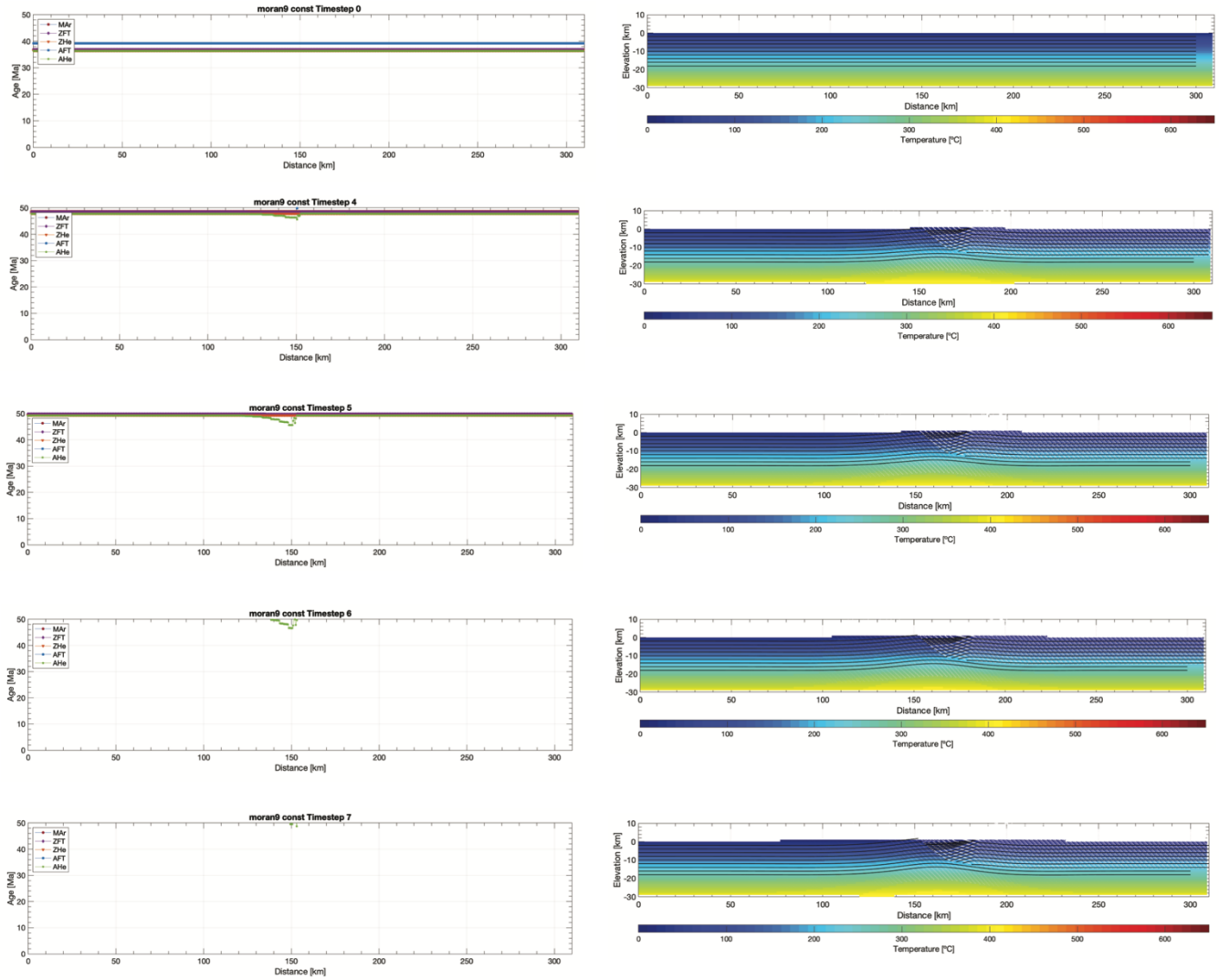

Thermal-kinematic model 9 evaluated in Pecube for a constant slip rate with fault slip onset at 19 Ma for D_{max} =13 km.

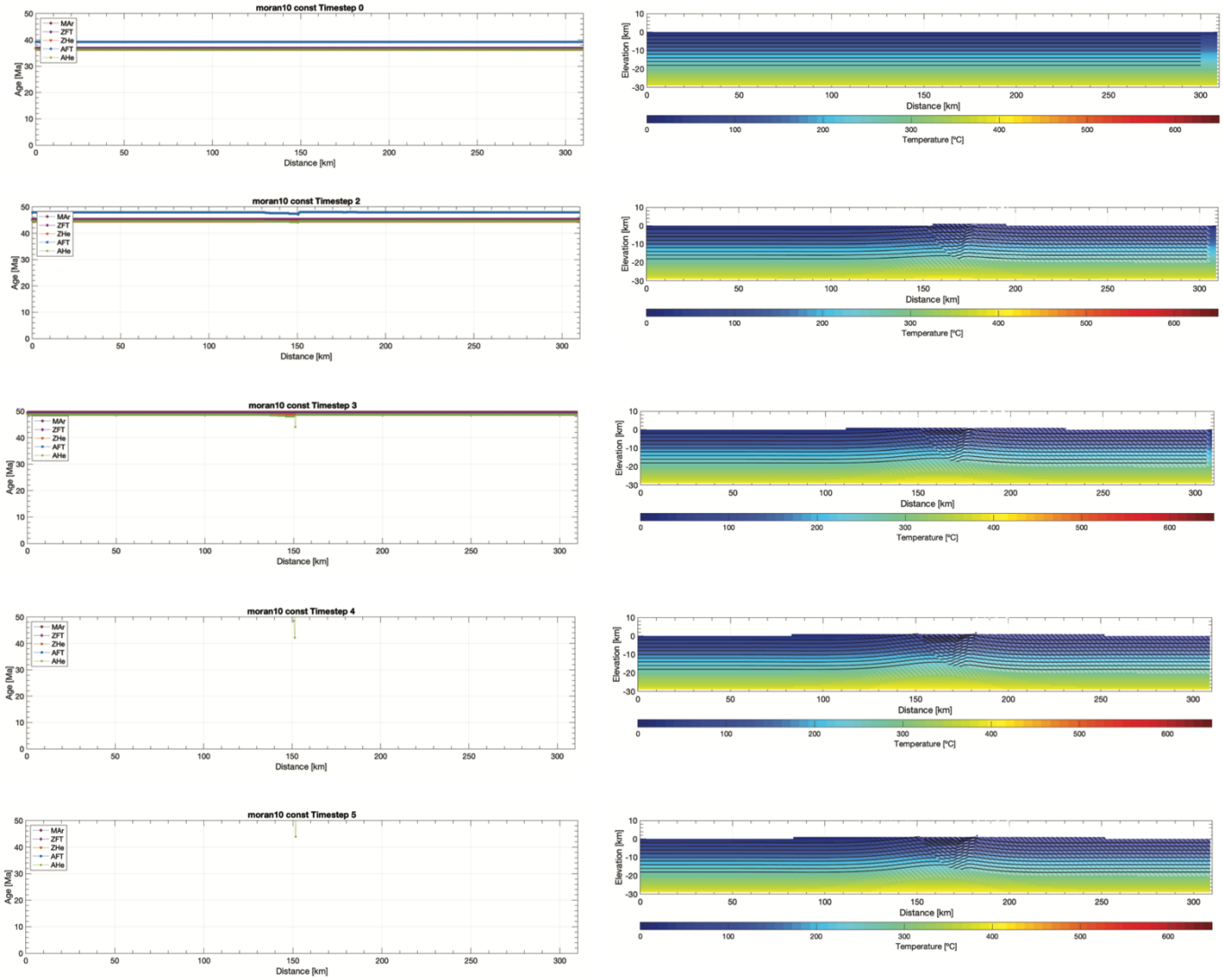

Thermal-kinematic model 10 evaluated in Pecube for a constant slip rate with fault slip onset at 19 Ma for D_{max} =9 km.

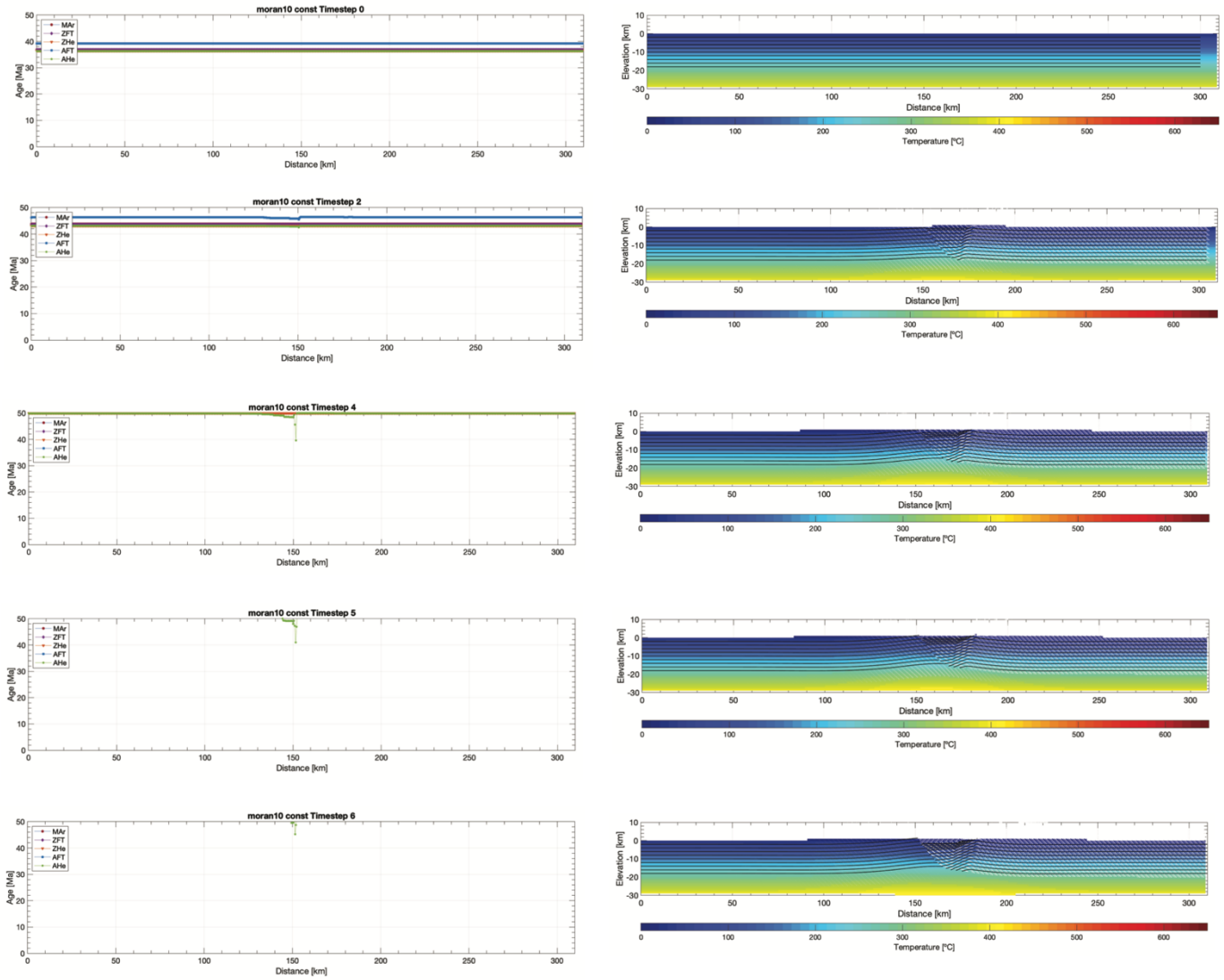

Thermal-kinematic model 10 evaluated in Pecube for a constant slip rate with fault slip onset at 19 Ma for D_{max} =11 km.

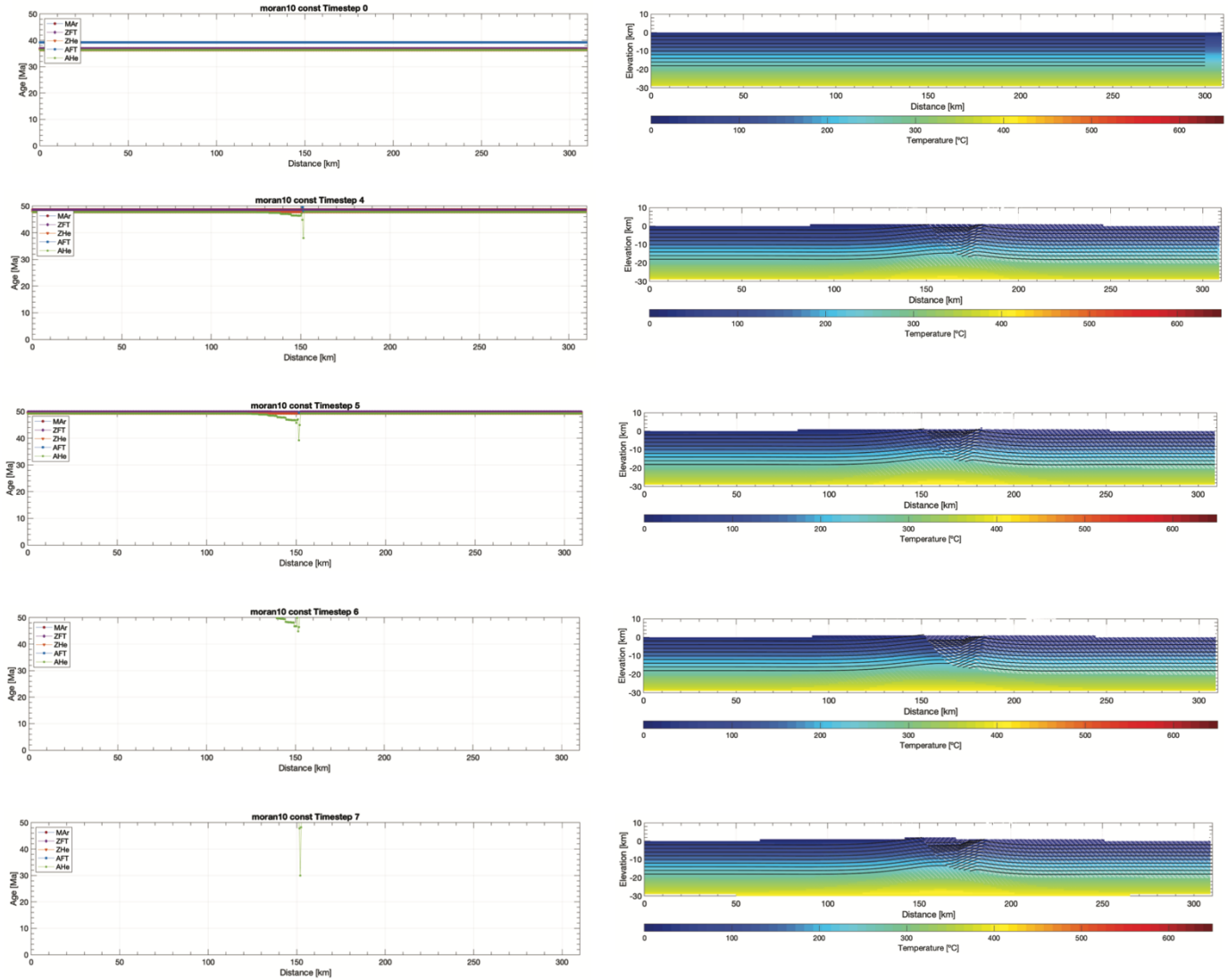

Thermal-kinematic model 10 evaluated in Pecube for a constant slip rate with fault slip onset at 19 Ma for D_{max} =13 km.

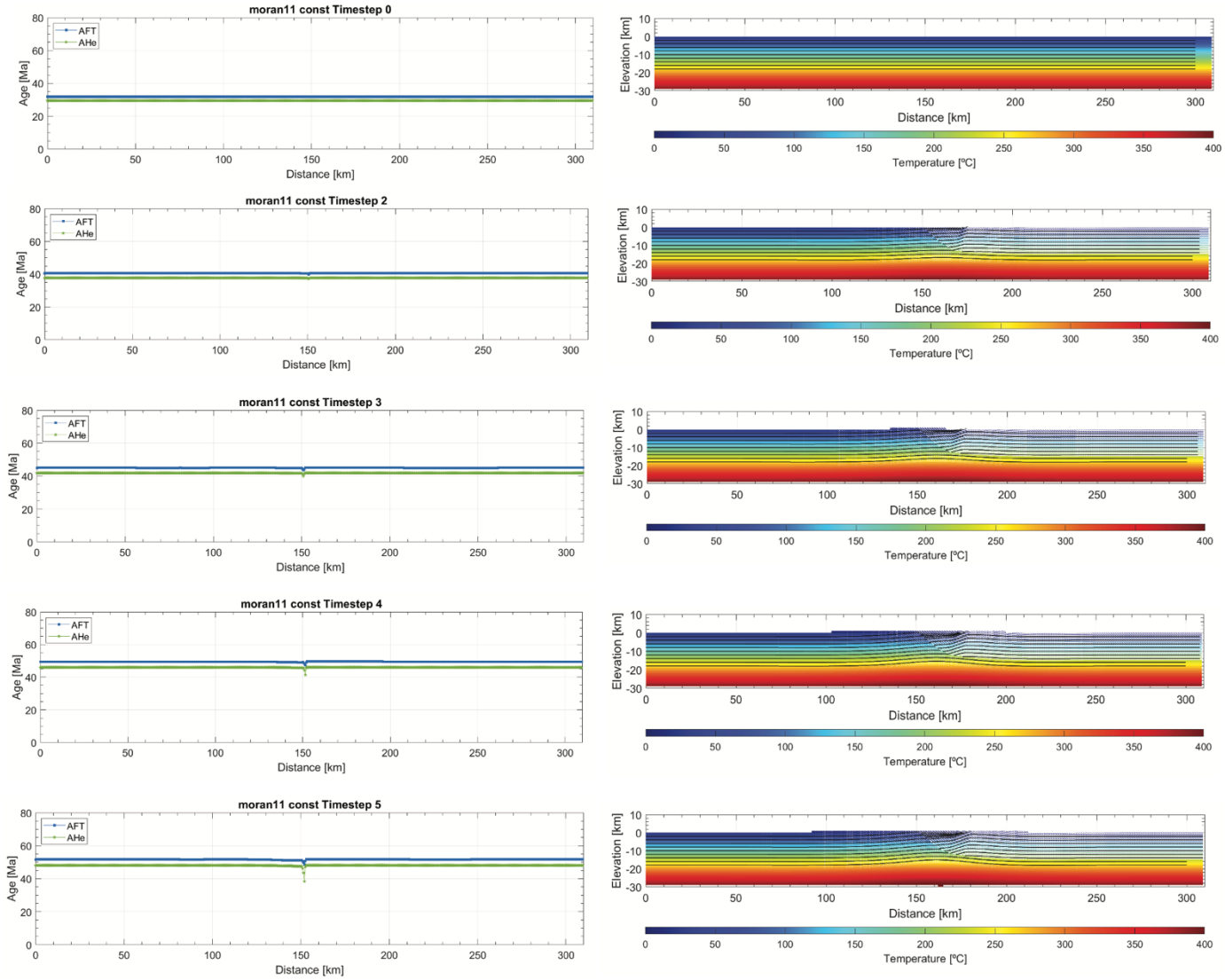

Thermal-kinematic model 11 evaluated in Pecube for a constant slip rate with fault slip onset at 19 Ma for D_{max} =9 km.

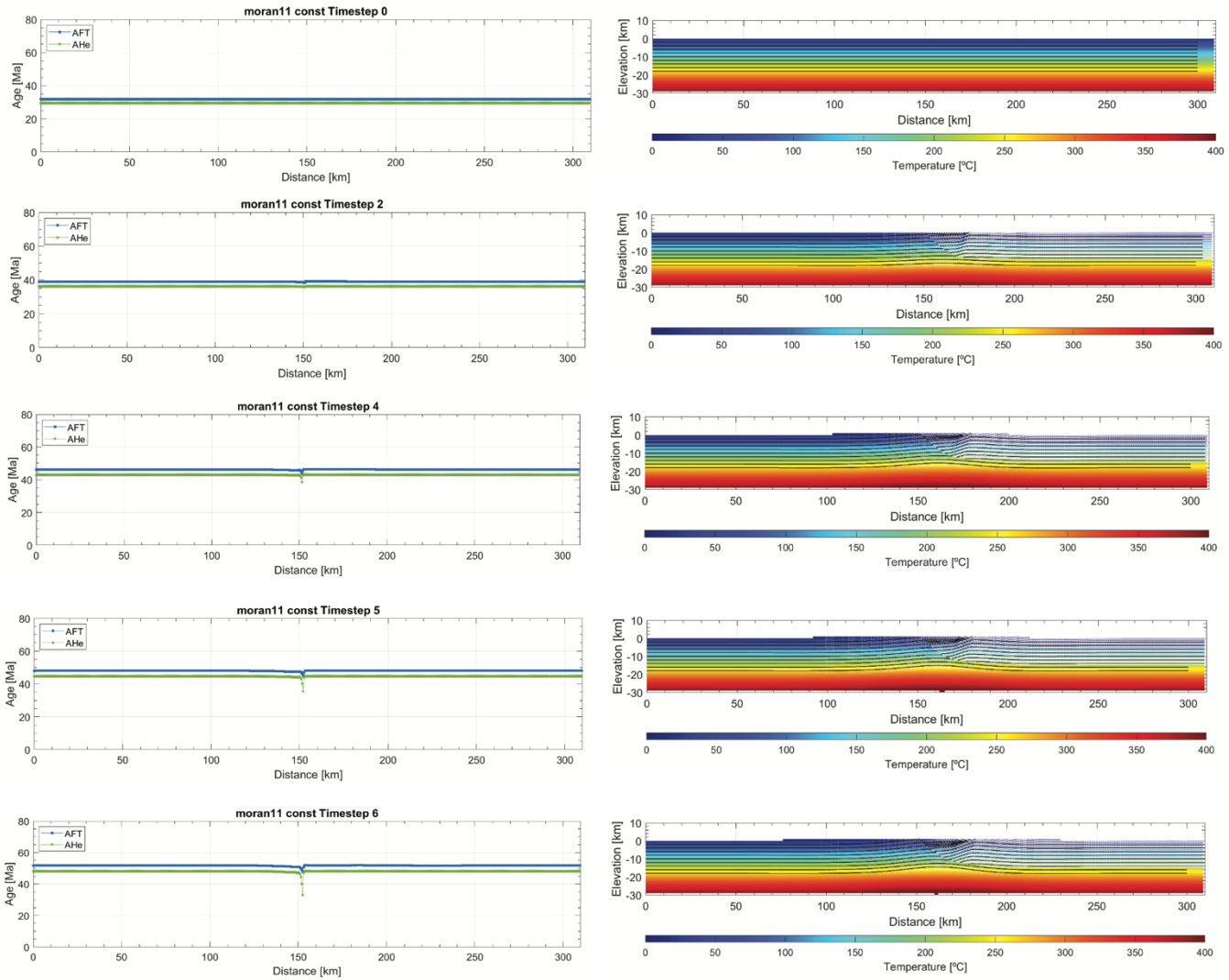

Thermal-kinematic model 11 evaluated in Pecube for a constant slip rate with fault slip onset at 19 Ma for D_{max} =11 km.

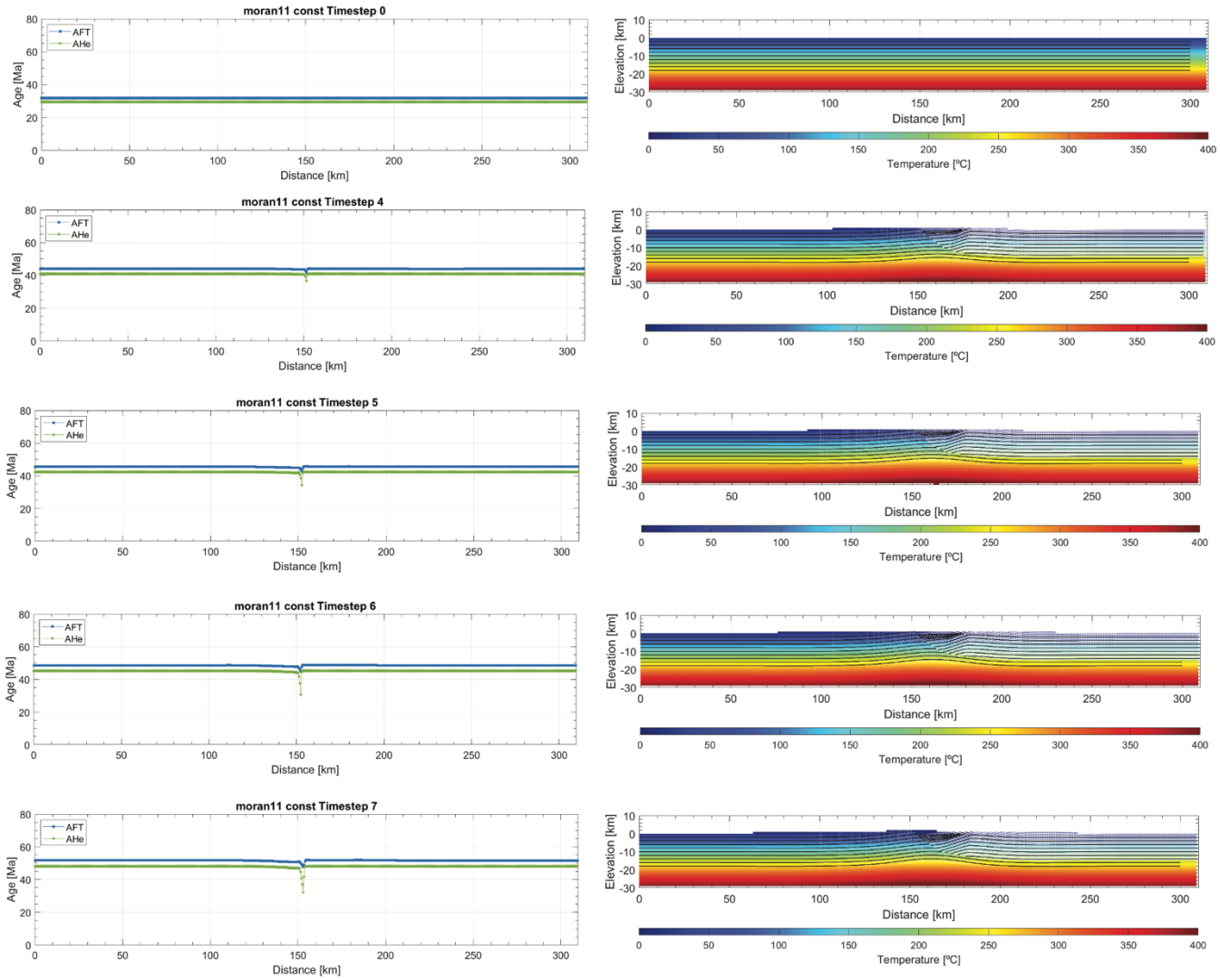

Thermal-kinematic model 11 evaluated in Pecube for a constant slip rate with fault slip onset at 19 Ma for D_{max} =13 km.

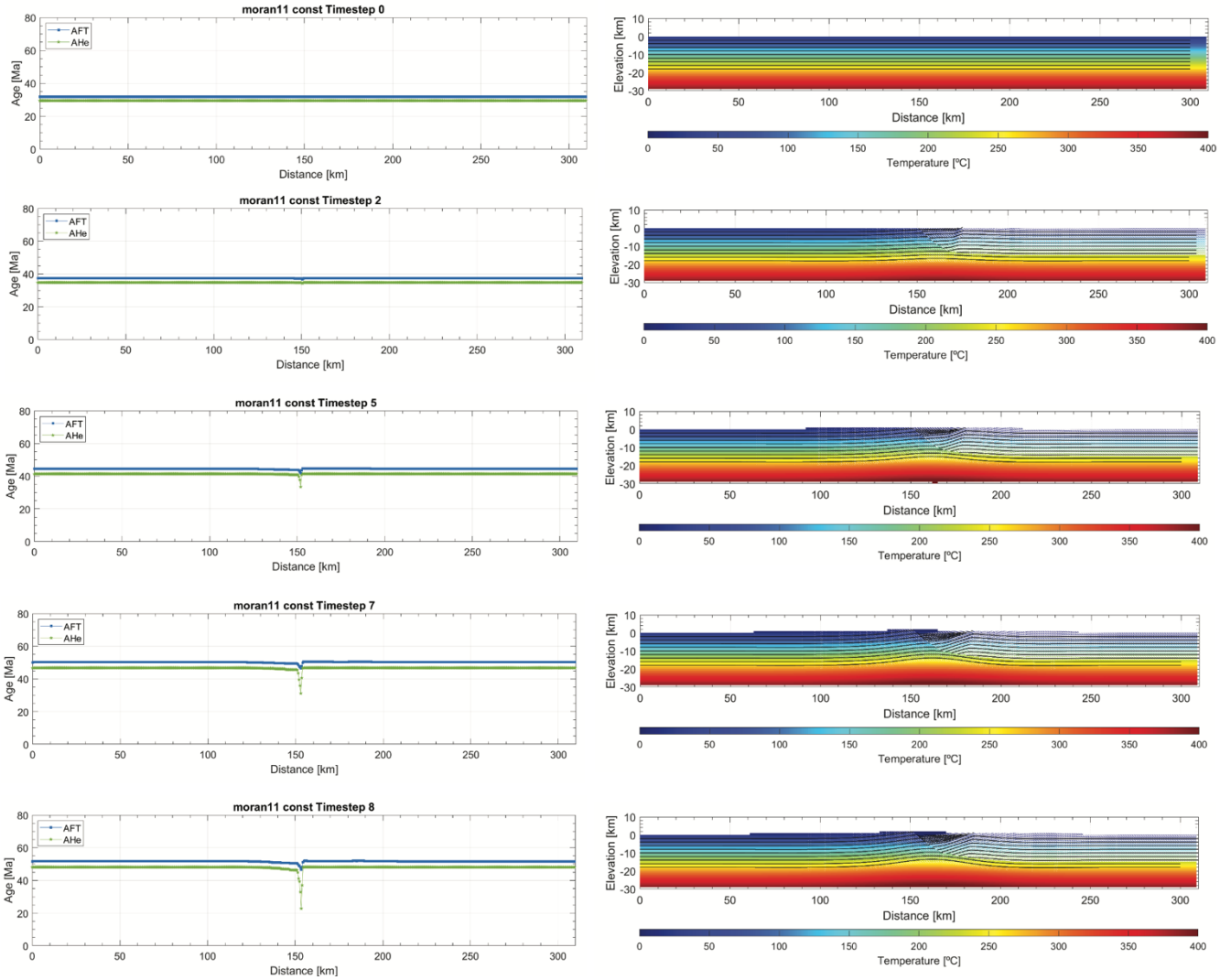

Thermal-kinematic model 11 evaluated in Pecube for a constant slip rate with fault slip onset at 19 Ma for D_{max} =14 km.

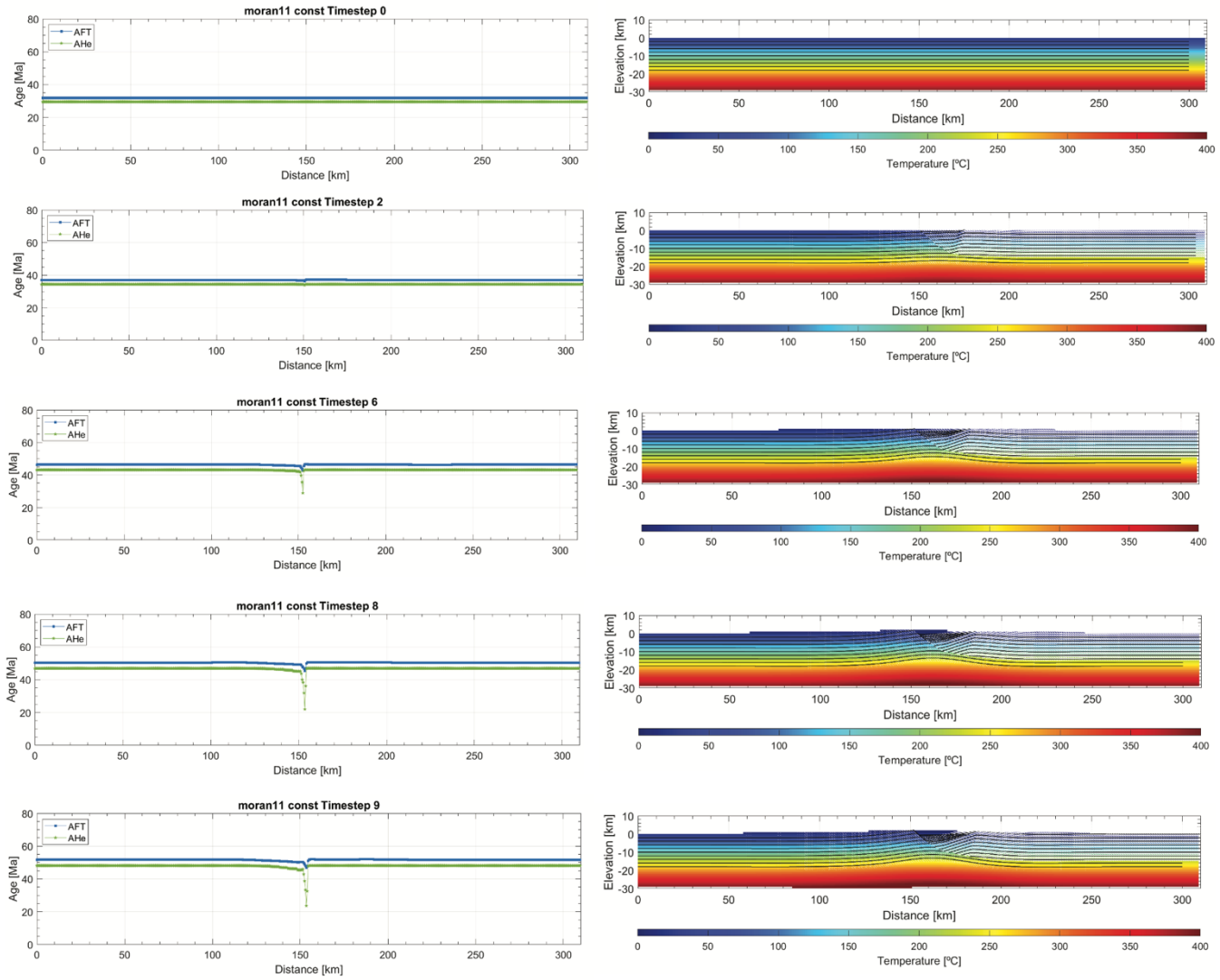

Thermal-kinematic model 11 evaluated in Pecube for a constant slip rate with fault slip onset at 19 Ma for D_{max} =15 km.

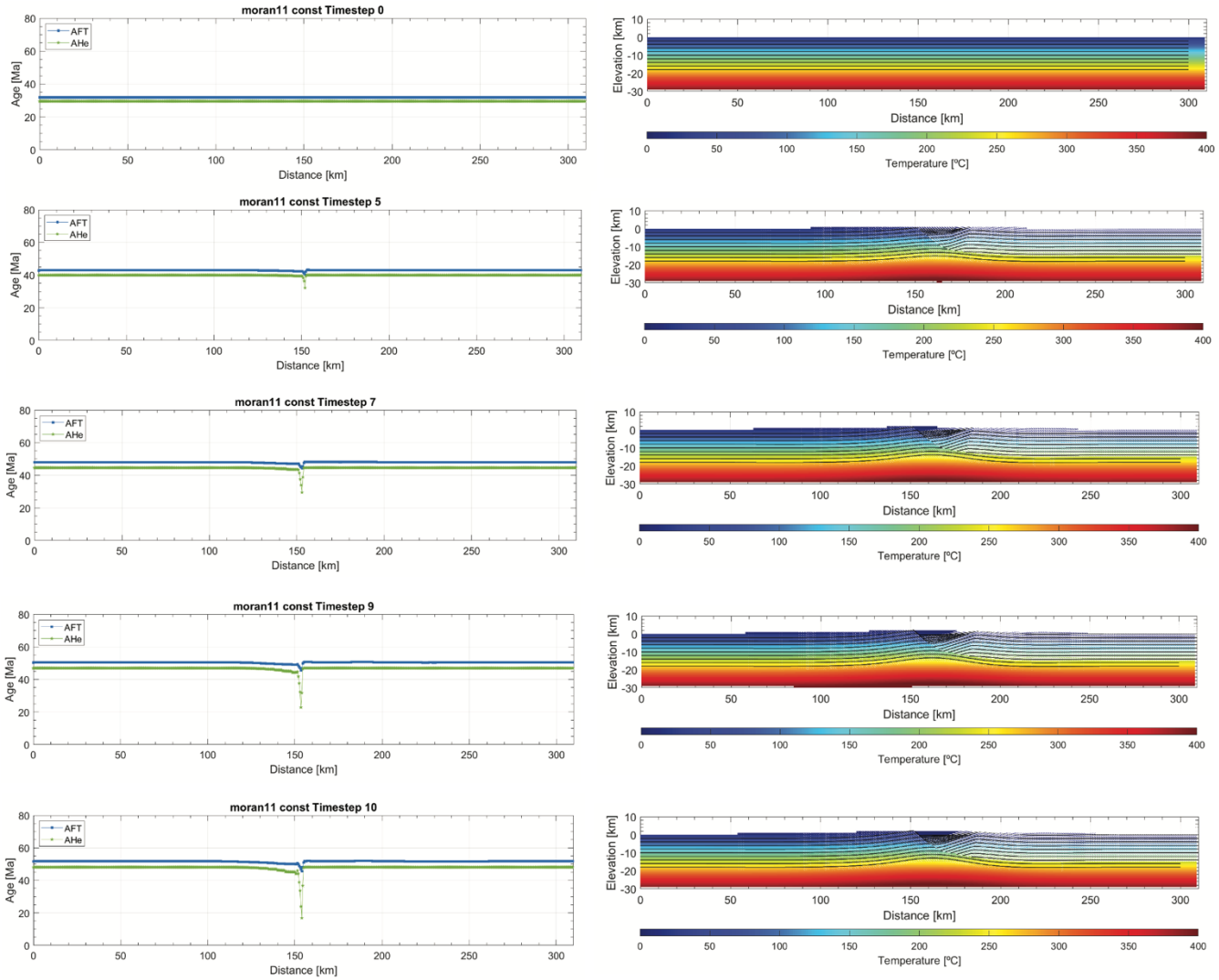

Thermal-kinematic model 11 evaluated in Pecube for a constant slip rate with fault slip onset at 19 Ma for D_{max} =16 km.

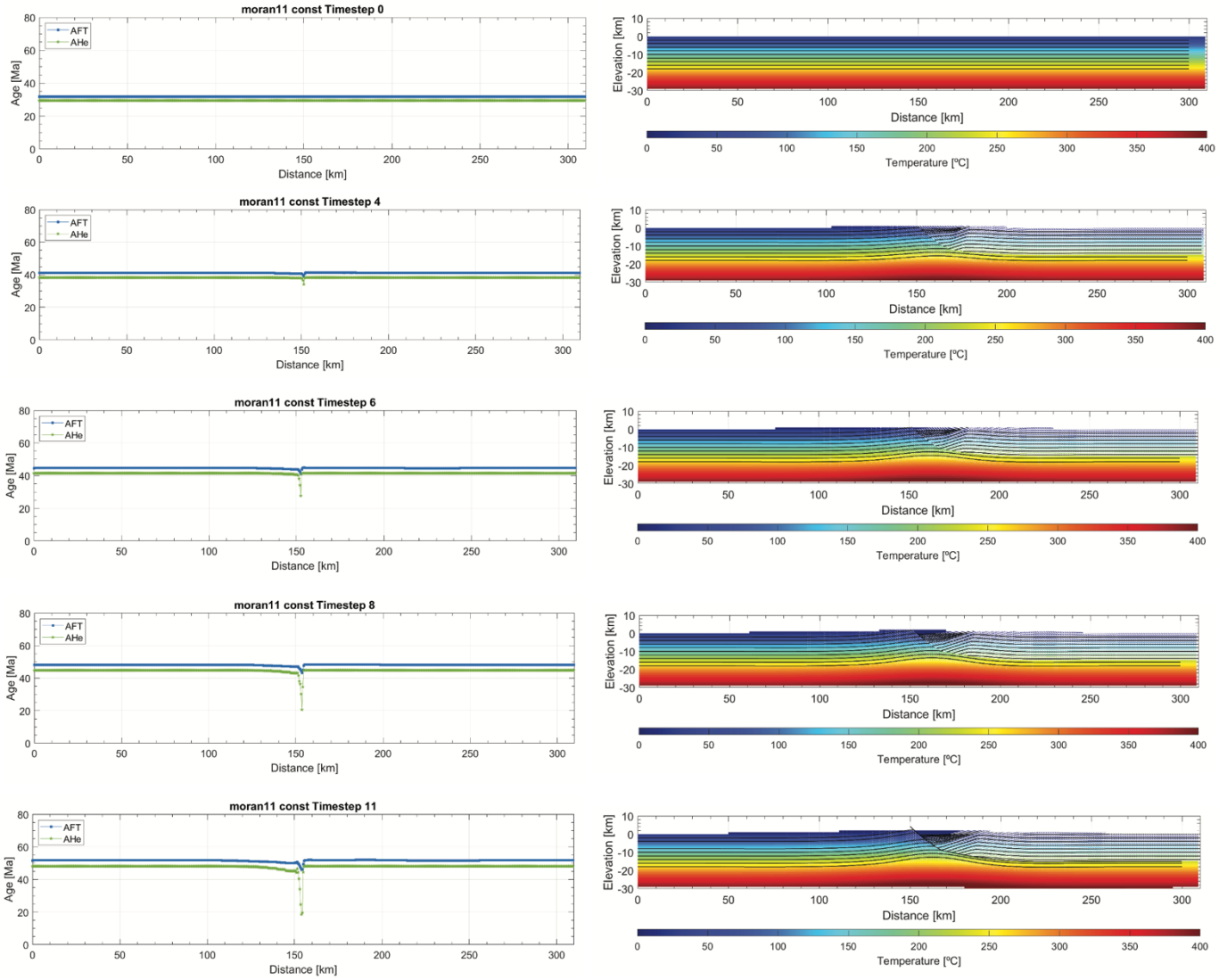

Thermal-kinematic model 11 evaluated in Pecube for a constant slip rate with fault slip onset at 19 Ma for D_{max} =17 km.

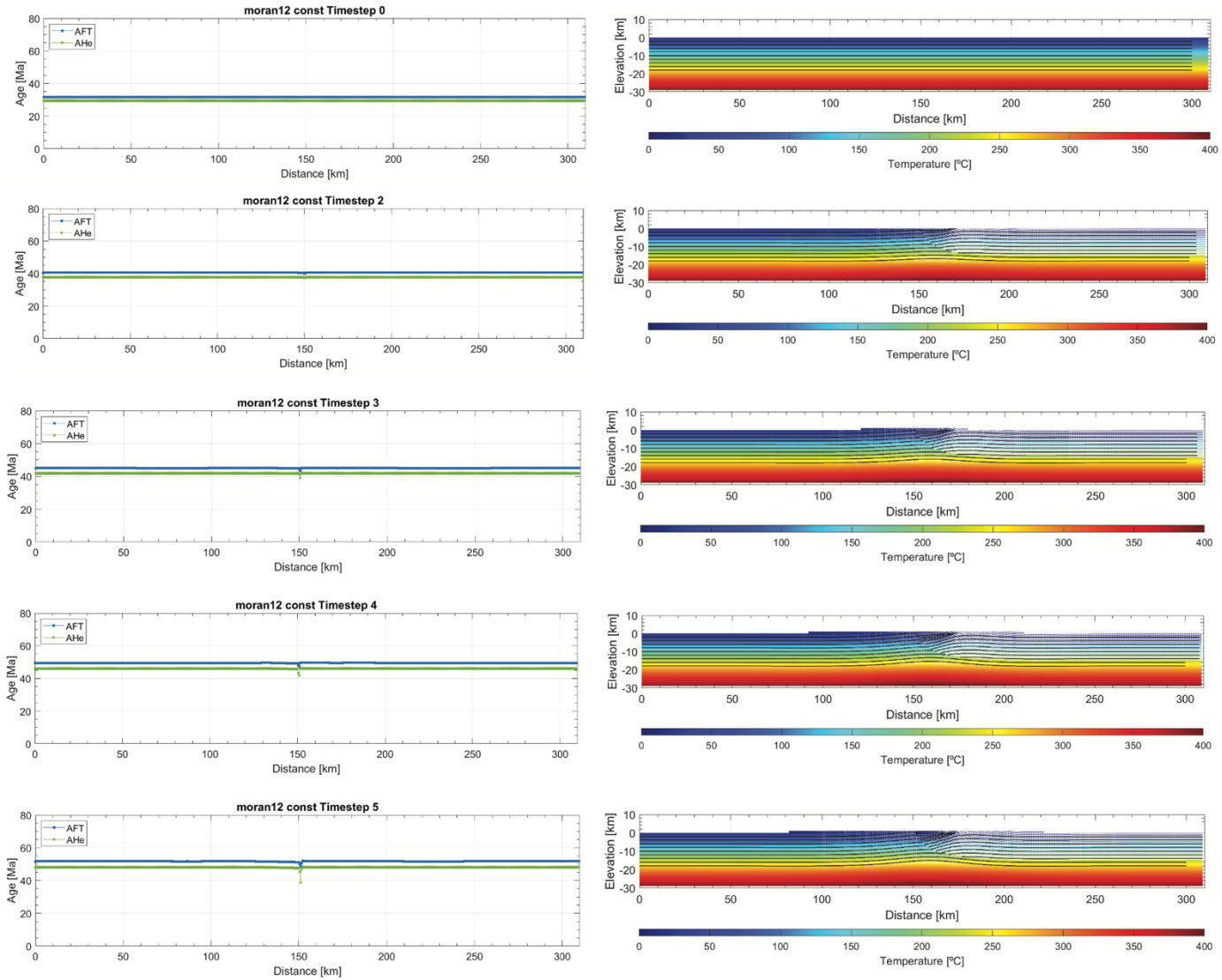

Thermal-kinematic model 12 evaluated in Pecube for a constant slip rate with fault slip onset at 19 Ma for D_{max} =9 km.

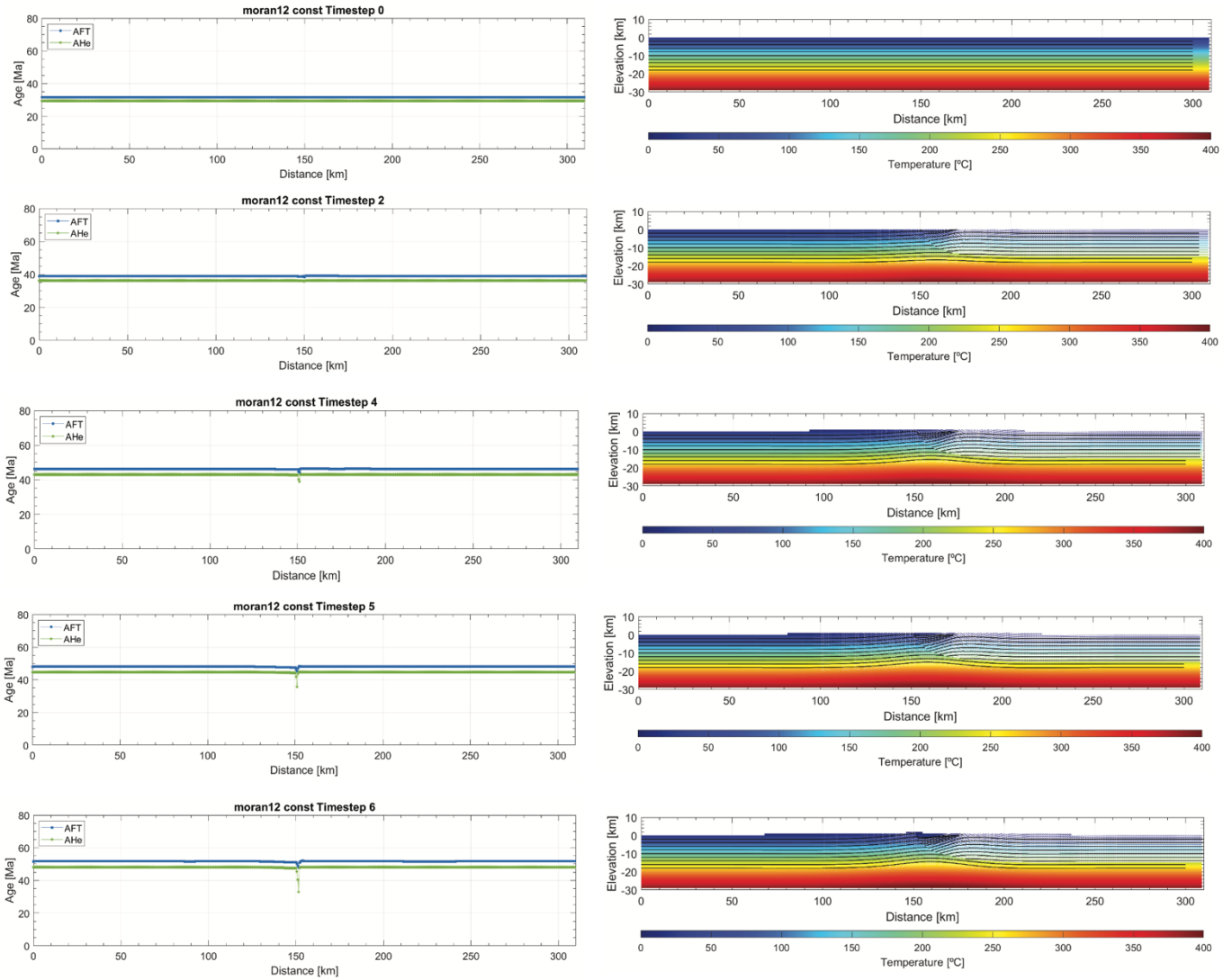

Thermal-kinematic model 12 evaluated in Pecube for a constant slip rate with fault slip onset at 19 Ma for D_{max} =11 km.

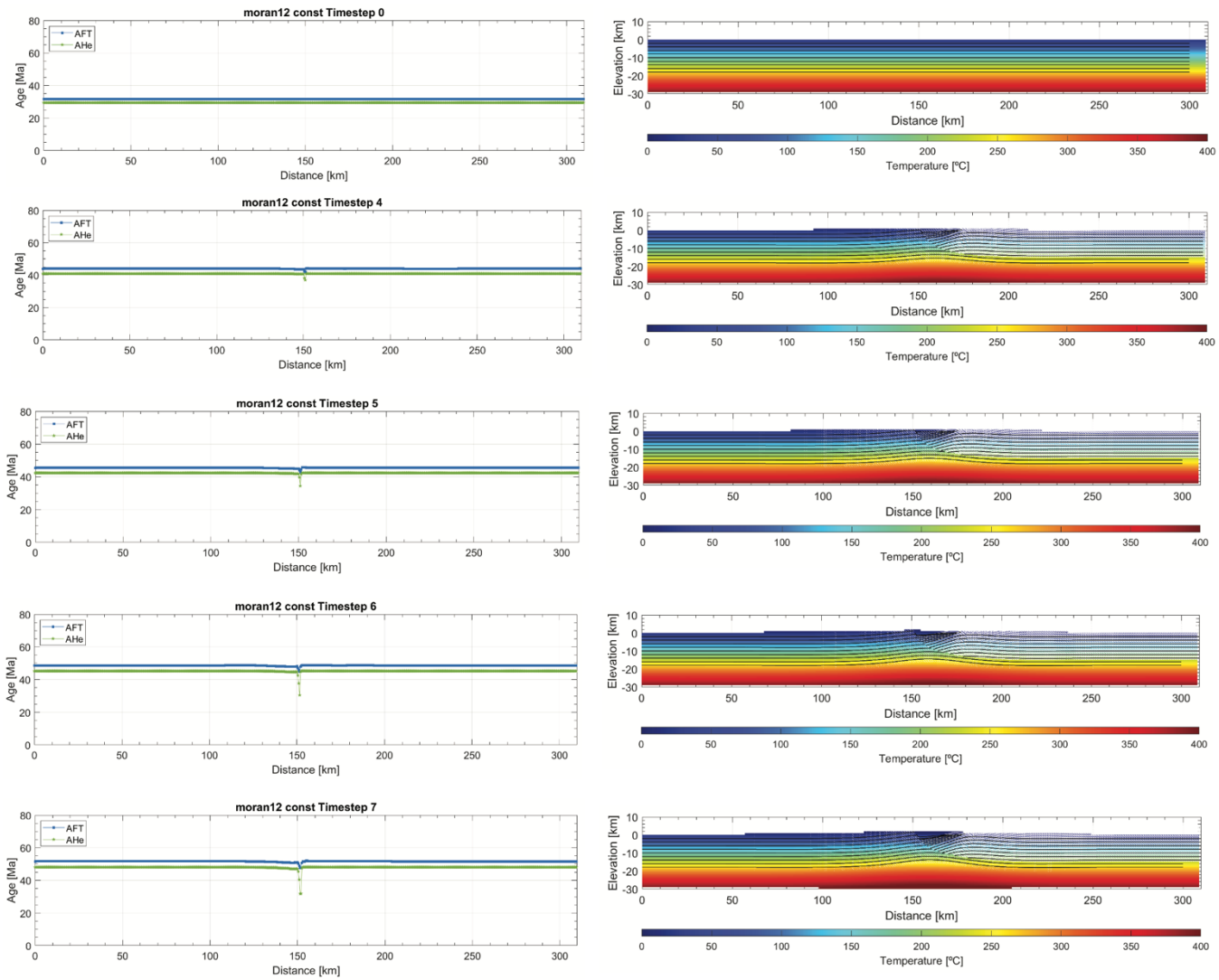

Thermal-kinematic model 12 evaluated in Pecube for a constant slip rate with fault slip onset at 19 Ma for D_{max} =13 km.

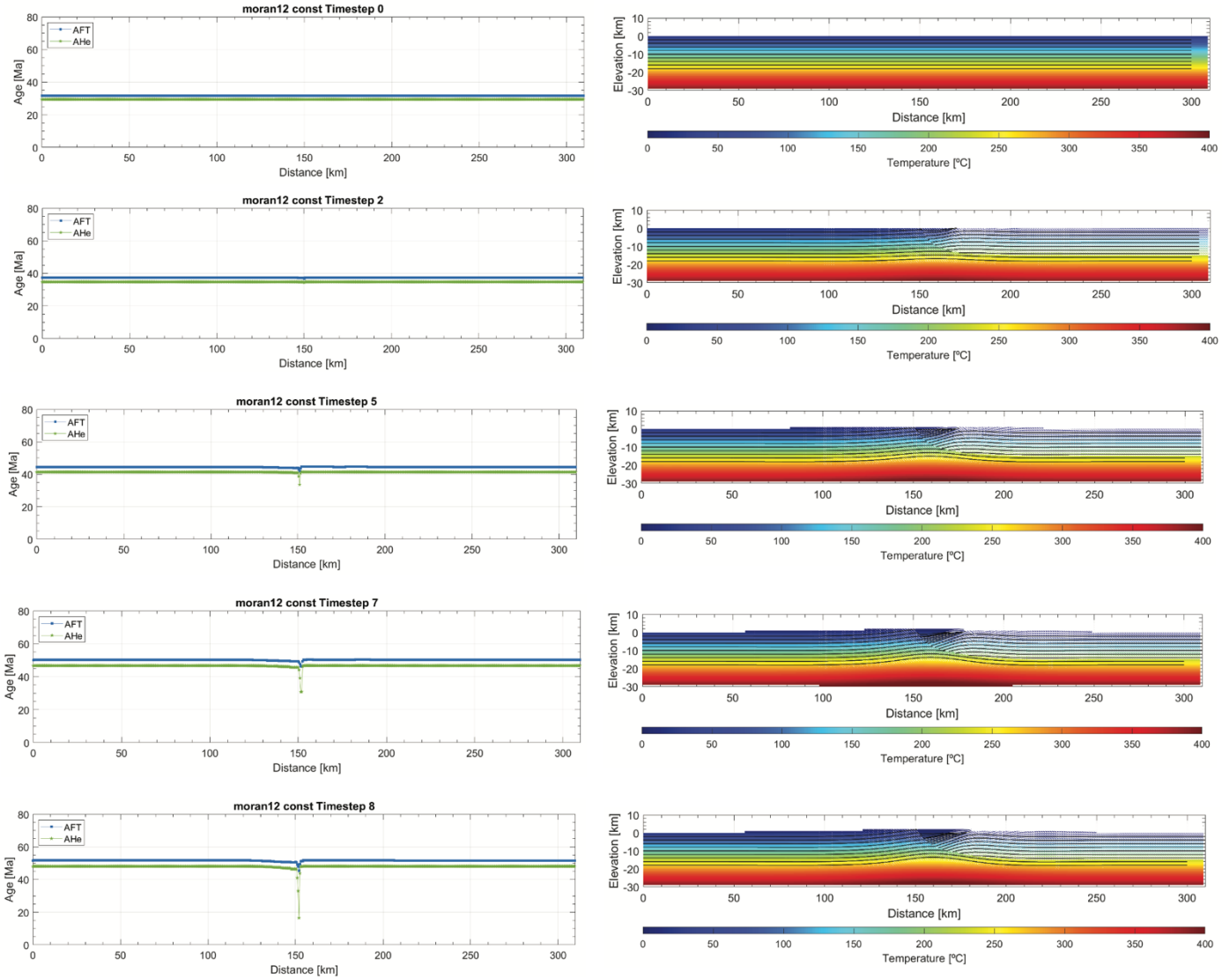

Thermal-kinematic model 12 evaluated in Pecube for a constant slip rate with fault slip onset at 19 Ma for D_{max} =14 km.

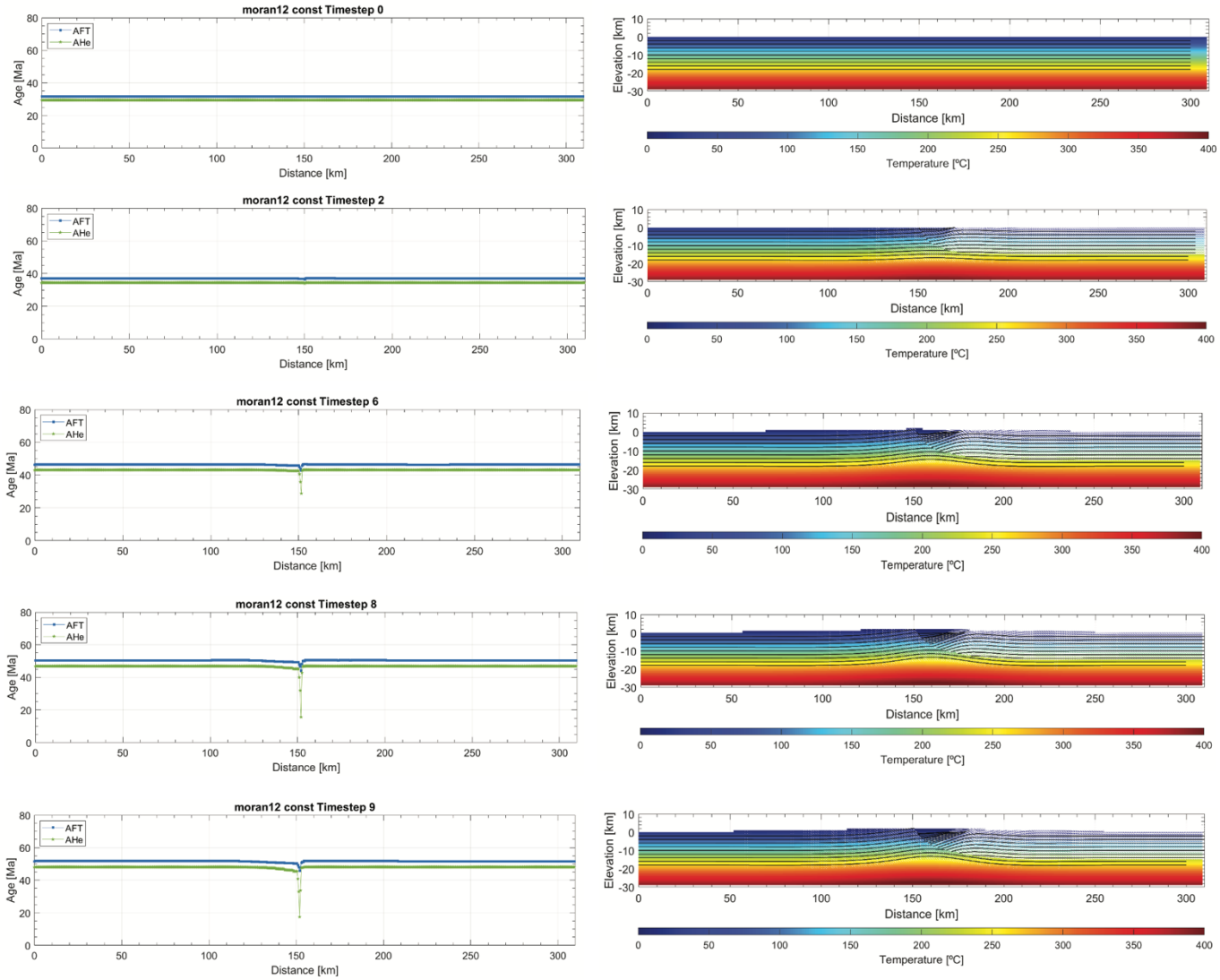

Thermal-kinematic model 12 evaluated in Pecube for a constant slip rate with fault slip onset at 19 Ma for D_{max} =15 km.

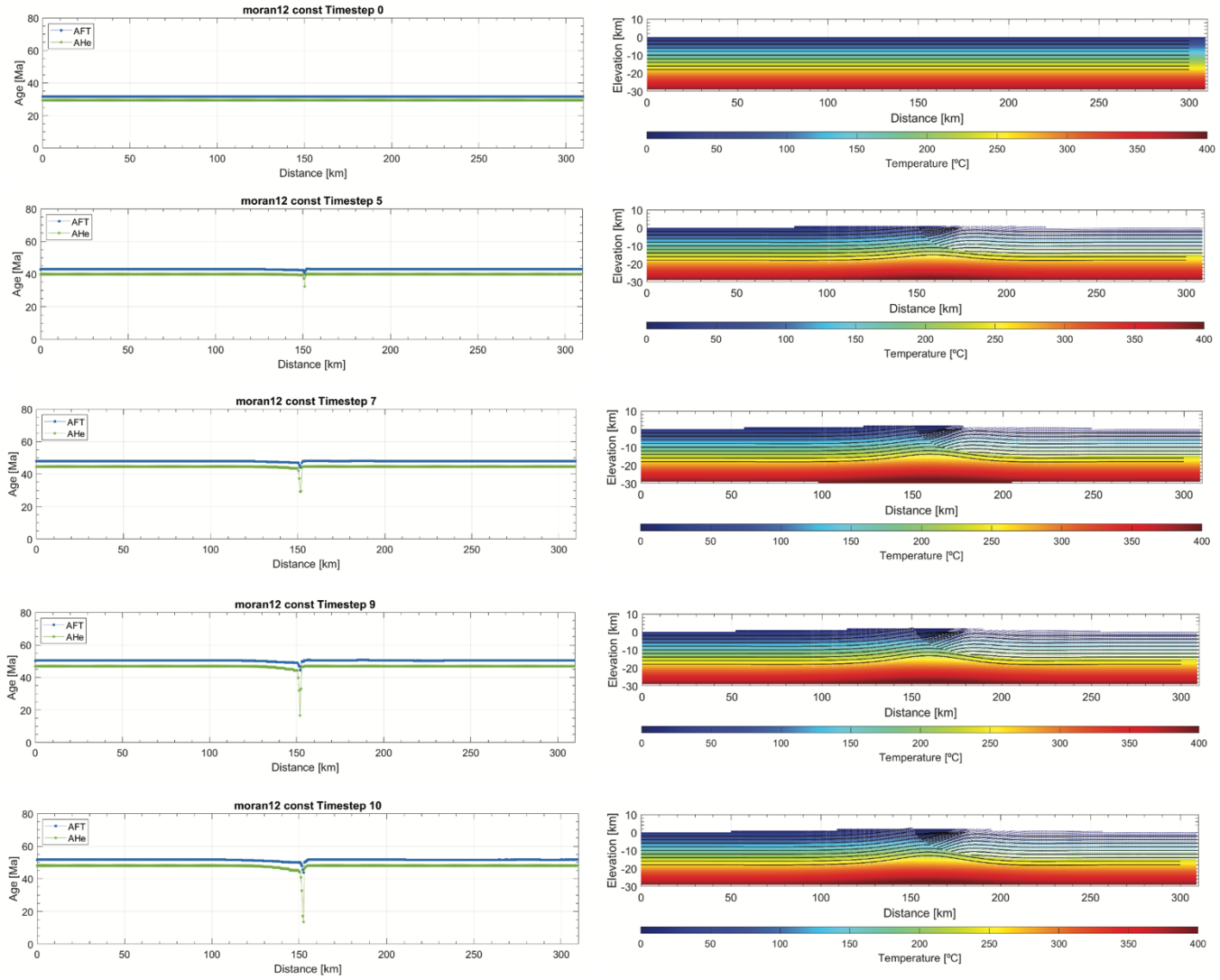

Thermal-kinematic model 12 evaluated in Pecube for a constant slip rate with fault slip onset at 19 Ma for D_{max} =16 km.

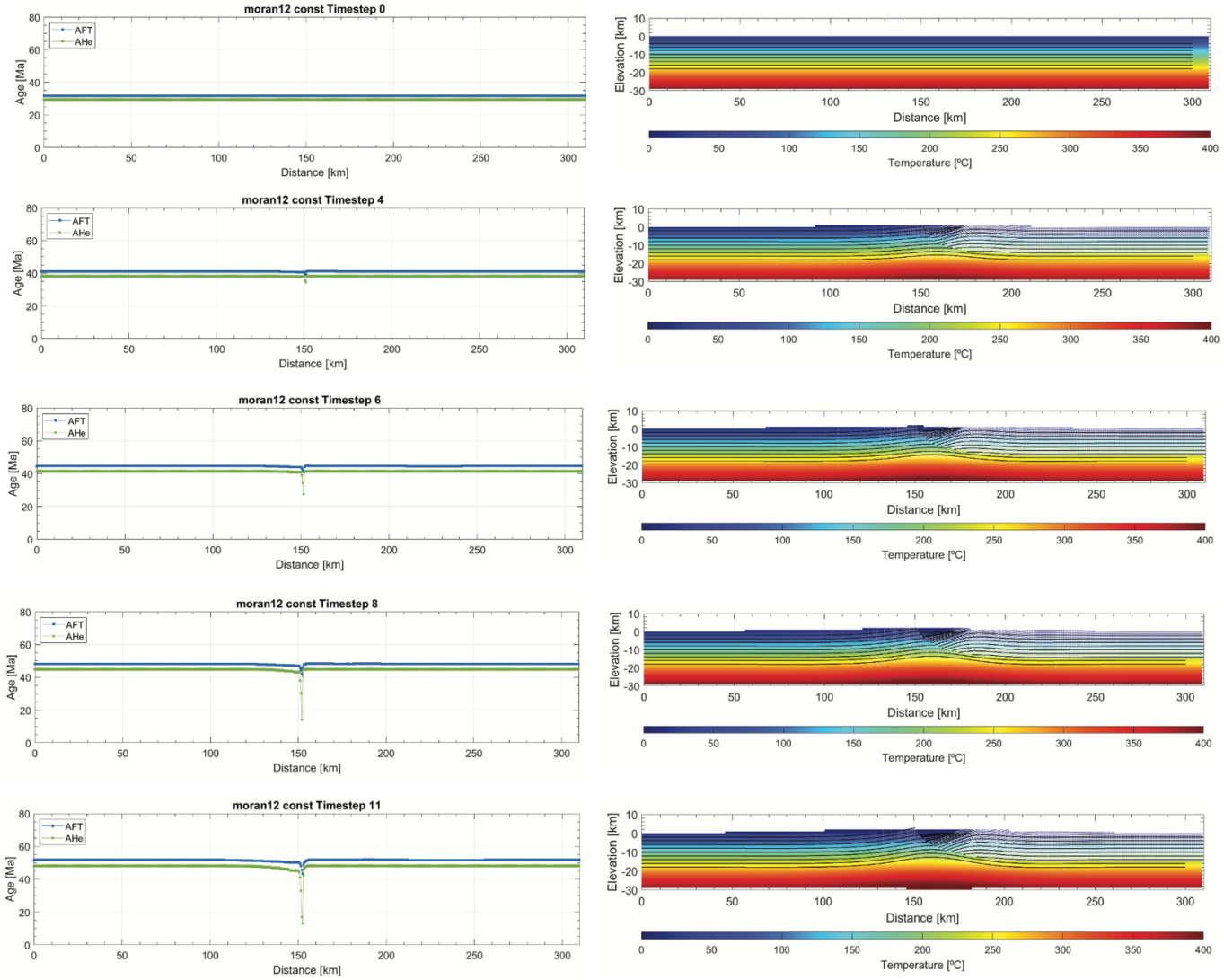

Thermal-kinematic model 12 evaluated in Pecube for a constant slip rate with fault slip onset at 19 Ma for D_{max} =17 km.

REFERENCES CITED

Anders, M.H. and Sleep, N.H., 1992, Magmatism and extension: The thermal and mechanical effects of the Yellowstone hotspot: Journal of Geophysical Research: Solid Earth, v. 97, no. B11, p. 15379-15393.

Anders, M.H., Geissman, J.W., Piety, L.A. and Sullivan, J.T., 1989, Parabolic distribution of circumeastern Snake River Plain seismicity and latest Quaternary faulting: Migratory pattern and association with the Yellowstone hotspot. Journal of Geophysical Research: Solid Earth, v. 94, no. B2, p. 1589-1621.

Arabasz, W.J., Smith, R.B. and Richins, W.D., 1980, Earthquake studies along the Wasatch Front, Utah: Network monitoring, seismicity, and seismic hazards: Bulletin of the Seismological Society of America, v. 70, no. 5, p. 1479-1499.

Armstrong, P.A., T.A. Ehlers, D.S. Chapman, K.A. Farley and P.J. Kamp., 2003, Exhumation of the central Wasatch Mountains, Utah: 1. Patterns and timing deduced from low-temperature thermochronology data: Journal of Geophysical Research, v. 108, no. B3, doi:10.1029/2001JB001708.

Barnosky, A. D., 1984, The Colter formation; evidence for Miocene volcanism in Jackson Hole, Teton County, Wyoming: Earth Science Bulletin, v. 17, no. 1, p. 49 – 97.

Beaumont, C., 1979, On rheological zonation of the lithosphere during flexure: Tectonophysics, v. 59, p. 347-365.

Behrendt, J.C., Tibbets, B.L., Bonini, W.E., Lavin, P.M., Love, J.D., and Reed, J.C. Jr., 1968, A geophysical study in Grand Teton National Park and vicinity, Teton County, Wyoming, with sections on stratigraphy and structure and Precambrian rocks: U.S. Geological Survey Professional Paper, 516-E.

Blackwell, D. D., Richards, M. C., 2004, Geothermal Map of North America. American Association of Petroleum Geologists, 1 sheet, scale 1:,500,000.

Blackwell, D.D., S. Kelley, and J.L. Steele, 1992, Heat flow modeling of the Snake River Plain, Idaho, U.S. Department of Energy Report for contract DE-ACO7-761D01570, p. 109.

Braun, J., 2002, Quantifying the effect of recent relief changes on age–elevation relationships: Earth and Planetary Science Letters, v. 200, no. 3-4, p. 331-343.

Braun, J., 2003, Pecube: A new finite-element code to solve the 3D heat transport equation including the effects of a time-varying, finite amplitude surface topography: Computers & Geosciences, v. 29, no. 6, p. 787-794.

Braun, J., Van Der Beek, P., Valla, P., Robert, X., Herman, F., Glotzbach, C., Pedersen, V., Perry, C., Simon-Labric, T. and Prigent, C., 2012, Quantifying rates of landscape evolution and tectonic processes by thermochronology and numerical modeling of crustal heat transport using PECUBE: Tectonophysics, v. 524-525, pp.1-28, doi.org/10.1016/j.tecto.2011.12.035.

Brott, C.A., Blackwell, D.D. and Ziagos, J.P., 1981, Thermal and tectonic implications of heat flow in the eastern Snake River Plain, Idaho: Journal of Geophysical Research: Solid Earth, v. 86, no. B12, p.11709-11734.

Brown, S. J., Thigpen, J. R., Spotila, J. A., Krugh, W. C., Tranel, L. M., and Orme, D. A., 2017, Onset timing and slip history of the Teton fault, Wyoming: A multidisciplinary reevaluation: Tectonics, v. 36, p. 2669– 2692. https://doi.org/10.1002/2016TC004462.

Brown, S.J., 2010, Integrating apatite (U-Th)/He and fission track dating for a comprehensive thermochronological analysis: refining the uplift history of the Teton Range [Master's Thesis, Virginia Tech].

Buck, W.R., Martinez, F., Steckler, M.S. and Cochran, J.R., 1988, Thermal consequences of lithospheric extension: pure and simple: Tectonics, v. 7, no. 2, p. 213-234.

Byrd, J. O. D., 1991, Paleoseismicity of the southern section of the Teton fault, Wyoming: Geological Society of America Abstracts with Programs, v. 23, no. A481.

Byrd, J. O. D., R. B. Smith and J W. Geissman, 1994, The Teton fault, Wyoming: topographic signature, neotectonics and mechanism of deformation: Journal of Geophysical Research, v. 99, p. 20095-20122.

Byrd, J.O.D., 1995, Neotectonics of the Teton Fault, Wyoming [Ph.D. dissertation, University of Utah], 214 p.

Byrd, J.O.D., and R.B. Smith, 1990, Dating recent faulting and estimates of slip rates for the southern segment ofthe Teton fault, Wyoming, Geological Society of America Abstracts with Programs, v. 22, no. 6.

Byrd, J.O.D., Smith, R.B., and Geissman, J.W., 1994, The Teton fault, Wyoming: Topographic signature, neotectonics, and mechanisms of deformation: Journal of Geophysical Research, v. 99, no. B10, p. 20,095–20,122.

Chávez-Pérez, Sergio, John N. Louie, and Sathish K. Pullammanappallil., 1998, "Seismic depth imaging of normal faulting in the southern Death Valley basin." Geophysics. v. 63, no. 1, p. 223-230.

Crone, A.J., Machette, M.N., Bonilla, M.G., Lienkaemper, J.J., Pierce, K.L., Scott, W.E. and Bucknam, R.C., 1987, Surface faulting accompanying the Borah Peak earthquake and segmentation of the Lost River fault, central Idaho: Bulletin of the Seismological Society of America, v. 77, no. 3, p. 739-770.

Crowley, P. D., Reiners, P. W., Reuter, J. M., and Kaye, G. D., 2002, Laramide exhumation of the Bighorn Mountains, Wyoming: an apatite (U-Th)/He thermochronology study: Geology, v. 30, no. 1, p. 27-30.

Decker, E.R., Baker, K.R., Bucher, G.J. and Heasler, H.P., 1980, Preliminary heat flow and radioactivity studies in Wyoming: Journal of Geophysical Research: Solid Earth, v. 85, no. B1, p. 311-321.

Densmore, A. L., Dawers, N. H., Gupta, S., and Guidon, R., 2005, What sets topographic relief in extensional footwalls?: Geology, v. 33, no. 6, p. 453– 456, doi.org/10.1130/G21440.1.

Dirks, R.A., 1982, The climate of Yellowstone and Grand Teton National Parks, US Department of the Interior, National Park Service Occasional Paper, no. 6, p. 1-26.

Doser, D. I., 1985, Source parameters and faulting processes of the 1959 Hebgen Lake, Montana, earthquake sequence: Journal of Geophysical Research, v. 90, p. 4537–4555.

Doser, D.I. and Smith, R.B., 1983, Seismicity of the Teton-Southern Yellowstone region, Wyoming: Bulletin of the Seismological Society of America, v. 73, p. 1369-1394.

Doser, D.I. and Smith, R.B., 1985, Source parameters of the 28 October 1983 Borah Peak, Idaho, earthquake from body wave analysis: Bulletin of the Seismological Society of America, v. 75, no. 4, p.1041-1051.

DuRoss, C.B., Gold, R.D., Briggs, R.W., Delano, J.E., Ostenaa, D.A., Zellman, M.S., Cholewinski, N., Wittke, S.J. and Mahan, S.A., 2020, Holocene earthquake history and slip rate of the southern Teton fault, Wyoming, USA. Bulletin, v. 132, no. 7-8, p. 1566-1586.

Egan, S.S., Buddin, T.S., Kane, S.J. and Williams, G.D., 1997, Three-dimensional modelling and visualization in structural geology: new techniques for the restoration and balancing of volumes: In Proceedings of the 1996 Geoscience

Information Group Conference on Geological Visualization: Electronic Geology Special Volume, v. 1, p. 67-82.

Ehlers T.A., 2005, Crustal thermal processes and the interpretation of thermochronometer data: Reviews in Mineralogy and Geochemistry, v. 58, no.1, p. 315-350.

Ehlers, T. A., and Farley, K. A., 2003, Apatite (U–Th)/He thermochronometry: methods and applications to problems in tectonic and surface processes: Earth and Planetary Science Letters, v. 206, no. 1-2, p. 1-14.

Ehlers, T. A., Armstrong, P. A., and Chapman, D. S., 2001, Normal fault thermal regimes and the interpretation of low-temperature thermochronometers: Physics of the Earth and Planetary Interiors, v. 126, no. 3-4, p. 179– 194, doi.org/10.1016/S0031-9201(01)00254-0

Ehlers, T. A., Willett, S. D., Armstrong, P. A., and Chapman, D. S., 2003, Exhumation of the central Wasatch Mountains, Utah: 2. Thermokinematic model of exhumation, erosion, and thermochronometer interpretation: Journal of Geophysical Research: Solid Earth, v. 108, no. B3.

Farley, K.A., 2000, Helium diffusion from apatite: general behavior as illustrated by Durango fluorapatite: Journal of Geophysical Research, v. 105, p. 2903-2914.

Fitzgerald, P.G., Fryxell, J.E., and Wernicke, B.P., 1991, Miocene crustal extension and uplift in southeastern Nevada: Constraints from apatite fission track analysis: Geology, v. 19, p. 1013–1016, doi: 10.1130/0091-7613(1991)019<1013:MCEAUI>2.3.CO;2.

Fitzgerald, P.G., R.B. Sorkhabi, T.F. Redfield and E. Stump, 1995, Uplift and exhumation of the central Alaska Range: A case study in the use of apatite fission track thermochronology to determine absolute uplift parameters: Journal of Geophysical Research, v. 100, no. B10, p. 20, 175- 20, 191.

Foster, D.A., Gleadow, A.J.W., Reynolds, S.J., and Fitzgerald, P.G., 1993, Denudation of metamorphic core complexes and the reconstruction of the Transition Zone, west-central Arizona; constraints from apatite fission track thermochronology: Journal of Geophysical Research, v. 98, p. 2167-2185.

Gans, P. and Miller, E.L., 1984, Geologic and geophysical constraints on the geometry of crustal extension in the east Basin and Range Province. Geological Society of America Abstracts and Program, v. 16, p. 515.

Gilbert, J.D., Ostenaa, D., and Wood, C., 1983, Seismotectonic study Jackson Lake Dam and Reservoir, Minidoka Project, Idaho–Wyoming: Bureau of Reclamation Seismotectonic Report, vol. 83–8, p. 123.

Haenel R., Rybach L., and Stegena L., 1988, Handbook of Terrestrial Heat-Flow Density Determination: with Guidelines and Recommendations of the International Heat Flow Commission, Kluwer academic publishers, Dordrecht, p. 486.

Hampel, A., Hetzel, R., and Densmore, A.L., 2007, Postglacial slip-rate increase on the Teton normal fault, northern Basin and Range Province, caused by melting of the Yellowstone ice cap and deglaciation of the Teton Range?: Geology, v. 35, no. 12, p. 1107-1110.

Heasler, H.P., 1987, Geothermal modeling of Jackson Hole, Teton County Wyoming, No. DOE/ID/12607-T1, Wyoming University, Laramie (USA). Department of Geology and Geophysics.

Hoar, R.M., 2019, Refining the Onset Timing and Slip History Along the Northern Part of the Teton Fault. (Master's Thesis, University of Kentucky).

Jackson, J. and McKenzie, D., 1983, The geometrical evolution of normal fault systems. Journal of Structural Geology, v. 5, no. 5, p. 471-482.

Jaeger, J.C. and Carslaw, H.S., 1959, Conduction of Heat in solids, second edition, Clarendon Press, Oxford, p. 47.

Kane, S.J., Williams, G.D., Buddin, T.S., Egan, S.S. and Hodgetts, D., 1997, Flexural-slip based restoration in 3D, a new approach, AAPG Annual Convention Official Program, A58.

Lavin, P.M. and Bonini, W.E., 1957, Detailed gravity measurements in the Teton Range and Jackson Hole, Wyoming (Abstract): Geological Society of America Bulletin, v. 68, p.1760.

Leopold, E. B., Liu, G., Love, J. D., and Love, D. W., 2007, Plio-Pleistocene climatic transition and the lifting of the Teton Range, Wyoming: Quaternary Research, v. 67, no. 01, p. 1– 11, doi.org/10.1016/j.yqres.2006.10.006.

Love J.D., Reed J.C., Jr., Christiansen R.L. and Stacy J.R., 1973, Geologic block diagram and tectonic history of the Teton Range, Wyoming-Idaho, US Geological Survev. Misc. Geol. Invest. Map 1-730.

Love J.D., 1987, Teton mountain front, Wyoming, Geological Society of America, Centen. Field Guide, Rocky Mountain Section, p. 173-178.

Love, J.D. and Reed, J.C., 1971, Creation of the Teton landscape: Moose, Wyoming, Grand Teton Natural History Association, 120 p.

Love, J.D., 1977, Summary of upper Cretaceous and Cenozoic stratigraphy, and of tectonic and glacial events in Jackson Hole, northwest Wyoming: Wyoming Geological Association Guidebook, 29th Annual Field Conference, p. 585-593.

Love, J.D., Reed, J.C., and Christiansen A.C., 1992, Geologic Map of Grand Teton National Park, Teton County, Wyoming. United States Geological Survey, Miscellaneous Investigations Series, MAP I-2031.

Love, J.D., Reed, J.C., and Pierce, K.L., 2003, Creation of the Teton landscape; a geologic chronicle of Jackson hole and the Teton range: Grand Teton Natural History Association, Moose, Wyoming, USA. 2nd ed.

Lowry, A. R., and R. B. Smith, 1994, Flexural rigidity of the Basin and Range-Colorado Plateau-Rocky Mountain transition from coherence analysis of gravity and topography: Journal of Geophysical Research, v. 99, p. 20, 123 – 20, 140, doi: 10.1029/94JB00960.

Masbruch, M.D., Chapman, D.S. and Solomon, D.K., 2012, Air, ground, and groundwater recharge temperatures in an alpine setting, Brighton Basin, Utah: Water Resources Research, v. 48, no. 10.

McQuarrie, N. and Ehlers, T.A., 2015, Influence of thrust belt geometry and shortening rate on thermochronometer cooling ages: Insights from thermokinematic and erosion modeling of the Bhutan Himalaya: Tectonics, v. 34, no. 6, p. 1055-1079.

McQuarrie, N. and Rodgers, D.W., 1998, Subsidence of a volcanic basin by flexure and lower crustal flow: The eastern Snake River Plain, Idaho. Tectonics, v. 17, no. 2, p. 203-220.

Miller, E.L., Dumitru, T.A., Brown, R.W., and Gans, P.B., 1999, Rapid Miocene slip on the Snake Range–Deep Creek Range fault system, east-central Nevada: Geological Society of America Bulletin, v. 111, no. 6, p. 886–905, doi: 10.1130/0016-7606(1999)111< 0886:RMSOTS>2.3.CO;2.

Mohapatra, G.K. and Johnson, R.A., 1998, Localization of listric faults at thrust fault ramps beneath the Great Salt Lake Basin, Utah: Evidence from seismic imaging and finite element modeling: Journal of Geophysical Research: Solid Earth, v. 103, no. B5, p. 10047-10063.

Morgan, L. A., and McIntosh, W. C., 2005, Timing and development of the Heise volcanic field, Snake River Plain, Idaho, western USA: Geological Society of America Bulletin, v. 117, no. 3, p. 288– 306, doi.org/10.1130/B25519.1.

Myers, W. B., and Hamilton, W., 1964, Deformation accompanying the Hebgen Lake earthquake of August 17, 1959, U.S. Geological Survey Professional Paper 435, p. 55-98.

Pérez-Peña, J.V., Al-Awabdeh, M., Azañón, J.M., Galve, J.P., Booth-Rea, G. And Notti, D., 2017, Swathprofiler and NProfiler: Two new ArcGIS Add-ins for the automatic extraction of swath and normalized river profiles: Computers & Geosciences, v. 104, p.135-150.

Pierce, K.L., and Licciardi, J.M., 2018, History and dynamics of the Greater Yellowstone Glacial System during the last two glaciations: Quaternary Science Reviews, v. 200, p. 1–33, doi: 10.1016/j.quascirev.2018.08.027.

Pierce, K. L., and Morgan, L. A., 2009, Is the track of the Yellowstone hot spot driven by a deep mantle plume? Review of volcanism, faulting, and uplift in light of new data: Journal of Volcanology and Geothermal Research, v. 188, no. 1-3, p. 1– 25, doi.org/10.1016/j.jvolgeores.2009.07.009

Pierce, K.L. and Morgan, L.A., 1992, The track of the Yellowstone hot spot: Volcanism, faulting, and uplift. Regional geology of eastern Idaho and western Wyoming: Geological Society of America Memoir, v. 179, no. 322, p. 1-53.

Rahn, M. K., & Grasemann, B., 1999, Fission track and numerical thermal modeling of differential exhumation of the Glarus thrust plane (Switzerland). Earth and Planetary Science Letters, v. 169, no. 3-4, p. 245-259.

Reiners, P. W., Brady, R., Farley, K. A., Fryxell, J. E., Wernicke, B., and Lux, D., 2000, Helium and argon thermochronometry of the Gold Butte block, south Virgin Mountains, Nevada. Earth and Planetary Science Letters, v. 178, no. 3-4, p. 315–326, doi.org/10.1016/S0012-821X(00)00080-7.

Richins, W.D., Pechmann, J.C., Smith, R.B., Langer, C.J., Goter, S.K., Zollweg, J.E. and King, J.J., 1987, The 1983 Borah Peak, Idaho, earthquake and its aftershocks: Bulletin of the Seismological Society of America, v. 77, no. 3, p. 694-723.

Roberts, S.V., and Burbank, D.W., 1993, Uplift and thermal history of the Teton Range (northwestern Wyoming) defined by apatite fission-track dating: Earth and Planetary Science Letters, v. 118, p. 295-309.

Shuey, R.T., Ugland, R.O. and Schmit, C.R., 1977, Magnetic properties and secular variation in cores from Yellowstone and Jackson Lakes, Wyoming: Journal of Geophysical Research, v. 82, no. 26, p. 3739-3746.

Smith, R. B., Byrd, J. O. D., & Susong, D. D., 1990, Neotectonics and structural evolution of the Teton fault. Geologic field tours of western Wyoming and parts of adjacent Idaho, Montana, and Utah: Geological Survey of Wyoming Public Information Circular, no. 29, p. 126–138.

Smith, R. B., Byrd, J.O.D., 1989, Earthquake Hazards of Grand Teton National Park emphasizing the Teton Fault: University of Wyoming National Park Service Research Center Annual Report, v. 13, no. 1, p. 140-146.

Smith, R. B., K. L. Pierce and R. J. Wold, 1993b, Seismic surveys and Quaternary history of Jackson Lake, Wyoming, in Snoke A.W., J. Steidtmann J.R., and Roberts S.M., "Geology of Wyoming": Geological Survey of Wyoming Memoir, No. 5, p. 668-693.

Smith, R.B. and Arabasz, W.J., 1991, Seismicity of the Intermountain seismic belt, in Slemmons, D.B., Engdahl, E.R., Zoback, M.D., and Blackwell, D.D., eds., Neotectonics of North America: Geological Society of America, North America Decade Map, v.1, p. 185-228.

Smith, R.B. and Braile, L.W., 1993, Topographic signature, space–time evolution, and physical properties of the Yellowstone–Snake River Plain volcanic system: the Yellowstone hotspot. In: Snoke, A.W., Steidtmann, J., Roberts, S.M. (Eds.), Geology of Wyoming: Geological Survey of Wyoming Memoir No. 5, p. 694–754.

Smith, R.B. and Bruhn, R.L., 1984, Intraplate extensional tectonics of the eastern Basin-Range: Inferences on structural style from seismic reflection data, regional tectonics, and thermal-mechanical models of brittle-ductile deformation: Journal of Geophysical Research: Solid Earth, v. 89, no. B7, p. 5733-5762.

Smith, R.B. and Sbar, M.L., 1974, Contemporary tectonics and seismicity of the western United States with emphasis on the Intermountain Seismic Belt: Geological Society of America Bulletin, v. 85, no.8 , p. 1205-1218.

Smith, R.B., 1988, Seismicity and earthquake hazards of the Borah Peak-Hebgen Lake-Yellowstone-Teton region – Implications for earthquakes in extensional and active volcanic regimes, Abstracts with Programs, Ann. Meeting, Geol. Soc. Amer., A12.

Smith, R.B., Byrd, J.O.D., Susong, D.D., 1993a, The Teton fault: seismotectonics, Quaternary history and earthquake hazards. In: Snoke, A.W., Steidtmann, J., Roberts, S.M. (Eds.), "Geology of Wyoming", Geological Survey of Wyoming Memoir No. 5, p. 628–667.

Smith, R.B., W.D. Richins, and D.I. Doser, 1985, The Borah Peak earthquake: Seismicity, faulting kinematics and tectonic mechanism, in Workshop XXVII on "Evaluation of Regional and Urban Earthquake Hazards and Risk in Utah", U.S. Geological Survey Open-File Report, v. 85-290, p. 236-263.

Stockli, D.F., 2005, Application of low-temperature thermochronometry to extensional tectonic settings: Reviews in Mineralogy and Geochemistry, v. 58, no. 1, p. 411-448.

Stockli, D.F., K.A. Farley and T.A. Dumitru., 2000, Calibration of the (U-Th)/He thermochronometer on an exhumed fault block, White Mountains, California: Geology, v. 28, p. 983- 986.

Stüwe, K., White, L., and Brown, R., 1994, The influence of eroding topography on steady-state isotherms. Application to fission track analysis: Earth and Planetary Science Letters, v. 124, no. 1-4, p. 63-74.

Susong, D.L., Smith, R.B. and Bruhn, R.L., 1987, Earthquake Hazards of the Grand Teton National Park Emphasizing the Teton Fault. University of Wyoming-National Park Service Research Center, Eleventh Annual Report.

Swallom, M., 2019, Determining Rates of Landscape Response to Tectonic Forcing Across a Range of Temporal Scales and Erosional Mechanisms: Teton Range, WY. (Master's Thesis, University of Kentucky).

Tesauro, M., Kaban, M.K. and Mooney, W.D., 2015, Variations of the lithospheric strength and elastic thickness in North America: Geochemistry, Geophysics, Geosystems, v. 16, no. 7, p. 2197-2220.

Thackray, G.D., and Staley, A.E., 2017, Systematic variation of Late Pleistocene fault scarp height in the Teton Range, Wyoming, USA: Variable fault slip rates or variable landform ages?: Geosphere, v. 13, no. 2, p. 287–300, doi:10.1130/GES01320.1.

Thompson, G. A., & Parsons, T., 2009, Can footwall unloading explain late Cenozoic uplift of the Sierra Nevada crest? International Geology Review, v. 51, no. 9-11, p. 986– 993. doi.org/10.1080/00206810903059156

Tibbetts, B. L., J. C. Behrendt, and J. D. Love, 1969, Seismic refraction measurements in Jackson Hole, Wyoming: Geological Society of America Bulletin, v. 80, no. 6, p. 1109-1122.

Touloukian Y.S., Judd W.R., and Roy R.F. (eds), 1989, Physical Properties of Rocks and Minerals. CINDAS data series on material properties, Group II, Properties of special materials, II-2. McGraw-Hill, New York.

Turcotte, D. L., & Schubert, G., 1982, Applications of continuum physics to geological problems. John Wiley & Sons.

Turcotte, D.L. and Schubert, G., 2002, Geodynamics. 2nd ed., Cambridge University Press, Cambridge, UK.

Turcotte, D.L., 1979, Flexure: In Advances in Geophysics, v. 21, pp. 51-86.

Velasco, M. S., Bennett, R. A., Johnson, R. A., and Hreinsdóttir, S., 2010, Subsurface fault geometries and crustal extension in the eastern Basin and Range Province, western U.S. Tectonophysics, v. 488, no. 1-4, p. 131-142. doi.org/10.1016/j.tecto.2009.05.010

Von Tish, D. B., Allmendinger, R. W., & Sharp, J. W., 1985, History of Cenozoic extension in central Sevier Desert, west-central Utah, from COCORP seismic reflection data. AAPG Bulletin, v. 69, n. 7, p. 1077-1087.

Walcott, R.I., 1970, Flexural rigidity, thickness, and viscosity of the lithosphere: Journal of Geophysical Research, v. 75, no. 20, p. 3941-3954.

Watts, A.B. and Burov, E.B., 2003, Lithospheric strength and its relationship to the elastic and seismogenic layer thickness: Earth and Planetary Science Letters, v. 213, no. 1-2, p. 113-131.

Watts, A.B., 2001, Isostasy and Flexure of the Lithosphere: Cambridge University Press.

Watts, A.B., Karner, G. And Steckler, M.S., 1982, Lithospheric flexure and the evolution of sedimentary basins: Philosophical Transactions of the Royal Society of London. Series A, Mathematical and Physical Sciences, v. 305, no. 1489, p. 249-281.

Wernicke, B. And Axen, G.J., 1988, On the role of isostasy in the evolution of normal fault systems: Geology, v. 16, no. 9, p. 848-851.

Wernicke, B. And Burchfiel, B.C., 1982, Modes of extensional tectonics: Journal of Structural Geology, v. 4, no. 2, p. 105-115.

White, B.J.P., Smith, R.B., Husen, S., Farrell, J.M., Wong, I., 2009, Seismicity and earthquake hazard analysis of the Teton-Yellowstone region, Wyoming: Journal of Volcanology and Geothermal Research, doi:10.1016/j.volgeores.2009.08.015.

VITA

Autumn Lynne Helfrich

Education

B.S. Professional Geology (2018)

Bloomsburg University of Pennsylvania

Experience

Graduate Teaching / Research Assistant

Structure and Geodynamics Lab

Department of Earth and Environmental Sciences

University of Kentucky, 40506

Undergraduate Research Assistant

Department of Environmental, Geographical, and Geological Sciences

Bloomsburg University of Pennsylvania, 17815

Undergraduate Research Assistant

Department of Earth and Environmental Sciences / Department of Geology

Vanderbilt University, 37240 / Mercyhurst University, 16546